New Insights into the Verwey Transition in Magnetite

THÈSE N^{O} 8496 (2018)

PRÉSENTÉE LE 3 MAI 2018
À LA FACULTÉ DES SCIENCES DE BASE
LABORATOIRE POUR LA MICROSCOPIE ET LA DIFFUSION D'ÉLECTRONS
PROGRAMME DOCTORAL EN PHYSIQUE

ÉCOLE POLYTECHNIQUE FÉDÉRALE DE LAUSANNE

POUR L'OBTENTION DU GRADE DE DOCTEUR ÈS SCIENCES

PAR

Simone BORRONI

acceptée sur proposition du jury:

Prof. O. Schneider, président du jury
Prof. F. Carbone, Prof. H. Brune, directeurs de thèse
Prof. P. van Loosdrecht, rapporteur
Prof. D. Basov, rapporteur
Prof. N. Marzari, rapporteur

ÉCOLE POLYTECHNIQUE
FÉDÉRALE DE LAUSANNE
Suisse
2018

to my parents

Abstract

Magnetite (Fe_3O_4) is the first magnetic material discovered by mankind. Despite thousands of years of applications, from the magnetic compass to data storage, and decades of basic research, it remains among the most fascinating materials for physicists. The most important reason for the continuous interest in magnetite is the occurrence of discontinuous changes in its ground state around 120 K, the so-called Verwey transition, characterized by profound modifications in the electronic structure, mutually related to atomic displacements. The remarkable complexity of the transformation process still leaves open fundamental problems in the understanding of the microscopic mechanism of the Verwey transition. Further research efforts are needed to better describe the nature of the elementary excitations at the origin of the initial instability, how it propagates in different degrees of freedom and its relationship to precursor phenomena. This Thesis combines together the potentials of steady-state and time-resolved spectroscopy to study the critical dynamics of the lattice vibrations, and the fluctuations of electronic and structural order across the Verwey transition. Their signatures are identified in the coherent response of the optical functions to ultrashort laser pulses, and the inelastic scattering of light and neutrons, which provide complementary information, with selective sensitivity to different types of elementary excitations. Among the most important results, we manage to observe in the energy and time domain critical modes with different interplay of charge distribution and atomic displacements, and diffusive dynamics, typical of an order-disorder process.

Key words: magnetite, Verwey transition, critical dynamics, critical fluctuations, ordering field, ultrafast spectroscopy, Raman scattering, inelastic neutron scattering

Résumé

La magnétite est le premier matériau magnétique découvert par l'homme. Malgré des millénaires d'applications, de la boussole au stockage de données, et des décennies de recherche fondamentale, elle reste un des matériaux les plus fascinants pour les physiciens. Les raisons les plus importantes derrière l'intérêt continu pour la magnétite sont les changements discontinus qui ont lieu dans son état fondamental autour de 120 K, ce que l'on appelle la transition de Verwey, caractérisée par de profondes modifications dans la structure électronique, en relation mutuelle avec des déplacements atomiques. La complexité considérable du processus de transformation laisse ouverts des problèmes fondamentaux dans la compréhension du mécanisme microscopique de la transition de Verwey. Des efforts supplémentaires sont nécessaires dans la recherche fondamentale pour mieux décrire la nature des excitations élémentaires à l'origine de l'instabilité initiale, comment elle se propage dans les différents degrés de liberté et sa relation avec des phénomènes précurseurs. Cette Thèse combine les potentiels de la spectroscopie en régime permanent et avec résolution temporelle pour étudier la dynamique critique des vibrations du réseau, et les fluctuations de l'ordre électronique et structural à travers la transition de Verwey. Leurs caractéristiques distinctives sont identifiées dans la réponse cohérente des fonctions optiques à des impulsions laser ultracourtes, et dans la diffusion inélastique de lumière et neutrons, qui nous fournissent des informations complémentaires, avec une sensibilité sélective à différents types d'excitations élémentaires. Parmi les résultats les plus importants, nous pouvons observer dans le domaine du temps et de l'énergie des modes critiques avec différentes relations mutuelles de la distribution de charge et des déplacements atomiques, et dynamique diffusive, typique d'un processus ordre-désordre.

Mots clés : magnétite, transition de Verwey, dynamique critique, fluctuations critiques, champ d'ordre, spectroscopie ultrarapide, diffusion Raman, diffusion inélastique de neutrons

Sommario

La magnetite è il primo materiale magnetico scoperto dall'uomo. Nonostante millenni di applicazioni, dalla bussola allo stoccaggio dati, e decenni di ricerca di base, essa rimane uno dei materiali che più affascinano i fisici. Le ragioni più importanti alla base del continuo interesse per la magnetite sono i cambiamenti discontinui che si verificano nel suo stato fondamentale intorno a 120 K, la cosiddetta transizione di Verwey, caratterizzata da modifiche profonde nella struttura elettronica, in mutua relazione con spostamenti atomici. La notevole complessità del processo di trasformazione lascia tuttora aperti problemi fondamentali nella comprensione del meccanismo microscopico della transizione di Verwey. Sforzi ulteriori sono necessari nella ricerca di base per meglio descrivere la natura delle eccitazioni elementari all'origine dell'instabilità iniziale, come essa si propaga nei diversi gradi di libertà e la sua relazione con fenomeni precursori. Questa Tesi combina insieme i potenziali dello spettroscopia a stato stazionario e risolta in tempo per studiare la dinamica critica delle vibrazioni reticolari, e le fluttuazioni dell'ordine elettronico e strutturale attraverso la transizione di Verwey. Le loro caratteristiche distintive sono identificate nella risposta coerente delle funzioni ottiche ad impulsi laser ultrabrevi, e nella diffusione anelastica di luce e neutroni, le quali forniscono informazioni complementari, con sensibilità selettiva a diversi tipi di eccitazioni elementari. Tra i risultati più importanti, siamo in grado di osservare nel dominio del tempo e dell'energia modi critici con diverse relazioni reciproche della distribuzione di carica e degli spostamenti atomici, e dinamica diffusiva, tipica di un processo ordine-disordine.

Parole chiave: magnetite, transizione di Verwey, dinamica critica, fluttuazioni critiche, campo d'ordine, spettroscopia ultraveloce, diffusione Raman, diffusione anelastica di neutroni

Contents

Abstract (English/Français/Italiano) **v**

Acronyms **xiii**

Introduction **1**

1 Open Problems in Magnetite **5**
- 1.1 Structural, Charge and Orbital Order 5
- 1.2 Optical Response 8
- 1.3 Conduction Mechanism 10
- 1.4 Precursor Effects 14

2 Methods **17**
- 2.1 Spontaneous Raman Scattering 17
- 2.2 Ultrafast Broadband Reflectivity 19
- 2.3 Inelastic Neutron Scattering 24
- 2.4 Magneto-Optical Kerr Effect 26

3 Coherent Generation of Symmetry-Forbidden Phonons **31**
- 3.1 Experiments 32
- 3.2 Results 34
  - 3.2.1 Ultrafast Broadband Reflectivity 34
  - 3.2.2 Phonon Calculations and Mode Assignment 39
  - 3.2.3 Raman Matrix Element Analysis and Optical Constant Calculations . . . 40
  - 3.2.4 Fluctuation-Assisted Excitation of Phonons 45
- 3.3 Discussion 48
- 3.4 Conclusions 49

4 Light Scattering from Critical Modes **51**
- 4.1 Experiments 52
- 4.2 Results and Discussion 53
  - 4.2.1 Phonon Excitations 54
  - 4.2.2 Structural Anomalies 57
  - 4.2.3 Magnetic or Electronic Excitations 61
  - 4.2.4 Diffusive Excitations 65

4.3 Conclusions 69
4.4 Raman Scattering from Two Diffusive Modes 70

5 Neutron Scattering from Critical Modes 73
5.1 Experiments 75
5.2 Lattice Dynamical Anomaly of the Order Parameters 77
5.2.1 Results 77
5.2.2 Discussion and Conclusions 81
5.3 Polaron and Electronic Fluctuations 84
5.3.1 Pak and Kinase's Model 84
5.3.2 Results 88
5.3.3 Discussion and Conclusions 90

6 Spin-Reorientation Transitions in Magnetite 95
6.1 Introduction 96
6.2 Experiments 98
6.3 Results 99
6.4 Discussion 105
6.4.1 Spin-Reorientation Transitions 105
6.4.2 Anomalous Coercive Field 106
6.5 Preliminary Simulations 108

7 Clean Transfer of Graphene 113
7.1 Introduction 114
7.2 Methods 116
7.3 Results and Discussion 122
7.4 Conclusions and Perspectives 131

Conclusions and Perspectives 135

Bibliography 137

Acknowledgements 155

Curriculum Vitæ 157

Acronyms

BVS bond valence sum.

CDW charge density wave.

CVD chemical vapour deposition.

DFT density functional theory.

FASRS fluctuation-assisted stimulated Raman scattering.

FT Fourier transform.

GGA generalized gradient approximation.

h-BN hexagonal boron nitride.

INS inelastic neutron scattering.

ISRS impulsive stimulated Raman scattering.

KK Kramers-Kronig.

LSDA local spin density approximation.

MOKE magneto-optical Kerr effect.

NRIXS nonresonant inelastic x-ray scattering.

OOMMF Object Oriented Micromagnetic Framework.

OP order parameter.

PDMS polydimethylsiloxane.

PEN polyethylene naphthalate.

PET polyethylene terephtalate.

PMMA polymethilmethacrylate.

PVA polyvinyl alcohol.

RIXS resonant inelastic x-ray scattering.

RME Raman matrix element.

rms root mean square.

SLG single-layer graphene.

SP small polaron.

SVD singular value decomposition.

TA transverse acoustic.

TEM transmission electron microscopy.

TO transverse optical.

TSRS transient stimulated Raman scattering.

UHV ultrahigh vacuum.

Introduction

Magnetite (Fe_3O_4) is the magnetic material which has been known to mankind for the longest time. Nowadays, it is of technological interest in different fields, such as data storage, magnetic sensing and catalysis, and holds promise for prospect applications in spintronics. From a fundamental point of view, it has been the subject of extensive experimental and theoretical research, and still attracts continuous attention. Indeed, the complex interrelations of electronic, structural and magnetic phenomena have so far eluded a complete understanding of important physical properties. Basic questions on essential characteristics at room temperature have yet to be answered. For instance, it is not clearly established whether the ground state is half-metallic or semiconducting, the degree of delocalization of the charge carriers, the main conduction mechanism and the assignment of the interband transitions in the optical functions.

The competition between strong electronic correlations and electron-phonon interactions gives rise to the so-called Verwey transition at a critical temperature around 120 K. Important discontinuous modifications of both the electronic and crystal structures produce great consequences on different physical properties. The increase in resistivity by a factor of one hundred and the decrease in crystal symmetry from cubic to monoclinic are the most significant manifestations of the transformation process.

The Verwey transition is perhaps one of the most intensively investigated phase transitions in transition-metal oxides. Nevertheless, satisfactory answers to fundamental questions on the microscopic mechanism of the critical dynamics are still missing. The study of the ground state of charge and orbital order, and the more subtle atomic displacements in the monoclinic phase has long remained a theoretical and experimental challenge. The occurrence itself of long-range order in the monoclinic phase has been repeatedly questioned. Only recently it has been disclosed that delocalized electrons and structural distortions are coupled together in an arrangement of three-site polarons of impressive complexity. This has aroused renewed interest towards a comprehensive description of the Verwey transition.

Often, in phase transitions of solids, instabilities develop in the free energy, as a consequence of intrinsic characteristics and mutual interactions of elementary excitations. For instance, these can be collective modes of lattice vibrations and charge fluctuations, whose equilibrium configurations change across the transition temperature. In continuous phase transitions, progressive decrease in stability translates into softening or slowing down of critical modes on approaching the transition temperature, depending on whether they are propagating or diffusive.

In the simple case of displacive transitions of second order, for the onset of harmonic instabilities in the interionic potential, a subset of phonon modes gradually downshifts in frequency towards the transition temperature. In more complex cases, instabilities reside in elementary excitations of different nature or interactions among them. Modifications in the characteristics of the critical modes depend on their reciprocal coupling and dynamics. For instance, in the presence of instabilities of electronic excitations, strongly coupled to lattice vibrations, phonon softening still takes place, if the electronic excitations follow adiabatically the lattice vibrations. Fundamental problems to be solved in phase transitions of solids are the nature of the critical modes which first become unstable and thereby initiate the transformation process, whether or not a cause-effect hierarchy is established among the elementary excitations which take part in the critical dynamics, and their mutual interactions and time scales.

These important issues remain to be settled in the case of the Verwey transition in magnetite. Alternative scenarios have been proposed on theoretical and experimental grounds, with emphasis on electronic, structural or cooperative driving forces, in the framework of an order-disorder or a Peierls-like transition. Furthermore, different observations provided evidence of local dynamic order in the cubic phase, comprised of both atomic displacements and charge distributions. The temperature and wave-vector dependence of the precursor phenomena are suggestive of a continuous phase transition to a potential incommensurate phase bypassed by the Verwey transition. The relationship between short- and long-range order, respectively, in the cubic and monoclinic phase is unclear. So are the consequences of short-range order on the transformation process and the conduction mechanism in the cubic phase.

The main objective of this Thesis is to contribute to the solution of the above problems. For this purpose, we studied the critical dynamics of phonons and ordering field modes across the Verwey transition, both in the energy and time domain, by means of steady-state and time-resolved techniques sensitive to different degrees of freedom. This Thesis is organized as follows.

Chapter 1 introduces the general features of magnetite and the Verwey transition. We put emphasis on the open problems in the understanding of the physical properties of the material and the origin of the transformation process. We compare the different scenarios which have been proposed as possible solutions.

Chapter 2 presents an overview on the basic principles of the experimental techniques and a description of the set-ups used in this Thesis, in a problem-oriented approach, intended to combine together the potentials of different methods to gain complementary information.

Chapter 3 is devoted to the investigation of the coherent response of magnetite to impulsive photoexcitation across the Verwey transition by means of ultrafast spectroscopy. We show that

Raman-active phonons can be coherently generated, both at the center of the Brillouin zone, in the monoclinic phase, and at finite wave vector, in the cubic phase. We set up a theoretical model able to account for the role of short-range order in the photoexcitation mechanism. To identify the phonons, study how they couple to electronic excitations at high energy and thereby reexamine the assignment of the interband transitions in the optical functions, we combine together steady-state and time-resolved data, and *ab initio* computations of the phonon dispersion curves and the optical functions.

Chapter 4 is focused on the anomalies of the Raman-active phonons at the center of the Brillouin zone, from structural transformations and coupling to electronic excitations, measured through spontaneous Raman scattering. We also analyze the incoherent component of the Raman response. In particular, we investigate the dynamics of diffusive excitations with critical characteristics by means of a theoretical model.

Chapter 5 directly addresses the temperature dependence across the Verwey transition of phonons of finite wave vector at low energy. In particular, by means of inelastic neutron scattering, we study the transverse acoustic branch and phonons of the same symmetries proposed as the primary order parameters of the structural transformation. We also discuss the origin of the so-called central peak, coupled to the phonons, and compare the time scales of the diffusive excitations observable with light and neutron probes.

Chapter 6 deals with the modifications in the magnetic properties of magnetite associated with both the Verwey transition and precursor phenomena. In particular, we study the magnetic stability at the surface by means of magneto-optical Kerr effect. To better understand our observations, we analyze the results of preliminary micromagnetic simulations.

Chapter 7 discusses a parallel project on the clean transfer of graphene in ultrahigh vacuum to fabricate nanostructures for data storage. We outline the general directions of the project on the grounds of current methods and promising solutions for future developments. We interpret the results of procedures for graphene growth and clean transfer in air based on Raman characterization.

1 Open Problems in Magnetite

1.1 Structural, Charge and Orbital Order

The crystal structure of magnetite at room temperature was first determined by W. H. Bragg in one of the earliest publications on x-ray diffraction in 1915 [1]. In the same year, W. H. Bragg and his son W. L. Bragg were jointly awarded the Nobel Prize in Physics for the development of x-ray diffraction. The formula unit of magnetite is $\mathrm{Fe}_A^{3+}(\mathrm{Fe}^{2+}\mathrm{Fe}^{3+})_B\mathrm{O}_4^{2-}$, where A (B) denotes sites with tetrahedral (octahedral) coordination by O^{2-} ions. In normal spinels, the bivalent (trivalent) ions occupy A (B) sites. Instead, in inverse spinels such as magnetite, all of the bivalent ions occupy B sites, and the trivalent ions are equally distributed between A and B sites. The conventional cell of magnetite is a cube with lattice parameter $a = 8.39\,\text{Å}$ comprised of 8 formula units. 1/8 of the 64 A sites are occupied by Fe^{3+} ions, and 1/2 of the 32 B sites are occupied by an equal number of Fe^{3+} and Fe^{2+} ions. The primitive cell of magnetite, shown in Fig. 1.1(a), contains only 2 formula units, and can be thought of as three corner-sharing cubes. The A-type Fe ions at the centers of the two lower cubes coordinate tetrahedra of O^{2-} ions, and the upper cube is made of alternated B-type Fe ions and O^{2-} ions.

The phase transition discussed in this Thesis was named after the Dutch chemist E. Verwey, who first discovered a discontinuous change in the resistivity of magnetite by two orders of magnitude (see Fig. 1.2(a)) [2]. The critical temperature, also called Verwey temperature, T_V, depends on impurity content and stoichiometry deviations of the sample. Typical values in high-purity samples range between 110 and 125 K [3]. The temperature dependence of the resistivity below 300–350 K is characteristic of a semiconductor-like behaviour, which is possible to describe by Arrhenius laws, with different activation energies above and below T_V [4]. Instead, above 300–350 K, it is typical of a metal-like behaviour. Often, based on the resistivity values, the low- and high-temperature phases are also referred to, respectively, as the insulating and conductive phases, and the Verwey transition as a metal-insulator transition.

Verwey proposed that the microscopic explanation of his observations is the onset of long-range order among Fe_B^{2+} and Fe_B^{3+} ions in the low-temperature phase. In particular, according to his hypothesis, chains of Fe_B^{2+} and Fe_B^{3+} ions parallel to respectively the [110] and [1$\bar{1}$0]

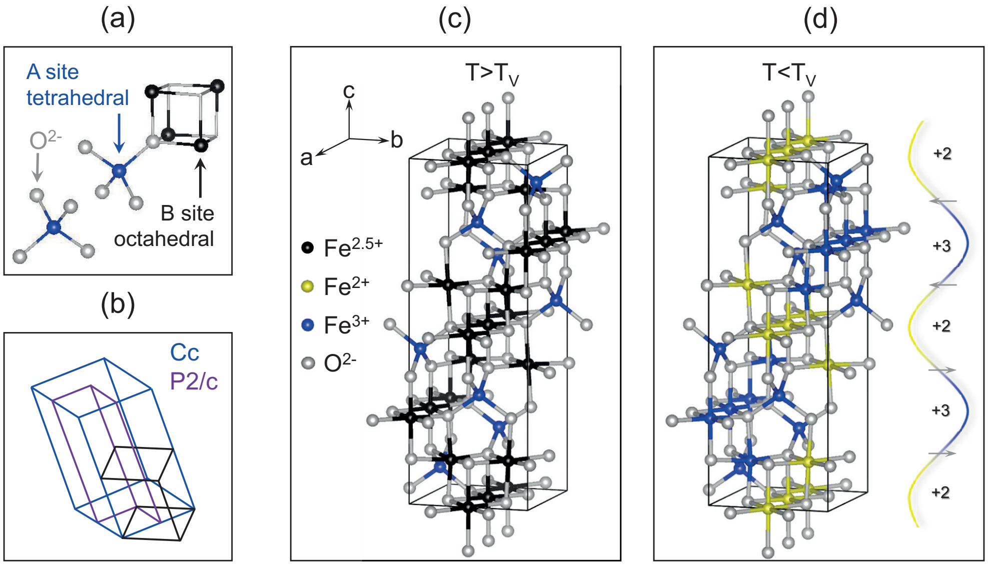

Figure 1.1 – (a) Primitive cell of magnetite in the high-temperature phase. (b) Relationship between (violet) *P2*/*c* and (blue) *Cc* cells used in refinements of the crystal structure of magnetite in the low-temperature phase. The pseudocubic cell originating from rhombohedral distortion along the cube diagonal is also plotted in black. Crystal structure of magnetite in the (c) high- and (d) low-temperature phase, visualized with VESTA [5], in the *P2*/*c* cell, based on Wright et al.'s refinement [6, 7]. Fe ions in octahedral sites are in mixed charge states. In the high-temperature phase, on average, the extra electrons are disordered. Instead, in the low-temperature phase, modulations of the charge states establish on the long range, represented by a colored line. Arrows denote the opposite phases of charge order along the *b* direction at $z = a/4, 3a/4$ and $z = 5a/4, 7a/4$.

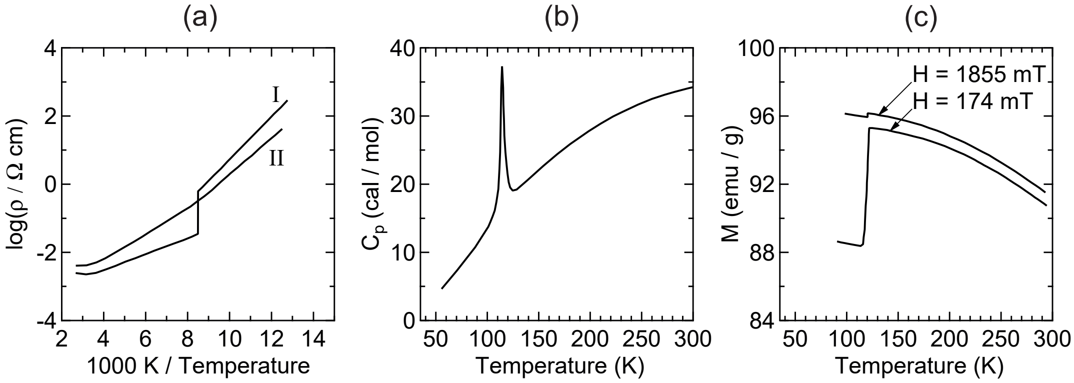

Figure 1.2 – Most important manifestations of the Verwey transition in magnetite, namely, (a) discontinuous change in the resistivity [2], (b) specific heat anomaly [8] and (c) discontinuous change in the magnetization [9]. The curves I and II in panel (a) refer to different FeO:Fe_2O_3 ratios of respectively 1:1.025 and 1:1.08.

directions alternate in the [001] direction [10]. This fulfills the criterion for minimum electrostatic repulsion within tetrahedra of B-type Fe ions proposed by Anderson [11]. He also first suggested the occurrence of short-range order, instead of complete disorder, above T_V, with better agreement with the experimental value of the entropy variation at the Verwey transition.

Additional important modifications in the physical properties of magnetite accompanying the Verwey transition were progressively discovered (see, for instance, Figs. 1.2(b,c)) [12]. One of the most prominent changes takes place in the crystal structure. As discussed in the following, complex atomic displacements cause lowering of the crystal symmetry on cooling across T_V. Verwey, Anderson, and subsequent Cullen and Callen's theoretical predictions [13] all account for electron-electron interactions alone. None of them was able to explain the intricate nature of the concomitant modifications in the crystal structure.

Structural, charge and orbital order of magnetite in the low-temperature phase are interrelated problems. Despite extensive research, they have long remained controversial. The occurrence itself of long-range charge and orbital order has been questioned [14, 15]. In early refinements, consistent to Verwey's hypothesis, it was proposed that the crystal system of magnetite changes from cubic to orthorhombic with decreasing temperature across T_V [16, 17]. In the same years, different diffraction studies provided evidence of a rhombohedral distortion of the cubic cell upon the Verwey transition, which first disproved Verwey's hypothesis [18, 19]. The observation of satellite reflections at half-integer indexes pointed out that the crystal system of the low-temperature phase of magnetite is in fact monoclinic with space group *Cc* and a $\sqrt{2}a \times \sqrt{2}a \times 2a$ supercell [20–22]. The first accurate refinement was carried out by Iizumi et al. in 1982 [23]. The intensity distribution of the reflections was analyzed in a $a/\sqrt{2} \times a/\sqrt{2} \times 2a$ subcell under the assumption of the space group *P2/c* (see Fig. 1.1(b)), and additional *Pmca* pseudosymmetry constraints, which together are able to account for most of the atomic displacements. An analogous refinement was performed by Wright and coworkers [6, 7]. In addition, based on bond valence sum (BVS) calculations, they proposed an approximate model of charge order.

Figures 1.1(c,d) provide a scheme of the charge states in magnetite based on Wright et al.'s refinement. For simplicity, the ions are labeled according to their nominal valences. Fe_B^{2+} and Fe_B^{3+} ions correspond to the so-called $B1$–$B4$ and $B2$–$B3$ Fe ions. These are two groups of Fe ions with different average Fe–O distances and, according to BVS calculations, different average charge states, equal to, respectively, +2.4 and +2.6. Modulations of the charge states are evident among B-type Fe ions along the c axis (see lines and arrows in Fig. 1.1(d)). An amplitude modulation with the same periodicity as the cubic cell is given by alternate high and low valence states in planes at $z = ka/2$, $k \in \mathbb{N}$, and mixed valence states in planes at $z = (2k+1)a/4$. A phase modulation with double the periodicity of the cubic cell is given by the opposite phases of the chains of Fe ions in the planes with mixed valence states, in the upper and lower half of the monoclinic cell.

According to the above refinements, the structural distortions in the monoclinic phase can be described by the freezing of a subset of phonon modes of the cubic phase at the Γ, Δ, X and W points of the Brillouin zone. The involvement of the structural degree of freedom in the transformation process was first accounted for by Yamada based on the symmetry of the atomic displacements at that time considered the most important [24]. He proposed that the main driving force for the Verwey transition is the condensation of fluctuations of charge order coupled to a transverse acoustic (TA) phonon mode of Δ_5 symmetry. More recent first-principle computations suggested that both phonon modes of Δ_5 and X_3 symmetry are the primary order parameters (OPs) for the structural transformation [25, 26]. Moreover, the coupling between atomic displacements of X_3 symmetry and electronic states close to the Fermi level was proposed as the main cause for the changes in the conduction mechanism of magnetite at the Verwey transition.

As shown in Fig. 1.1(b), Wright and coworkers' scheme is the average over four inequivalent $P2/c$ subcells of the Cc supercell. In fact, more complex modulations of the charge states are possible in the ab plane. More recently, Senn et al. performed a thorough refinement in the Cc supercell, with important consequences on the general understanding of the Verwey transition [27, 28]. According to Senn and coworkers, it is not possible to single out a subset of phonon modes whose condensation is responsible for the structural distortions altogether. Instead, local order is the driving force for the atomic displacements. In particular, Senn et al. argued that the building block of the low-temperature phase is a three-site polaron, named trimeron, which originates from the coupling between an extra electron, delocalized over three B-type Fe ions, and the displacements of the two end Fe ions towards the central Fe ion. In a pictorial interpretation, complexes of fluctuating trimerons constitute a liquid of quasiparticles, whose solidification process is the essential mechanism of the Verwey transition.

1.2 Optical Response

The conduction mechanism and the optical response at low energy depend on the electronic states close to the Fermi level. In magnetite, these mainly result from the strong correlations among the electrons in the $3d$ orbitals of the Fe ions, and mostly lie within a large band gap between O $2p$ and Fe $4s$ states. The local symmetry of the crystal field at A (B) sites splits the Fe $3d$ states into e and t_2 (t_{2g} and e_g) states. For the large exchange splitting, all Fe ions are in high-spin configurations. Therefore, in principle, only the minority-spin $3d$ t_{2g} states of Fe_B^{2+} ions can cross the Fermi level. Both *ab initio* calculations [25, 26, 31–36] and photoemission experiments [37–40] show that the large onsite Coulomb repulsion in the monoclinic phase splits these states into different bands above and below the Fermi level. In contrast, the results from photoemission experiments in the high-temperature phase are controversial on whether or not a finite band gap at the Fermi level persists above T_V [37–44].

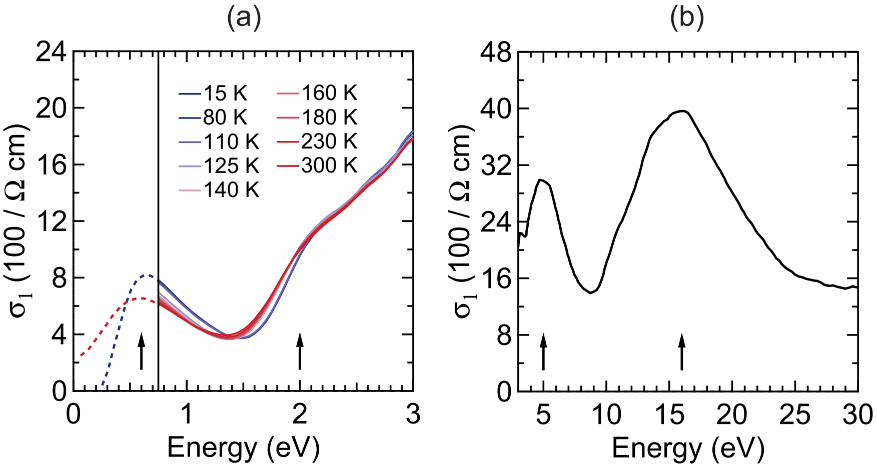

Figure 1.3 – Real part of the optical conductivity, σ_1, (a) as a function of temperature, below 3 eV, from ellipsometry data, and (b) at 290 K, between 3 and 30 eV, from a Kramers-Kronig (KK) analysis of reflectivity data. Dashed lines represent extrapolations below 0.75 eV based on fits to the data at 15 and 300 K. Arrows indicate the energy positions of the four main features discussed in the text. A vertical line denotes the lower boundary of the detection range in the ellipsometry experiments. Adapted from Refs. [29, 30].

Figure 1.3 shows the real part of the optical conductivity of magnetite, in different energy ranges, from recent ellipsometry data [29] and a KK transformation of previous reflectivity data [30]. The strongly correlated nature of magnetite manifests itself in transfers of spectral weight among different regions of the spectrum [45]. The most important features in the temperature dependence of the optical response are the precursor modifications in the cubic phase and the discontinuous changes at the transition temperature, which are direct consequences of the different electronic structures in the two phases [29, 30].

An optical gap opens below the transition temperature. Available estimates of its size are 0.2 [29, 46] and 0.14 eV [30]. The four main features observable in the optical conductivity, indicated by arrows in Fig. 1.3, are centered at respectively 0.6, 2, 5 and 16 eV. In general, the absorption structures below 2.5 eV were attributed to interband transitions between Fe 3d states. However, alternative interpretations were proposed, at variance on whether only B or also A sites are involved [29–31, 47]. Figure 1.4 provides a schematic picture of possible assignments. Based on local spin density approximation (LSDA) calculations [47], Park et al. ascribed the above four features respectively to (i) intersite transitions between 3d t_{2g} states of Fe_B^{2+} and Fe_B^{3+} ions, (ii) analogous processes, but between 3d states of respectively Fe_B^{2+} and Fe_A^{3+} ions, (iii) charge transfer excitations between O 2p and Fe 3d states, and (iv) optical absorption between O 2p and Fe 4s states [30]. For simplicity, B-type Fe ions are referred according to their nominal valence states, although in fact the differences in charge state are small.

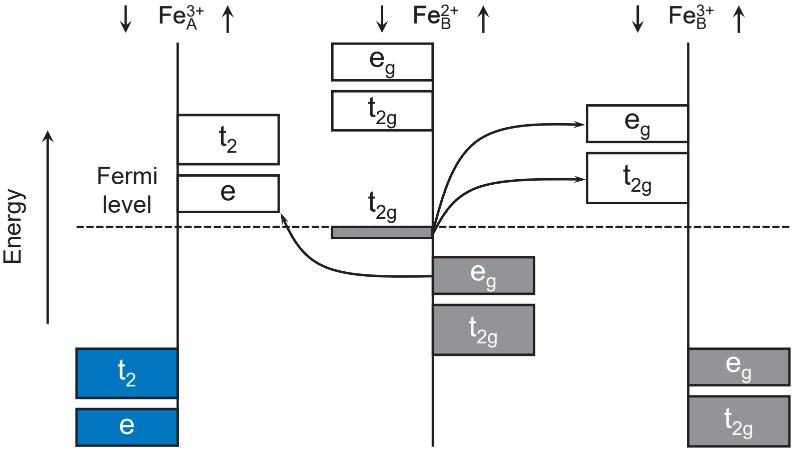

Figure 1.4 – Simplified representation of the band structure in the monoclinic phase. Only Fe $3d$ states are shown. Majority and minority spin states are labeled by upward and downward arrows, respectively. The relative energy positions of the bands are qualitatively based on Leonov and coworkers' estimates of the exchange and crystal-field splitting, and the effects of the onsite Coulomb repulsion [31]. Arrows illustrate the interband transitions below 2.5 eV under discussion in the assignments of Refs. [30, 31].

Leonov and coworkers revised previous assignments according to advanced LSDA+U calculations [31]. They proposed that the feature at 2 eV does not involve A-type Fe ions, but only B-type Fe ions with different charge states, similarly to the feature at 0.6 eV, but with $3d$ e_g final states. The overall agreement of the theoretical predictions by Leonov and coworkers to the experimental data is better compared to previous *ab initio* computations. However, they do not to reproduce the energy position of the feature at 0.6 eV and the intensity of the feature at 2 eV, possibly for the assumption of an approximate symmetry $P2/c$. Therefore, the discussion on the interpretation of the optical response of magnetite is not yet closed.

1.3 Conduction Mechanism

The origin of the conducting state in the cubic phase of magnetite is also under discussion. In particular, there is no general consensus on the degree of localization of the electronic states and, as a consequence, the nature itself of the charge carriers, and the relative importance of processes of band conduction of electrons and transport of small polarons (SPs). The open problems on the driving forces for the Verwey transition and the conduction mechanism in the cubic phase are mutually related. Indeed, the scenario of an order-disorder transformation in the electronic degree of freedom is more consistent with the predominance of charge carriers made of SPs with large effective mass and low propensity to coherent motion. Opposite considerations hold true for a mechanism which better resembles a Peierls transition.

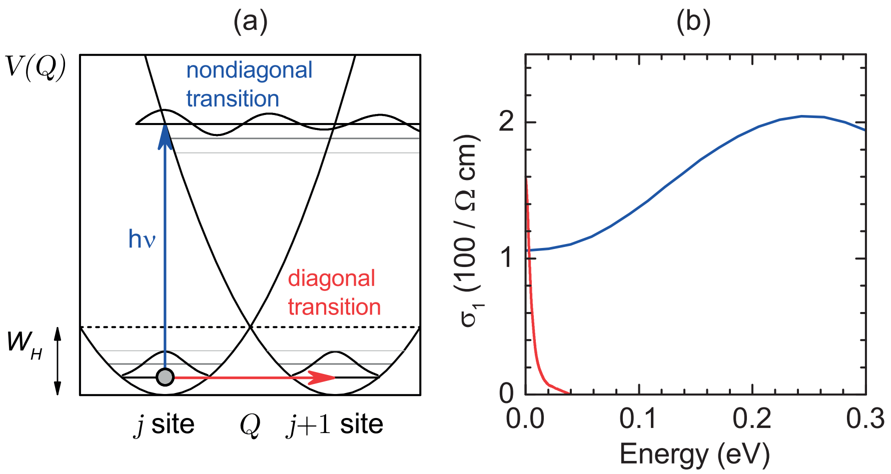

Figure 1.5 – (a) Pictorial representation of (red arrow) diagonal and (blue arrow) nondiagonal transitions of SPs between two sites, starting from the ground state, where Q and $V(Q)$ are respectively the configurational coordinate and the potential energy of the polaron. (b) Contributions to the real part of the optical conductivity, σ_1, at 300 K, from (red) diagonal and (blue) nondiagonal transitions, according to Ihle and Lorenz's theoretical prediction [48].

The occurrence of local dynamical correlations supports the preeminence of polaronic conduction (see Section 1.4). However, the consequences of precursor effects on the conducting state are poorly explored. In principle, even within a polaronic picture, two types of conduction mechanisms are possible. SPs can move via both diagonal and nondiagonal transitions, with different contributions to the optical conductivity, and characteristic energy and temperature dependences [49]. These processes are exemplified in Fig. 1.5(a). According to an illustrative description, in diagonal transitions, SPs tunnel through the hopping barrier, without the assistance of phonons. In analogy to band conduction, upon line broadening from disorder, diagonal transitions give rise to a Drude peak at low frequency in the optical conductivity. At finite temperatures, nondiagonal transitions also contribute to the spectral weight of the Drude peak. The most probable nondiagonal transitions are analogous to Franck-Condon processes, in which electrons hop from occupied to unoccupied sites, without lattice relaxation. These produce the so-called polaron peak at finite energy in the optical conductivity.

Ihle and Lorenz identified the polaron peak with a broad weak feature at 0.2 eV observable in the optical conductivity calculated by means of a KK transformation of early reflectivity data [50, 51]. More recent experiments did not confirm the presence of this feature [30, 46], which probably originates from impurities [52] or artifacts of the KK analysis. Based on their erroneous assumption, Ihle and Lorenz put forth a microscopic theory for SP conduction in magnetite, which predicts a leading role of diagonal transitions below 400 K. Figure 1.5(b) exemplifies the components of the optical conductivity originating from diagonal and nondiagonal transitions in Ihle and Lorenz's model. More recent studies suggested that the polaron peak in fact corresponds to the feature at 0.6 eV [30, 46]. This implies that nondiagonal transitions are equivalent to intersite transitions between $3d$ t_{2g} states of Fe_B^{2+} and Fe_B^{3+} ions.

The reflectivity data available in the mid-infrared are inconclusive on the possible occurrence of a small Drude peak at low frequency [30, 46, 50]. The tail of the feature at 0.6 eV and features of optical phonons predominate in the same energy range, and reliability limitations are intrinsic to the KK transformation of reflectivity data. On the other hand, ellipsometry data, which directly provide the complex dielectric function, are only available between 0.75 and 3.5 eV [29].

Let us consider the possible implications of the more recent assignment of the polaron peak [30, 46], with reference to the simple model of an electron that moves between two sites, coupled to a harmonic oscillator. The energy barrier that the electron must overcome to hop between sites with the assistance of phonons is $W_H \approx h\nu/4$, where $h\nu$ is the photon energy required to change the position of the electron, without any modification in the configuration of the atoms (see Fig. 1.5(a)). The process being considered is the analogous of the Franck-Condon process with the highest probability which takes place at the central position of the polaron peak in optical conductivity. Therefore, if this is identified with the 0.6 eV peak, an approximate estimate of W_H is 0.15 eV. Clearly, the large value of W_H rules out both band conduction of electrons and any meaningful contribution to the dc conductivity from diagonal transitions. Quantitatively speaking, the effective mass and the probability of diagonal transitions respectively increase and decrease on increasing W_H following exponential laws [49]. Using the above values and the energy of the hardest phonon with optical activity, $E_0 = 83$ meV, Ref. [46] provided the following approximate estimate of the effective to free electron mass ratio, computed according to Mott equation [53, 54], which is indeed consistent with polaron conduction,

$$\frac{m^*}{m} \approx 5 \exp\left(\frac{2W_H}{E_0}\right) \approx 200. \tag{1.1}$$

In fact, this approximate estimate only represents a lower bound. m^*/m becomes much larger, if softer phonons are accounted for. The most important phonons which come into play in the formation of the SPs are the same phonons whose condensation produces the atomic displacements with the largest amplitude in the trimerons. The cooperative contribution of different phonons with comparable amplitudes does not allow us to define any simple hierarchy, and thus single out phonons of prevalent importance, to provide more accurate estimates [27].

The above considerations confirm that it is needful to account for the consequences of heavy localized SPs on the critical dynamics of the Verwey transition. For the purpose, let us start from a general description, based on the model Hamiltonian [49]

$$\begin{aligned} H = {} & \sum_i c_i^\dagger c_i \left[\varepsilon_c + \sum_{\boldsymbol{q}\lambda} M_{\boldsymbol{q}\lambda} \left(a_{\boldsymbol{q}\lambda} + a_{\boldsymbol{q}\lambda}^\dagger \right) e^{-i\boldsymbol{q}\cdot\boldsymbol{r}_i} \right] + \sum_{\boldsymbol{q}\lambda} \hbar\omega_{\boldsymbol{q}\lambda} a_{\boldsymbol{q}\lambda}^\dagger a_{\boldsymbol{q}\lambda} \\ & + \frac{1}{2} \sum_{i\neq j} U_{ij} c_i^\dagger c_i c_j^\dagger c_j - t \sum_{\langle ij\rangle} c_i^\dagger c_j, \end{aligned} \tag{1.2}$$

where $c_i^\dagger$ (c_i) and $a_{\boldsymbol{q}\lambda}^\dagger$ ($a_{\boldsymbol{q}\lambda}$) are the creation (destruction) operators of a SP at the ith site, located at $\boldsymbol{r}_i$, and a phonon mode of wave vector $\boldsymbol{q}$ and branch index λ, respectively. ε_c is the electron energy in the absence of electron-phonon interactions. $M_{\boldsymbol{q}\lambda}$ is the electron-phonon coupling constant. t is the transfer integral between nearest neighbors. U_{ij} is the pair interaction energy between SPs at sites i and j. The first term of the model Hamiltonian accounts for the energy gain from electron localization in potential wells induced by electron-phonon interactions. The second term is the energy of the phonons, treated as independent bosons. The third term introduces mutual interactions among the SPs, at the origin of correlations and consequent collective phenomena. The last term accounts for the energy gain from SP delocalization over multiple sites. Clearly, the same term also describes diagonal transitions of SPs.

In our general description, two limit cases are possible. If SPs are light and delocalized, the SP and phonon dynamics are interwoven, in a Peierls mechanism. Their common instability, intrinsic to electron-phonon coupling, first causes the critical softening of a Kohn anomaly in a phonon branch, accompanied by pretransitional fluctuations, and then, below the transition temperature, the condensation of a charge density wave (CDW), coupled to atomic displacements. The electronic excitations in the low-temperature phase are comprised of collective modes of amplitude and phase modulation of the CDW at finite energy.

An exact solution of the model Hamiltonian is not possible. However, the main effect of the phonons is the renormalization of t to t^*, such that $t/t^* = m^*/m$. In the case considered in the foregoing, due to the large value of W_H, t^* is negligible. This prevents the formation of effective bands of SPs. Owing to the large value of m^*/m, SPs can be treated as classical variables. Therefore, it is possible to define Ising operators, which group together number operators of SPs at different sites. An additional index can be introduced to account for the possible symmetries of the charge density modes [24]. Otherwise, Potts operators can be defined, with an arbitrary number of states. For simplicity, let us refer to pseudospin variables $\{\sigma_i\}$, with consistent redefinition of the sites $\{i\}$, and the parameters ε_c, $M_{\boldsymbol{q}\lambda}$ and U_{ij}. The model Hamiltonian can thus be rewritten as

$$H = \sum_i \sigma_i \left[\varepsilon_c + \sum_{\boldsymbol{q}\lambda} M_{\boldsymbol{q}\lambda} \left(a_{\boldsymbol{q}\lambda} + a_{\boldsymbol{q}\lambda}^\dagger \right) e^{-i\boldsymbol{q}\cdot\boldsymbol{r}_i} \right] + \sum_{\boldsymbol{q}\lambda} \hbar\omega_{\boldsymbol{q}\lambda} a_{\boldsymbol{q}\lambda}^\dagger a_{\boldsymbol{q}\lambda} + \frac{1}{2} \sum_{i \neq j} U_{ij} \sigma_i \sigma_j. \tag{1.3}$$

The above Hamiltonian is formally equivalent to Yamada's Hamiltonian for a pseudospin-phonon coupled system [24, 55]. In the presence of heavy localized SPs, the pseudospin dynamics is slow compared to the phonon dynamics. Therefore, it is possible to rewrite the Hamiltonian in a simple form, which neglects the phonon dynamics. For the purpose, let us suppose that the bilinear coupling between pseudospins and phonons is meaningful only for one phonon mode, and accordingly drop the wave vector $\boldsymbol{q}$ and branch index λ. To change the formalism from second to first quantization, the destruction and creation operators of the phonon mode are replaced with the canonical coordinate and conjugate momentum of the same phonon mode, defined as, respectively, [49]

$$Q = \sqrt{\frac{\hbar}{2\omega}}\left(a^\dagger + a\right) \tag{1.4}$$

and

$$P = i\sqrt{\frac{\hbar\omega}{2}}\left(a^\dagger - a\right). \tag{1.5}$$

We approximate the dynamics of the phonon mode to an instantaneous response to the modifications of the charge configuration. This leads to the coordinate transformation

$$Q = -\sqrt{\frac{2}{\hbar\omega^3}} M \sum_i \sigma_i e^{i\boldsymbol{q}\cdot\boldsymbol{r}_i}. \tag{1.6}$$

Yamada's Hamiltonian can thus be reexpressed in a more convenient form as follows.

$$H = \sum_i \sigma_i \varepsilon_c + \sum_{i\neq j} U_{eff,ij}\sigma_i\sigma_j, \tag{1.7}$$

where

$$U_{eff,ij} = \frac{U_{ij}}{2} - \frac{M^2}{\hbar\omega}\cos\left[\boldsymbol{q}\cdot\left(\boldsymbol{r}_i - \boldsymbol{r}_j\right)\right] \tag{1.8}$$

is the effective pair interaction energy between pseudospins at sites i and j. In a way, in this case, the transformation process is opposite to a Peierls mechanism. The SP and phonon dynamics are independent. The instability resides only in the liquid of SPs. It first causes a progressive cooperative ordering of the pseudospin variables, concomitant to atomic displacements, and then, below the transition temperature, the crystallization of a solid of SPs.

1.4 Precursor Effects

In the cubic phase, a broad set of precursor effects anticipates the Verwey transition, in all degrees of freedom. Continuous changes in the optical functions, with redistributions of spectral weight among different energy ranges, take place before the discontinuous modifications at the transition temperature [29]. In particular, in the optical conductivity, the loss of spectral weight in the low-energy range, counterbalanced by an intensity gain around 0.6 eV, already starts far from the transition temperature.

Different macroscopic properties posses anomalous temperature dependences in the pre-transition region. The elastic constant c_{44} sizably softens from room temperature to the transition temperature and hardens discontinuously in the critical region [56,57]. This atypical behaviour has been explained in terms of bilinear coupling of the elastic stain field to a fluctuation mode of the charge ordering field of T_{2g} symmetry at the center of the Brillouin zone [57].

The first magnetocrystalline anisotropy constant K_1 shows a nonmonotonic dependence on temperature, which also resembles a softening curve in absolute value [58–60]. First, from high temperature to about 250 K, it decreases. Then, between about 250 K and the transition temperature, it increases and changes sign from negative to positive at a characteristic temperature, also referred to as the isotropic point, about 10 K above the transition temperature. One of the scenarios proposed to explain the increase in K_1 assumes the thermal population of degenerate states of local order, analogous to twin domains of the monoclinic phase, at a finite energy which progressively decreases on cooling [60]. This gives rise to an effective anisotropy energy equivalent to a positive contribution to K_1. The magnetostriction constants λ_{111} and λ_{100} also show a critical behaviour in a wide temperature range above the transition temperature, which has been related to the ordering of the extra electrons among B-type Fe ions [61].

Scattering techniques with momentum resolution provide direct information on the microscopic origin of the precursor effects. Lorenzo et al. examined the temperature dependence of the intensity and linewidth of the diffracted x rays around the transition temperature [62]. They chose different absorption edges and reflections based on presumed sensitivity to different degrees of freedom. They concluded that fluctuations of charge and orbital order already set in at the isotropic point and, in particular, precursor correlations of charge order extend over longer lengths compared to structural order. This suggests that the onsite Coulomb repulsion is the most important among the possible driving forces for the Verwey transition. According to the same interpretation, the onset of long-range structural order at the transition temperature prevents the further growth of charge order. Instead, the correlation length of fluctuations of orbital order remains short throughout the critical region. García and coworkers carried out analogous experiments, with different choices of reflections and absorption edges, which question the previous results [63]. In contrast to Lorenzo et al., they observed a concomitant disappearance of all Bragg spots at the transition temperature. In this regard, Tabis et al. proposed that sample-dependent effects are responsible for systematic differences observable by means of resonant x-ray diffraction [64]. In particular, they argued that the mechanical polishing of the sample surface right before the experiments favors discontinuous onset of charge and orbital order at the transition temperature, which otherwise, in the absence of local strain, evolves continuously starting from the isotropic point.

Diffuse scattering of electrons [65], neutrons [66–68] and x rays [69] with relative maxima at incommensurate points in reciprocal space is observable starting from tens of Kelvins above the transition temperature. It completely disappears in the monoclinic phase. The onset temperature for diffuse scattering depends on the nature of the probe and the detection sensitivity of the instrument. Remarkably, the extrapolated intensity of diffuse scattering corrected for the thermal occupation factor diverges at a virtual temperature below the transition temperature. Only in a narrow temperature range close to the transition temperature, diffuse scattering gains intensity at commensurate points in reciprocal space, *i.e.* within narrow spots centered around the same wave vectors as the superlattice reflections of the monoclinic phase [70].

By means of inelastic neutron scattering (INS) experiments, Shapiro et al. showed that diffuse scattering in reciprocal space corresponds to peaks centered at zero energy in the energy domain, the so-called central peaks, coupled with TA phonons [66]. Through a quantitative examination of the intensity distribution of diffuse scattering among the X points, Siratori and coworkers concluded that intrinsic X_3 symmetry dominates the critical fluctuations [68]. Hoesch et al. focused on the temperature dependence of the anharmonic effects from the coupling between phonons and critical fluctuations [71]. In particular, by means of nonresonant inelastic x-ray scattering experiments, they measured anomalously broad linewidths of the phonons at room temperature, which further increase on cooling down to 150 K. This is in contrast to the typical narrowing from the decrease in the rate of phonon-phonon scattering. The largest anharmonicity occurs at the same incommensurate points in reciprocal space where diffuse scattering is the most intense. Direct evidence of the local dynamic persistence of the atomic displacements of the monoclinic phase above the transition temperature was also provided by measurements of the instantaneous configuration of the crystal structure around the Fe ions by means of x-ray absorption [72].

2 Methods

2.1 Spontaneous Raman Scattering

Raman scattering is at one time a widely used and powerful technique for the study of excitations at low energy in solids, since it gives access to energy, lifetime and symmetry of a broad group of excitations, such as phonons, magnons, plasmons and polaritons, without the need for complex set-ups. Raman scattering experiments are easily performed as a function of different control parameters, such as temperature, pressure and magnetic and electric fields, all across the phase diagrams of solids. Therefore, as shown in this Thesis, Raman scattering is a well-suited technique to investigate phase transitions in solids. The main drawback of Raman scattering is that, for the constraint of wave-vector conservation and the small wave vector of light compared to the sizes of the Brillouin zones in solids, only excitations in a narrow region around the center of the Brillouin zone can be studied.

A fundamental classification of Raman scattering is based on whether the process takes place in a *stimulated* or *spontaneous* manner [73]. In the former case, two fields whose frequency difference is resonant with the frequency of the excitation are sent to the sample. The initial phases of the elementary oscillators depend on the phase difference of the two fields. In the particular case of transient stimulated Raman scattering (TSRS), discussed in Section 2.2, the two fields are among the different components within the bandwidth of the same laser pulse. Instead, in spontaneous Raman scattering, only one continuous-wave field is sent to the sample. The initial phases of the elementary oscillators are random.

In a simple description of spontaneous Raman scattering, photons are inelastically scattered by excitations at low energy. In particular, in a *Stoke* (*anti-Stoke*) process, an incident photon is annihilated and a scattered photon at lower (higher) energy is created, with creation (annihilation) of an excitation. In the following, we provide the main results of the general theory of spontaneous Raman scattering from lattice vibrations [74, 75], which are the most common type of excitations accessible in light scattering studies. The physical quantity that is accounted for to describe the optical response of the solid is the dielectric susceptibility tensor $\boldsymbol{\chi}$. Its matrix element χ_{ij} expresses how the ith component of the polarization $\boldsymbol{P}$ in the material responds to the jth component of a field $\boldsymbol{E}$ at a frequency ω, according to the following definition, with ε_0 the dielectric constant of vacuum.

$$\chi_{ij}(\omega) = \frac{1}{\varepsilon_0}\frac{\partial P_i}{\partial E_j}(\omega). \tag{2.1}$$

From a microscopic viewpoint, the optical functions of the material depend on the motion of electrons bound to nuclei under the action of a field. The large difference in inertia between electrons and nuclei causes decoupled dynamics in the two degrees of freedom. In particular, according to the Born-Oppenheimer approximation, the electronic potential is a parametric function of the instantaneous positions of the nuclei. Hence, it is not surprising that the displacements of the nuclei from their equilibrium positions cause a modulation of the dielectric susceptibility tensor as a function of time. It is possible to expand the instantaneous deviation of the dielectric susceptibility tensor from its average value in a power series of the canonical coordinates of the phonon modes of wave vector $\boldsymbol{q}$ and branch index λ, denoted by $Q_{\boldsymbol{q}\lambda}(t)$, as follows.

$$\begin{aligned}\delta\chi_{ij}(\omega,t) = &\sum_{\boldsymbol{q}\lambda}\frac{\partial\chi_{ij}}{\partial Q_{\boldsymbol{q}\lambda}}(\omega)\left[Q_{\boldsymbol{q}\lambda}(t) - \langle Q_{\boldsymbol{q}\lambda}(t)\rangle\right]\delta_{\boldsymbol{q}} \\ &+ \sum_{\substack{\boldsymbol{q}_1\lambda_1\\ \boldsymbol{q}_2\lambda_2}}\frac{\partial^2\chi_{ij}}{\partial Q_{\boldsymbol{q}_1\lambda_1}\partial Q_{\boldsymbol{q}_2\lambda_2}}(\omega)\left[Q_{\boldsymbol{q}_1\lambda_1}(t)Q_{\boldsymbol{q}_2\lambda_2}(t) - \langle Q_{\boldsymbol{q}_1\lambda_1}(t)Q_{\boldsymbol{q}_2\lambda_2}(t)\rangle\right]\delta_{\boldsymbol{q}_1+\boldsymbol{q}_2}.\end{aligned} \tag{2.2}$$

The Kronecker delta accounts for the conservation of the wave vector. If meaningful, the terms of the second order in $Q_{\boldsymbol{q}\lambda}$ imply that, in fact, the polarizability also changes in response to pairs of phonon modes at finite, opposite wave vectors, $\boldsymbol{q}_1 = -\boldsymbol{q}_2$, and not only at the center of the Brillouin zone. However, in general, they provide a noticeable contribution to Raman scattering only in the presence of a high phonon density of states, at the critical points of the Brillouin zone. The frequency transfer dependence of the Raman scattering intensity for polarization of the scattered field along the direction of the unit vector $\boldsymbol{n}$ can be written as

$$I(\Omega) = \frac{\omega^4}{2\pi c^3}\sum_{\alpha\beta\gamma\delta} n_\alpha n_\beta\,\sigma_{\alpha\gamma\beta\delta}(\Omega)\,E_\gamma E_\delta, \tag{2.3}$$

where

$$\sigma_{\alpha\gamma\beta\delta}(\Omega) = \int_{-\infty}^{\infty} d\tau\,\langle\delta\chi^*_{\alpha\gamma}(0)\delta\chi_{\beta\delta}(\tau)\rangle\,e^{-i\Omega\tau} \tag{2.4}$$

is the Raman cross section. Hence, in the lattice vibrational contribution to the Raman spectra, for first-order Raman scattering, the lineshapes are related to the Fourier transform (FT) of the time autocorrelation of the atomic displacements at zero wave vector. For second-order Raman scattering, the frequency dependence of the phonon density of states around Van Hove singularities also plays an important role.

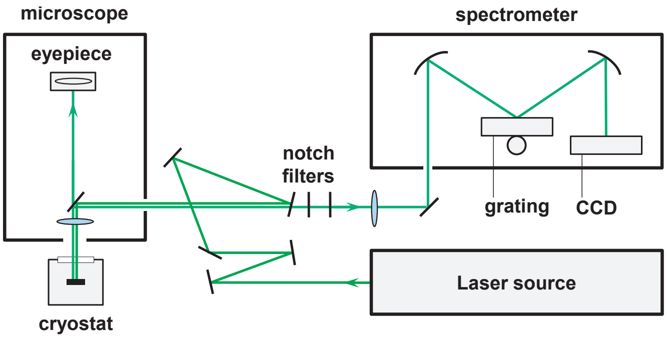

Figure 2.1 – Diagram of our set-up for spontaneous Raman scattering.

Our spontaneous Raman scattering experiments (see Chapter 4) were carried out at the Department of Quantum Matter Physics, University of Geneva, by means of a home-made set-up. Figure 2.1 provides an overview of our experimental apparatus. An Ar ion and a diode laser source provide excitations, respectively, at 2.4 and 3.1 eV photon energy. The laser light is delivered to the confocal point of an optical microscope through a 20× objective lens. The backscattered light is collected and collimated by the same optical system. The elastic component is rejected by multiple notch filters. The inelastic component is focused at the entrance slit of a monochromator with 50 cm focal length. The grating of the monochromator is fixed to a rotation stage which allows the selection of the Raman shift range of interest. The detection system is equipped with a charge-coupled device (CCD) cooled with liquid nitrogen.

2.2 Ultrafast Broadband Reflectivity

The advances in laser technology over the last decades have provided to basic research new experimental techniques to study the dynamics of different phenomena on short time scales. In particular, the development of self-mode locking [76] and chirped pulse amplification [77] has led to the commercial availability of laser sources able to provide laser pulses of subpicosecond duration, with broad potential in the study of phase transitions in solids, at the focus of this Thesis.

The basic principle of ultrafast spectroscopy is the *pump-probe* scheme [78, 79]. A sequence of laser pulses, the *pump* pulses, is sent to the sample. To measure the consequent response, delayed replica of the pump pulses, the *probe* pulses, are also sent to the sample, in a small spot wherein the intensity of the pump pulses is homogeneous. The repetition rate and the fluence, *i.e.* the energy per unit area, of the pump pulses are chosen so that the sample returns to equilibrium between consecutive pump pulses. Therefore, for a given time delay between pump and probe pulses, all probe pulses measure an identical state of the sample. After enough statistics on the probe pulses is collected, the time delay between pump and probe pulses is changed, to progressively construct a sequence of data points, representative of the dynamics upon impulsive photoexcitation. It is possible to tune the photon energy of the laser pulses in different spectral ranges, from the far infrared to the x-ray region, by means

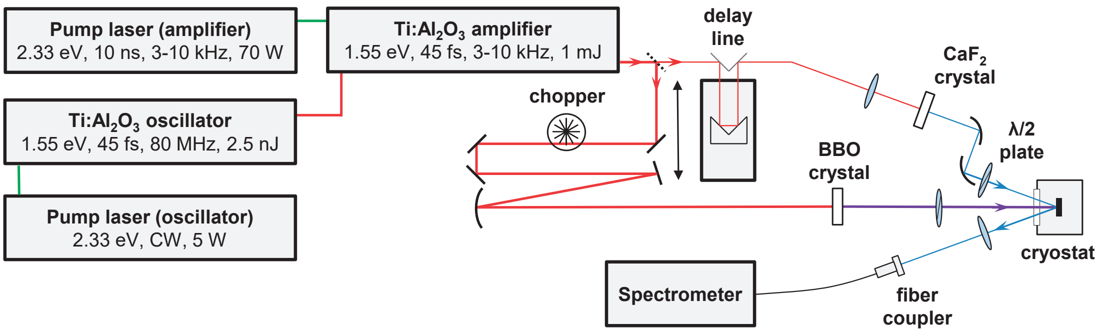

Figure 2.2 – Diagram of our set-up for ultrafast broadband reflectivity.

of nonlinear optical processes of energy conversion. The probe pulses can also be electron pulses produced via photoemission starting from the laser pulses [80].

Depending on both the nature of the probe pulses and the detection scheme, different observables are accessible. In our case, both pump and probe pulses are optical, and as the name of the technique suggests, the observable under consideration is the reflectivity in a broad spectral range, namely, the visible region. The advantages of our technique are manifold. Indeed, as discussed in the following, it allows us to study in the time domain both the relaxation dynamics of incoherent excitations and the oscillation dynamics of collective modes coherently generated by means of TSRS. In all processes, slow variables, *i.e.* excitations at low energy (~1–10 meV), are coupled to fast variables, *i.e.* electronic excitations at high energy (~1 eV), responsible for the optical functions. The broadband nature of our probe allows us to investigate the renormalization of the electronic structure in response to the excitations at low energy, and therefore the relation between phenomena on low and high energy scales.

Figure 2.2 provides an overview of our set-up for ultrafast broadband reflectivity. The sample is in thermal contact with the cold head of a closed-cycle He cryostat, which allows temperature control in between 8 and 340 K, in a base pressure of 10^{-8} mbar. An amplified Ti:Al$_2$O$_3$ laser source (Wyvern-1000 amplifier, seeded by Griffin oscillator, KM Labs) provides laser pulses of about 45 fs duration, center at 1.55 eV photon energy, at a repetition rate of 3–10 kHz, and pulse energy up to 3 mJ. A beam splitter separates the laser beam into a pump and a probe beam. The pump beam is responsible for the impulsive photoexcitation of the sample at normal incidence. The probe beam is focused into a CaF$_2$ crystal to generate a white light continuum from 1.7 to 2.9 eV. In the experiments discussed in this Thesis (see Chapter 3), the fundamental frequency of the pump beam is doubled by means of a β-BaB$_2$O$_4$ (BBO) crystal. The broadband pulses are then reflected onto the sample surface at an angle of 15–20°. An optical fiber couples the probe beam reflected from the sample surface to a spectrometer synchronized to the repetition rate of the laser pulses. A mechanical chopper modulates the sequence of pump pulses at one quarter of their repetition rate, so that, in each cycle, a pair of pump pulses is passed and the next one is blocked. This averages out characteristic gain fluctuations in the active medium of the amplifier at half the repetition rate of the laser pulses.

A retroreflector mounted on a mechanical stage controls the length of the probe path and, by that, the time delay between pump and probe pulses. The pump and probe beams are focused onto the sample surface by means of parabolic mirrors. The typical full width at half maximum of their intensity profiles at the sample surface are respectively $150 \times 150\ \mu\mathrm{m}^2$ and $50 \times 50\ \mu\mathrm{m}^2$. Further information on our experimental apparatus, with particular reference to the sample environment and the operation of the synchronization electronics, is provided in Ref. [81].

For each acquisition, the reflectivity spectra, R_p (R_u), are averaged over 1000 couples of probe pulses, in the presence (absence) of impulsive photoexcitation, *i.e.* whenever the pump pulses are passed (blocked) by the chopper. The relative change of reflectivity produced by the pump pulse as a function of probe photon energy E and time delay between pump and probe pulses t is computed according to the below definition. To further improve the signal-to-noise ratio, the data are also integrated over up to 100 acquisitions. Sensitivities down to 10^{-4} are thereby achieved.

$$\frac{\Delta R}{R}(E,t) = \frac{R_\mathrm{p}(E,t) - R_\mathrm{u}(E,t)}{R_\mathrm{u}(E,t)}. \tag{2.5}$$

Over the years, the understanding of the basic processes that take place out-of-equilibrium in pump-probe experiments on different types of systems has become an active area of research [82, 83]. The immediate effect of a pump pulse of subpicosecond duration in a solid is the photoexcitation of carriers across bandgaps. Indeed, during the pump pulse, for the small specific heat of carriers compared to lattice vibrations, the most important interactions take place between field and carriers, by means of dipole-allowed processes. First, starting from strong nonequilibrium conditions, the excess energy is redistributed among the carriers themselves, through carrier-carrier scattering. On time scales comparable to the duration of the pump pulse, a Fermi-Dirac distribution with a well-defined temperature is reestablished within the carrier subsystem. Then, the excess energy is transferred to different degrees of freedom, such as the lattice vibrational and magnetic subsystems, on time scales of tens or hundreds of femtoseconds. At this stage, the most important process is the emission of optical phonons, by means of phonon-carrier scattering. In turn, in the first picoseconds or tens of picoseconds, they decay into optical and acoustic phonons at lower energy, through multiphonon processes, governed by the anharmonic terms of the interionic potential. For longer times, if the carriers were photoexcited across bandgaps, they recombine, via radiative or nonradiative processes.

On top of the above dynamics, pump pulses can also produce the coherent excitation of collective modes (for instance, again, phonons) which in turn can give rise to the coherent modulation of the optical functions. A necessary condition for all processes discussed here is that the duration of the pump pulses is shorter than the periods of the collective modes. The excitation is referred to as *coherent* if the relative phases of the elementary oscillators (ions, in the case of phonons) are correlated in space and constant in time. Accordingly, the effect of a second, identical pump pulse on the amplitude of the oscillations only depends on the time delay from the first pump pulse.

For illustrative purposes, let us refer to a heuristic description of the generation mechanism of the collective modes [84], which goes under the general definition of TSRS, to avoid possible confusion with spontaneous Raman scattering. We take into account phonon modes, but our considerations hold true for any kind of bosonic excitation. We model the pump pulse as a field $\boldsymbol{E}$, with carrier at frequency ω_L, and a slowly varying modulation $\boldsymbol{\mathcal{E}}$, such that $\boldsymbol{E}(t) = \boldsymbol{\mathcal{E}}(t)e^{i\omega_L t}$. Let us assume that the dielectric susceptibility tensor $\boldsymbol{\chi}$ is real, *i.e.* absorption is absent. The energy stored in a solid of volume V is given by

$$H_E = -\frac{V}{2}\boldsymbol{E}(t)\cdot\boldsymbol{\chi}(\omega)\cdot\boldsymbol{E}(t) = -\frac{V}{4}\boldsymbol{\mathcal{E}}(t)\cdot\boldsymbol{\chi}(\omega_L)\cdot\boldsymbol{\mathcal{E}}(t), \tag{2.6}$$

where the additional factor $1/2$ comes from the average over one carrier period $T = 2\pi/\omega_L$. Let us now account for the modulation of the dielectric susceptibility tensor by the atomic displacements, and therefore replace it with the series expansion of Eq. 2.2, rewritten to the first order in the tensor form

$$\boldsymbol{\chi}(\omega) = \boldsymbol{\chi}_0(\omega) + \sum_\lambda \frac{\partial\boldsymbol{\chi}}{\partial Q_{0\lambda}}(\omega)Q_{0\lambda}(t). \tag{2.7}$$

We introduce the boson creation (destruction) operator $a^\dagger_{\boldsymbol{q}\lambda}$ ($a_{\boldsymbol{q}\lambda}$) of a phonon mode of wave vector $\boldsymbol{q}$, branch index λ and frequency $\omega_{\boldsymbol{q}\lambda}$. The canonical coordinate $Q_{\boldsymbol{q}\lambda}$ and the conjugate momentum $P_{\boldsymbol{q}\lambda}$ of the same phonon mode are related to both operators according to Eqs. 1.4 and 1.5. If the elastic scattering term is neglected, the total Hamiltonian can be written as $H = H_{ph} + H_R$, where

$$H_{ph} = \frac{1}{2}\sum_{\boldsymbol{q}\lambda}\left(P_{\boldsymbol{q}\lambda}P_{-\boldsymbol{q}\lambda} + \omega^2_{\boldsymbol{q}\lambda}Q_{\boldsymbol{q}\lambda}Q_{-\boldsymbol{q}\lambda}\right) = \sum_{\boldsymbol{q}\lambda}\hbar\omega_{\boldsymbol{q}\lambda}\left(\frac{1}{2} + a^\dagger_{\boldsymbol{q}\lambda}a_{\boldsymbol{q}\lambda}\right) \tag{2.8}$$

and

$$H_R = \sum_\lambda -\frac{V}{4}\,\boldsymbol{\mathcal{E}}(t)\cdot\frac{\partial\boldsymbol{\chi}}{\partial Q_{0\lambda}}(\omega_L)\cdot\boldsymbol{\mathcal{E}}(t)\,Q_{0\lambda}(t) = \sum_\lambda -F_\lambda(t)\,Q_{0\lambda}(t) \tag{2.9}$$

are respectively the phonon Hamiltonian, in first and second quantization formalism, and the Hamiltonian for TSRS of the first order, equivalent to the application of generalized forces F_λ on the phonon modes of zero wave vector and branch index λ. In this Thesis, the simultaneous generation of two collective modes at finite wave vectors via second-order processes is also at focus, and discussed in detail in Subsection 3.2.4. In the following, let us consider a single phonon mode, and therefore drop the branch index λ. If Q is regarded to as a classical variable, the dynamics can be described by the equation of motion of a forced harmonic oscillator of frequency Ω ($\equiv \omega_{\boldsymbol{q}\lambda}$),

$$\ddot{Q}(t) + \Omega^2 Q(t) = F(t), \tag{2.10}$$

of solution

$$Q(t) = \int_{-\infty}^{t} dt' \, \frac{\sin\left[\Omega\left(t-t'\right)\right]}{\Omega} \, F(t'), \tag{2.11}$$

for initial conditions $Q(-\infty) = F(-\infty) = 0$. If Q is considered a quantum operator, the dynamics, now referred to the quantum average of Q and computed according to the Kubo formula, does not change, since

$$\langle Q\rangle(t) = \frac{i}{\hbar}\int_{-\infty}^{t} dt' \, \langle\left[Q(t), Q(t')\right]\rangle F(t') = -\int_{-\infty}^{\infty} dt' \, D(t-t')F(t'), \tag{2.12}$$

where

$$D(t) = -\frac{i}{\hbar}\Theta(t)\langle[Q(t), Q(0)]\rangle = -\Theta(t)\frac{\sin(\Omega t)}{\Omega} \tag{2.13}$$

is the retarded noninteracting phonon propagator and $\Theta(t)$ is the Heaviside function. The above equations provide a reasonable description of the real phenomena in transparent media. The time dependence of the generalized force is indeed coincident with the envelope of the pump pulse, which can be approximated to a Dirac delta. Therefore, sinelike oscillations are produced, by means of a mechanisms generally referred to as impulsive stimulated Raman scattering (ISRS) [85].

The real phenomena in opaque media are more complex. In the presence of meaningful absorption, still, the model of a forced harmonic oscillator can be applied. However, the generalized force depends on both dynamics and interactions with phonons of the electron-hole excitations produced by the pump pulse. If the electron-hole excitations are long lived, they cause a transient change in the potential energy surface, with different equilibrium positions of the ions [86]. The coupling between the charge distribution in the excited state and the phonon modes gives rise to a generalized force with steplike profile. Therefore, cosinelike, instead of sinelike, oscillations are produced. In general, the generation process of coherent phonons is in between the opposite limits of impulsive and displacive excitation. It has been argued that the latter limit can also be treated in the framework of TSRS [87, 88]. However, not all generation mechanisms can be described by a Raman process. For instance, a hot but thermalized gas of long-lived electron-hole pairs in a semiconductor can produce changes in the interatomic potential outside the framework of Raman scattering. In general, for non-Raman processes, the memory of the polarization of the pump pulse is lost during thermalization. Therefore, these are expected to coherently generate phonon modes which do not break the symmetry of the crystal structure, *e.g.* breathing modes. Instead, Raman processes are the most probable generation mechanisms for phonon modes of lower symmetry.

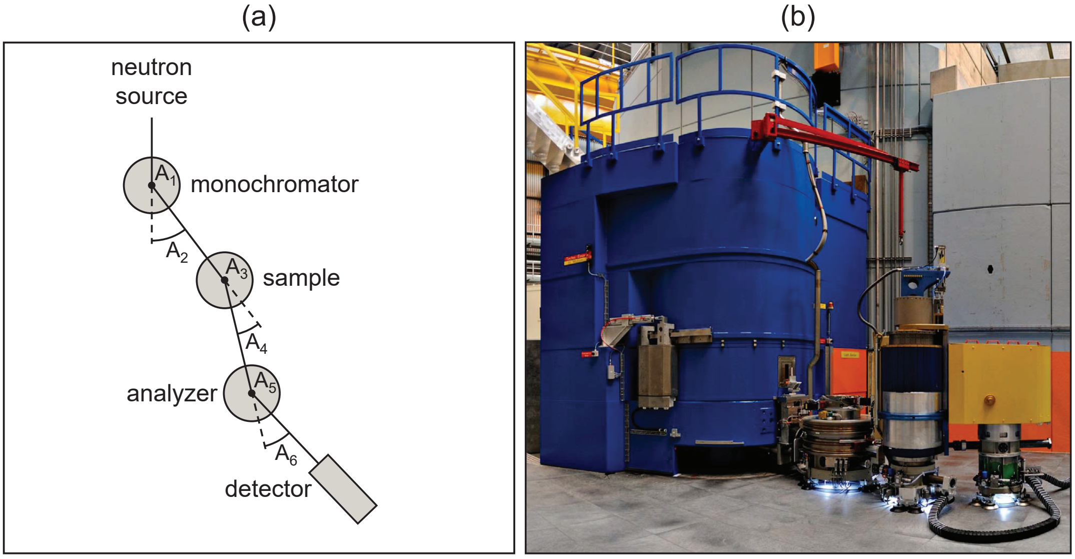

Figure 2.3 – (a) Diagram of a triple-axis spectrometer for INS. A1–A6 denote the degrees of freedom in orientation and relative position of the three axes. (b) Picture of the thermal triple-axis neutron spectrometer EIGER, located at the Swiss Spallation Neutron Source (SINQ), Paul Scherrer Institute (PSI), Switzerland. Adapted from Ref. [89].

2.3 Inelastic Neutron Scattering

Important results of this Thesis on the critical behaviour of phonon modes at finite wave vectors (see Chapter 5) come from INS experiments, in particular, triple-axis spectroscopy with thermal neutrons. INS represents a powerful tool to gain access to the dynamics of solids, with unique potentials in the study of structural and magnetic transitions. It provides direct measurements of correlations in energy and reciprocal space of excitations in structural and magnetic degrees of freedom. Indeed, the combination of energy (~10 meV) and wave vector (~1 Å^{-1}) of thermal neutrons is fortunate, since they are comparable to respectively the characteristic energies and length scales in reciprocal space of structural and magnetic correlations. Structural sensitivity arises from the interaction between neutrons and nuclei through the strong nuclear force. Instead, magnetic sensitivity originates from the intrinsic magnetic moment of neutrons. In both cases, the interaction potential is weak. Therefore, neutrons behave as a nondestructive bulk probe. Let us note that INS is also sensitive to excitations in charge and orbital degrees of freedom, though indirectly, via the effect that they produce on the nuclei.

The obvious reason why the technique being discussed is named triple-axis spectroscopy is that the instrument is comprised of three rotational axes, located in correspondence of three essential components, namely, the monochromator, the sample and the analyzer. Figure 2.3 shows a schematic representation and a picture of the instrument used in our work. Starting from a polychromatic beam, the monochromator selects and delivers towards the sample a beam centered around a wave vector $\boldsymbol{k}_i$, by means of Bragg reflection on a mosaic of pyrolytic graphite crystals. The neutrons are then diffracted and inelastically scattered by the sample in different directions. Based on the same working principle as the monochromator, the analyzer reflects towards the detector only the neutrons centered around a wave vector $\boldsymbol{k}_f$. The detector counts the number of neutrons at a point in wave-vector-energy space $(\boldsymbol{Q}, E)$. To provide a reference for normalization, a monitor located in between the monochromator and the sample counts the number of incident neutrons. The wave-vector and energy transfer are given by, respectively,

$$\boldsymbol{Q} = \boldsymbol{k}_i - \boldsymbol{k}_f \tag{2.14}$$

and

$$E = \frac{\hbar^2 k_i^2}{2m_n} - \frac{\hbar^2 k_f^2}{2m_n}, \tag{2.15}$$

where m_n is the neutron mass. The degrees of freedom of the three rotational axes consist of the six angles labeled as A1–A6 in Fig. 2.3(a). A1 and A2 (A5 and A6) define the desired k_i (k_f). A4 is the scattering angle. A3 defines the orientation of the sample in the scattering plane. In our experiments, A3 and A4 are not independent. Different experimental geometries are possible for a same point in wave-vector-energy space $(\boldsymbol{Q}, E)$. The choice of the most suitable experimental geometry is a compromise between requirements on resolution and intensity. In our experiments, we only carried out inelastic scans in constant-$\boldsymbol{Q}$ mode, with fixed k_f. For each value of energy transfer, a different k_i is set, by changing A1 and A2. To let $\boldsymbol{Q}$ unchanged, a different direction of $\boldsymbol{k}_f$ is also set, by changing A3 and A4.

The quantity that is measured in the experiments is the number of detector counts per monitor count as a function of wave-vector and energy transfer. The differential cross section for nuclear scattering is defined as the rate of the neutrons that the sample scatters into a solid angle $d\Omega$ with energy between E and $E + dE$. The wave-vector and energy transfer dependence of the contribution from one-phonon processes is given by [90]

$$\frac{\partial^2 \sigma}{\partial \Omega \partial E}(\boldsymbol{Q}, E) = \sum_{\lambda\lambda'} F_\lambda^*(\boldsymbol{Q}) F_{\lambda'}(\boldsymbol{Q})\, \phi_{QQ}^{\lambda\lambda'}(\boldsymbol{q}, E), \tag{2.16}$$

where

$$\phi_{QQ}^{\lambda\lambda'}(\boldsymbol{q}, E) = \int_{-\infty}^{\infty} d\tau \langle Q_{-\boldsymbol{q}\lambda}(0) Q_{\boldsymbol{q}\lambda'}(\tau)\rangle\, e^{-iE\tau/\hbar} \tag{2.17}$$

and

$$F_\lambda(\boldsymbol{Q}) = \sum_i b_i\, \boldsymbol{Q} \cdot \boldsymbol{\Delta}_{i\lambda}\, e^{i\boldsymbol{Q}\cdot\boldsymbol{r}_i} \tag{2.18}$$

are respectively the spectral function and the dynamical structure function. It is clear that the spectral function is the counterpart in the energy domain of the time autocorrelation of the atomic displacements. The relation between the wave vector of the mode being considered and the wave-vector transfer is $\boldsymbol{Q} = \mathbf{G} + \boldsymbol{q}$, with $\mathbf{G}$ a reciprocal lattice point. $\boldsymbol{\Delta}_{i\lambda}$ denotes the displacement vector of the ith atom, for the λth branch, with nuclear scattering length b_i and position in the unit cell $\boldsymbol{r}_i$. In the harmonic approximation, $\{Q_{\boldsymbol{q}\lambda}\}$ are independent variables, thus only autocorrelation terms, with $\lambda = \lambda'$, are meaningful. Instead, in the presence of important anharmonic interactions, the coherent superpositions of the eigenstates become significant, and cross correlation terms, with $\lambda \neq \lambda'$, must be considered [91].

2.4 Magneto-Optical Kerr Effect

The interaction between matter and a continuous-wave field reflected from a sample surface does not restrict itself to absorption and scattering, discussed in Section 2.1, with particular reference to spontaneous Raman scattering. In a magnetic medium, the magnetization induces anisotropy in the optical functions. This allows one to measure the average direction and relative magnitude of the magnetization in the probed region based on the changes in the polarization state of light. Again, as in the case of spontaneous Raman scattering, experiments as a function of different control parameters enable one to investigate the phase diagrams of solids, yet with focus on the magnetic degree of freedom alone. This provides a valuable complementary tool in the study of the complex interplay among structural, electronic and magnetic modifications of phase transitions in solids.

In 1845, M. Faraday first discovered that the polarization direction of linearly polarized light transmitted through magnetic media changes in the presence of magnetization. J. Kerr later observed an analogous phenomenon upon reflection from magnetic surfaces. Both effects originate from the dependence of the optical functions on spin-orbit coupling. In a simplified classical description, for linearly polarized light, the left and right circular components of the electric field cause circular motions of free electrons, with opposite chiralities, but equivalent to each other. As a result, no net polarization is induced. Instead, if a magnetic field is switched on in the propagation direction of light, Lorentz forces act on the electrons, in opposite directions for left and right circular motions, which therefore become inequivalent. Accordingly, the left and right circular components of the electric field experience different refractive indexes, and accumulate a phase difference during propagation in the magnetic medium.

In a more general description, magneto-optical coupling gives rise to an antisymmetric contribution to the dielectric tensor $\boldsymbol{\varepsilon}$. In the simple case of an isotropic medium, for zero magnetization, the dielectric tensor reduces to a scalar ε. In the presence of magnetization, the constitutive relationship between the electric displacement and the electric field becomes

$$\boldsymbol{D} = \varepsilon\,(\boldsymbol{E} + iQ\boldsymbol{m} \times \boldsymbol{E})\,, \tag{2.19}$$

where Q is the complex *Voigt* or *magneto-optical* constant and $\boldsymbol{m}$ is the normalized magnetization vector [93]. It is easy to prove that the dielectric tensor can be rewritten as

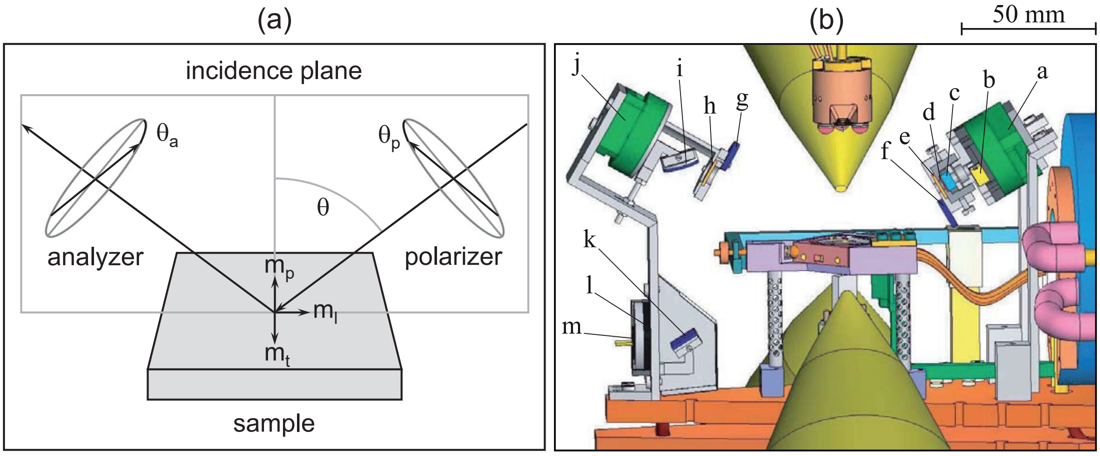

Figure 2.4 – (a) Experimental geometry of our experiments. The magnetic field can be applied at any angle in the m_t–m_p plane perpendicular to both the laser incidence plane and the sample surface. (b) Schematic representation of the optomechanical components of our magneto-optical Kerr effect (MOKE) set-up, namely, a and j – rotation stages, b – laser diode, c – lens, d – aperture, e and h – pairs of dichroic sheets, f and g – shutters, i and k – mirrors, l – near-infrared filter and m – photodiode. Adapted from Ref. [92].

$$\boldsymbol{\varepsilon} = \varepsilon \begin{pmatrix} 1 & -iQm_z & iQm_y \\ iQm_z & 1 & -iQm_x \\ -iQm_y & iQm_x & 1 \end{pmatrix}. \tag{2.20}$$

The relationship between magnitude and polarization of the incident and reflected electric fields can be computed starting from the above dielectric tensor and the boundary conditions at the interfaces by means of Maxwell equations. It is thereby possible to demonstrate that the following linear transformation holds true between the s and p components of the incident and reflected electric fields [94], by definition, respectively perpendicular and parallel to the light incidence plane.

$$\begin{pmatrix} E_p^r \\ E_s^r \end{pmatrix} = \left(m_l^2 \mathfrak{R}_l + m_t^2 \mathfrak{R}_t + m_p^2 \mathfrak{R}_p \right) \cdot \begin{pmatrix} E_p^i \\ E_s^i \end{pmatrix}. \tag{2.21}$$

$\mathfrak{R}_l$, $\mathfrak{R}_t$ and $\mathfrak{R}_p$ are the Fresnel reflection matrices for the longitudinal, transverse and polar projections of the normalized magnetization vector, m_l, m_t and m_p, defined in Fig. 2.4(a). They can be written in the form of Ref. [95],

$$\mathfrak{R}_l = \begin{pmatrix} r_{pp} & r_{ps}^l / m_l \\ -r_{ps}^l / m_l & r_{ss} \end{pmatrix}, \tag{2.22}$$

$$\mathfrak{R}_t = \begin{pmatrix} r_{pp}(1 + r_0^t / m_t) & 0 \\ 0 & r_{ss} \end{pmatrix}, \tag{2.23}$$

$$\mathfrak{R}_p = \begin{pmatrix} r_{pp} & r_{ps}^p / m_p \\ r_{ps}^p / m_p & r_{ss} \end{pmatrix}. \tag{2.24}$$

The Fresnel coefficients r_{ij}^{k} depend on Q, the complex refractive index of the medium n and the incidence angle of light θ, according to the below definitions [95, 96], where $\beta = \cos\theta$, $\beta' = \left(1 - \sin^2\theta / n^2\right)^{1/2}$ and $\gamma = \sin\theta$.

$$r_{pp} = \frac{n\beta - \beta'}{n\beta + \beta'}, \tag{2.25}$$

$$r_{ss} = \frac{\beta - n\beta'}{\beta + n\beta'}, \tag{2.26}$$

$$r_0^t = \frac{2\gamma\beta i n^2 Q}{n^2(n^2\beta^2 - 1) + \gamma^2}, \tag{2.27}$$

$$r_{ps}^p = -\frac{\beta i n Q}{\left(n\beta + \beta'\right)\left(\beta + n\beta'\right)}, \tag{2.28}$$

$$r_{ps}^l = \frac{\gamma\beta i n^2 Q}{n^2\beta'\left(n\beta + \beta'\right)\left(\beta + n\beta'\right)}. \tag{2.29}$$

The quantity that is measured in the experiments is the intensity transmitted by an analyzer with transmission axis at an angle θ_a to the incidence plane,

$$I = \left|E_p^r \cos\theta_a + E_s^r \sin\theta_a\right|^2. \tag{2.30}$$

where the proportionality factors are omitted for simplicity. In the following, we provide approximate expressions of the measured intensity normalized to the intensity incident on the magnetic surface, I_p and I_s, respectively, for s and p polarization of the incoming electric field [95, 96]. All the terms of the second order in m_l, m_t and m_p, which are also of the second order in Q, are assumed negligible.

$$\begin{aligned} I_p &= \left|\left(1 + m_t r_0^t\right) r_{pp} \cos\theta_a + \left(m_p r_{ps}^p - m_l r_{ps}^l\right) \sin\theta_a\right|^2 \\ &= \left(A + B m_t\right)\cos^2\theta_a + \left(C m_l + D m_p\right)\sin\theta_a\cos\theta_a, \end{aligned} \tag{2.31}$$

$$\begin{aligned} I_s &= \left|\left(m_l r_{ps}^l + m_p r_{ps}^p\right)\cos\theta_a + r_{ss}\sin\theta_a\right|^2 \\ &= E\sin^2\theta_a + \left(F m_l + G m_p\right)\sin\theta_a\cos\theta_a, \end{aligned} \tag{2.32}$$

where

$$A = \left|r_{pp}\right|^2, \tag{2.33}$$

$$B = 2\left|r_{pp}\right|^2 \mathbb{R}\mathrm{e}\left(r_0^t\right), \tag{2.34}$$

$$C = -2\,\mathbb{R}\mathrm{e}\left(r_{ps}^l r_{pp}^*\right), \tag{2.35}$$

$$D = 2\,\mathbb{R}\mathrm{e}\left(r_{ps}^p r_{pp}^*\right), \tag{2.36}$$

$$E = \left|r_{ss}\right|^2, \tag{2.37}$$

$$F = 2\,\mathbb{R}\mathrm{e}\left(r^{l}_{ps} r^{*}_{ss}\right), \tag{2.38}$$

$$G = 2\,\mathbb{R}\mathrm{e}\left(r^{p}_{ps} r^{*}_{ss}\right). \tag{2.39}$$

Figure 2.4(b) provides an overview of the most important components of our set-up for MOKE. The entire apparatus is mounted inside a ultrahigh vacuum (UHV) chamber designed for *in situ* preparation and characterization of the surface morphology of the sample by means of scanning tunneling microscopy (STM). The sample is in thermal contact with the cold finger of a helium-flux cryostat. The sample environment is equipped with standard tools to control the temperature down to 60 K with an accuracy of 1 K or better. The light source is a laser diode of 785 nm wavelength. The laser beam is collimated to 1 mm spot size throughout the optical path using the combination of a lens and an aperture. Pairs of dichroic sheets are used both as polarizers and analyzers, respectively, in front of the laser diode and the detector. Both optical systems for excitation and detection are mounted on rotation stages to control the polarization direction of the laser beam and the transmission axis of the analyzer. A magnetic field up to 310 mT can be applied in any direction within the plane perpendicular to both the laser incidence plane and the sample surface, by means of four soft iron yokes, magnetized by coils outside the UHV chamber.

3 Coherent Generation of Symmetry-Forbidden Phonons

Phase transitions cause symmetry breaking in structural, electronic and magnetic subsystems. The consequent changes in the selection rules lead to the emergence of optical and Raman-active modes. Upon completion of the transformation, new excitations can be detected and generated coherently, respectively, by means of steady-state and pump-probe spectroscopy. In second-order and weakly first-order transitions, the ordering field fluctuates around its average value, even when it is zero, above the ordering temperature. Local dynamical correlations of the ordering field give rise to interesting precursor phenomena, analogous to, for instance, critical opalescence in fluids.

In this Chapter, we demonstrate that in magnetite impulsive photoexcitation couples to the fluctuations of the ordering field and coherently generates modes of lattice vibrations of the ordered phase above the critical region of the Verwey transition. By means of ultrafast broadband reflectivity, we detect and analyze the temperature dependence of coherent oscillations of the optical functions. We combine our time-resolved data with our steady-state data from spontaneous Raman scattering, further discussed in Chapter 4, and theoretical calculations of both the phonon dispersion curves and the optical functions. We thereby unveil the coupling between structural and electronic excitations, at the origin of the Verwey transition. Our methodology represents an effective tool to study in the time domain the dynamics of critical fluctuations across phase transitions.

The content of this Chapter is adapted from the article "Coherent generation of symmetry-forbidden phonons by light-induced electron-phonon interactions in magnetite" by S. Borroni, E. Baldini, V. M. Katukuri, A. Mann, K. Parlinski, D. Legut, C. Arrell, F. van Mourik, J. Teyssier, A. Kozłowski, P. Piekarz, O. V. Yazyev, A. M. Oleś, J. Lorenzana, and F. Carbone, Phys. Rev. B 96, 104308 (2017). We relied on the theoretical model developed by Prof. J. Lorenzana (University of Rome, La Sapienza) and on the ab initio *computations of the optical functions and the phonon dispersion curves, respectively, by the group of Prof. O. V. Yazyev (EPFL) and the group of Prof. A. M. Oleś (Jagiellonian University, Kraków).*

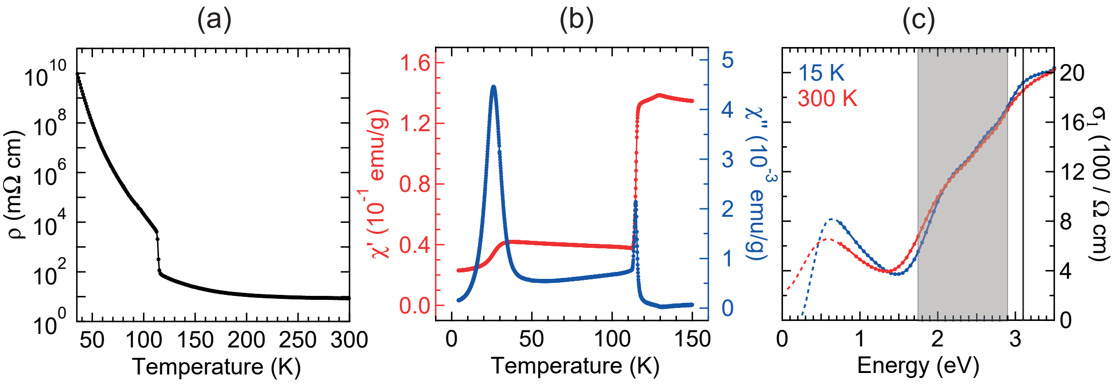

Figure 3.1 – Resistivity and ac susceptibility characterization of our sample, and steady-state optical properties of magnetite. (a) Temperature dependence of the resistivity of our sample. (b) Temperature dependence of the ac susceptibility of our sample (red line — real part χ', blue line — imaginary part χ''). The frequency and the amplitude of the driving field are respectively 7 Hz and 0.64 Oe. (c) Real part of the optical conductivity at 15 and 300 K from the ellipsometry measurements of Ref. [29]. Dashed lines represent extrapolations based on fits to the data. The vertical line and the shaded area respectively correspond to the energy of the impulsive photoexcitation and the probed region in our time-resolved experiments.

3.1 Experiments

A natural single crystal of magnetite was purchased from Surface Preparation Laboratory (SPL), Zaandam, Netherlands. Our sample was cut and polished to optical quality along the (110) plane. To characterize the quality of our sample, with particular reference to the Verwey temperature and the order of the Verwey transition, we measured resistivity and ac susceptibility as a function of temperature, respectively, in the 35–300 and 5–150 K ranges. Our results are summarized in Figs. 3.1(a,b). Both data sets show that the Verwey transition is discontinuous. The Verwey temperature is $T_V = 116$ K, below typical values for highly stoichiometric samples, around 120 K, for the impurity content inherent to samples of natural origin.

Nevertheless, all the features in the ac susceptibility of our sample are analogous to the synthetic crystals of Refs. [97, 98] (see Fig. 3.1(b)). In agreement with the same studies, in contrast to the anomaly at low temperature, the magnetic response in the critical region does not depend on frequency. According to Ref. [98], the dynamics of the magnetic response is dominated by the motion of domain walls. In the monoclinic phase, as a result of crystal microtwinning, the sample is divided into structural domains with inequivalent orientations. The magnetic domains are coincident with the ferroelastic domains, *i.e.*, within a domain, spontaneous magnetization is coupled with spontaneous strain. For the additional cost of elastic energy, a higher field is required for the motion of domain walls, compared to the cubic phase. As a result, the real part of the ac susceptibility χ' decreases abruptly below the critical temperature of the structural transition, coincident with that of the electronic transition.

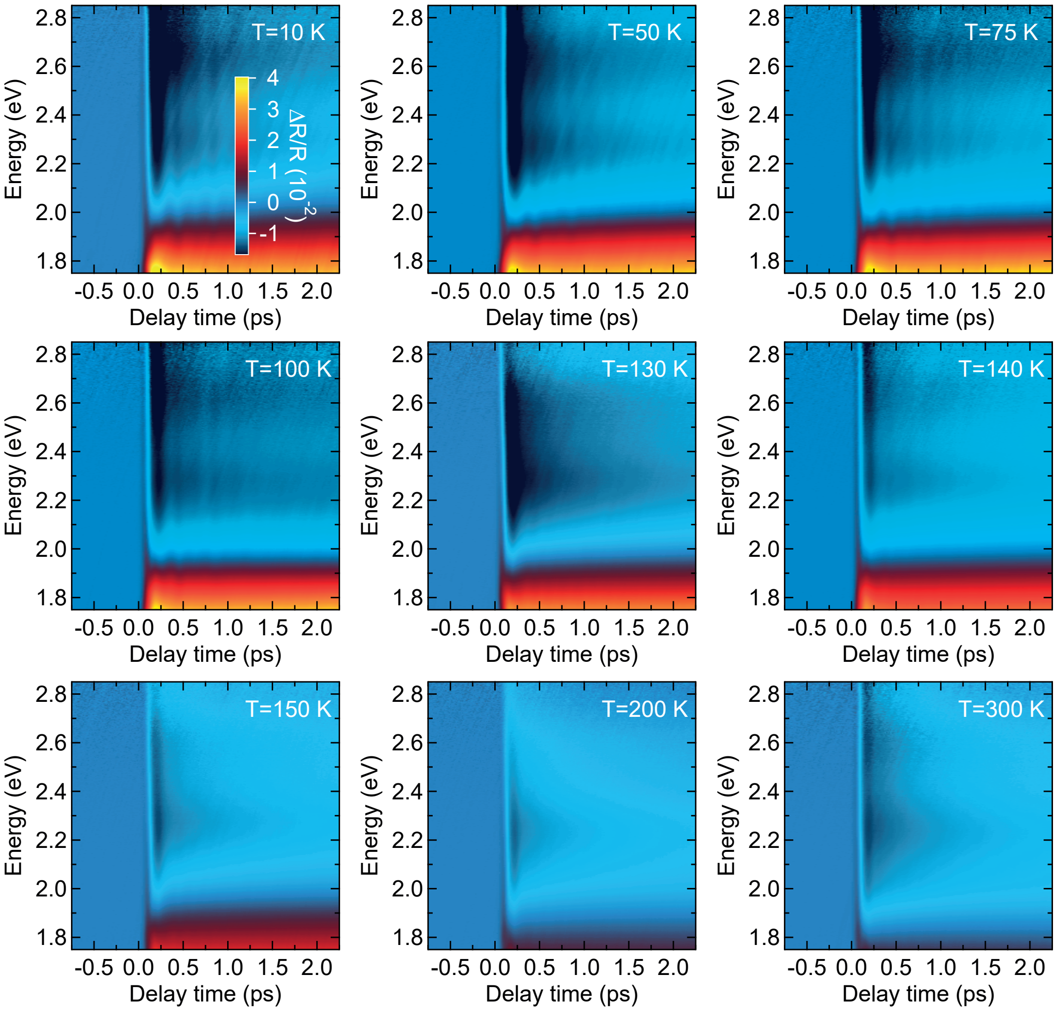

Figure 3.2 – Summary of our time-resolved data. Color-coded maps of differential reflectivity spectra as a function of pump-probe delay time at different temperatures and ~1 mJ/cm^2 fluence.

Figure 3.1(c) shows the optical conductivity of magnetite below 3.5 eV, in steady state conditions, both above and below the Verwey temperature, discussed in Section 1.2. In our ultrafast broadband reflectivity experiments, the photon energy of the impulsive photoexcitation was equal to 3.1 eV, above the onset of charge transfer excitations between O $2p$ and Fe $3d$ states. The photon energy of the probe pulses spanned the spectral region of the interband transitions between $3d$ states of Fe ions, from 1.7 to 2.9 eV. Section 2.2 presents an overview on the basic principles of ultrafast broadband reflectivity and a description of our set-up. To discriminate between equilibrium and nonequilibrium effects, we also compare our data from ultrafast broadband reflectivity with a subset of our data from spontaneous Raman scattering at 2.4 and 3.1 eV excitations, discussed in Chapter 4.

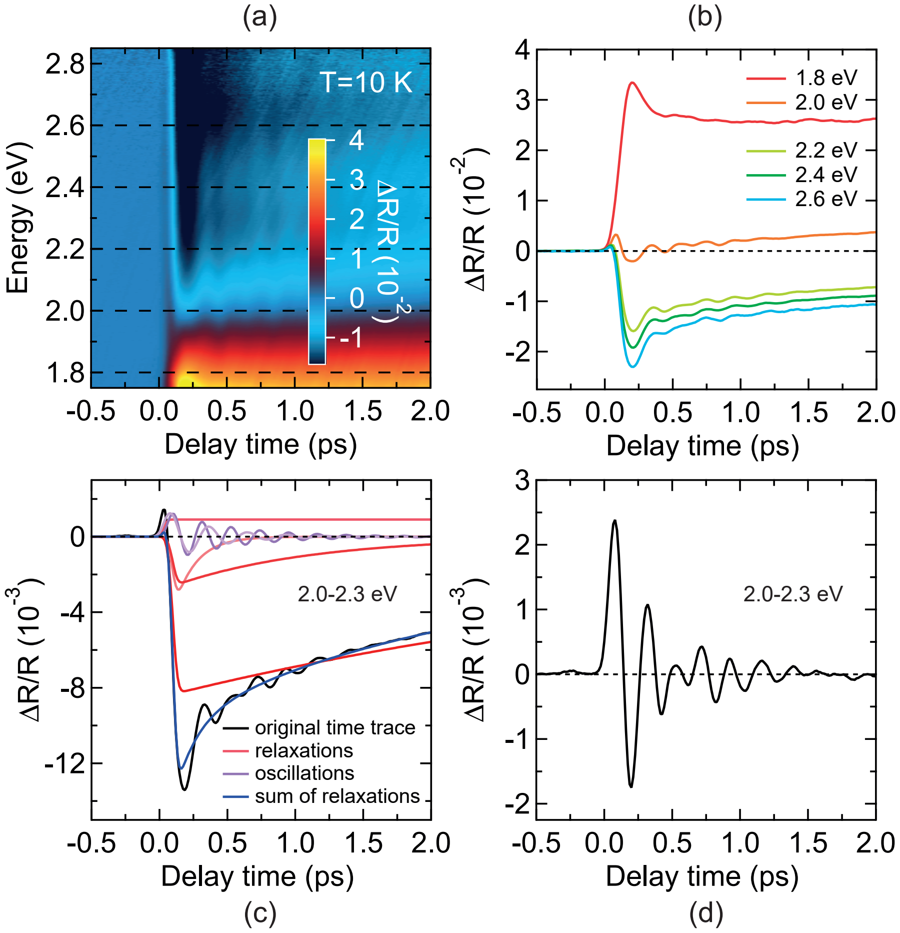

Figure 3.3 – Response to the impulsive photoexcitation in the monoclinic phase. (a) Color-coded map of differential reflectivity as a function of pump-probe delay time and probe photon energy at 10 K and ~1 mJ/cm^2 fluence. (b) $\Delta R/R$ time traces averaged over 0.2 eV wide windows centered on the horizontal lines of panel (a). (c) Fit analysis of $\Delta R/R$ integrated between 2.0 and 2.3 eV. Fitting functions are displayed in different colors. (d) Coherent response isolated through fit analysis of $\Delta R/R$ integrated between 2.0 and 2.3 eV.

3.2 Results

3.2.1 Ultrafast Broadband Reflectivity

The complete data set of our pump-probe experiments all across both the monoclinic and cubic phases is summarized in Fig. 3.2. The spectrum of the transient reflectivity as a function of pump-probe delay time, $\Delta R/R(E,t)$, at 10 K and ~1 mJ/cm^2 fluence is shown in Fig. 3.3(a). The time traces of the transient reflectivity averaged over energy ranges of 0.2 eV width are displayed in Fig. 3.3(b). The occurrence of multiple exponential decays, superimposed to damped coherent oscillations of 1.5 ps duration, clearly emerge from close inspection of both figures.

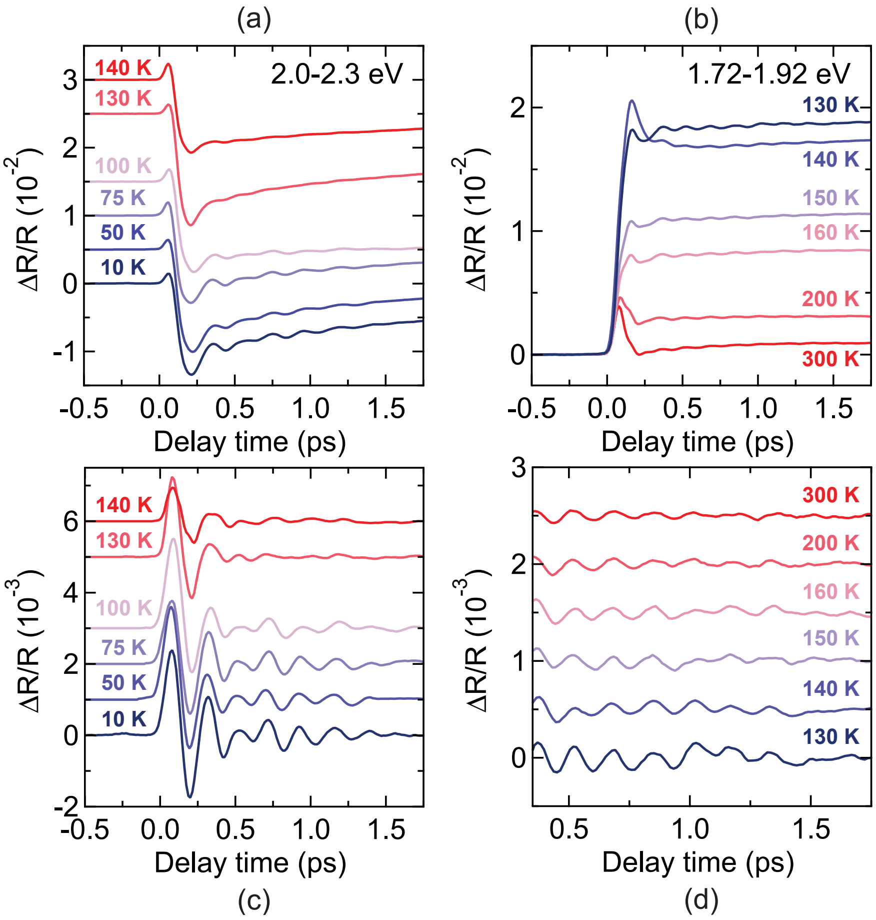

Figure 3.4 – Temperature dependence of the coherent response in the time domain. Left (Right) panels refer to the A_g (T_{2g}) phonon modes. (a,b) Differential reflectivity as a function of pump-probe delay time averaged over 2.0–2.3 and 1.72–1.92 eV energy ranges at different temperatures. (c,d) Oscillatory component singled out from the time traces of panels (a) and (b) by subtracting the non-oscillatory transient. Since the T_{2g} phonon mode is not the focus of our work, a simple polynomial function was fit to the incoherent response, after the initial transient.

To carry out a fit analysis, the differential reflectivity is averaged over the energy range between 2.0 and 2.3 eV, which provides the best compromise between signal-to-noise ratio and oscillation intensities. The best fit, displayed in Fig. 3.3(c), is comprised of the sum of two damped coherent oscillations and multiple exponential decays, convolved with a Gaussian response function. The beating oscillations, shown in Fig. 3.3(d), are thereby isolated.

The same fit analysis is performed for all temperatures at the same ~1 mJ/cm^2 fluence. The temperature dependence of the oscillations is displayed in Figs. 3.4(a,c). The oscillations are Fourier transformed, to study the temperature dependence of oscillation intensities and power spectra, shown in Figs. 3.5(a,c). No meaningful changes are noticeable in the energies of the oscillations, respectively, in the 13.9–15.6 and 18.5–19.6 meV ranges. Remarkably, the

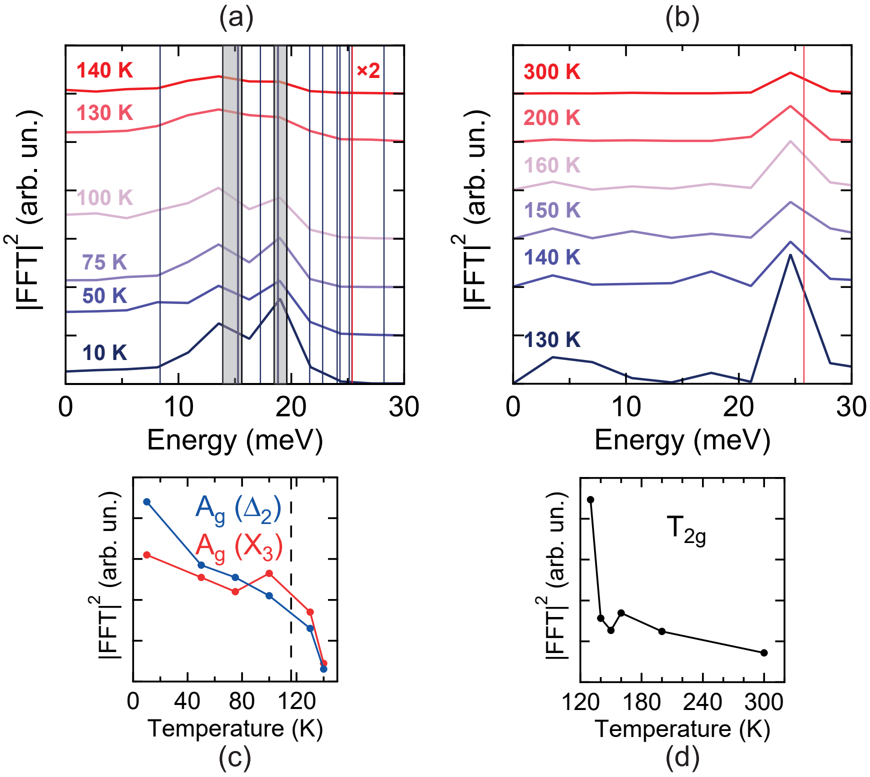

Figure 3.5 – Temperature dependence of the coherent response in the energy domain. Left (Right) panels refer to the A_g (T_{2g}) phonon modes. (a,b) Power spectrum of the coherent response from a FT of the oscillatory component. Blue (Red) vertical lines indicate the energy of the A_g (T_{2g}) phonon modes at the Γ point in $P2/c$ ($Fd\bar{3}m$) symmetry from *ab initio* calculations. Shaded areas extend over the energy ranges of the beating oscillations in the monoclinic phase as estimated based on the fit analysis. (c,d) Temperature dependence of the peak $|\mathrm{FFT}|^2$ corresponding to the oscillations visible by eye. A vertical dashed line denotes T_V.

oscillation intensities decrease rapidly in the cubic phase, but they do not vanish up to 140 K. In addition, as displayed in Figs. 3.4(b,d), a weak oscillation of 25.9 meV energy is observable only in the cubic phase, below 1.9 eV. According to the Fourier analysis shown in Figs. 3.5(b,d), the oscillation intensity decreases progressively with increasing temperature.

Next, Fig. 3.6 shows the fluence dependence of the transient reflectivity averaged between 2.0 and 2.3 eV, at 120 K, *i.e.* right above the transition temperature, both in the time and Fourier domains. As evidenced in Fig. 3.6(d), the 13.9-15.6 and 18.5-19.6 meV oscillations are completely quenched with increasing fluence above ~1 mJ/cm^2. In contrast, the intensity of the 25.9 meV oscillation increases with fluence and saturates above ~4 mJ/cm^2.

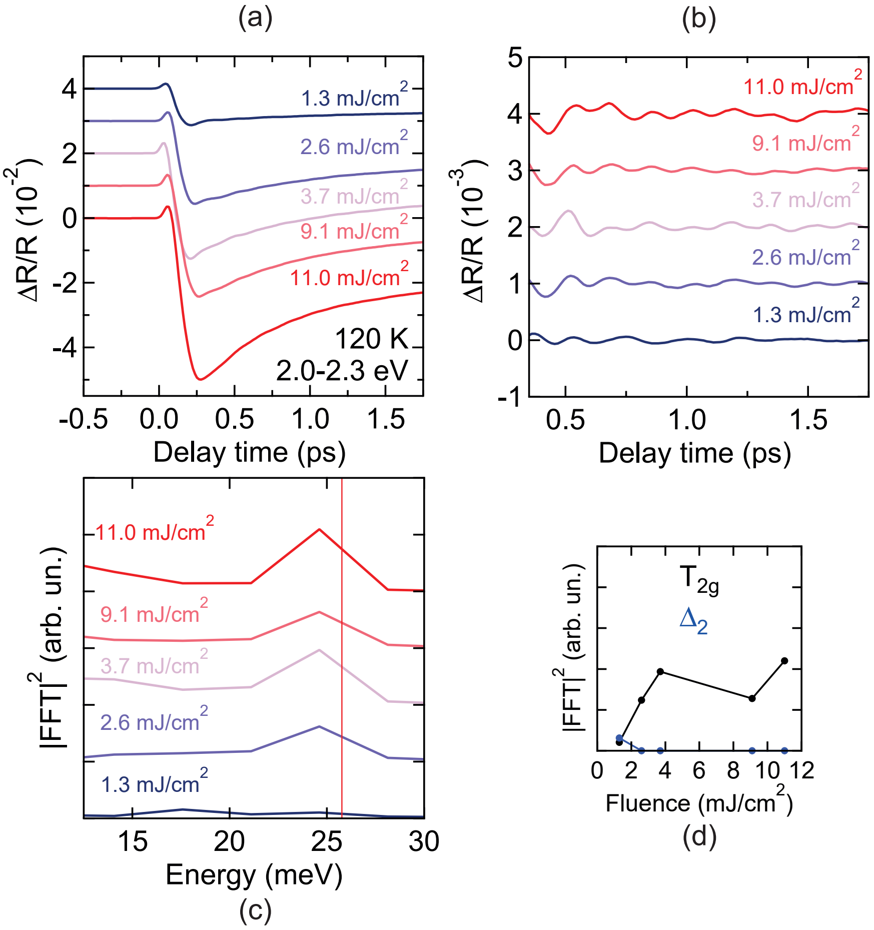

Figure 3.6 – Fluence dependence of the coherent response at 120 K. (a) Differential reflectivity as a function of pump-probe delay time averaged in between 2.0 and 2.3 eV at different fluences. (b) Oscillatory component singled out from the time traces of panel (a) by subtracting the non-oscillatory transient. (c) Power spectrum of the coherent response from the FT of the oscillatory component. A red vertical line indicates the energy of the T_{2g} phonon mode at the Γ point in $Fd\bar{3}m$ symmetry from *ab initio* calculations. (d) Temperature dependence of the peak $|\mathrm{FFT}|^2$ corresponding to the oscillations visible by eye.

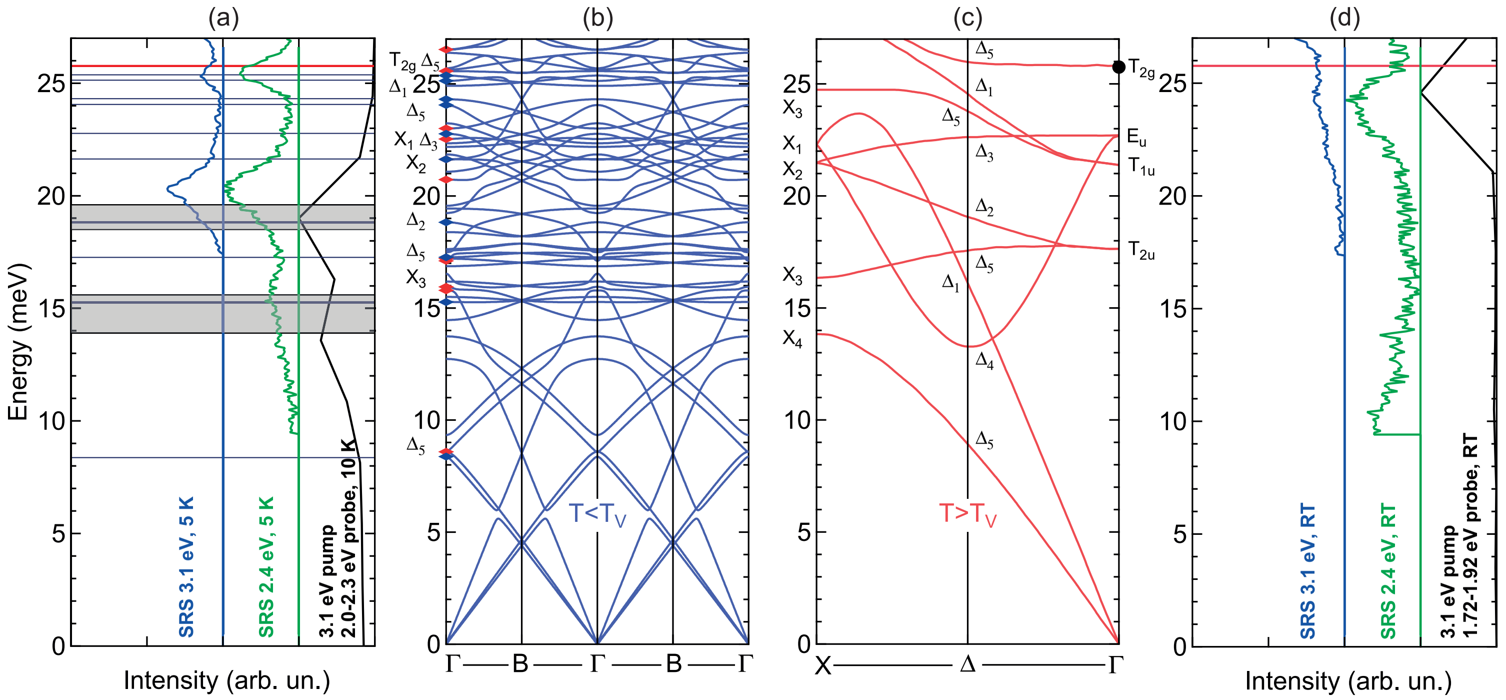

Figure 3.7 – Assignment of the phonon modes in pump-probe and spontaneous Raman scattering experiments. (a,d) Comparison between (colored lines) our spontaneous Raman spectra at different excitation energies and (black line) $|\mathrm{FFT}|^2$ of the coherent response in our time-resolved experiments, respectively, in the monoclinic and cubic phase. Blue (Red) horizontal lines indicate the energy of the A_g (T_{2g}) phonon modes at the Γ point in $P2/c$ ($Fd\bar{3}m$) symmetry from *ab initio* calculations. Shaded areas extend over the energy ranges of the beating oscillations in the monoclinic phase as estimated based on the fit analysis. (b,c) *Ab initio* calculations of the phonon dispersion curves, respectively, in $P2/c$ and $Fd\bar{3}m$ symmetry. Labels indicate the symmetry of the phonon modes at the Γ, Δ and X point in $Fd\bar{3}m$ symmetry, and the cubic counterparts of the Raman-active phonon modes at the center of the Brillouin zone in $P2/c$ symmetry. Blue (Red) diamonds refer to A_g (B_g) phonon modes.

3.2.2 Phonon Calculations and Mode Assignment

The phonon dispersion curves were calculated in the monoclinic phase, with the approximate space group *P2/c*, using the *ab initio* direct method [99, 100]. The electronic structure and atomic positions were optimized using the projector augmented-wave [101] and generalized gradient approximation (GGA) [102] implemented in the VASP program [103]. The strong electron interactions in the Fe 3*d* states were included within the GGA+*U* method [104]. The Hellmann-Feynman forces were calculated by displacing all inequivalent atoms from their equilibrium positions and the force-constant matrix elements were obtained in the 112-atom supercell. The phonon dispersions along the high-symmetry directions in reciprocal space were calculated by the diagonalization of the dynamical matrix. The phonon dispersions in the cubic phase were computed using the same approach in Refs. [25, 26].

Figure 3.7 compares FTs of the oscillations, spontaneous Raman spectra and theoretical predictions. In particular, the *ab initio* calculations of the phonon dispersion curves in the cubic phase from Refs. [25, 26] are plotted with red lines in Fig. 3.7(c). The spontaneous Raman spectra at 2.4 and 3.1 eV excitations, and the FT of the oscillations at room temperature are shown in Fig. 3.7(d). Only one mode of T_{2g} symmetry is Raman active at the center of the Brillouin zone in the energy region under consideration.

Our *ab initio* calculations of the phonon dispersion curves in the monoclinic phase are plotted with blue lines in Fig. 3.7(b). The structural transformation causes a quadrupling of the unit cell below the transition temperature, with the consequent development of new phonon branches. As illustrated by horizontal lines in Fig. 3.7(a), different modes are folded from finite wave vector to the center of the Brillouin zone, where they are potentially observable by means of spontaneous Raman scattering in the visible region. Figure 3.7(a) also displays the spontaneous Raman spectra at 2.4 and 3.1 eV excitations at 5 K, and the FT of the oscillations at 10 K. Shaded areas highlight the energy ranges of the oscillations inferred from our fit analysis.

In the space group *P2/c*, modes with Raman activity are either of A_g or B_g symmetry. For modes of B_g symmetry, the signs of the oscillations should change, upon modifying the polarizations of the pump and probe beams from parallel to orthogonal. This was not the case in our experiments. Therefore, we conclude that the modes are of A_g symmetry. Based on the comparison shown in Fig. 3.7, the oscillations at 13.9–15.6 and 18.5–19.6 meV are ascribed to the monoclinic modes of A_g symmetry closest in energy, which in turn originate from the cubic modes of respectively X_3 and Δ_2 symmetry at the lowest energies. Henceforth, they will be referred to, respectively, as the X_3 and Δ_2 modes. Instead, the oscillation at 25.9 meV is unambiguously identified with the cubic mode of T_{2g} symmetry, or T_{2g} mode.

Let us note that the peaks in the FT of the oscillations extend over a broad range from 11.5 to 21.0 meV. The estimates of the central energies of the oscillations from our analysis in the Fourier domain are lower compared to spontaneous Raman scattering. A possible explanation of both observations is the occurrence of oscillation dephasing and energy renormalization from anharmonic effects in the out-of-equilibrium conditions of our pump-probe experiments. The approximation of the space group in the monoclinic phase to $P2/c$ in our *ab initio* calculations underestimates the energy renormalization of the lattice vibrations from the onset of charge and orbital order. As an incidental result, our theoretical predictions are in better agreement with our time-resolved data than our spontaneous Raman data.

According to our first-principle computations, a cubic mode of Δ_5 symmetry gives rise to a monoclinic mode of A_g symmetry in the energy range intermediate between the 13.9–15.6 and 18.5–19.6 meV oscillations (see Figs. 3.7(a,b)). This casts doubts on the above assignment, following from energy considerations alone, which will be dispelled in the next Subsection.

3.2.3 Raman Matrix Element Analysis and Optical Constant Calculations

To corroborate our assignment of the oscillations, we benefit from the broadband nature of our probe, which gives us access to the energy dependences of the Raman matrix elements (RMEs) of the oscillations, and compare them to *ab initio* calculations. First, by means of singular value decomposition (SVD), we separated the $\Delta R/R$ matrix into the energy dependences of the incoherent excitations, *i.e.* the exponential decays, and the collective modes generated coherently, *i.e.* the oscillations. We thereby gained qualitative information on the coupling between atomic displacements and electronic excitations.

The $\Delta R/R$ matrix is comprised of N_t (N_E) columns (rows), corresponding to the values of pump-probe delay time (probe photon energy). Our algorithm decomposed it into the sum of outer products between time and energy vectors, respectively, $\{\boldsymbol{u}'_i(t)\}$ and $\{\boldsymbol{v}_i(E)\}$, according to

$$\frac{\Delta R}{R}(E,t) = \sum_{i=1}^{r} \lambda_i \boldsymbol{u}'_i(t) \otimes \boldsymbol{v}_i(E) = \sum_{i=1}^{r} \boldsymbol{u}_i(t) \otimes \boldsymbol{v}_i(E), \tag{3.1}$$

where r is the rank of the $\Delta R/R$ matrix, the coefficients $\{\lambda_i\}$ are termed singular values, and $\{\boldsymbol{u}'_i(t)\}$ and $\{\boldsymbol{v}_i(E)\}$ are orthonormal bases of, respectively, $\mathbb{R}^{N_t}$ and $\mathbb{R}^{N_E}$, referred to as canonical traces. The singular values are positive and in decreasing order, *i.e.* $\lambda_1 \geq \lambda_2 \geq \cdots \geq \lambda_r > 0$. To account only for the physically meaningful terms and, by that, reduce the noise level, we truncated the sum to the first two terms. As shown in Figs. 3.8(a,b), the two canonical time traces, $\boldsymbol{u}_1(t)$ and $\boldsymbol{u}_2(t)$, were fit with the same set of five model functions $\{\boldsymbol{U}'_j(t)\}$, with different amplitudes, $\{c_{1j}\}$ and $\{c_{2j}\}$, such that they can be rewritten as

$$\begin{aligned} \boldsymbol{u}_1(t) &= \sum_{j=1}^{5} c_{1j} \boldsymbol{U}'_j(t), \qquad (3.2) \\ \boldsymbol{u}_2(t) &= \sum_{j=1}^{5} c_{2j} \boldsymbol{U}'_j(t). \end{aligned}$$

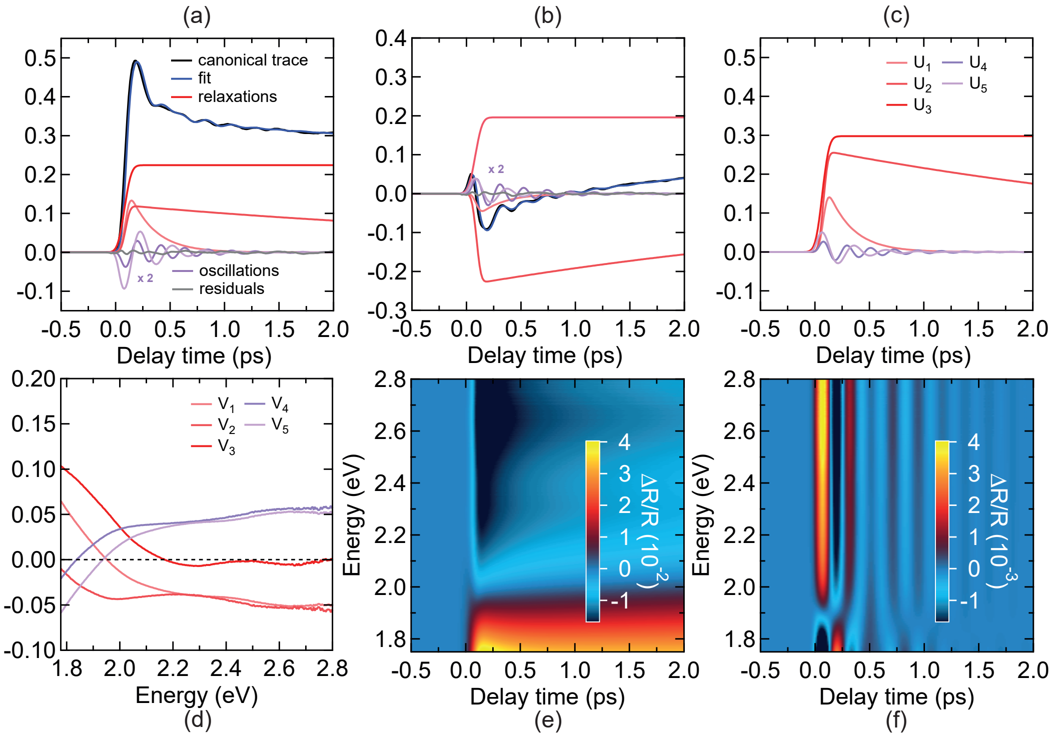

Figure 3.8 – SVD of the differential reflectivity matrix and fit of the canonical traces with model functions. Canonical time traces (a) $u_1(t)$ and (b) $u_2(t)$ obtained from our SVD algorithm. The fitting functions are comprised of the sum of two exponential decays, a step function and two damped coherent oscillations, convolved with a Gaussian response function. (c) Time and (d) energy dependences of the physical traces obtained from SVD, respectively, $\{U_i(t)\}$ and $\{V_i(E)\}$, which include relaxations (i=1,2,3) and damped coherent oscillations (i=4,5). Reconstruction of the (e) incoherent and (f) coherent contribution to the $\Delta R/R$ matrix at 10 K and ~1 mJ/cm^2 fluence through our SVD-based method.

To reconstruct the $\Delta R/R$ matrix starting from the model functions, we defined the physical traces, $\{\boldsymbol{U}_j(t)\}$ and $\{\boldsymbol{V}_j(E)\}$, such that

$$\frac{\Delta R}{R}(E,t) = \sum_{j=1}^{5} \boldsymbol{U}_j(t) \otimes \boldsymbol{V}_j(E). \tag{3.3}$$

Different valid choices of the physical traces were possible. We arbitrarily imposed that the normalization condition $\boldsymbol{V}_j(E) \cdot \boldsymbol{V}_j(E) = 1$ is fulfilled for any j. Accordingly, the physical traces, shown in Figs. 3.8(c,d), were computed as follows. It is easy to prove that the below definitions of the physical traces satisfy Eq. 3.3.

$$\boldsymbol{U}_j(t) = \left(c_{1j}^2 + c_{2j}^2\right)^{1/2} \boldsymbol{U}'_j(t), \tag{3.4}$$

$$\boldsymbol{V}_j(E) = \left(c_{1j}^2 + c_{2j}^2\right)^{-1/2} \left[c_{1j}\boldsymbol{v}_1(E) + c_{2j}\boldsymbol{v}_2(E)\right]. \tag{3.5}$$

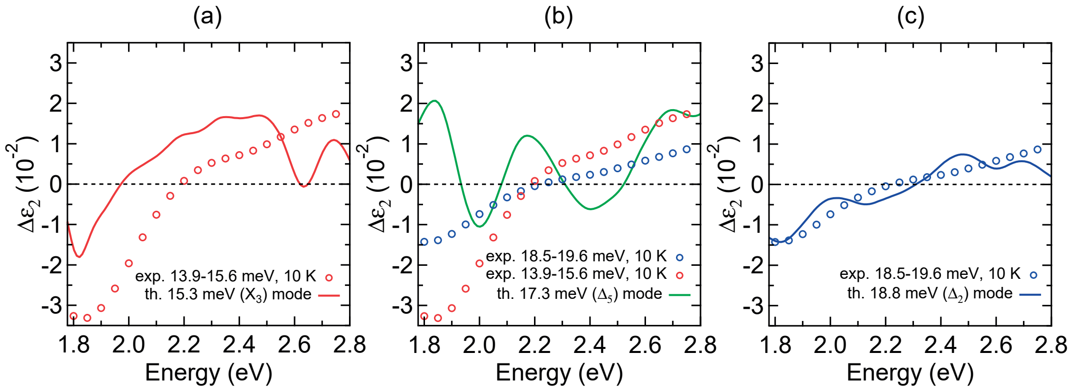

Figure 3.9 – Energy dependence of the coherent response. (Symbols) Energy profiles of the contributions to the imaginary part of the differential dielectric function, $\Delta\varepsilon_2$, from the oscillations at maximum displacement amplitude at 10 K and ~1 mJ/cm^2, and (lines) calculated RMEs for the A_g phonon modes in the same energy region, in the monoclinic phase. The cubic counterparts of the phonon modes are specified between parentheses. The computed RMEs correspond to maximum atomic displacements of about 5×10^{-2} Å for the 15.3 and 18.8 meV phonon modes, and 1×10^{-2} Å for the 17.3 meV phonon mode.

As shown in Figs. 3.8(e,f), if the sum in Eq. 3.3 is restricted to the exponential decays (oscillations), the incoherent (coherent) contribution to the $\Delta R/R$ matrix alone is isolated. Instead, the maximum contributions to the $\Delta R/R$ matrix from the oscillations, at the pump-probe delay time for the largest amplitudes of the atomic displacements t_M, is given by

$$\begin{aligned} \frac{\Delta R}{R}^{osc\,1}(E, t_M) &= \boldsymbol{U}_4(t_M) \otimes \boldsymbol{V}_4(E), \\ \frac{\Delta R}{R}^{osc\,2}(E, t_M) &= \boldsymbol{U}_5(t_M) \otimes \boldsymbol{V}_5(E). \end{aligned} \tag{3.6}$$

To compute the corresponding changes in the complex dielectric function, a Lorenz model was fit to the optical functions at 10 K from the ellipsometry measurements of Ref. [29], and the out-of-equilibrium reflectivity in the presence of the pump pulse, calculated according to $R_p(E, t_M) = R_u(E) + R_u(E)\,\Delta R/R^{osc}(E, t_M)$. For consistency, the equilibrium reflectivity in the absence of the pump pulse $R_u(E)$ was also computed based on the data of Ref. [29]. The changes in the imaginary part of the dielectric function are plotted with symbols in Fig. 3.9.

To compute the theoretical predictions of the RMEs, we used the following procedure, also described in Ref. [105]. First, the frequency-dependent dielectric function was calculated for a series of monoclinic cells, with approximate space group $P2/c$, in the absence of structural distortions. Then, the same calculation was repeated, with atoms displaced along the eigenvectors of the phonon modes in the 11.5–21.0 meV range of the oscillations, namely, the monoclinic modes of A_g symmetry which originate from the cubic modes of X_3, Δ_5 and Δ_2 symmetry. The differences between the above quantities, in the linear displacement regime, represent our estimates of the RMEs.

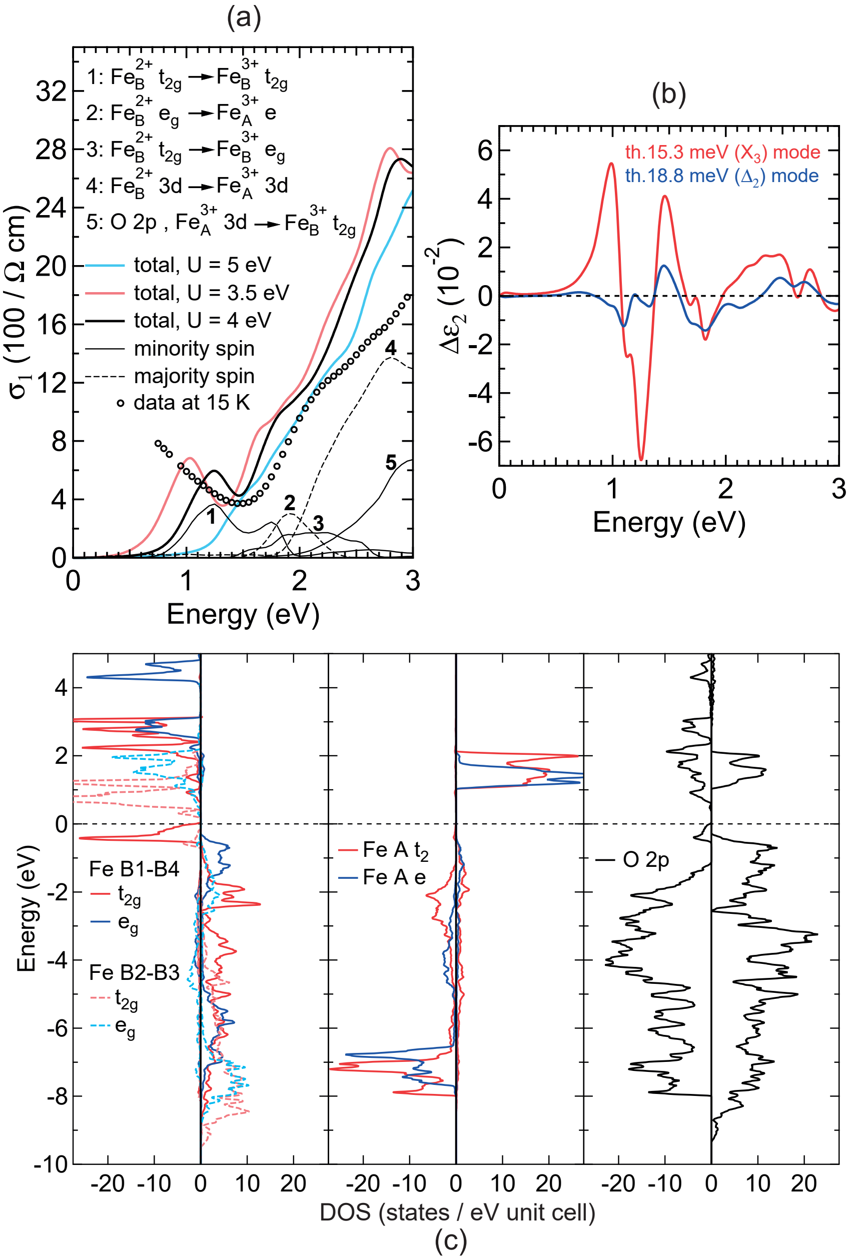

Figure 3.10 – *Ab initio* calculations of the optical functions. (a) Comparison between (symbols) the real part of the optical conductivity at 15 K from the ellipsometry measurements of Ref. [29] and (thick lines) the theoretical predictions from our GGA+U calculations with $U = 3.5$, 4 and 5 eV and J = 1 eV. The main contributions from different interband transitions to the features around 1.2 and 1.7–2.2 eV for $U = 4$ eV are plotted with thin lines and labeled according to the predominant character of the initial and final states. (b) Calculated RMEs for the modes corresponding to the oscillations in the low-energy region below 3 eV. (c) Calculated partial density of states corresponding to inequivalent Fe and O ions in the $P2/c$ subcell. The notation $B1$–$B4$ refers to inequivalent Fe ions in the $P2/c$ subcell (see Ref. [6]). The Fermi level (dashed line) is set to the top of the valence band.

The self-consistent charge density of the electronic ground state was determined from density functional theory (DFT) calculations in the GGA+U approximation implemented in the QUANTUM ESPRESSO package [104, 106]. Subsequently, the frequency-dependent dielectric function was calculated with the linear response method within the random phase approximation using the YAMBO package [107].

The theoretical predictions of the RMEs depend on the energy ranges of the interband transitions. Let us note that, in general, *ab initio* calculations are unable to predict them in an accurate manner. In common practice, to improve the agreement between experimental data and theoretical predictions of the optical functions, the energy scales are offset by arbitrary values. Therefore, in the following, only a qualitative comparison between RMEs from experiments and first-principle computations is possible. Only major features of the theoretical predictions, *e.g.* zero crossings and main peaks, are accounted for, with an uncertainty margin on the energy positions. Based on our criteria, for onsite Coulomb repulsion $U = 4$ eV, and Hund's exchange coupling $J = 1$ eV, our experimental and theoretical RMEs for the X_3 and Δ_2 modes are in mutual qualitative agreement (see Figs. 3.9(a,c)). This is not the case for the Δ_5 mode (see Fig. 3.9(b)). Therefore, overall, our RME analysis provides an anchor point to our assignment of the oscillations in the foregoing.

Furthermore, as shown in Fig. 3.10(a), our *ab initio* calculations qualitatively reproduce the characteristic features of the optical conductivity at 15 K, except for the position of the lowest-energy peak. Let us note that the agreement with the experimental data does not improve for $U = 3.5$ or 5 eV. In consideration of the reasonable consistency of our experimental and theoretical RMEs in our probed region, we reexamine the absorption structure of magnetite in the monoclinic phase, to better substantiate the assignment of the interband transitions. As shown in Fig. 3.10(a), the optical response was decomposed into the main contributions from different electronic transitions, singled out based on the origin and symmetry of the energy bands, summarized in Fig. 3.10(c). Three main charge transfers dominate the debated feature around 2 eV, namely, between the minority-spin t_{2g} and e_g states of B-type Fe ions of respectively +2 and +3 nominal valence (peak 3), the minority-spin t_{2g} states of the same ions (peak 1), and the top of the highest filled band and the bottom of the lowest empty band formed by respectively B- and A-type Fe ions in the majority-spin channel (peak 2). Earlier calculations [31] attributed the debated feature only to the first of the above electronic transitions, based purely on energy considerations, albeit with negligible calculated intensity. In contrast, our assignment relies on the computed spectral weights, which point out that the contributions from states of A-type Fe ions are also meaningful, and the excitations of the t_{2g} electrons across the bandgap extend over the energy region of the 2 eV feature in the form of a satellite peak.

Let us note that RME effects are also responsible for changes in the oscillation intensity of the T_{2g} mode as a function of temperature, shown in the right panels of Fig. 3.5. The T_{2g} mode is not observable within out detection limits in any spectral region in the monoclinic phase. Instead, it resonates in the energy range of positive incoherent response in the cubic

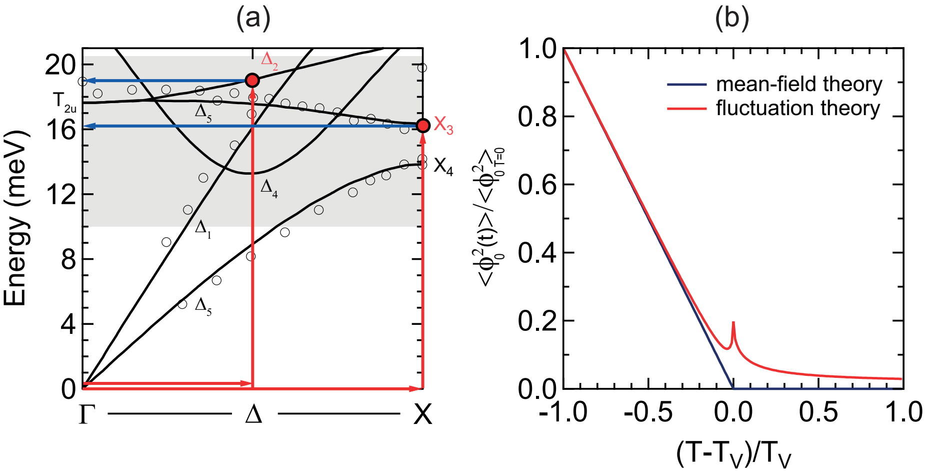

Figure 3.11 – (a) Two-mode photoexcitation mechanism. Schematic representation of wave-vector conservation in the photoexcitation mechanism of the X_3, Δ_2 and ordering field modes above T_V. The phonon dispersion curves in the cubic phase (symbols) as measured by means of INS [108] and (lines) predicted according to *ab initio* calculations are shown. The energy and wave vector of the phonon and ordering field modes are represented by red and blue arrows, respectively. The combination of the two types of modes allows wave-vector conservation in the Raman scattering process. The shaded area extends over the energy range of the oscillations in the cubic phase, in the vicinity of T_V, as estimated based on a FT analysis. (b) Temperature dependence of the normalized equal-time autocorrelation of the ordering field across the ordering temperature. The plotted curves refer to a one-component ϕ^4 model at the Gaussian level. The results for a two-component model are qualitatively similar, but the details depend on the interactions among the modes. In these units, the intensity of the anomaly at T_V is regulated by the inverse Ginzburg length [109].

phase. The more intense peak in spontaneous Raman spectra for 2.4 compared to 3.1 eV excitation is consistent with the energy dependence of the experimental RME of the T_{2g} mode (see Figs. 3.7(a,d) and Chapter 4). With increasing temperature in the cubic phase, the energy range of positive incoherent response moves out of our probed region (see Fig. 3.2). As a consequence, the oscillation intensity of the T_{2g} mode integrated in the 1.72–1.92 eV range decreases progressively.

3.2.4 Fluctuation-Assisted Excitation of Phonons

Wave-vector conservation in first-order Raman scattering requires that the phonon modes are close to the center of the Brillouin zone. Instead, as illustrated in Fig. 3.7, the X_3 and Δ_2 modes are at finite wave vectors in the cubic phase. Therefore, neither of them can be excited by means of single-mode processes, and they are referred to as *forbidden* modes. Here, we argue that ordering field modes of diffusive character at critical wave vectors assist the excitation of forbidden modes in the cubic phase. In particular, it has been demonstrated that intrinsic fluctuations of coupled charge density and structural distortions in the cubic phase preempt the Verwey transition [66–69]. Figure 3.11(a) is a pictorial representation of our proposed mechanism. The above fluctuations provide the $(0,0,2\pi/a)$ and $(0,0,\pi/a)$ contributions necessary for wave-vector conservation in second-order Raman scattering. In past studies of nearly first-order transitions by means of spontaneous Raman scattering, low-lying modes of precursor order, such as soft phonons, were also suggested to assist the excitation of forbidden modes [110].

Our starting point is the general theory of TSRS discussed in Section 2.2. We introduce an additional variable to describe the ordering field, which can be either bosonic or classical, depending on the mechanism of the phase transition. Indeed, if the transformation is a Peierls process, quantum fluctuations play an important role [111]. Instead, if it is an order-disorder process, the dynamical response reduces to a central peak [109]. The following Hamiltonian for TSRS of the second order describes the time-dependent perturbation introduced by the pump field. This is equivalent to a time-dependent interaction between a phonon mode and an ordering field mode controlled by the impulsive photoexcitation.

$$H_R = \sum_{\boldsymbol{q}\lambda} g_{\boldsymbol{q}\lambda}(t)\rho_{\boldsymbol{q}} Q_{-\boldsymbol{q}\lambda}, \tag{3.7}$$

where

$$g_{\boldsymbol{q}\lambda}(t) = -\frac{V}{4}\boldsymbol{\mathcal{E}}(t)\cdot\frac{\partial^2\boldsymbol{\chi}}{\partial\rho_{\boldsymbol{q}}\partial Q_{-\boldsymbol{q}\lambda}}(\omega_L)\cdot\boldsymbol{\mathcal{E}}(t) \tag{3.8}$$

and $\rho_{\boldsymbol{q}}$ is the canonical coordinate of the ordering field mode of wave vector $\boldsymbol{q}$. The Raman tensor, $\partial^2\boldsymbol{\chi}/\partial\rho_{\boldsymbol{q}}\partial Q_{-\boldsymbol{q}\lambda}$, is the second derivative of the dielectric susceptibility evaluated at the carrier frequency of the pump pulse ω_L. For simplicity, the bare electron-phonon interactions are incorporated in the definitions of the quasiparticle field operators.

In the response regime linear in fluence, if we assume that the ordering field is classical, we can compute the dynamics of the coupled modes according to the Kubo formula, as follows

$$\begin{aligned}\langle\rho_{\boldsymbol{q}}Q_{-\boldsymbol{q}\lambda}\rangle(t) &= -\frac{i}{\hbar}\int_{-\infty}^{t} dt'\,\langle[\rho_{\boldsymbol{q}}(t)Q_{-\boldsymbol{q}\lambda}(t), Q_{\boldsymbol{q}\lambda}(t')\rho_{-\boldsymbol{q}}(t')]\rangle\, g_{\boldsymbol{q}}(t') \\ &= -\int_{-\infty}^{t} dt'\langle\rho_{\boldsymbol{q}}(t)\rho_{-\boldsymbol{q}}(t')\rangle\,\frac{e^{-(t-t')/\tau_{ph}}\sin[\omega_{\boldsymbol{q}}(t-t')]}{\omega_{\boldsymbol{q}}}\, g_{\boldsymbol{q}}(t'),\end{aligned} \tag{3.9}$$

where $\langle\cdots\rangle$ denotes thermal and quantum averages, and τ_{ph} and $\omega_{\boldsymbol{q}}$ are respectively the phenomenological lifetime and the frequency of the phonon mode. For simplicity, let us consider a single phonon branch, and therefore drop the branch index λ.

If the time profile of $g_{\boldsymbol{q}}$ is impulsive, sinelike oscillations of the correlation between the phonon and the ordering field mode are produced, with envelope given by the autocorrelation of the ordering field mode $\langle\rho_{\boldsymbol{q}}(t)\rho_{-\boldsymbol{q}}(0)\rangle$. Instead, in the case of a steplike time profile of $g_{\boldsymbol{q}}$, cosine-like oscillations are produced. The mechanism here proposed represents a generalization of TSRS which can be referred to as fluctuation-assisted stimulated Raman scattering (FASRS).

The optical functions are modulated via their dependence on the dielectric susceptibility, which in turn is modified through the same Raman tensor at play in the generation mechanism, but evaluated at the probe frequency, according to

$$\delta\boldsymbol{\chi}(\omega,t)=\sum_{\boldsymbol{q}}\frac{\partial^2\boldsymbol{\chi}}{\partial\rho_{\boldsymbol{q}}\partial Q_{-\boldsymbol{q}}}(\omega)\langle\rho_{\boldsymbol{q}}Q_{-\boldsymbol{q}}\rangle(t). \tag{3.10}$$

To exemplify the application of the FASRS mechanism to our observations, we assume an instability of the ordering field at the X point of the Brillouin zone, corresponding to the wave vector $\boldsymbol{Q}=(0,0,2\pi/a)$, comprised of extra charges $-\delta$, 0, δ, 0 in the planes of B-type Fe ions separated by $a/4$ along the z direction. The space profile of the ordering field can be written as

$$\rho(\boldsymbol{r})=\phi_1(\boldsymbol{r})\cos(\boldsymbol{Q}\cdot\boldsymbol{r})+\phi_2(\boldsymbol{r})\sin(\boldsymbol{Q}\cdot\boldsymbol{r}). \tag{3.11}$$

The trigonometric factors account for the rapidly varying components of charge order. Instead, ϕ_1 and ϕ_2 account for the real, slowly varying components of charge order, in the following referred to as the ordering field itself. The phase transition can be described in a phenomenological manner by means of a Ginzburg-Landau expansion of the free energy density in power series of the ordering field and its gradient [109].

Near the transition temperature, around the critical wave vectors, the amplitudes of the ordering field modes become large. Therefore, we can neglect the wave-vector dependence of the ordering field in Eq. 3.10, and account only for the ordering field mode at $\boldsymbol{Q}$, as follows

$$\begin{aligned}\delta\boldsymbol{\chi}(\omega,t)=&-\frac{\partial^2\boldsymbol{\chi}}{\partial\rho_{\boldsymbol{Q}}\partial Q_{-\boldsymbol{Q}}}(\omega)\frac{N^2}{2}\\&\times\int_{-\infty}^{t}dt'\sum_{\alpha=1,2}\langle\phi_{\alpha0}(t)\phi_{\alpha0}(t')\rangle\frac{e^{-(t-t')/\tau_{ph}}\sin[\omega_{\boldsymbol{Q}}(t-t')]}{\omega_{\boldsymbol{Q}}}\,g_{\boldsymbol{Q}}(t'),\end{aligned} \tag{3.12}$$

where N is the number of sites and $\langle\phi_{\alpha0}(t)\phi_{\alpha0}(t')\rangle$ is the autocorrelation of the ordering field at $\boldsymbol{r}=0$. In the Landau theory, the fluctuations are neglected, and thus the autocorrelation reduces to a time independent quantity, $\langle\phi^2_{\alpha0}\rangle$, identical to the squared OP, $\langle\phi_{\alpha0}\rangle^2$, which by definition is different from zero only below the transition temperature (see blue line in Fig. 3.11(b)). This corresponds to the notion that the phonon modes become active in the broken-symmetry phase upon folding from the boundary to the center of the Brillouin zone.

If the fluctuations are taken into account, the results are different. The equal-time autocorrelation, $\langle\phi^2_{\alpha0}(t)\rangle$, determines the initial amplitude of the oscillations (see red line in Fig. 3.11(b), based on calculations at the Gaussian level). This shows that the fluctuations make the phonon modes active even above transition temperature. Furthermore, if the oscillations are shorter than the phenomenological lifetime of the phonon mode, it means that the decay is dominated by the factor $\langle\phi_{\alpha0}(t)\phi_{\alpha0}(t')\rangle$ in Eq. 3.12 and it is possible to gain information on the dynamics of the ordering field in the time domain. For weakly first-order transitions, such as the case under study, the temperature dependence of the equal-time correlation is qualitatively similar, except for a small discontinuity at the transition temperature.

3.3 Discussion

To avoid confusion, it is important to point out the difference between phase coexistence and critical fluctuations. In general, the Verwey transition is regarded to as a weakly first-order transition. Even in high-quality single crystals, such as our sample, close to the transition temperature defects promote the progressive nucleation and growth of disordered domains. However, as shown in Figs. 3.1(a,b), the disordered and ordered phases coexist only in a narrow temperature range, on the order of 1 K. In contrast, critical fluctuations are correlations of precursor order, of local dynamic nature, which extend over wide temperature ranges in the disorder phase (see Section 1.4). To date, the role of imperfections on the degree of precursor order is controversial. However, its occurrence also in highly-stoichiometric synthetic crystals points to phenomena intrinsic to the ideal mechanism of the Verwey transition, rather than sample dependent. In any case, it would certainly be interesting to study the effects of different levels of disorder on the excitation of the forbidden modes in the cubic phase by means of spontaneous Raman scattering experiments.

Within the above framework, the coherent generation and detection of monoclinic modes in the cubic phase in our pump-probe experiments can only be rationalized taking into account the effects of critical fluctuations, and provide information on their dynamics. In particular, Eq. 3.12 implies that in the presence of long-lived fluctuations of the ordering field, phonon modes at finite wave vectors can be coherently generated, with coherence time limited by the correlation time of the fluctuations themselves. Practically, the oscillation frequencies do not show any meaningful change across the critical region. Therefore, our results clarify that the fluctuations are comprised of relaxational responses, consistent with Yamada's interpretation of the Verwey transition in terms of concomitant order-disorder and displacive transformations [24]. Instead, if a Peierls-like mechanism played a significant role in the Verwey transition, the fluctuations would consist of periodic amplitude and phase modulations of the charge density, both in space and time, and accordingly possess finite frequencies. For example, in the approximation of the electronic spectrum of the critical modes to a single pole at ω_{CDW}, second-order Raman scattering is supposed to give rise to Stokes and anti-Stokes oscillations at frequencies $\omega_{\boldsymbol{Q}} \pm \omega_{CDW}$, with sizable temperature dependence, in sharp contrast to our observations.

By means of SVD, we were able to determine the energy dependence of the experimental RMEs. Comparison with *ab initio* calculations allowed us to unambiguously identify the forbidden modes. This assignment methodology has the advantage to rely on the phonon eigenvector instead of the phonon energy, and therefore provides accurate information.

Our pump-probe experiments give direct access to the decay time of the oscillations. According to Eq. 3.12, this is dominated by the phenomenological lifetime of the phonon modes or the correlation time of the fluctuations, whichever is shorter. If the fluctuations are the limiting factor, the lineshapes of the oscillations in the Fourier domain are supposed to become broader above the critical temperature, which is indeed the case in our observations (see Fig. 3.5(a)). With these considerations in mind, in Subsection 5.3.3 we provide an estimate of the correlation time of the fluctuations and compare it with observations from INS.

Gaussian fluctuations are supposed to result in a cusp anomaly in the initial amplitude of the oscillations centered at the transition temperature (see Fig. 3.11(b)). Unfortunately, our temperature and energy resolutions are not high enough to test this hypothesis. In any case, the persistence of oscillations above the transition temperature (see Fig. 3.5(c)) is in qualitative agreement with the theoretical predictions. As shown in Fig. 3.6(d), fluences above ~1 $\mathrm{mJ/cm^2}$ are high enough to suppress the oscillations close to the critical region, as a result of the rapid decrease in coherence time and length of the fluctuations with increasing temperature. In contrast, the T_{2g} mode at the center of the Brillouin zone is coherently generated by means of a first-order process of TSRS [85, 87], with typical increase in the oscillation intensity in a linear regime, below ~ 4 $\mathrm{mJ/cm^2}$, followed by saturation at higher fluences.

In contrast to our pump-probe experiments, in our spontaneous Raman scattering experiments at 2.4 and 3.1 eV excitations, no forbidden mode was detected below 27 meV in the cubic phase (see Chapter 4). Let us note that, as already mentioned in the foregoing, the analogue in spontaneous Raman scattering experiments of our observations from pump-probe experiments was reported for structural transitions [110]. The absence of forbidden modes in our spontaneous Raman spectra in the cubic phase is indicative of the different sensitivity of the two techniques to phonon modes at low energy, but could also suggest that nonlinear effects enhance the coherent response in our pump-probe experiments. One can easily check that the time-dependent electron-phonon interaction expressed in Eq. 3.7 promotes a transient stabilization of the ordered phase, equivalent to an increase of the effective ordering temperature in steady-state conditions. Possibly, the above effect amplifies the coherent response, since it induces a symmetry breaking limited in time and confined in space. Experimentally, to validate this hypothesis, one would need to carry out a thorough study of the fluence dependence of the coherent response near the transition temperature. This requires accurate temperature control across the specific heat anomaly in the critical region and high enough signal-to-noise ratio to detect weak oscillations at low fluences.

3.4 Conclusions

Typically, ultrashort laser pulses are used to melt the OP in the ordered phase, and thus establish the electronic and structural properties of the disordered phase [29, 112]. In this Chapter, we discussed a more subtle effect, with implications on the coherent control of transition-metal oxides. In particular, we demonstrated that impulsive photoexcitation at 3.1 eV photon energy, above the onset of charge transfer excitations between O $2p$ and Fe $3d$ states, transiently promotes the coupling between phonon modes at finite wave vectors and fluctuation modes of the ordering field above the critical region of the Verwey transition in magnetite. In principle, it is also possible that, in suitable conditions, the coherent control of the electron-phonon coupling temporarily induces the buildup of long-range order.

We developed a method able to measure the dependence of amplitude and correlation time of the fluctuations on temperature and characteristics of the photoexcitation, and thus gain insight into the critical dynamics of the fluctuations in correspondence of phase transitions. Moreover, our approach enabled us to describe the atomic displacements associated with the fluctuations and the interplay between structural and electronic degrees of freedom. This further elucidated the microscopic mechanism of the Verwey transition and the interpretation of the optical response in magnetite.

4 Light Scattering from Critical Modes

Inelastic light scattering is an effective tool to gain direct insight into lattice-dynamical effects in structural transitions. In this Chapter, we present inelastic light scattering data across the Verwey transition in magnetite, on a natural single crystal. We address the intricate puzzle of the transformation process from different perspectives. We take advantage of the broad potential of Raman spectroscopy in the study of lattice vibrations to single out the structural anomalies associated with the Verwey transition, with particular reference to the consequences of strong coupling to electronic excitations.

At the same time, we provide evidence of the contribution to the spectral response from diffusive modes of mainly electronic nature. Notably, we reveal the spectroscopic fingerprints of correlations of the ordering field, with fast dynamics, compared to analogous observations from inelastic neutron scattering. The comparison of data from light and neutron probes is suggestive of prevalent electronic, rather than polaronic, character of the excitations visible in the Raman spectra. An additional contribution to the spectral response from charge carriers sets in above the Verwey temperature. The thermal variations of its intensity mimic the dc conductivity. Overall, we improve the understanding of the critical dynamics of magnetite and the hierarchy among structural and electronic modes in the mechanism of the Verwey transition.

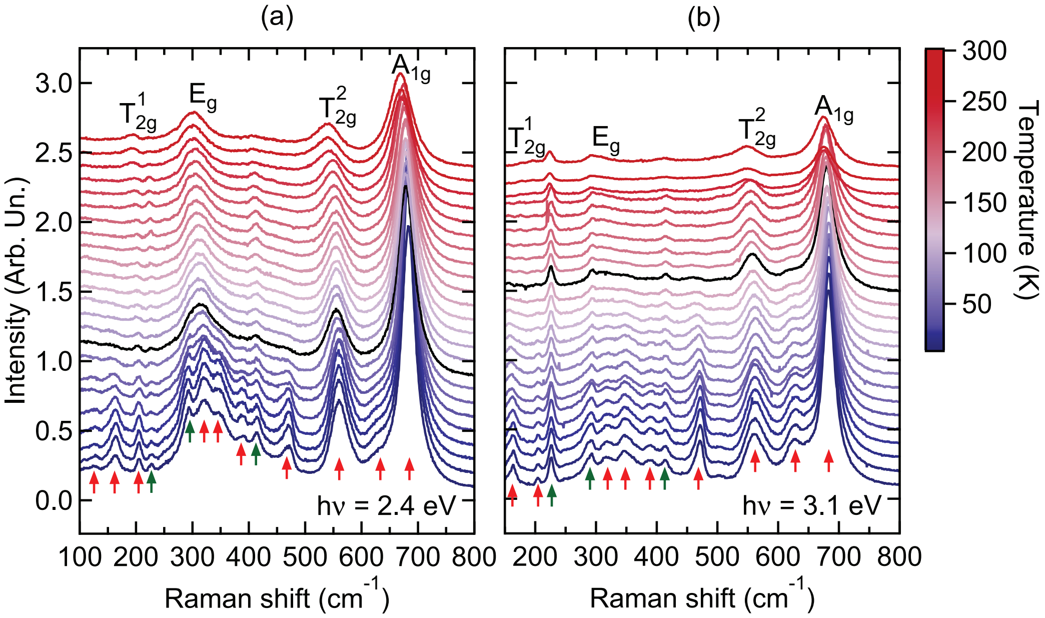

Figure 4.1 – Complete data sets of Raman spectra as a function of nominal temperature for (a) 2.4 and (b) 3.1 eV excitation. Data are normalized to the background intensity integrated between 800 and 810 cm^{-1}. Red (Green) arrows indicate magnetite (hematite) phonon modes in the monoclinic phase. Blue-to-red color coding refers to increasing nominal temperature. Black color denotes the Verwey temperature.

4.1 Experiments

The magnetite sample measured in our experiments is a natural single crystal purchased from Surface Preparation Laboratory (SPL), Zaandam, Netherlands. Based on ac susceptibility characterization, analogous to that of Chapter 3, it presents a discontinuous transition, at the Verwey temperature, $T_V = 116$ K. The sample was mounted on the cold finger of a liquid helium cryostat in a base pressure of 10^{-6} mbar. The sample surface was polished to optical quality without any specific orientation of the crystal face.

Raman experiments were conducted in the 5–330 K temperature range by means of the Raman spectrometer described in Section 2.1. In two different sets of experiments, the sample was illuminated by the 514.5 nm output of an argon ion laser and the 405 nm emission line of a diode laser, with 10 mW nominal power incident onto the sample surface. In the following, the two different excitations are denoted by their photon energies, $h\nu = 2.4$ and 3.1 eV, respectively. Raman spectra were acquired in unpolarized backscattering configuration. For experimental limitations in the rejection of the Rayleigh light, the lower boundaries of our detection ranges are 75 and 140 cm^{-1}, respectively, for 2.4 and 3.1 eV excitation. As a result of large effects of laser heating, for 2.4 eV excitation the Verwey transition occurs at a nominal temperature $T_V^* = 85$ K. Asterisks in superscripts denote reference to the nominal temperature for 2.4 eV excitation. To compensate for the difference in the nominal temperatures, combined data

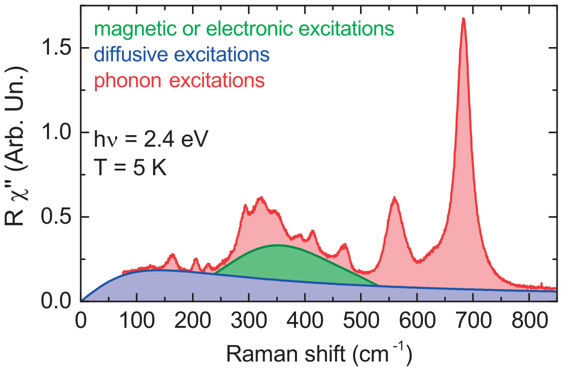

Figure 4.2 – Pictorial representation of the different contributions to the Raman response function of magnetite from phonons, magnons and electrons, with diffusive or propagating dynamics.

are plotted as a function of the reduced temperature, defined as $T^*/T_V^* - 1$ and $T/T_V - 1$, respectively, for 2.4 and 3.1 eV excitation. Accordingly, our approximate estimate of the effective temperature at the laser spot for 2.4 eV excitation is $T = T^*\, T_V/T_V^*$. Data sets in the full temperature range of our experiments are shown in Fig. 4.1.

4.2 Results and Discussion

As illustrated in Fig. 4.2, in our study we take into account three possible contributions to the Raman spectra, namely, scattering of light by phonons, magnons and electrons, with propagating or diffusive dynamics. Typically, the first two types of collective excitations respectively produce narrow and broad peaks, superimposed to an intensity continuum from electronic Raman scattering. In a phenomenological description, the total Raman response, $S(\omega)$, can be fit by the sum of three separate components, $S_{\mathrm{ph}}(\omega)$, $S_{\mathrm{ma}}(\omega)$ and $S_{\mathrm{el}}(\omega)$, respectively associated with lattice vibrational, magnetic and electronic degrees of freedom. According to the fluctuation-dissipation theorem, the scattering cross section in Raman experiments, $S(\omega)$, is proportional to the imaginary part of the Raman response function, $\chi''(\omega)$,

$$S(\omega) = [1 + n(\omega)]\, R\,\chi''(\omega), \tag{4.1}$$

where $1 + n(\omega) = [1 - \exp(-\omega/k_B T)]^{-1}$ is the Bose-Einstein thermal factor. Matrix element effects are incorporated in the proportionality factor R. To a first approximation, it can be assumed temperature and frequency independent. In the following, Raman spectra corrected by the Bose factor, $R\,\chi''(\omega)$, are accounted for. For simplicity, they are referred to as the spectral response.

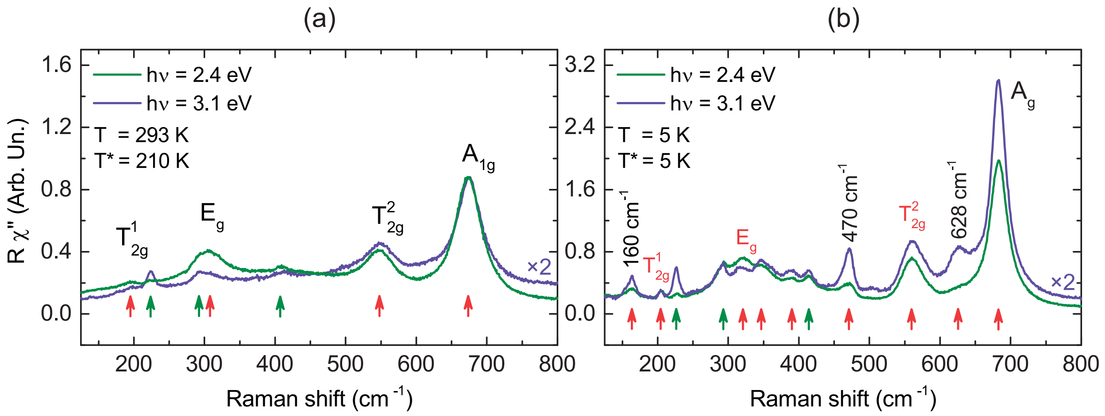

Figure 4.3 – Spectral response obtained for 2.4 eV excitation at (a) 293 and (b) 5 K, and for 3.1 eV excitation at the same reduced temperatures. Red (Green) arrows indicate magnetite (hematite) phonon modes. Labels in red refer to the cubic counterparts of the phonon modes in the monoclinic phase. For better comparison, data are normalized to the background intensity integrated between 800 and 810 cm^{-1}.

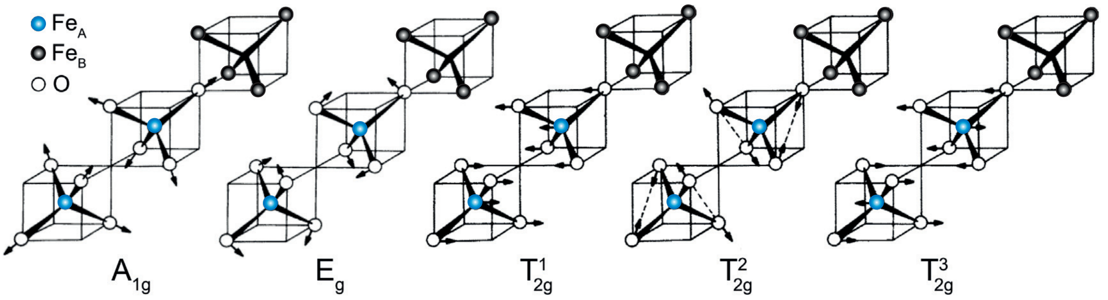

Figure 4.4 – Pictorial representation of the eigenvectors of the Raman-active modes in the primitive cell of magnetite according to Verble's description. Adapted from Ref. [113].

4.2.1 Phonon Excitations

First, we focus on the contribution to the spectral response from the phonon modes with Raman activity, generally modeled by Lorentzian functions, with frequency ω_i, linewidth Γ_i and amplitude A_i,

$$S_{\text{ph}}(\omega) = [1 + n(\omega)] \sum_{i=1}^{N} \frac{A_i \omega \Gamma_i}{(\omega^2 - \omega_i^2)^2 + \omega^2 \Gamma_i^2}. \tag{4.2}$$

The crystal structure of magnetite above T_V is an inverse cubic spinel with space group $Fd\bar{3}m$. According to factor-group analysis, the space group $Fd\bar{3}m$ is decomposed into irreducible representations, which are further grouped into $(T_{1g} + 2A_{2u} + 2E_u + 2T_{2u})$ inactive modes, $(A_{1g} + E_g + 3T_{2g})$ Raman-active modes and $(5T_{1u})$ infrared-active modes. Raman- and infrared-active modes are mutually exclusive for the presence of inversion symmetry.

Verble first analyzed the eigenvectors of the five Raman-active modes of the cubic phase with reference to Waldron's molecular model [113, 114]. Based on symmetry considerations, only tetrahedral Fe^{3+} ions and O^{2-} ions participate to Raman-active modes. In particular, according to Verble's description, summarized in Fig. 4.4, they comprise symmetric stretching of O^{2-} ions along Fe^{3+}–O^{2-} bonds (A_{1g} mode), symmetric and asymmetric O–Fe–O bending (E_g and T_{2g}^2 modes, respectively), asymmetric stretching of Fe^{3+} and O^{2-} ions (T_{2g}^3 mode) and rigid displacements in opposite directions of the two $Fe^{3+}O_4^{2-}$ tetrahedra in the primitive cell (T_{2g}^1 mode, the numbering of the T_{2g} modes, different from Verble's, is the same as Ref. [115]). The validity of Waldron's molecular model depends on the relative importance of the interactions within and among B-type Fe tetrahedra and $Fe^{3+}O_4^{2-}$ tetrahedra. Combined theoretical and experimental studies of the phonon density of states suggest comparable contributions to the overall structural dynamics from both tetrahedral and octahedral Fe ions below 320 cm^{-1} [3, 116]. On the other hand, first-principle computations of the eigenvectors of the Raman-active modes under considerations are in qualitative accordance with Verble's description [117].

As displayed in Fig. 4.3(a), in our spectral responses at room temperature, four out of the five Raman-active modes predicted by group theory are observable. The same figure summarizes our mode assignment, which relies on polarized Raman studies by Shebanova and Lazor, with particular reference to the controversial attribution of the 307 cm^{-1} peak to the E_g or T_{2g}^3 mode [115]. Let us note that Shebanova and Lazor's assignment is also supported by *ab initio* calculations of the phonon dispersion curves in the cubic phase in quantitative agreement with the experimental data [26, 117]. The additional peaks at 291 and 412 cm^{-1} were identified with the $E_g^2 + E_g^3$ and E_g^4 hematite modes, respectively [118]. Our fit analysis allowed us to discriminate the E_g modes of hematite and magnetite which are close in energy and give rise to a broad asymmetric band from 280 to 340 cm^{-1} (see Figs. 4.8(a,b), in Subsection 4.2.2). The presence of hematite impurities is not surprising in consideration of the natural origin of our sample.

In the structural transition of magnetite, complex atomic displacements, with small amplitudes, down to 0.01 Å, give rise to a change in crystal symmetry, which is reflected into modifications of a number of physical properties [6, 27, 28, 119]. A monoclinic cell four times larger than the cubic cell accounts for the complete set of structural distortions that take place on decreasing the temperature from above to below T_V. As a direct consequence, the number of normal modes of vibration also quadruplicates, from 42 to 168. Therefore, as illustrated in Fig. 4.3(b), the phase transition is accompanied by the emergence of a rich spectrum of new phonon modes. For a complete assignment of the Raman-active modes in the monoclinic phase, first-principle computations able to reproduce mode frequencies and Raman cross sections with quantitative accuracy are needful. For our purposes, we restrict ourselves to simpler considerations. The highest-frequency mode is the monoclinic counterpart of the A_{1g} mode in the cubic phase, now labeled A_g. The linewidths of the T_{2g} modes increase, instead of decreasing for anharmonic effects, on lowering the temperature in the pretransition region (see Figs. 4.6(d,f), in Subsection 4.2.2). This is here interpreted as the result of mode splitting

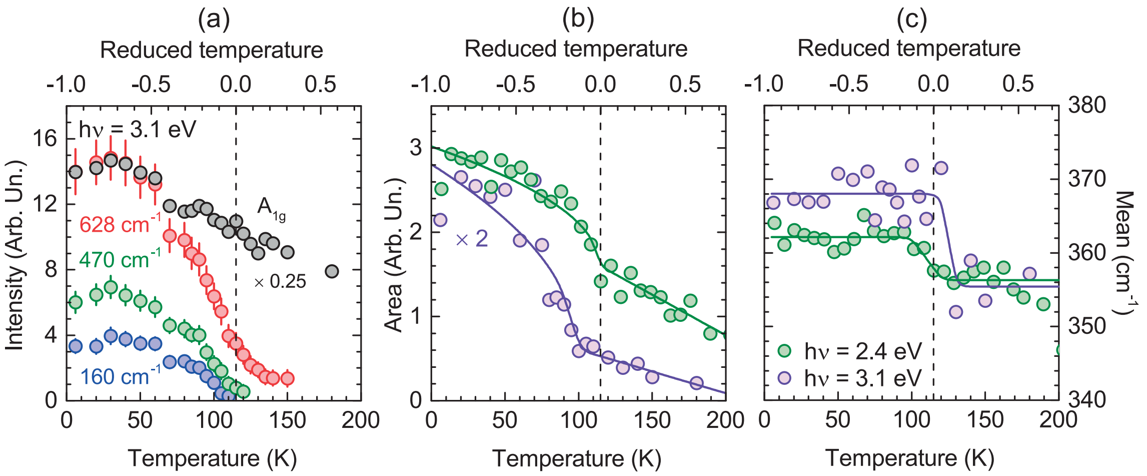

Figure 4.5 – (a) Temperature dependence of the intensity of the critical modes for 3.1 eV excitation. Reference data for the A_{1g} mode are also plotted. Temperature dependence of the (b) area and (c) center of gravity of the background distribution in the 240–500 cm^{-1} Raman shift range. Violet (Green) symbols refer to 3.1 eV (2.4 eV) excitation. Lines are guides to the eye. Vertical dashed lines denote the Verwey temperature.

into submodes close in energy. Its occurrence tens of Ks above T_V, rather than at T_V, is among the precursor effects discussed at the end of Subsection 4.2.2. No further consideration is here possible on the relation between the shoulder mode around 628 cm^{-1} and the A_{1g} mode, as well as between the two new modes in the 300–400 cm^{-1} frequency range and the E_g mode, which thus remain unassigned.

Two sharp peaks unrelated to any Raman-active mode of the cubic phase appear around 160 and 470 cm^{-1}, consistent with previous observations on magnetite thin films [120]. In our pump-probe studies, discussed in Chapter 3, based on the comparison between experimental data and theoretical computations of the phonon dispersion curves and the optical functions, we attributed the onset of the 160 cm^{-1} peak to the folding to the center of the Brillouin zone of a phonon mode of Δ_2 symmetry at $\boldsymbol{q}_\Delta = (0,0,0.5)$ reciprocal lattice units (r.l.u., 1 r.l.u. = $2\pi/a$, with a the lattice parameter in the cubic phase). With the use of the same method, we assigned an additional mode at 125 cm^{-1} to the monoclinic counterpart of a phonon mode of X_3 symmetry at the boundary of the Brillouin zone in the [001] direction. The latter mode is visible as a broad weak peak in our data at 5 K and 2.4 eV excitation (see Fig. 4.1(a)), and not discussed any further.

In early Raman experiments, the 470 cm^{-1} band was observed at 130 and 300 K, and proposed to originate from an optical magnon [121–123]. Indeed, the band position is compatible with energy estimates for the lowest-energy optical magnon of the cubic phase from INS [124]. However, in more recent experiments, the 470 cm^{-1} band was not observed at high temperatures [46, 115, 120, 125–127]. In particular, in our measurements the temperature dependence of the band intensity is consistent with that of a phonon mode of the monoclinic

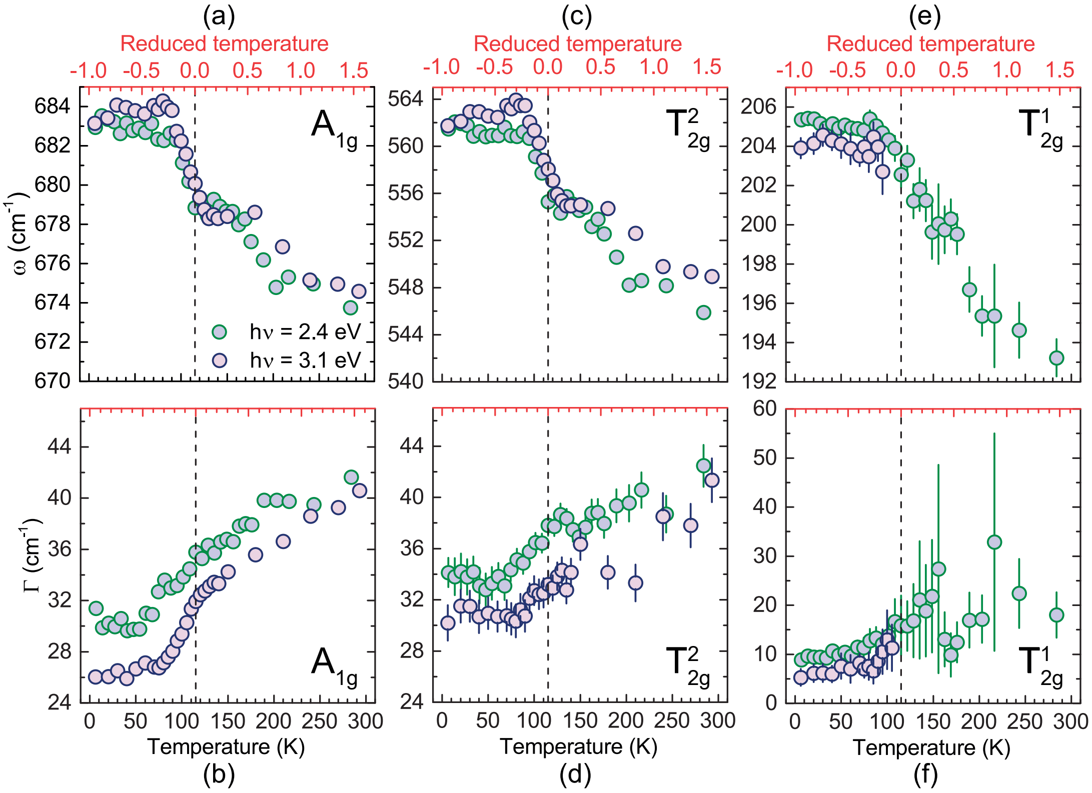

Figure 4.6 – Temperature dependence of the frequency and linewidth of the (a,b) A_{1g}, (c,d) T_{2g}^2 and (e,f) T_{2g}^1 modes of the cubic phase, visible in the form of single peaks both above and below T_V. Violet (Green) symbols refer to 3.1 eV (2.4 eV) excitation. A vertical dashed line denotes the Verwey temperature. The lower horizontal axis is the nominal temperature for 3.1 eV excitation and our approximate estimate of the effective temperature at the laser spot for 2.4 eV excitation.

phase. The intensity decreases rapidly across the Verwey transition, but residual intensity persists in the cubic phase, for the precursor effects discussed in the next Subsection (see Fig. 4.5(a)). Conversely, if an optical magnon of the cubic phase was the cause for the band under consideration, the intensity would decrease on heating, but no complete band suppression would take place far above T_V. The observation of the 470 cm^{-1} band at 300 K in Refs. [121,123] is hardly explainable by invoking precursor effects. An alternative suggestion is that the peak observed at room temperature is in fact a different phonon mode of the cubic phase, namely, the T_{2g}^3 mode predicted in the same energy range based on theoretical computations [26,115, 117]. Sample-dependent effects may play a role in its intensity enhancement [121–123].

4.2.2 Structural Anomalies

Figures 4.6 and 4.7 illustrate the temperature dependence of the frequencies and linewidths of the phonon modes across the Verwey transition. In our experiments, small temperature steps

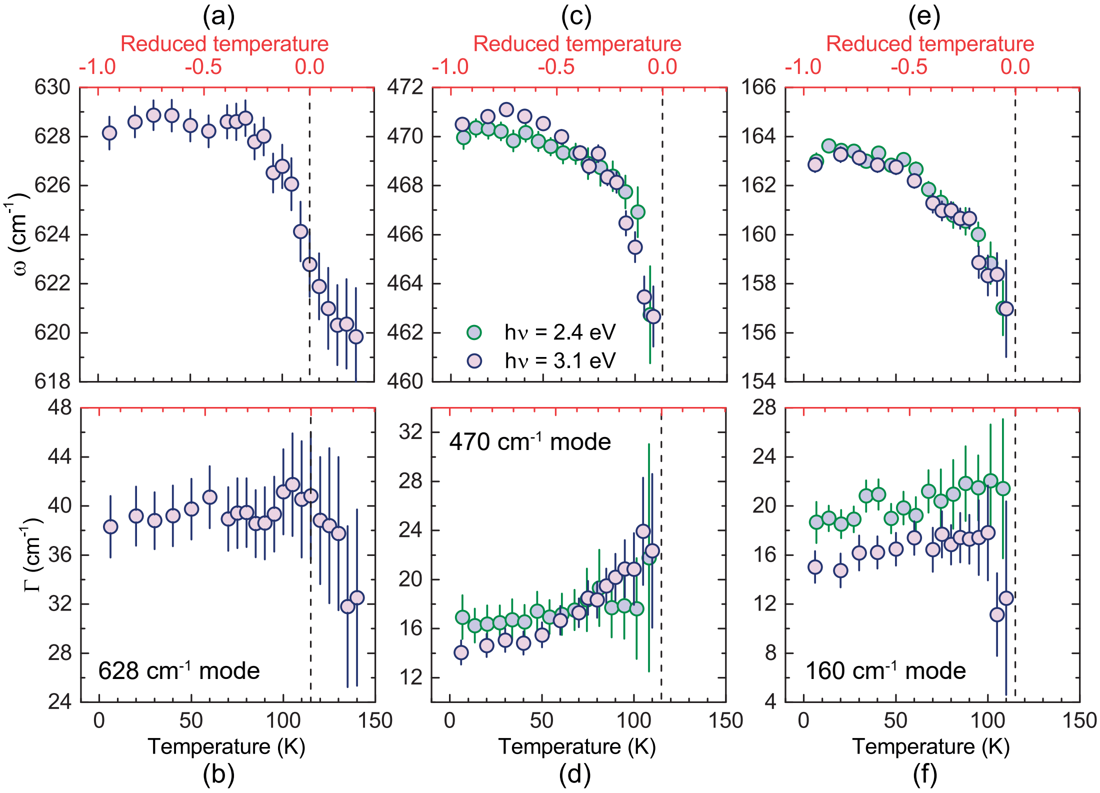

Figure 4.7 – Temperature dependence of the frequency and linewidth of Raman-active modes of the monoclinic phase. Violet (Green) symbols refer to 3.1 eV (2.4 eV) excitation. The shoulder mode of the A_{1g} mode in panels (a) and (b) is clearly observable only for 3.1 eV excitation. A vertical dashed line denotes the Verwey temperature. The lower horizontal axis is the nominal temperature for 3.1 eV excitation and our approximate estimate of the effective temperature at the laser spot for 2.4 eV excitation.

down to 5 K were used, in order to best resolve the possible occurrence of structural anomalies by means of a quantitative analysis. The single peaks associated with the phonon modes were fit with Lorentzian functions according to Eq. 4.2, after subtraction of a linear baseline in the Raman shift range around the peak. The fit analysis of the features in between 240 and 440 cm^{-1} required a different method, briefly described in Subsection 4.2.3. Modifications in mode parameters are rapid for all modes. Large frequency decrease and linewidth increase by respectively 5–10 and 3–6 cm^{-1} take place in correspondence of the Verwey transition. Inhomogeneous laser heating broadens the critical region and thus causes a rounding of the temperature dependence of the mode parameters on the lower temperature side. Instead, the steep decrease of the mode frequency between T_V and $T_V + 14$ K is an intrinsic effect, consistent with the measurements of the lattice dynamics from the INS experiments discussed in Chapter 5. The onset of linewidth broadening, about 40 K below T_V, precedes the decrease of the mode frequencies, starting from 95 K.

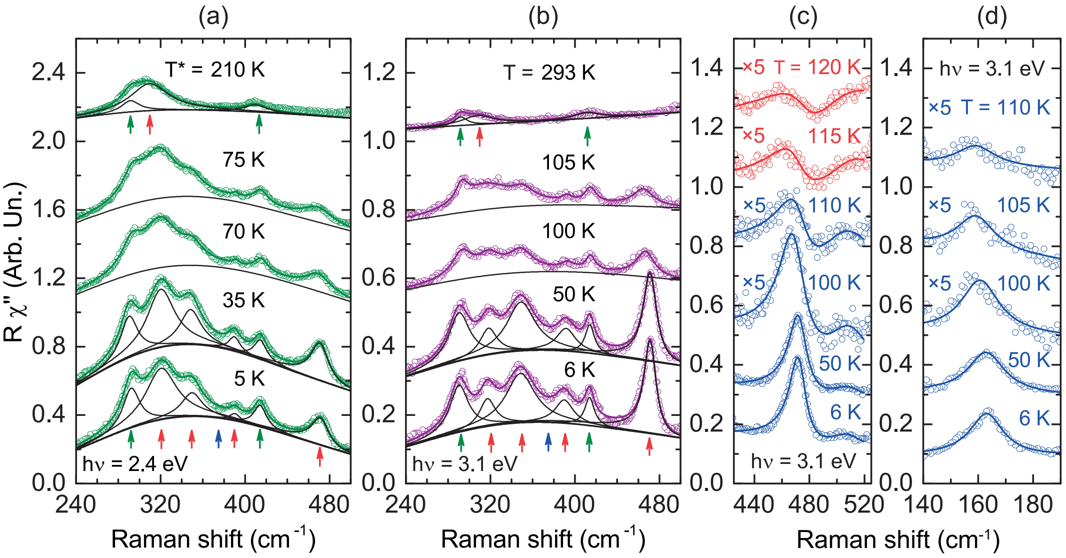

Figure 4.8 – Temperature dependence of phonon modes and background intensity in the 240–500 cm^{-1} Raman shift range for (a) 2.4 and (b) 3.1 eV excitation. Red (Green) arrows indicate magnetite (hematite) phonon modes. A blue arrow denotes the central energy of the higher-energy acoustic magnon at the Δ point at 115 K < T_V from INS [128]. Data are offset for clarity. Temperature dependence of the monoclinic modes at (c) 470 and (d) 160 cm^{-1} for 3.1 eV excitation. Red (Blue) color refers to the cubic (monoclinic) phase. For better comparison, data are normalized to the background intensity integrated between 800 and 810 cm^{-1}. For clarity, data are offset and multiplied by a factor 5 close to the Verwey temperature. Data and fitting functions are plotted with colored symbols and lines, respectively. Black lines represent separate fit components.

Our data provide unequivocal evidence of the concurrent lattice dynamical and electronic character of the Verwey transition. According to the most recent theoretical and experimental estimates, charge differences between Fe ions in the insulating state are on the order of one tenth of an elementary charge [27, 28, 36]. This explains why the occurrence itself of charge order has long remained controversial [14, 15]. However, the occupations of different 3d orbitals at B-type Fe ions constitute an unambiguous basis to define OPs. Orbital, rather than charge, order was suggested to play the most important role in the modifications of the electronic structure from the conducting to the insulating state [26]. The important renormalization of the mode frequencies here observed despite the small amplitude of the atomic displacements is a direct consequence of the onset of orbital polarization below the transition temperature. Moreover, the comparable values of the frequency changes support a cooperative picture of the Verwey transition. According to this scenario, no significant hierarchy is established among the phonon modes, since they all participate in the transformation process, although with measurable differences in their contributions, in particular, in terms of coupling with different types of modes.

In this regard, the temperature dependences of both the 160 and 470 cm^{-1} modes resemble phonon softening, yet, only partial (see Figs. 4.7(c,e)). This is different from the general behavior of the phonon modes, including the 628 cm^{-1} mode and those close to the E_g mode, which are also intrinsic to the monoclinic phase alone. None of them exhibits any important change in frequency over the temperature range below 95 K (see the upper panels of Fig. 4.6 and Fig. 4.7(a)). Figures 4.8(c,d) show the temperature dependence of the lineshapes of the 160 and 470 cm^{-1} modes to the highest temperatures at which they are visible. The distribution of scattering intensity from the two modes and the temperature range over which they contribute to Raman scattering are anomalous. In both cases, starting from the lowest temperature, the best fit quality is obtained with Fano, rather than Lorentzian, functions. Unlike Lorentzian peak shapes, the two modes are asymmetric and, in particular, the spectral weight is larger on the low-frequency side. Close to the transition temperature, a dip develops on the high-frequency side, in further agreement with a Fano lineshape. To gain reliable information on the temperature dependence of the lineshape anomaly, the two peaks are also fit with bi-Gaussian functions. Fano functions correctly reproduce the peaks within the local frequency range, however, the accuracy of the fit parameters depends on the quality of the background subtraction over a broad frequency range. To quantify the degree of asymmetry, an asymmetry parameter is defined, $\beta \equiv (\Gamma_1 - \Gamma_2)(\Gamma_1 + \Gamma_2)^{-1}$, where Γ_1 and Γ_2 are respectively the left and right half widths at half maximum from the fit with bi-Gaussian functions. The asymmetry parameter of the 470 cm^{-1} mode does not present any meaningful dependence on temperature throughout the monoclinic phase. Instead, it suddenly diverges in correspondence of the critical region. The degree of asymmetry does not change for different excitations. In particular, $\beta = 0.27 \pm 0.03$ and $\beta = 0.29 \pm 0.06$, respectively, for 3.1 and 2.4 eV excitation. The degree of asymmetry of the 160 cm^{-1} mode is lower than that of the 470 cm^{-1} mode and does not depend on excitation energy either, namely, $\beta = 0.16 \pm 0.15$ and $\beta = 0.18 \pm 0.11$, respectively, for 3.1 and 2.4 eV excitation.

The phonon modes of the monoclinic phase which are not associated with any Raman-active mode in the cubic phase are supposed to disappear altogether upon an abrupt decrease in intensity in the critical region. The intensity of the 470 cm^{-1} mode does decrease suddenly around T_V, however, a broad weak feature is observable up to 120–125 K nominal temperature, which corresponds to an effective temperature more than 5–10 K above the transition temperature (see Fig. 4.8(c)). Analogous considerations hold true for the shoulder mode of the A_{1g} mode (see Figs. 4.1(b) and 4.5(a)). A reliable fit analysis of the A_{1g} and T_{2g}^2 modes requires an additional peak in the 600–650 cm^{-1} Raman shift range up to 150 K nominal temperature. However, the superposition of the spectral weight associated with the A_{1g} peak does not allow us to study possible anomalies in lineshape.

Our pump-probe studies, discussed in Chapter 3, reveal that the 125 and 160 cm^{-1} modes persist up to $T_V + 24$ K. Artifacts from ineffective rejection of the Rayleigh light in the low-frequency range prevent any conclusion on whether or not the 160 cm^{-1} mode is visible also in our steady-state experiments for the same 3.1 eV photon energy of light excitation. Here, we refer to the same interpretation as in our pump-probe studies. The anticipated onset of

Raman scattering from phonon modes of finite wave vectors in the cubic phase is associated with manifestations of precursor order with large correlation length and time close to T_V. We suggest that electronic modes comprised of fluctuations of the charge density couple to the phonon modes and light is scattered by both types of excitations. Equivalently, a second-order Raman process takes place, in which an electronic mode of wave vector $\boldsymbol{q}$ is excited together with a phonon mode of wave vector $-\boldsymbol{q}$, so that the total wave vector is conserved. The cross section for the above Raman mechanism is meaningful only for large amplitude and high enough degree of correlation of the critical fluctuations, near the Verwey temperature. The diffusive character of the electronic modes explains why they do not contribute any energy. The Fano lineshapes observed for the critical modes is a further confirmation of the fluctuation-assisted process being discussed. Indeed, Fano-like peaks point to interference effects between scattering of light by phonon modes and a continuous spectrum of electronic excitations and, therefore, to strong electron-phonon coupling for the lattice vibrations under consideration.

4.2.3 Magnetic or Electronic Excitations

As illustrated in Fig. 4.1, intensity builds up in the monoclinic phase in the form of a broad background in the Raman shift range from 240 to 500 cm^{-1}. Gasparov et al. suggested a possible electronic or magnetic origin of this feature, rather than the simple onset of a rich structure of new phonon modes [126]. In our fit analysis in Figs. 4.8(a,b), baseline estimation via an asymmetric least square method singles out the phonon modes from the background. It is thereby possible to study the temperature dependence of the background. The integrated intensity of the background decreases rapidly with increasing temperature across the Verwey transition (see Fig. 4.5(b)). The center of gravity of the baseline does not change noticeably throughout the monoclinic phase, and is about 362±2 and 368±3 cm^{-1}, respectively for 2.4 and 3.1 eV excitation (see Fig. 4.5(c)).

INS measurements of the spin-wave dispersion of magnetite below T_V revealed the formation of a large gap in the acoustic branch at $\boldsymbol{q}_\Delta$. The modifications of the spin-wave and phonon dispersions of magnetite upon the Verwey transition are qualitatively analogous. Indeed, the sizes of the magnetic moments and the exchange constants depend significantly on the charge distribution and the bond lengths and angles, all of which change discontinuously upon the ordering process of the Verwey transition [128]. On decreasing temperature across T_V, the volume of the primitive cell quadruplicates, both for the magnetic and electronic structures. In reciprocal space, $\boldsymbol{q}_\Delta$ becomes the center of the Brillouin zone. In correspondence of both edges of the gap, the spin-wave dispersions become flat and thus give rise to a high magnon density of states, along with potential contribution to the optical and Raman responses [128].

The center of gravity of the background distribution is close to the 375 cm^{-1} frequency estimate of the higher-energy magnon at the gap from the same INS experiments at 115 K $< T_V$ (see blue arrows in Figs. 4.8(a,b)) [128]. However, it is arguable whether or not a one-magnon excitation is responsible for the broad peak observable in our Raman spectra. According to the microscopic theory by Fleury and Loudon, the same mechanism is responsible for first-order scattering in all types of magnetic materials, namely, indirect electric-dipole coupling, mediated by spin-orbit interaction [129, 130]. The selection rule on the $\boldsymbol{\epsilon}_1$ and $\boldsymbol{\epsilon}_2$ polarizations of respectively incoming and outgoing light is $\left|\boldsymbol{\epsilon}_1^z\boldsymbol{\epsilon}_2^+ - \boldsymbol{\epsilon}_1^+\boldsymbol{\epsilon}_2^z\right| \neq 0$, where $\boldsymbol{\epsilon}^+ = \boldsymbol{\epsilon}^x + i\boldsymbol{\epsilon}^y$ and z is the direction of spin order. Therefore, in polarized Raman studies, Raman scattering from one-magnon excitations is supposed to disappear if $\boldsymbol{\epsilon}_1$ and $\boldsymbol{\epsilon}_2$ are parallel. This is not the case for the broad peak being considered, which is also observable in XX geometry [46, 126]. Its large linewidth further questions its possible origin from a one-magnon excitation. In fact, first-order scattering is restricted to the center of the Brillouin zone and thus supposed to give rise to narrow peaks.

An alternative suggestion is the occurrence of second-order scattering from magnon excitations of opposite wave vectors close to the boundaries of the Brillouin zone in the monoclinic phase at $(0, 0, \pm 0.25)$ r.l.u.. Energy conservation is fulfilled because they are at about half the energy of the magnon excitations at $\boldsymbol{q}_\Delta$ [128]. In contrast to first-order processes, second-order processes take place via different mechanisms depending on the type of magnetic material [129, 130]. The so-called exchange scattering mechanism is characterized by the absence of intrinsic selection rules on $\boldsymbol{\epsilon}_1$ and $\boldsymbol{\epsilon}_2$, *i.e.*, both symmetric and antisymmetric components of the Raman tensor. Moreover, typical cross sections are comparable or larger than those for one-magnon scattering, and the multiple combinations of magnon excitations possible around the critical points of the Brillouin zone produce broad peaks, similar to our observations. However, available data from INS experiments do not show any noticeable gap at $(0, 0, \pm 0.25)$ r.l.u. [128]. A small gap may still be present. To determine whether or not Van Hove singularities develop at $(0, 0, \pm 0.25)$ r.l.u., data with better energy and momentum resolution are needful.

An electronic origin of the feature being discussed is also possible. The onset of charge and orbital order, and the different electronic structure in the monoclinic phase, compared to the cubic phase, may indeed produce rearrangements of the spectral weight in the Raman response. However, before any further speculation, additional Raman experiments are needful, to rule out magnon excitations altogether, for instance, high magnetic field and polarization dependences on an oriented single crystal in the monoclinic phase.

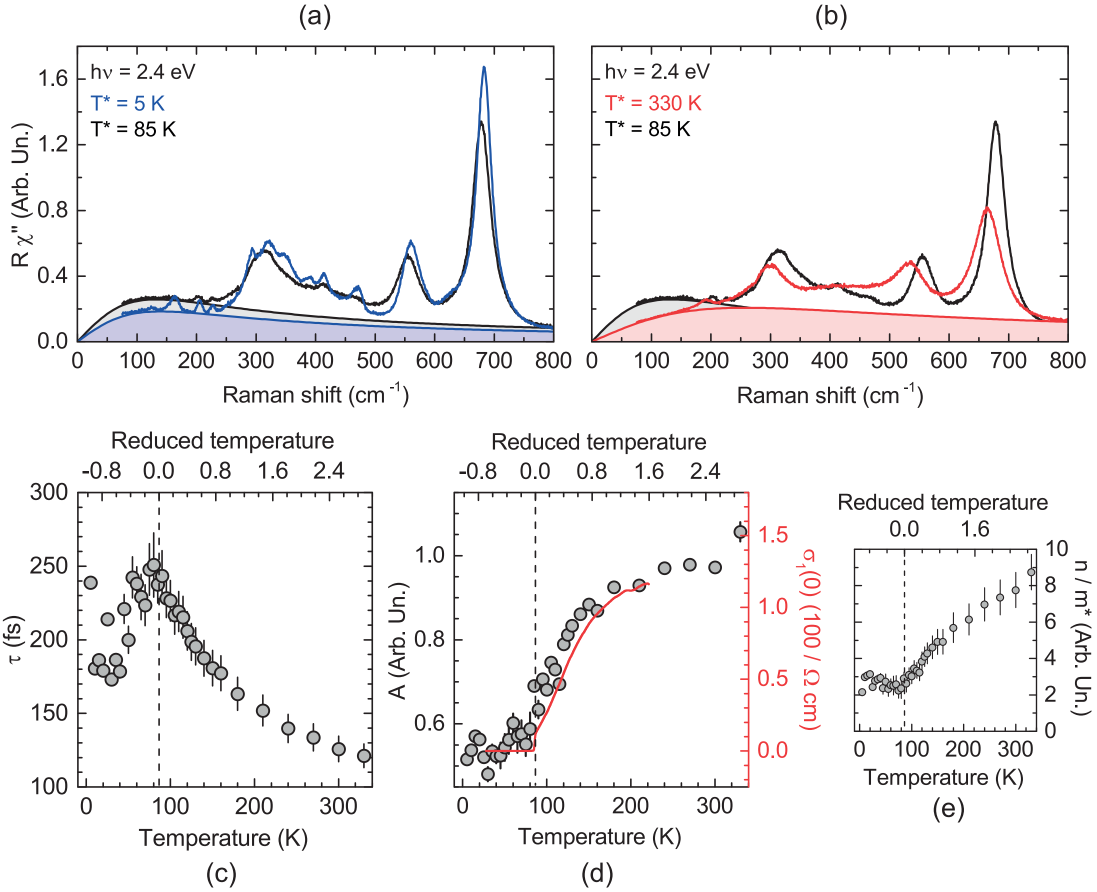

Figure 4.9 – Comparison between the spectral response, $R\chi''(\omega)$, (black) at the transition temperature and in the (a, blue) monoclinic and (b, red) cubic phase. The fitting functions to the background intensity defined in Eq. 4.3 are plotted together with the data, with the same color coding. Shaded areas highlight the diffusive contribution to the spectral response. (c–e, black symbols) Temperature dependence of the fit parameters. The reduced temperature dependence of the dc conductivity of our sample is also plotted with a red line in panel (d). The lower horizontal axis of panels (c–e) is the nominal temperature. Vertical dashed lines denote T_V^*. To account for effects of laser heating, fits are repeated for $R\chi''(\omega)$ computed from $S(\omega)$, respectively, with reference to our estimate of the effective temperature, T, and the nominal temperature, T^*. Error bars correspond the differences between the fit parameters in the above two cases. Data points are average values.

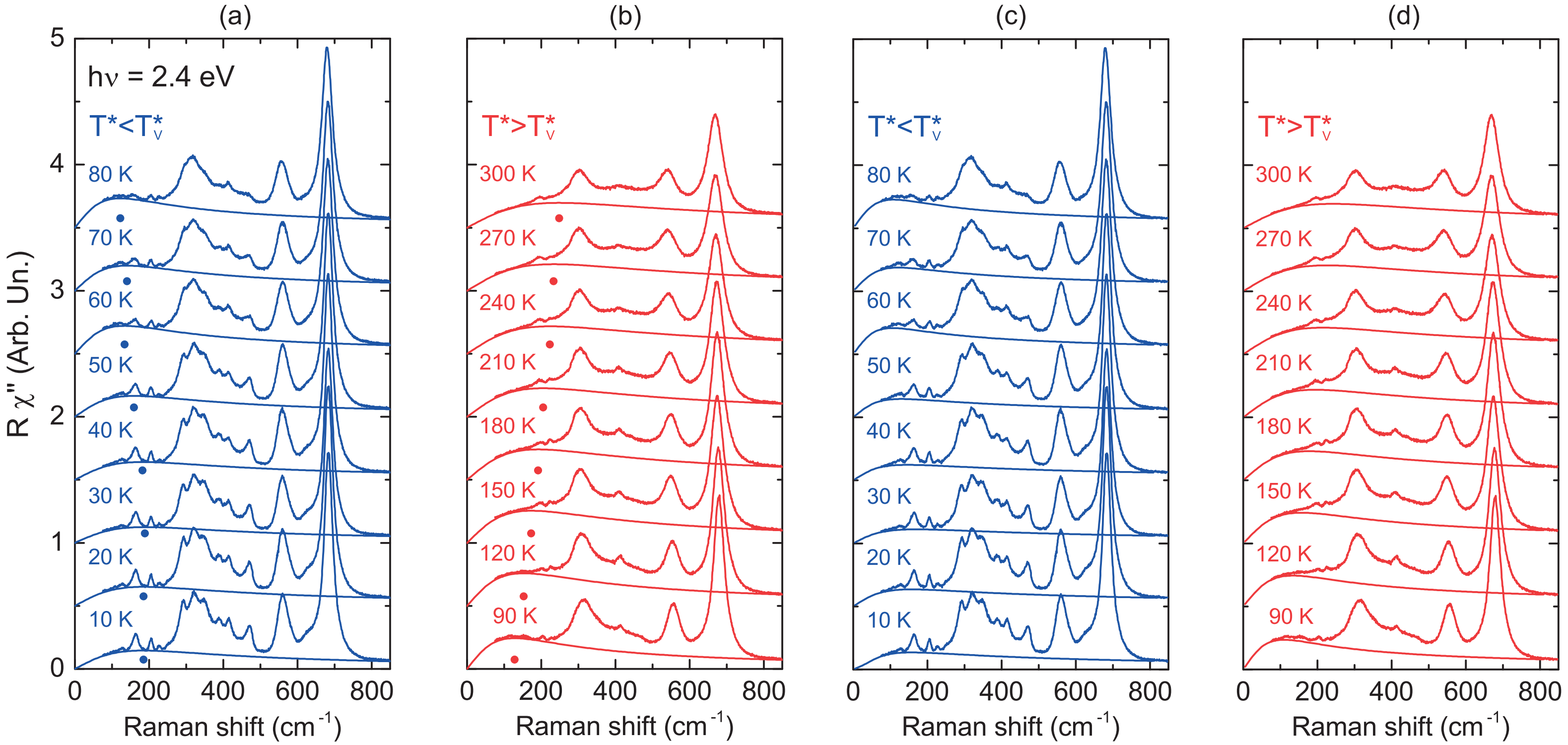

Figure 4.10 – Temperature dependence of the spectral response and the fitting function to the background intensity (a and c, blue) below and (b and d, red) above T_V, for 2.4 eV excitation. Left (a and b) and right panels (c and d) refer to our fit analysis with a Drude peak (see Eq. 4.3) and the contribution of fluctuation modes to Raman scattering (see Eq. 4.5), respectively. Circles in panels (a) and (b) denote estimates of the mean transport relaxation rate, equivalent to the frequency of the maximum background intensity.

4.2.4 Diffusive Excitations

In our discussion of the diffusive response, we take into account data at 2.4 eV excitation, which in contrast to data at 3.1 eV excitation are available on a spectral range suitable for an analysis down to low frequency. Interestingly, an anomaly in the background intensity occurs at low frequency in the critical region. First, in the monoclinic phase, the background intensity increases on heating. Then, in the cubic phase, an atypical transfer of spectral weight to higher frequency takes place on further increasing the temperature. Accordingly, in Figs. 4.9(a,b), the background intensity at low frequency is below that of reference data at T_V both in the monoclinic and cubic phase.

The following function represents the simplest model to fit the background intensity in our data, with particular reference to the low-frequency range.

$$R\chi''_{\mathrm{el}}(\omega) = \frac{A\omega}{1+(\omega\tau)^2}, \tag{4.3}$$

where A is a phenomenological amplitude and τ is a phenomenological time constant. Our fit analysis is exemplified in Figs. 4.9(a,b). Data sets and fitting functions at different temperatures throughout both the cubic and monoclinic phase are shown in Figs. 4.10(a,b). The fitting parameters A and τ are plotted as a function of temperature in Figs. 4.9(c,d). It has been shown that, to a first approximation, the simple relation $R\chi''_{\mathrm{el}}(\omega) \propto \omega\sigma_1(\omega)$ holds true between the electronic contribution to the spectral response, $\chi''_{\mathrm{el}}(\omega)$, and the real part of the optical conductivity, $\sigma_1(\omega)$, at low enough frequency [131]. Therefore, it is possible that our data contain the Drude peak which originates from the diffusive dynamics of the charge carriers. If this is the case, the phenomenological amplitude A is supposed to account for the contribution to $\sigma_1(0)$ from the transport mechanism under consideration, $A \propto \sigma_1(0) = ne^2\tau m^{*-1}$, where n and m^* are respectively the density and effective mass of the charge carriers. Indeed, as shown in Fig. 4.9(d), the temperature dependences of A and $\sigma_1(0)$ are qualitatively similar in the cubic phase. Our estimate of the ratio between density and effective mass of the charge carriers, $n/m^* \propto A/\tau$, shown in Fig. 4.9(e), increases continuously on heating, which is suggestive of thermally activated processes. Our data do not allow us any further consideration on the nature of the transport mechanism being discussed. Ihle and Lorenz proposed a microscopic theory for SP conduction in magnetite, according to which diagonal transitions give rise to a Drude peak in $\sigma_1(\omega)$, which dominates $\sigma_1(0)$ below 400 K [48]. However, as discussed in Section 1.3, their considerations are questioned by the erroneous assignment of the polaron peak. Let us also point out that the occurrence of band conduction is in contrast to the scenario of an order-disorder transformation argued in Chapters 3 and 5.

The presence of a Drude peak alone is inconsistent with the complete temperature dependence of the diffusive response. In fact, if this was the only component, the background intensity at low energy would disappear discontinuously below T_V, in concomitance with the onset of the insulating state, with negligible optical conductivity below the band gap.

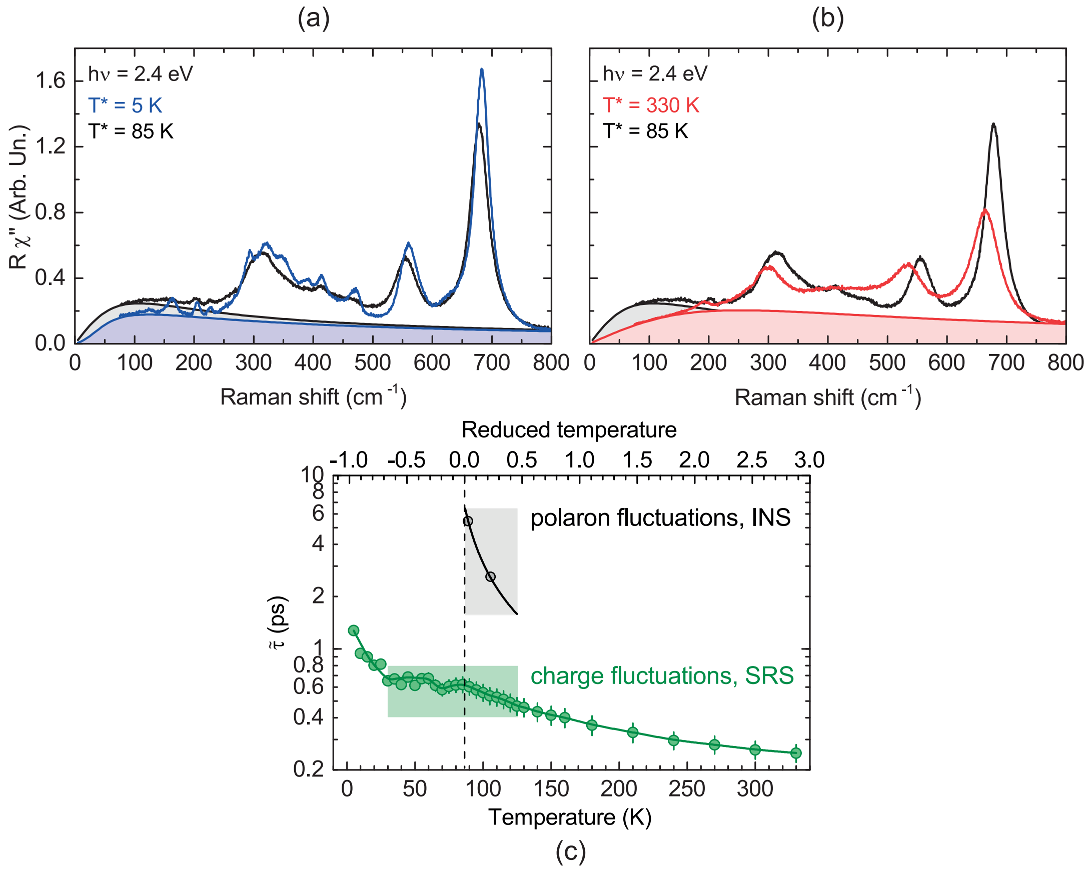

Figure 4.11 – Comparison between the spectral response, $R\chi''(\omega)$, (black) at the transition temperature and in the (a, blue) monoclinic and (b, red) cubic phase. The fitting functions to the background intensity defined in Eq. 4.5 are plotted together with the data, with the same color coding. Shaded areas highlight the electronic contribution to the spectral response. (c) Our data from spontaneous Raman scattering (SRS, green symbols and shaded area) are compared with data from INS (black symbols and shaded area) [66]. The black line is the theoretical prediction for the correlation time of polaron fluctuations of Δ_5 symmetry at $(0,0,0.75)$ r.l.u. based on experimental estimates of the microscopic parameters of Yamada's model [55]. The lower horizontal axis of panel (c) is the nominal temperature. A vertical dashed line denotes T_V^*. As in Figs. 4.9(c–e), data points and error bars account for the uncertainty from effects of laser heating.

Furthermore, the above interpretation alone cannot explain the temperature dependence of the mean transport relaxation time, τ, plotted in Fig. 4.9(c) either. Indeed, it can be argued that, due to critical slowing down, τ increases close to the transition temperature. However, the scattering of the charge carriers by fluctuations of the OP is by no mean the only relaxation channel. Phonons, magnons and different types of fluctuations are also at play. According to Matthiessen's rule, in the presence of competing processes, τ is in any case dominated by the shortest relaxation time. Any possible increase of the time constant in one of the relaxation channels is cut off by the higher scattering rate from different mechanisms.

We believe that an important contribution to the observed anomaly in the background intensity also comes from the critical modes of the Verwey transition. In particular, in the following, we argue that diffusive collective excitations of charge fluctuations provide a scattering channel for the electronic spectral response, in addition to the processes of single-particle excitations. A similar explanation was advanced for Raman scattering in cuprates [132].

A generic fluctuation mode of wave vector $\boldsymbol{q}$, $\delta\rho_{\boldsymbol{q}}(t)$, is defined as the instantaneous deviation of the FT of an ordering field mode, $\rho_{\boldsymbol{q}}(t)$, from its equilibrium value, $\langle\rho_{\boldsymbol{q}}\rangle$, also termed OP, *i.e.* $\delta\rho_{\boldsymbol{q}}(t) = \rho_{\boldsymbol{q}}(t) - \langle\rho_{\boldsymbol{q}}\rangle$. Above the ordering temperature, which in our case is T_V, $\langle\rho_{\boldsymbol{q}}\rangle = 0$ by definition, and $\delta\rho_{\boldsymbol{q}}(t)$ and $\rho_{\boldsymbol{q}}(t)$ are equivalent. Instead, below the ordering temperature, $\langle\rho_{\boldsymbol{q}}\rangle \neq 0$ at the critical wave vectors, which we generically indicate as $\{\boldsymbol{q}_c\}$.

The ordering field modes here accounted for are represented by electron density modulations. The fluctuation modes are here treated as classical variables with relaxational responses, consistent with our observation of a diffusive response, along with the general interpretation of the Verwey transition in terms of an order-disorder transformation (see Chapters 3 and 5). We suppose that quantum tunneling of charges does not occur, since charges are self-trapped, due to polaronic effects. Still, the treatment is not purely classical, because we do not assume that the thermal energy is much higher than the energy scale of the ordering field modes.

To compute the diffusive response, we start from the Ginzburg-Landau expansion of the free energy density in reciprocal space, given by Eq. 4.4. In principle, this formalism is suitable only for second-order transitions. Nevertheless, we apply it to the Verwey transition, with the following caveats. First, the ordering temperature, T_V, must be replaced by the theoretical limit of metastability for the disordered phase, $T_c < T_V$. Second, the critical wave vectors for the discontinuous transition, $\{\boldsymbol{q}_c\}$, commensurate, must be replaced by the critical wave vectors for the continuous precursor effects, $\{\boldsymbol{q}_c^*\}$, incommensurate, where diffuse scattering is the most intense far enough from T_V [65–69]. The sums over $\boldsymbol{q}$ in Eq. 4.4 are restricted to neighborhoods of $\{\boldsymbol{q}_c^*\}$.

$$\mathscr{F}\left(\{\rho_{\boldsymbol{q}}(t)\}\right) = \sum_{\boldsymbol{q}_c^*}\sum_{\boldsymbol{q}} \frac{1}{2}\left[a(T-T_c) + b\left|\boldsymbol{q}-\boldsymbol{q}_c^*\right|^2\right]\rho_{\boldsymbol{q}}(t)\rho_{-\boldsymbol{q}}(t) + \sum_{\boldsymbol{q}_c^*}\sum_{\boldsymbol{q}} f_{\boldsymbol{q}}(t)\rho_{-\boldsymbol{q}}(t) + o\left(\rho^3\right). \quad (4.4)$$

Below T_V, a similar development holds true, to a reasonable approximation, yet around the finite values of $\langle\rho_{\boldsymbol{q}}\rangle$. Terms of higher order implicit in $o\left(\rho^3\right)$ are responsible for the discontinuous transformation at T_V. a and b are temperature-independent coefficients. An external field $f_{\boldsymbol{q}}(t)$ linearly coupled to the ordering field is here introduced for the computation of the diffusive propagator. The details of our calculations are provided in Section 4.4. According to our theoretical model, the contribution of the fluctuation modes to the spectral response is given by Eq. 4.5. We defined $m = \gamma a(T - T_c)$, with γ a phenomenological relaxation rate (see Eq. 4.7). $\omega_M = \gamma b q_M^2$ is the frequency cutoff associated with the upper limit of the summation over the fluctuation modes in reciprocal space, q_M, large enough to contain the fluctuation modes that contribute the most to the spectral response, and of the order of π/a.

$$\begin{aligned} R\chi''(\omega) = -\int_{-\infty}^{+\infty} d\xi \frac{1}{\omega\xi} \left[\frac{1}{e^{(\xi+\omega/2)/k_B T}-1} - \frac{1}{e^{(\xi-\omega/2)/k_B T}-1} \right] \\ \times \left\{ \left(\xi + \frac{\omega}{2}\right) \left[\arctan\left(\frac{m+\omega_M}{\xi-\omega/2}\right) - \arctan\left(\frac{m}{\xi-\omega/2}\right) \right] \right. \\ \left. - \left(\xi - \frac{\omega}{2}\right) \left[\arctan\left(\frac{m+\omega_M}{\xi+\omega/2}\right) - \arctan\left(\frac{m}{\xi+\omega/2}\right) \right] \right\}. \end{aligned} \tag{4.5}$$

To understand the meaning of the parameter m, let us consider a simple analogy to experimental techniques with wave-vector resolution, and selective sensitivity to charge and orbital order, such as resonant inelastic x-ray scattering (RIXS) at suitable absorption edges and reflections. Starting from the transport equation for the free energy density (see Eq. 4.7), it is easy to compute the imaginary part of the dynamical susceptibility at the wave vector $\boldsymbol{q}$, $\chi''\left(\boldsymbol{q},\omega\right)$, defined as the change in the fluctuation mode at the same point in reciprocal space, consequent to an external field,

$$\chi''\left(\boldsymbol{q},\omega\right) = \mathrm{Im}\left[\frac{\rho_{\boldsymbol{q}}(\omega)}{f_{\boldsymbol{q}}(\omega)}\right] = \frac{\gamma\omega}{\omega^2+(\Gamma/2)^2}, \tag{4.6}$$

with $\Gamma/2 = m + \gamma b\left|\boldsymbol{q}-\boldsymbol{q}_c^*\right|^2$. The scattering intensity calculated from the above response function according to the fluctuation-dissipation theorem (see Eq. 4.1) is a central peak, *i.e.* a peak centered at zero energy, of linewidth Γ. This originates from the relaxational dynamics of electronic excitations with correlation time proportional to $1/\Gamma$. Indeed, the scattering intensity is given by the FT of the time autocorrelation of the observable under consideration, in our case, the electronic degree of freedom.

Under our assumption of a Ginzburg-Landau functional, the linewidth increases quadratically around the critical wave vector. Therefore, the parameter m represents the minimum linewidth, proportional to the maximum inverse correlation time, in correspondence of the critical wave vector. Deviations from our theoretical model, for instance, the variable degree of instability at different wave vectors, give rise to complications. In the following, $\tilde{\tau} \propto 1/m$ will be generically referred to as the correlation time of the fluctuation modes.

As exemplified in Figs. 4.11(a,b), the theoretical model defined in Eq. 4.5 is fit to our data. Extended data sets and fitting functions are shown in Figs. 4.10(c,d). A first fit analysis is carried out with independent values of the parameter ω_M. Then, in a second step, the theoretical model is fit again to our data, with parameter ω_M constrained to a same value, equal to the mean from the first step. Our estimate of the correlation time is plotted against temperature in Fig. 4.11(c). Above 150 K nominal temperature, equivalent to 0.76 reduced temperature, the correlation time does not show any large change as a function of temperature, and decreases continuously with -1 fs/K rate. Instead, near the transition temperature, the temperature dependence of the correlation time displays a cusp-like shape. A more noticeable divergence also sets in on approaching the lowest temperature.

Any possible conclusion on the temperature dependence of the correlation time in the cubic phase is questioned by the superposition of the contribution from the processes of single-particle excitations discussed in the foregoing. More reliable considerations are feasible close to, or below T_V, where this is expected to be negligible. An important question is, what is the true nature of the ordering field modes in our observations? Are they indeed electron density modulations or in fact they also involve atomic displacements? To address this issue, let us compare our 0.4–0.8 ps estimate of the correlation time around the critical region, down to the onset for the divergence at the lowest temperature, to analogous estimates from INS.

Diffuse scattering of neutrons and nonresonat x rays was observed above T_V [66–69]. In analogy to our observations, it originates from fluctuation modes. In contrast to Raman scattering, in INS and nonresonant inelastic x-ray scattering (NRIXS), the wave-vector transfer is also resolved, and the direct observables are structural, instead of electronic. Indeed, the expression for the spectral function in both techniques is given by Eq. 2.17. The more intense is diffuse scattering at a given wave vector, the longer is the correlation time of the fluctuation mode at the same point in reciprocal space. Relative maxima in intensity of diffuse scattering are located at critical wave vectors, *i.e.* in correspondence of the fluctuation modes which manifest the highest instability. In the case of magnetite, above T_V, the critical dynamics is governed by intrinsic instabilities in the liquid of SPs, at incommensurate points in reciprocal space, such as $(0,0,0.75)$ r.l.u. (see Chapter 5). The black line and symbols plotted in Fig. 4.11(c) are respectively theoretical predictions and experimental estimates of the correlation time of the fluctuation mode of Δ_5 symmetry at $(0,0,0.75)$ r.l.u. from the linewidths of the central peaks in INS [55, 66].

The above time scale on the order of picoseconds and the absence of phonon softening are both consistent with the scenario of combined electronic and structural fluctuations, with slow dynamics, compared to the phonon modes (see Chapter 5). Instead, interestingly, the 0.4–0.8 ps time scale of the ordering field modes in our observations in the temperature range for reliable estimates (see green shaded area in Fig. 4.11(c)) suggests smaller effective mass, compatible with excitations of mainly electronic character.

4.3 Conclusions

In summary, in our study we disentangled the different contributions to light scattering in magnetite, from structural, magnetic and electronic degrees of freedom. We thereby gained important information on the critical modes of the Verwey transition. We suggested a possible magnetic or electronic origin of light scattering in the 240–500 cm^{-1} range, as a consequence of modifications in the spin-wave dispersions and electronic structure of magnetite upon the Verwey transition. In general, our results are consistent with the concerted contribution of different modes to the essential mechanism of the Verwey transition. Nonetheless, from a quantitative analysis of the structural anomalies, we identified three phonon modes of the monoclinic phase, around 160, 470 and 538 cm^{-1}, which possess atypical lineshape and temperature dependence. We proposed that the distinctive features of all three phonon modes are the result of strong electron-phonon coupling.

Special focus was placed on the electronic contribution to light scattering in magnetite, which also manifests critical characteristics. Indeed, a redistribution of spectral weight takes place in the background intensity around the transition temperature. We proposed that processes from two different types of excitations determine our observations. Namely, Raman scattering from single-particle excitations account for the temperature dependence of the transport properties of magnetite, although here it is not possible to gain any further insight into the conduction mechanism at the origin of our observations. An additional component which prevails in the monoclinic phase was identified with the diffusive dynamics of fluctuation modes.

In INS experiments, critical fluctuations were also observed, in the form of diffuse scattering in reciprocal space, associated with central peaks in the inelastic spectra. The 12–26 cm^{-1} linewidth of the central peak at $(0,0,0.75)$ r.l.u. in the 125–150 K temperature range corresponds to a correlation time on the order of 2.6–5.4 ps, which would further diverge, in the absence of the discontinuous transition at T_V. In contrast, in our observations, the time scale of the diffusive response around the critical region is on the order of 0.4–0.8 ps. The large ratio between the above time constants suggests different characteristics of the critical fluctuations measured in INS and our experiments. They are supposed to originate respectively from excitations with mainly polaronic and electronic character.

Electronic excitations weakly coupled to lattice vibrations are invisible to structure-sensitive probes, such as INS and NRIXS. In contrast, if suitable absorption edges and reflections are chosen, RIXS can serve as a charge-sensitive probe. RIXS experiments are thus needful to provide direct evidence of the electronic excitations discussed in the foregoing, and study the wave-vector and temperature dependence of possible instabilities. In particular, based on our observations, they are supposed to give rise to broad central peaks, compared to INS, with ~10 meV linewidth around the critical wave vectors.

4.4 Raman Scattering from Two Diffusive Modes

In our theoretical model, we describe the return to equilibrium of a generic ordering field mode upon the perturbation of an external field, in a phenomenological manner, by means of the Landau-Khalatnikov equation of motion,

$$\frac{d\rho_{\boldsymbol{q}}}{dt} = -\gamma \frac{d\mathscr{F}}{d\rho_{-\boldsymbol{q}}} = -\left(m + \nu \left|\boldsymbol{q} - \boldsymbol{q}_c^*\right|^2\right) \rho_{\boldsymbol{q}}(t) - \gamma f_{\boldsymbol{q}}(t), \tag{4.7}$$

with $\nu = \gamma b$. Here, γ is a phenomenological transport coefficient, which depends on the physics beyond our theoretical model. To extend our treatment to the quantum regime, where the thermal energy is of the same order as the energy scale of the ordering field modes, we turn to Matsubara formalism, and consider the diffusive propagator associated with Eq. 4.7 (see Ref. [132] for a similar approach in cuprates).

$$D\left(\boldsymbol{q},\omega_m\right)=\frac{\rho_{\boldsymbol{q}}(\omega_m)}{f_{\boldsymbol{q}}(\omega_m)}=\frac{-\gamma}{|\omega_m|+m+\nu\left|\boldsymbol{q}-\boldsymbol{q}_c^*\right|^2}. \tag{4.8}$$

We compute the dynamical susceptibility, $\chi(\omega_n)$, as the FT of the linear response function, $R(\tau)$, given by the Kubo formula, again, in Matsubara representation.

$$\chi\left(\omega_n\right)=\int_0^\beta d\tau\, e^{i\omega_n\tau}\, R(\tau)=\frac{1}{\hbar}\int_0^\beta d\tau\, e^{i\omega_n\tau}\,\langle T_\tau H_R(\tau)H_R(0)\rangle\,, \tag{4.9}$$

with $\beta=1/k_BT$, $\omega_n=2n\pi/\beta$ the bosonic frequencies, H_R the effective Raman operator and T_τ the time ordering operator. In the Raman processes under consideration, to fulfill wave-vector conservation, mode pairs of opposite wave vectors $\boldsymbol{q}$ and $-\boldsymbol{q}$ are excited together. Therefore, the effective Raman operator is assumed to contain two fluctuation modes,

$$H_R(\tau)=\sum_{\boldsymbol{q}} g_{\boldsymbol{q}}\,\delta\rho_{\boldsymbol{q}}(\tau)\delta\rho_{-\boldsymbol{q}}(\tau). \tag{4.10}$$

We replace the above expression in Eq. 4.9. We develop the correlation factor, taking into account that, to the leading order, two fluctuation modes of different wave vectors are independent variables.

$$\begin{aligned}\chi\left(\omega_n\right)&=\frac{1}{4\hbar}\sum_{\boldsymbol{q}\boldsymbol{q}'} g_{\boldsymbol{q}}g_{\boldsymbol{q}'}\int_0^\beta d\tau\, e^{i\omega_n\tau}\,\left\langle T_\tau\delta\rho_{\boldsymbol{q}}(\tau)\delta\rho_{-\boldsymbol{q}}(\tau)\delta\rho_{\boldsymbol{q}'}(0)\delta\rho_{-\boldsymbol{q}'}(0)\right\rangle\\&=\frac{1}{2\hbar}\sum_{\boldsymbol{q}} g_{\boldsymbol{q}}^2\int_0^\beta d\tau\, e^{i\omega_n\tau}\,\left\langle T_\tau\delta\rho_{\boldsymbol{q}}(\tau)\delta\rho_{-\boldsymbol{q}}(0)\right\rangle\left\langle T_\tau\delta\rho_{\boldsymbol{q}}(\tau)\delta\rho_{-\boldsymbol{q}}(0)\right\rangle.\end{aligned} \tag{4.11}$$

We recognize that the above correlation factors are by definition the diffusive propagator in the time domain, *i.e.* the inverse FT of Eq. 4.8 from Matsubara frequency space to the time domain,

$$D\left(\boldsymbol{q},\tau\right)=\frac{1}{\beta}\sum_n e^{-i\omega_n\tau}D\left(\boldsymbol{q},\omega_n\right). \tag{4.12}$$

Analytical calculations of the above integral and summation in the complex plane eventually lead to the model function of Eq. 4.5.

5 Neutron Scattering from Critical Modes

In this Chapter, we present inelastic neutron scattering data across the Verwey transition in magnetite, on a natural single crystal. We apply an effective detwinning method. The coexistence of structural domains with different orientations in the monoclinic phase would otherwise prevent any dynamical probe at finite momentum. We provide direct evidence of the influence of charge and orbital order on the transverse acoustic phonons. In particular, we measure a discontinuous hardening and narrowing of the transverse acoustic phonons at the transition temperature, and an energy splitting for different polarizations. In contrast to the theoretical predictions, the transverse optical mode of X_3 *symmetry at the lowest energy does not show any anomaly.*

Overall, our data point to a transformation process in which intrinsic incommensurate fluctuations of polarons lock to the lattice potential at the critical temperature, in analogy to the crystallization of a two-dimensional liquid on a solid surface. Our results also contribute to clarify the independent dynamics and the mutual interactions of polaron fluctuations and phonon modes in the Verwey transition.

The content of Section 5.2 is adapted from the article "Mapping the lattice dynamical anomaly of the order parameters across the Verwey transition in magnetite" by S. Borroni, G. S. Tucker, F. Pennacchio, J. Rajeswari, U. Stuhr, A. Pisoni, J. Lorenzana, H. M. Rønnow and F. Carbone, New J. Phys. 19, 103013 (2017).

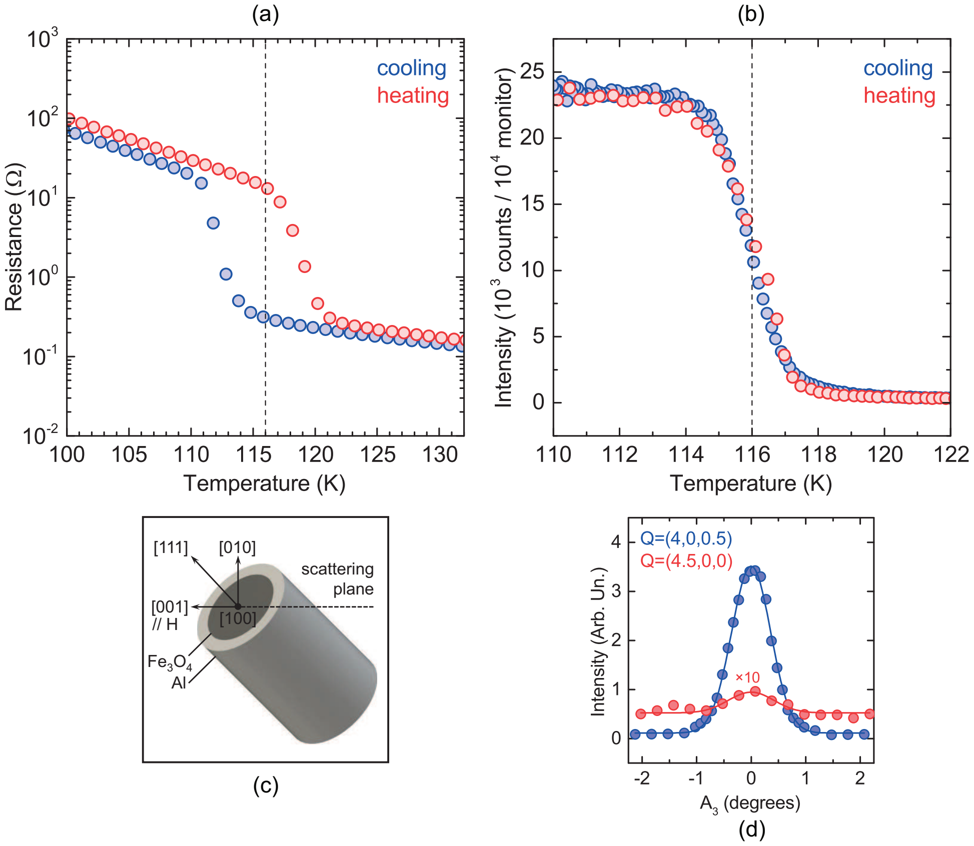

Figure 5.1 – Temperature dependence of (a) the resistance of our sample and (b) the intensity of the $(3.5,0,4)$ reflection measured on increasing and decreasing the temperature across the Verwey transition with no field applied. The heating (cooling) rates were 2.5 (-2.5) K/min for the resistance measurements and 1 (-0.5) K/min for the diffraction measurements. A vertical dashed line denotes T_V. (c) Schematic representation of the experimental geometry for detwinning our magnetite sample through cylindrical compression and field cooling. (d) Intensity profiles as function of the orientation angle of the sample, A_3, at the $(4,0,0.5)$ and $(4.5,0,0)$ superlattice reflections of the monoclinic phase, which arise from the doubling of the unit cell, respectively, along the [001] and [100] direction. Data and Gaussian fits are plotted with respectively circles and continuous lines.

5.1 Experiments

A natural single crystal of magnetite of 1.7 g mass was purchased from Surface Preparation Laboratory (SPL), Zaandam, Netherlands. Based on resistance characterization, our sample shows a discontinuous transition, at the Verwey temperature, $T_V = 116$ K (see Fig. 5.1(a)). INS measurements were performed at the thermal triple-axis neutron spectrometer EIGER, located at the Swiss Spallation Neutron Source (SINQ), Paul Scherrer Institute (PSI), Switzerland [89].

Our sample is comprised of a cylinder with 12 mm length, 6 mm diameter and axis parallel to the [111] direction. In our first set of experiments, discussed in Section 5.2 and focused on both phases, to prevent crystal microtwinning in the monoclinic phase, the sample was inserted into an aluminum ring. With decreasing temperature, aluminum contracts more than magnetite, and thus generates a biaxial compression perpendicular to the [111] direction. The combination of mechanical stress and a 1.1 T field in the [001] direction, applied upon cooling across the critical region, favors in energy one out of the 12 possible twin domains [133]. Figure 5.1(c) displays our experimental geometry. The crystal was aligned with the [100] and [001] directions in the horizontal scattering plane, and installed into a horizontal-field cryomagnet.

In our second set of experiments, discussed in Section 5.3 and focused on the cubic phase alone, no field was applied. To avoid possible damage, our sample was not removed from the aluminum ring. Again, INS measurements were carried out in the [010] zone. Our sample was installed into a standard orange cryostat.

Hereafter, for simplicity, the reflections will be indexed according to the cubic scheme, $\boldsymbol{Q} = \frac{2\pi}{a}(h\boldsymbol{i} + k\boldsymbol{j} + l\boldsymbol{k}) \equiv (h,k,l)$ (where a is the lattice parameter in the cubic phase), in spite of the monoclinic symmetry below T_V. The critical temperature of the structural transition was determined with higher accuracy in our second set of experiments, by measuring the elastic intensity at $(3.5,0,4)$, a superlattice reflection of the monoclinic phase, which originates from the doubling of the unit cell in the [100] direction (see Fig. 5.1(b)). Based on the above characterization, both critical temperatures for the electronic and structural transition are equal to 116 K. The temperature range for phase coexistence extends from 114 to 118 K. Figure 5.1(d) illustrates the experimental verification of the effectiveness of our detwinning procedure. Namely, the elastic intensities at $(4,0,0.5)$ and $(4.5,0,0)$ below T_V were compared to rule out any meaningful contribution from twin domains with c axis perpendicular to the field direction, under the assumption of equivalent [100] and [010] directions (being an out-of-plane reflection, $(4,0.5,0)$ was not accessed).

In our first set of experiments, inelastic scans were performed in the $(4,0,0)$ and $(0,0,4)$ Brillouin zones. The final neutron wave vector was fixed at $k_f = 2.662$ Å^{-1}. The intensity at the detector was normalized against the flux on a low efficiency monitor between the monochromator and the sample. TA phonons were measured along the [001] direction near T_V and at our 2 K base temperature. The TA dispersion was also measured along the [100] direction at 2 K. Measurements of the temperature dependences of the phonon modes of Δ_5

and X_3 symmetry at the lowest energies were performed across T_V, respectively, at the Δ point $(4,0,-0.5)$ and the X point $(4,0,-1)$. For simplicity, in the following they will be referred to, respectively, as the Δ_5 mode and the X_3 mode.

In our second set of experiments, in the same experimental configuration, inelastic scans were performed at different temperatures, across zero energy. The presence of the $(1,1,1)$ and $(2,0,0)$ diffraction rings of aluminum prevented measurements of the elastic peak in the $(4,0,0)$ and $(0,0,4)$ Brillouin zones. Therefore, in contrast to our first set of experiments, inelastic scans were performed at $(3.5,0,4)$. Elastic scans were also performed at different temperatures, in two perpendicular directions, in the same Brillouin zone.

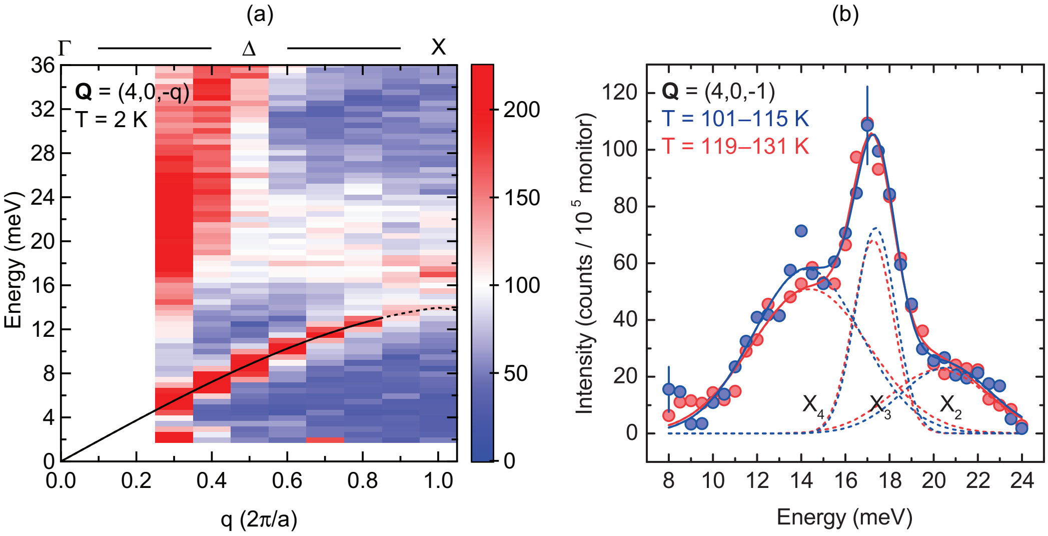

Figure 5.2 – (a) Color-coded map of scattering intensity along the [001] direction around the $(4,0,0)$ reflection at our 2 K base temperature. Our fit to the dispersion curve of the TA phonons is plotted with a continuous line. Extrapolations are represented by a dashed line. (b) Inelastic spectra at the X point below (101–115 K) and above T_V (119–131 K). Error bars are displayed only for representative points. Total fit curves are represented by solid lines, for data in the (red) high- and (blue) low-temperature phase. Single Gaussian peaks are plotted with dashed lines and labeled according to the symmetry assignment of Ref. [26].

	Below T_V (101–115 K)		Above T_V (119–131 K)	
Mode	Energy / meV	FWHM / meV	Energy / meV	FWHM / meV
X_4	14.3 ± 0.9	5.6 ± 1.6	14.4 ± 1.3	6.3 ± 2.0
X_3	17.4 ± 0.2	2.1 ± 0.6	17.3 ± 0.2	2.1 ± 0.6
X_2	20.6 ± 1.8	4.8 ± 3.9	20.3 ± 2.5	5.1 ± 4.3
Δ_5	8.6 ± 0.1	2.0 ± 0.1	8.3 ± 0.1	2.4 ± 0.1

Table 5.1 – Values of parameters from fits to the data at the X point (X_4, X_3 and X_2 modes) and the Δ point (Δ_5 mode), respectively.

5.2 Lattice Dynamical Anomaly of the Order Parameters

5.2.1 Results

Figure 5.2(a) exemplifies a complete set of our data. The dominant contribution from magnetic scattering visible at low wave vectors prevented us from measuring any phonon peak at points in reciprocal space closer than 0.3 reciprocal lattice units (r.l.u.) to the center of the Brillouin zone. To provide accurate estimates of the phonon energies and linewidths, the inelastic spectra were fit by functions comprised of multiple Gaussian peaks, after subtraction of a linear background contribution.

First, we address the lattice vibrational effects at the boundary of the Brillouin zone in the [001] direction, labeled as the X point. The energy range below 24 meV contains the X_3 mode, which belongs to the lowest-lying transverse optical (TO) branch. Recently, the X_3 mode was proposed as a primary OP of the structural transition [25, 26]. Moreover, it was suggested to play a leading role in the electronic transition. Indeed, according to the theoretical predictions, in the presence of strong onsite interactions, the atomic displacements of X_3 symmetry are interrelated with orbital order and small differences in the charge states of the B-type Fe ions, with distribution similar to the Verwey model. Together, they suffice to determine the change of state from conductive to insulating.

To improve statistics, the data at the X point were averaged in two different temperature ranges, above and below the transition temperature. Figure 5.2(b) and table 5.1 summarize the comparison between the resulting spectra.

Our data elucidate that the Verwey transition does not cause any discontinuity in the characteristics of the X_3 mode. Namely, neither the linewidth nor the energy of the X_3 mode changes between 101 and 131 K, within respectively 0.6 and 0.2 meV uncertainty. Therefore, we rule out the possible softening of the X_3 mode. The linewidth of the X_3 mode remains close to the 1.9 meV instrumental resolution all across the critical region. This is at odds with recent observations of anharmonic effects on different phonon modes between room temperature and T_V [71]. More remarkably, the absence of any noticeable modification in the linewidth and energy of the X_3 mode is in contrast with the first-principle calculations discussed in the foregoing.

The lowest-energy feature in Fig. 5.2(b) is identified with the TA mode of X_4 symmetry. For simplicity, in the following it will be referred to as the X_4 mode. Our data confirm previous observations on the anomalous linewidth of the X_4 mode in the cubic phase [71]. In addition, they provide information on how the characteristics of the X_4 mode change across the Verwey transition. In particular, they show that the atypical linewidth of the X_4 mode persists in the monoclinic phase.

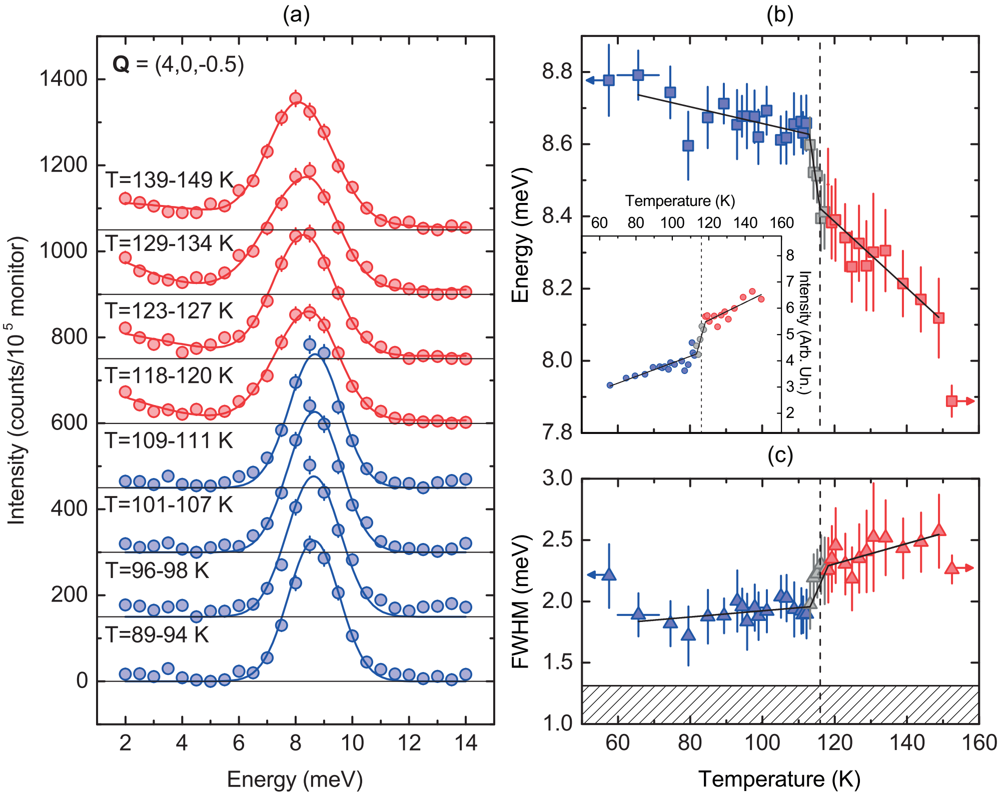

Figure 5.3 – (a) Inelastic spectra averaged over different temperature ranges across the Verwey transition. Data are offset by 150 counts / 10^5 monitor for clarity. Constant levels of background intensity are subtracted and horizontal lines are drawn to accentuate the onset of critical scattering above T_V. Fitting functions comprised of symmetric and asymmetric Gaussian peaks are plotted with continuous lines. (b) Energy and (c) linewidth of the Δ_5 mode as a function of temperature across the Verwey transition. Left and right horizontal arrows are associated with data points at 2 and 293 K, respectively. The hatched area represents the instrumental resolution. Inset: integrated area of linear background in the same temperature range, between 2 and 14 meV. Continuous lines are a piecewise linear fit to the data, where the fit parameters are the slope and the temperature limits for the high- and low-temperature phase. A vertical dashed line denotes T_V.

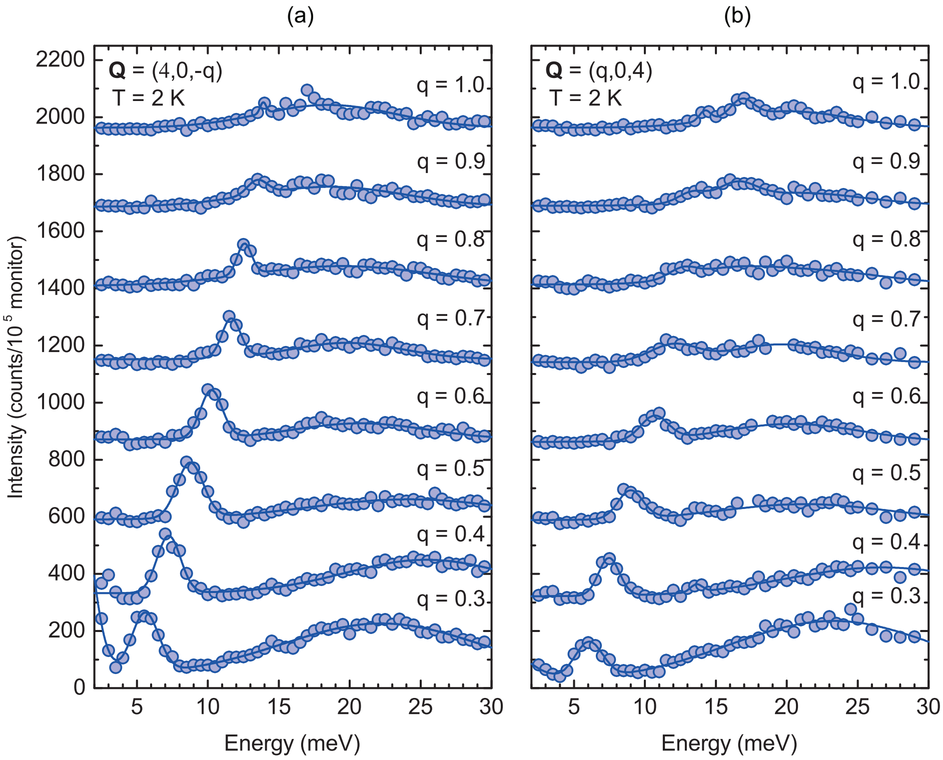

Figure 5.4 – Inelastic spectra along the (a) [001] and (b) [100] direction at 2 K, respectively, in the $(4,0,0)$ and $(0,0,4)$ Brillouin zones. Data are offset by 275 counts / 10^5 monitor for clarity. Total fit curves are represented by solid lines.

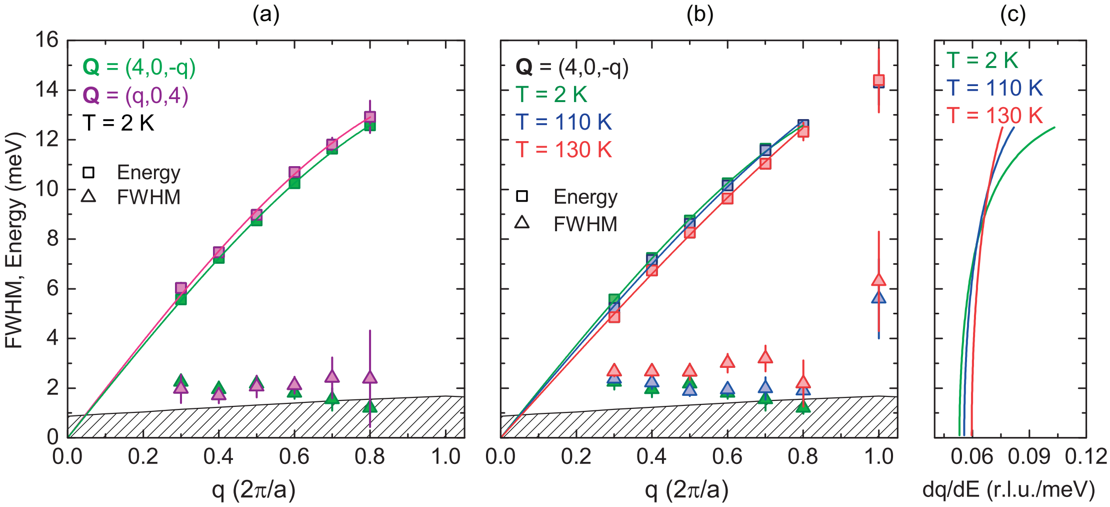

Figure 5.5 – (Squares) Energy and (triangles) FWHM dispersion of the TA phonons (a) along the [001] and [100] direction at 2 K, and (b) along the [001] direction above (130 K) and below T_V (110 K), and at 2 K. Third-order polynomial fits to the data are plotted with lines. The hatched areas represent the instrumental resolution. (c) Reduced vibrational density of states, $dq/dE \propto g(E)/E^2$, in the low-energy range, as calculated from the fits to the data in panel (b).

The highest-energy feature in Fig. 5.2(b) is assigned to the second TO mode at the X point, labeled as the X_2 mode. Considerations analogous to the above for the X_4 mode hold true for the X_2 mode. However, let us note that the quantitative reliability of any possible analysis on the X_2 mode is questioned by the absence of a well-defined peak.

Next, as illustrated in Fig. 5.3, we measured the structural dynamics at $(4, 0, -0.5)$, in the energy range which contains the Δ_5 mode. Since the earliest lattice dynamical studies of the Verwey transition, the Δ_5 mode has been regarded to as the most probable candidate for phonon softening [24]. More recently, the Δ_5 mode was proposed as a primary OP of the structural transition [25, 26]. In the monoclinic phase, the atomic displacements of Δ_5 symmetry are strongly coupled with the phase modulation of the extra electrons on the B-type Fe sites with identical periodicity [7].

Figure 5.3(a) shows inelastic spectra at $(4, 0, -0.5)$, averaged in different temperature ranges in both phases, to improve the signal-to-noise ratio. To emphasize the possible contribution of critical scattering to the intensity at low energy in the cubic phase, the incoherent background estimated from the data at 110 K was subtracted from all the spectra.

Figures 5.3(b,c) show the temperature dependence of the energy and linewidth of the Δ_5 mode across the critical region. Table 5.1 summarizes the average values of the parameters of all modes being measured near the transition temperature in the two different phases. In contrast to the X_3 mode, the Δ_5 mode shows abrupt energy renomalization and linewidth decrease in the critical region. Our data do not contain any evidence of softening of the Δ_5 mode. On the contrary, with decreasing temperature from 150 K to T_V, the Δ_5 mode hardens at a high rate, $dE/dT = -9.2 \times 10^{-3}$ meV/K, which is anomalous compared to the four times lower rate below T_V. The difference in mode energy between 150 and 293 K further suggests that the slope of the energy change as a function of temperature increases considerably below 150 K. In contrast, the linewidth of the Δ_5 mode slightly decreases from 150 K to T_V. The smaller linewidth at 293 K compared to that at 150 K is consistent with previous observations of atypical broadening on cooling starting from room temperature [71].

Between 2 and 14 meV, background intensity builds up on warming, with a steplike change at the transition temperature (see inset in Fig. 5.3(b)). As illustrated in Fig. 5.3(a), a minor lineshape distortion of the Δ_5 mode also develops discontinuously across the critical region. The increase of the scattering intensity at energies intermediate between the central peak and the Δ_5 mode, and the onset of the lineshape asymmetry of the Δ_5 mode are both signatures of the critical dynamics of lattice vibrations coupled with fluctuations [55] (see Section 5.3).

Finally, we studied the dispersion curves of the TA modes at 2 K, in the [001] and [100] directions, which become inequivalent upon symmetry breaking in the monoclinic phase, and the effect of the Verwey transition on the energies and linewidths of the TA modes. Figure 5.4 shows data and fitting functions at 2 K. Figures 5.5(a,b) display the dispersion curves of the TA modes in the [001] and [100] directions at 2 K, and in the [001] direction at different temperatures across the Verwey transition. The linewidth of the TA modes is largest at the X

point. A relative maximum is located at the incommensurate wave vectors q_z=0.6–0.7 r.l.u.. In the monoclinic phase, the linewidths of the TA modes at the same points in reciprocal space approach the instrumental resolution, in contrast to the linewidth of the X_4 mode, which remains abnormal. Remarkably, the Verwey transition is accompanied by an overall hardening of the TA modes. As noticeable in Figs. 5.4 and 5.5(a), in the monoclinic phase the dispersion curve of the TA modes along the [100] direction is slightly harder compared to that in the [001] direction.

5.2.2 Discussion and Conclusions

According to x-ray nuclear inelastic scattering experiments, upon the onset of charge and orbital order in the monoclinic phase, the vibrational density of states below 12 meV shows an abrupt modification, which is suggestive of lattice stiffening [3, 116]. However, due to the uncertainty in the subtraction of the elastic peak, it was not possible to draw any reliable conclusion.

Here, we provide more solid evidence of lattice stiffening. Indeed, as clearly visible in Fig. 5.5(b), the TA modes show a sudden hardening by 0.3–0.6 meV across the critical region. To demonstrate qualitative agreement with Refs. [3, 116], in Fig. 5.5(c) we plotted the inverse slope of our dispersion curves, dq/dE, proportional to the contribution of the TA modes to the vibrational density of states normalized to the squared energy, $g(E)/E^2$, under the simplifying assumption of isotropy.

It is also interesting to note that at 2 K the dispersion curve of the TA modes with polarization along [001] is slightly harder than that for displacement vector aligned to [100] (see Figs. 5.4 and 5.5(a)). According to naive symmetry considerations, the isotropy of the dispersion curves along $\langle 100\rangle$ in the cubic phase is lost below the transition temperature. Furthermore, the sign of the energy difference provides nontrivial information on the physical effects that break the symmetry. In particular, there is a relation between our observations and charge order in the monoclinic phase. This is comprised of small, but nonnegligible modulations of the average charge density along [001]. Therefore, the force constants are larger between atomic planes perpendicular to [001], compared to along the directions that lie within the same atomic planes.

Since the Verwey transition is not strongly first order, but close to continuous, the primary OP is expected to show enhanced susceptibility near the transition temperature, along with either softening or slowing down, depending on whether the dynamics of the critical modes is propagating or diffusive. If the critical modes consist of fluctuations, diffusive in nature, with correlation time longer than the lattice vibration periods, then the dynamics of the critical modes and the phonon modes are independent, and thus phonon softening does not occur. Let us note that the above scenario does not imply that the modes themselves are decoupled. Simply, in the presence of linear coupling between them, but independent dynamics, the change of the primary OP from zero to finite value causes a discontinuous displacement in the equilibrium positions of the ions, yet without any direct consequence on the phonon frequency. Clearly, additional anharmonic effects, such as a cubic term in the interionic potential, can determine a renormalization of the phonon frequency, but only as an indirect consequence of the new equilibrium positions of the ions.

Without any assumption on the dynamics, the most legitimate candidates for phonon softening in magnetite are the modes proposed as OPs of the structural transition, yet with particular reference to the approximate symmetry $P2/c$ for the monoclinic phase [25, 26]. In particular, the modes of X_3 and Δ_5 symmetry were suggested as primary OPs. Among the structural distortions regarded to as secondary OPs, the modes of X_1 symmetry are also associated with important atomic displacements. Our data show that near the transition temperature neither of the lowest-lying modes of X_3 and Δ_5 symmetry softens (see Figs. 5.2(b) and 5.3(b)), and the TA branch does not present any Kohn anomaly along [001] at wave vectors $q_z \geq 0.3$ r.l.u. (see Fig. 5.5(b)). On the contrary, the Δ_5 mode hardens significantly in the pretransition region (see Fig. 5.3(b)).

The most natural explanation for the absence of phonon softening in our observations is that the cubic phase is unstable against critical modes of diffusive nature, with slow dynamics, rather than phonon modes. As discussed above, this does not rule out strong linear coupling of the critical modes to the lattice vibrations, but only the mutual dependence of their dynamics. Indeed, the anharmonic effects observed on different phonon modes suggest that strong interactions are present and may be the main driving forces for the transformation process. Moreover, as pointed out by recent refinements of the crystal structure below T_V [27, 119], a large set of frozen modes needs to be accounted for to describe the atomic displacements from the parent to the distorted phase. Accordingly, the notion itself of phonon condensation loses relevance in the mechanism of the Verwey transition, in favor of a process dominated by local distortions.

The general picture of our results is consistent with the interpretation of the precursor effects of the Verwey transition in terms of critical fluctuations coupled to phonon modes. Broader linewidths in the inelastic spectra and thus larger coupling constants occur at q_z=0.6–0.7 and 1 r.l.u. (see Figs. 5.2(b) and 5.5(b)), in correspondence of local maxima in the intensity of diffuse scattering. A careful examination of the data in Fig. 5.5(b) reveals that larger energy changes take place at T_V at the same q_z=0.6–0.7 r.l.u.. Below T_V, linewidths closer to the instrumental resolution are restored at $q_z \neq 1$ r.l.u. (see Figs. 5.3(a,c) and 5.5(b)). Analogous incommensurate-commensurate transitions are common in charge-ordered systems [134].

The characteristics of the critical fluctuations, such as density, temperature and interactions of the fluctuation quasiparticles, are in mutual competition and cause intrinsic instabilities at wave vectors independent of the periodicity of the lattice potential. In the pretransition region, far enough from the transition temperature, the amplitude of the critical fluctuations is small. As a result, an incommensurate modulation of the charge density prevails over the effects of the lattice potential. These are comprised of coupling terms of third order between structural and electronic variables. In the regime of robust polaron order in the monoclinic phase, the energy gain from the same terms locks in a commensurate modulation of the charge density. Electron-phonon interactions at incommensurate wave vectors lose importance, in agreement with our observations on the TA modes at $q_z \neq 1$ r.l.u.. A simple analogy to the mechanism being discussed is the solidification of a two-dimensional liquid on a crystal surface. In the liquid phase, the structure factor of the overlayer consists of broad peaks centered at incommensurate wave vectors, which originate from local dynamical correlations, inherent to the characteristics of the overlayer itself. Below the freezing point, they become narrower and shift to positions commensurate to the underlying lattice, due to substrate-overlayer interactions [135].

The behavior of the X_4 mode is more puzzling. Contrary to the TA modes at incommensurate wave vectors, it remains anomalously broad below T_V (see Figs. 5.2(b) and 5.5(b)). If on one hand the persistence of anharmonic interactions at commensurate wave vectors below T_V is not surprising, on the other hand anomalously large linewidth is observed also at room temperature [71], which is suggestive of an intrinsic characteristic of the X_4 mode, independent of the Verwey transition.

To summarize the conclusions of this Section, we observed discontinuous changes of the phonon modes across the Verwey transition. We interpreted the frequency renormalization of the lattice vibrations in terms of incipient charge order. Instead, the steplike modifications in the linewidth of the phonon modes provide evidence of the abrupt suppression of incommensurate correlations of critical fluctuations. Overall, our observations illustrate that commensurate and incommensurate interactions play different roles in the mechanism of the Verwey transition. The absence of softening of the phonon modes, despite the strong coupling to critical fluctuations, implies independent dynamics. Namely, critical fluctuations are correlated on long time scales compared to the periods of the lattice vibrations. This is at the opposite limit with respect to the adiabatic approximation valid for wide-band solids, and is indicative of a strongly correlated system, with significant electron-phonon coupling. In this Section, we purposely used the generic term *critical fluctuations*, without specifying the nature of the instability, which is instead the subject of the next Section.

5.3 Polaron and Electronic Fluctuations

5.3.1 Pak and Kinase's Model

Correlations of precursor order are the most probable origin of the manifold effects which anticipate the Verwey transition in electronic, structural and magnetic degrees of freedom (see Section 1.4). INS gives access to the mutual interactions and relative time scales of precursor order and phonons, and thus enables one to gain direct insight into pretransitional phenomena. In particular, according to past INS studies of magnetite, diffuse scattering in reciprocal space is associated with intensity contributions around zero energy in the inelastic spectra, the so-called central peaks, and anomalous broadening of the phonon peaks [66].

To better understand the meaning of the above features, let us observe that, in INS, the spectral function is the FT of the time autocorrelation of the atomic displacements (see Eq. 2.17). Hence, clearly, the possible sources of central peaks are either propagating excitations, which have become overdamped, or diffusive excitations. The broad temperature range of the pretransitional phenomena in magnetite rules out the second possibility. In fact, even in the presence of phonon softening, typically, soft phonons are overdamped only in a narrow temperature range, around the transition temperature.

Let us then focus on the second possibility. Phenomenological models were developed to describe the spectral function in the case of continuous transitions, with diffusive excitations [55, 136]. In the following, to provide a simple theoretical ground, needful for further considerations, we refer to Pak and Kinase's model [136]. The basic hypothesis is that phonon variables, *i.e.* atomic displacements $Q_{\boldsymbol{q}\lambda}$, interact with pseudospin variables $\sigma_{\boldsymbol{q}\lambda}$, where $\boldsymbol{q}$ and λ are respectively the wave vector and the branch index of the mode being considered. The notion of pseudospin variable was briefly introduced in Section 1.3. This is a fictitious Ising operator. Depending on the system under consideration, different definitions are possible for the pseudospin lattice and the physical meaning of the pseudospin variables. In general, the two values of the pseudospin variable $\sigma_{i\lambda}$ correspond to two different configurations of atomic displacements and/or charge distributions of λth symmetry, at multiple sites in the ith cell. For instance, in Yamada's interpretation of the Verwey transition, these are the different arrangements of the extra charges among the B-type Fe ions in the primitive cell, of Δ_1, Δ_4 or Δ_5 symmetry [24]. Here, we generically refer to Fourier components of pseudospin variables, $\sigma_{\boldsymbol{q}\lambda} = \sum_i \sigma_{i\lambda} e^{-i\boldsymbol{q}\cdot\boldsymbol{r}_i}$, to represent fluctuation modes of precursor order.

Intrinsic instabilities in either or both pseudospin and phonon variables are at play in the transformation processes described by Pak and Kinase's model. In the case of magnetite, the incommensurate character and the intensity divergence of diffuse scattering at a virtual temperature below T_V, instead of at T_V, point out that the precursor effects are of second order. Therefore, they are not the direct cause of the discontinuous modifications in the crystal structure at T_V, but are suitable for the application of Pak and Kinase's model.

In the following, we provide the main results of Pak and Kinase's model. The derivation of the spectral function starts from the below equations of motion of two coupled phonon and pseudospin variables. For simplicity, we drop both the wave vector $\boldsymbol{q}$ and the branch index λ. We define ω_0 and γ_Q respectively the frequency and damping constant of the phonon mode. γ_σ is the pseudospin relaxation rate and g is the pseudospin-phonon coupling constant.

$$\begin{cases} \ddot{Q} + \gamma_Q \dot{Q} + \omega_0^2 Q = g\sigma + E \\ \dot{\sigma} + \gamma_\sigma \sigma = gQ \end{cases} \tag{5.1}$$

The external field E is introduced for the below computation of the spectral function, from the imaginary part of the dynamic susceptibility, $\chi_{QQ}(\omega) = Q(\omega)/E(\omega)$, according to the fluctuation-dissipation theorem. $1 + n(\omega) = [1 - \exp(-\omega/k_B T)]^{-1}$ is the Bose-Einstein thermal factor. $\widetilde{\omega}_0^2$ and $\widetilde{\gamma}$ are respectively a squared renormalized frequency and a frequency-dependent damping coefficient, defined in Eqs. 5.3 and 5.4.

$$\phi_{QQ}(\omega) = 2[1 + n(\omega)]\,\mathrm{Im}[\chi_{QQ}(\omega)] = 2[1 + n(\omega)]\,\frac{\omega g^2/\gamma_\sigma^2}{\left(\widetilde{\omega}_0^2 - \omega^2\right)^2 + \omega^2\widetilde{\gamma}^2}. \tag{5.2}$$

$$\widetilde{\omega}_0^2 = \frac{\omega_0^2\gamma_\sigma - g^2}{\gamma_\sigma + \gamma_Q}. \tag{5.3}$$

$$\widetilde{\gamma} = \frac{\omega_0^2 + \gamma_\sigma\gamma_Q - \omega^2}{\gamma_\sigma + \gamma_Q}. \tag{5.4}$$

Shapiro et al. fit the spectral response at $(4, -0.2, -0.2)$ and $(4, 0, 3.25)$, at 125 and 150 K, with Yamada's model function, which is equivalent to Eq. 5.2, but with $\gamma_Q = 0$, *i.e.* negligible phonon damping [55, 66]. Their results, combined with our failure to observe any phonon softening (see Section 5.2), suggest that intrinsic instabilities of the pseudospin variables, with slow dynamics compared to the phonon variables, represent the initial driving forces for the transition process. The cooperative ordering of the pseudospins translates into the critical slowing down of the pseudospin relaxation rate, $\gamma_\sigma = \gamma_{\sigma 0} k_B (T - T_0)$, where $\gamma_{\sigma 0}$ is a constant and T_0 is the pseudospin ordering temperature in the absence of couping with phonons. Let us also replace in Eq. 5.3 the critical temperature of the pseudospin-phonon coupled system, $T_c = T_0 + g^2/k_B\gamma_{\sigma 0}\omega_0^2$, derived in Subsection 5.3.3. Therefore, Eqs. 5.3 and 5.4 become

$$\widetilde{\omega}_0^2 = \omega_0^2\,\frac{T - T_c}{T - T_0 + \gamma_Q/k_B\gamma_{\sigma 0}}, \tag{5.5}$$

$$\widetilde{\gamma} = \frac{\omega_0^2 + \gamma_{\sigma 0}\gamma_Q k_B (T - T_0) - \omega^2}{\gamma_{\sigma 0} k_B (T - T_0) + \gamma_Q}. \tag{5.6}$$

Spectroscopic signatures of local dynamic order are not restricted to INS. In Chapters 3 and 4, we discussed how macroscopic order across structural transitions causes the emergence of new phonons in the spectral response from inelastic scattering of light, upon folding from finite wave vectors to the center of the Brillouin zone in the ordered phase. We also argued that, close enough to the transition temperature, precursor order mediates Raman scattering

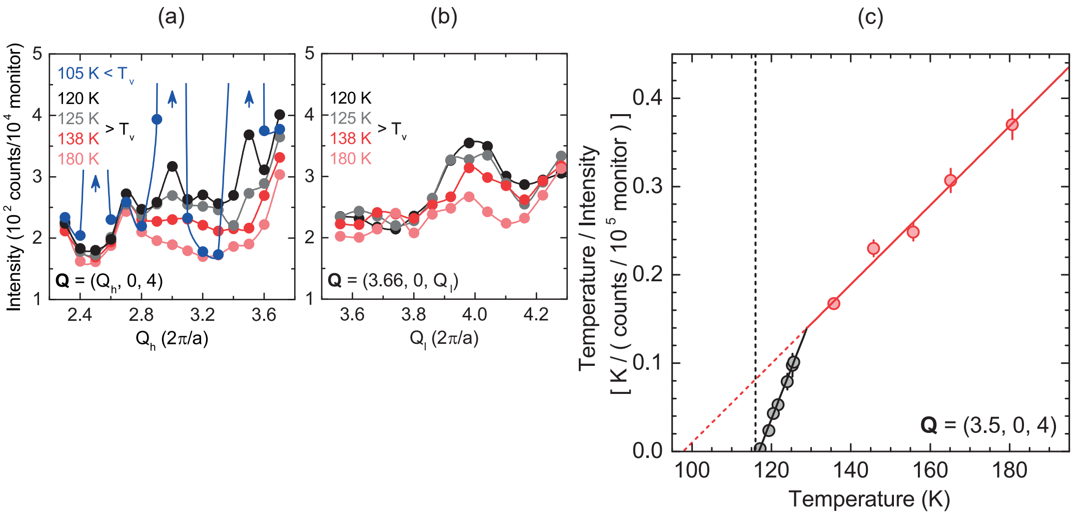

Figure 5.6 – Wave-vector and temperature dependence of elastic scattering intensity across the Verwey transition. Elastic scattering intensity as a function of wave vector along the lines (a) from $Q_h = 2.3$ to $Q_h = 3.7$, and (b) from $Q_l = 3.56$ to $Q_l = 4.28$, in the orthogonal directions $Q_l = 4$ and $Q_h = 3.66$, (red and black colors) at different temperatures above T_V and (blue color) at 105 K < T_V. Error bars lie within data points. Lines are guides to the eye. Blue arrows denote the onset of the superlattice reflections of the monoclinic phase. (c) Temperature dependence of the inverse intensity of diffuse scattering corrected for the thermal factor. Solid lines are linear fits to the data, in different critical regimes, respectively, (black color) between T_V and 129 K, and (red color) above 129 K. A red dashed line indicates the virtual instability of the critical regime above 129 K. A vertical dashed line denotes T_V.

from the same phonons in the disordered phase. With reference to the Verwey transition in magnetite, we showed that fluctuation modes of precursor order at the Δ and X points in reciprocal space assist the excitation of phonons of opposite wave vectors in the cubic phase.

Our observations from light probes, and the occurrence of central peaks and anomalously broad phonon peaks in INS, raise the important question of what is the physical origin of the relaxational response, which so far we addressed only from an empirical point of view. In the following, to better understand the characteristics of the critical fluctuations, we discuss the diffusive modes at the Δ point, with focus on how they couple to the phonon modes in the cubic phase. Our data from light and neutron probes are combined together to gain a more complete understanding. The reason for the choice of the Δ point is twofold. A symmetry analysis based on group theory identified the Δ_5 mode as a primary OP for the structural transition [25, 26]. Indeed, even according to the most recent structural refinements, the atomic displacements from the parent to the distorted phase along the eigenvectors of Δ_5 symmetry are the largest in amplitude [27, 28]. Moreover, our data from light probes contain information restricted to the Δ and the X points. Therefore, comparison is only possible for either wave vector.

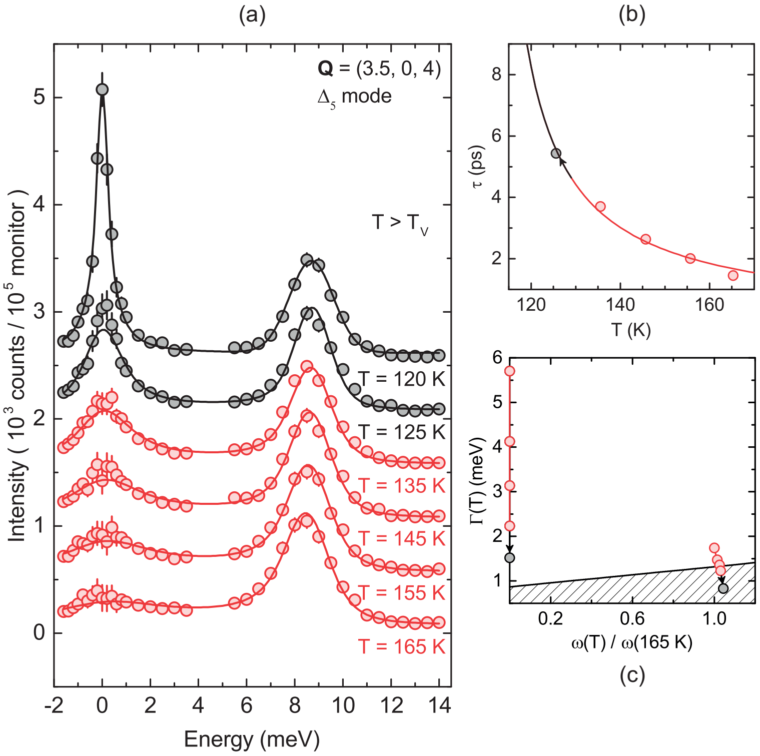

Figure 5.7 – (a) Inelastic spectra at the Δ point $(3.5, 0, 4)$, at different temperatures above T_V, in the energy range from -1.6 to 14 meV, which contains the elastic peak and the Δ_5 mode. For clarity, error bars are doubled and data points at different temperatures are offset by 5×10^2 counts / 10^5 monitor. The estimate of the incoherent peak from the data at 180 K and at the same point in reciprocal space is subtracted from all the inelastic spectra. Lines in the 125–165 K temperature range are fits to the data according to the model function defined by Eqs. 5.2, 5.5 and 5.6. The line at 120 K is a guide to the eye. (b) Estimate of the inverse linewidth of the central peak as a function of temperature from the fit analysis. The line is a guide to the eye. (c) Temperature dependence of the two poles of the dynamical susceptibility in the first quadrant of the complex plane. The real and imaginary part of the poles correspond respectively to the energy and linewidth of the central peak and the phonon peak. Red (Black) color denotes the critical regime above 129 K (between T_V and 129 K). The hatched area represents the instrumental resolution, within which estimates are not reliable.

T/K	γ_σ	γ_Q/meV	T_0/K	T_c/K	Γ_{cp}/meV	Γ_{ps}/meV	τ/ps
165	0.48	0.29	56	94	5.7	1.7	1.4
155	0.41	0.23	56	94	4.1	1.5	2.0
145	0.37	0.11	56	94	3.1	1.4	2.6
135	0.34	0.00	56	94	2.2	1.2	3.7
125	0.28	0.00	60	95	1.5	0.8	5.4

Table 5.2 – Parameter values from fit analysis.

5.3.2 Results

Figures 5.6(a,b) show the distribution of the elastic scattering intensity in reciprocal space around the $(4,0,4)$ reflection, along the $[Q_h\,0\,4]$ and the $[3.66\,0\,Q_l]$ directions, as a function of temperature. The unchanged features around $(3.66,0,4.3)$ and $(2.7,0,4)$ are artifacts, which probably originate, respectively, from the $(2,2,0)$ diffraction ring of aluminum and a $\langle 2,2,4\rangle$ reflection of a misaligned crystallite. In the absence of diffuse scattering, in the cubic phase, far enough from the transition temperature, and in the monoclinic phase, the base intensity originates from incoherent scattering alone. Indeed, intensity levels are comparable around $(3.2,0,4)$, at 105 K $< T_V$ and 180 K $\gg T_V$, and thus here regarded to as our reference for incoherent scattering. Below T_V, superlattice reflections appear in correspondence of the blue arrows in Fig. 5.6(a), namely at the half-integer indexes $(2.5,0,4)$ and $(3.5,0,4)$, upon unit cell doubling, and at the even-odd mixed index $(3,0,4)$, for the breaking of the translational symmetry along the $\langle 100\rangle$ directions [66]. Diffuse scattering is responsible for the progressive buildup of intensity above the background observable in the 125–180 K temperature range. The narrow feature around $(3.66,0,4)$ in Fig. 5.6(b) points out the streaklike character of diffuse scattering in the [100] direction at all temperatures. The pronounced intensity of the E=0 constant-$\boldsymbol{Q}$ scans in the 3.1–3.3 Q_h range at 138 and 125 K in Fig. 5.6(a) signals the incommensurate nature of diffuse scattering in the same temperature range. The bumps observable around $(3,0,4)$ and $(3.5,0,4)$ at the temperature closest to T_V, 120 K $= T_V + 4$ K, are related to the appearance of new Bragg peaks at the same wave vectors in the monoclinic phase and generally referred to as spotlike scattering, to distinguish them from diffuse scattering.

Figure 5.6(c) shows the temperature dependence of the inverse intensity of critical scattering, multiplied by the temperature, to account for the occupation number of the diffusive excitations at the origin of critical scattering. Our reference for incoherent scattering is subtracted from the scattering intensity to single out the contribution from critical scattering alone. A piecewise fit with linear functions identifies two critical regimes, above 129 K, and between T_V and 129 K, which are denoted with respectively red and black shades in the color coding of Figs. 5.6(c) and 5.7. The extrapolation of the temperature-to-intensity ratio to zero for the critical regime above 129 K provides the approximate estimate $T_c = 97.7 \pm 14.7$ K. Instead, in the critical regime between T_V and 129 K, clearly, the scattering intensity diverges at T_V.

Figure 5.7(a) shows the temperature dependence of the central peak at the Δ point and the Δ_5 mode in the cubic phase. The elastic peak at $(3.5,0,4)$ and 180 K, far enough from the transition temperature, is here assumed as our reference for the incoherent peak and subtracted from all the inelastic spectra at lower temperature and the same point in reciprocal space. The model function defined by Eqs. 5.2, 5.5 and 5.6 is convolved with the resolution function of the spectrometer and fit to the data. To provide reasonable constraints, a simultaneous fit analysis, with common values of the fitting parameters T_0 and T_c, is carried out for the data set in the critical regime above 129 K. The following expressions provide approximate estimates of the linewidths of the central peak, Γ_{cp}, and the phonon peak, Γ_{ps}, corrected for the experimental resolution.

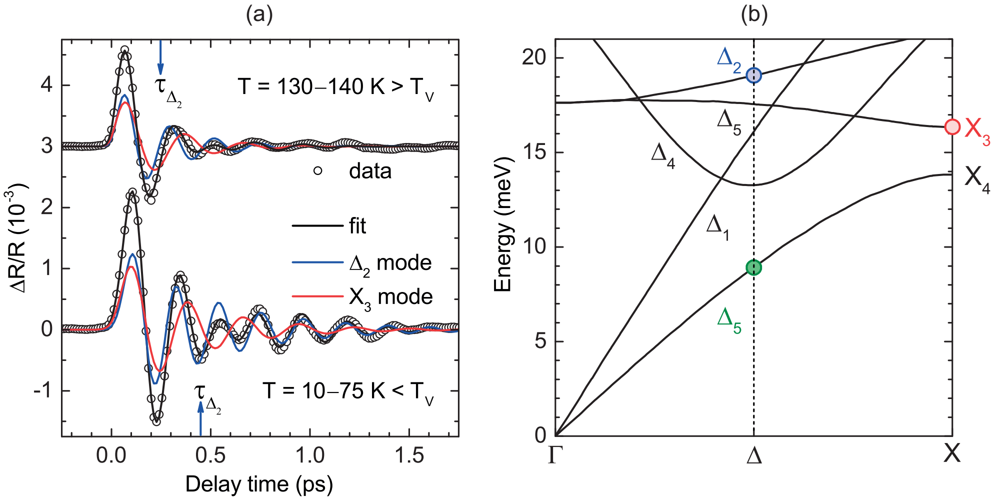

Figure 5.8 – (a) Coherent oscillations of the differential reflectivity as a function of pump-probe delay time, averaged between 2.0 and 2.3 eV probe photon energy, and in two different temperature ranges, below (10–75 K, lower time trace) and above T_V (130–140 K, upper time trace). Data (Fitting functions) are plotted with symbols (lines). Blue (Red) color corresponds to the Δ_2 (X_3) mode. Black color is associated with the total fit functions. Vertical arrows indicate approximate estimates of the coherence time of the Δ_2 mode. (b) *Ab initio* calculations of the phonon dispersion curves in the cubic phase along the ⟨100⟩ directions (lines). A vertical dashed line denotes the Δ point. Symbols and colored labels indicate the modes at the focus of our INS and pump-probe experiments.

$$\Gamma_{cp} = \frac{2\omega_0^2 \gamma_{\sigma 0} k_B (T - T_c)}{\omega_0^2 + \gamma_Q \gamma_{\sigma 0} k_B (T - T_0)}. \tag{5.7}$$

$$\Gamma_{ps} = \frac{\gamma_{\sigma 0} k_B}{\omega_0} \sqrt{2 (T - T_0)^2 \gamma_Q^2 + (T_c - T_0)^2 \omega_0^2}. \tag{5.8}$$

In turn, under the assumption of a single decay channel, the correlation time of the excitation responsible for the central peak is evaluated according to $\tau = 2h/\Gamma_{cp}$. The model function does not apply to the data at 120 K, owing to the onset of spotlike scattering. However, the instrumental resolution provides a lower boundary for τ at 120 K. The fitting functions are superimposed to the data in Fig. 5.7(a). The fit results, and the approximate estimates of Γ_{cp}, Γ_{ps} and τ are summarized in table 5.2. τ is plotted against temperature in Fig. 5.7(b). Figure 5.7(c) shows the energy and linewidth of the central peak and the phonon peak at different temperatures, in analogy to Fig. 1(a) of Ref. [136], to emphasize the agreement with the case of pseudospin ordering, with slow pseudospin relaxation and meaningful pseudospin-phonon coupling. Pak and Kinase computed the above quantities respectively as the real and imaginary part of the poles of the dynamical susceptibility.

To compare data from neutron and light probes, let us summarize the results discussed in Chapter 4. Two oscillations of the optical functions were observed upon impulsive photoexcitation, and assigned to the monoclinic counterparts of the X_3 mode and the TO mode of Δ_2 symmetry, hereafter simply labeled as the Δ_2 mode. The coherent response, averaged in two different temperature ranges to improve the signal-to-noise ratio, is shown in Fig. 5.8(a). The fit components corresponding to each oscillation are also plotted. All the modes under discussion are shown in Fig. 5.8(b). In the 10–75 K temperature range, the modes are at the center of the Brillouin zone and the photoexcitation mechanism is TSRS of the first order (see Fig. 5.8(a), lower time trace) [85, 87]. Instead, in the 130–140 K temperature range, the modes are at finite wave vectors, but still observable for the occurrence of second-order Raman processes, assisted by fluctuation modes of precursor order at opposite wave vectors (see Fig. 5.8(a), upper time trace). Vertical arrows in Fig. 5.8(a) indicate approximate estimates of the coherence time of the oscillation of the Δ_2 mode, $\tau_m = 460$ fs and $\tau_c = 240$ fs, respectively, in the monoclinic and cubic phase.

5.3.3 Discussion and Conclusions

To provide a basis to describe the critical dynamics of the Verwey transition, and thus interpret our complete set of observations, let us consider the expansion of the free energy density to the fourth order over power series of phonon and pseudospin variables of any possible wave vector $\boldsymbol{q}$ and branch index λ,

$$\begin{aligned}\mathscr{F}\left(\left\{Q_{\boldsymbol{q}\lambda},\sigma_{\boldsymbol{q}\lambda}\right\}\right) &= \sum_{\boldsymbol{q}\lambda}\omega^2_{\boldsymbol{q}\lambda}Q^*_{\boldsymbol{q}\lambda}Q_{-\boldsymbol{q}\lambda} + \sum_{\boldsymbol{q}\lambda}\chi^{-1}_{\sigma\boldsymbol{q}\lambda}\sigma^*_{\boldsymbol{q}\lambda}\sigma_{-\boldsymbol{q}\lambda} + \sum_{\boldsymbol{q}\lambda}g_{\boldsymbol{q}\lambda}\left(Q^*_{\boldsymbol{q}\lambda}\sigma_{-\boldsymbol{q}\lambda} + Q_{-\boldsymbol{q}\lambda}\sigma^*_{\boldsymbol{q}\lambda}\right)\\ &+ \sum_{\substack{\boldsymbol{q}_1\boldsymbol{q}_2\\ \boldsymbol{q}_3\lambda}} g'_{\substack{\boldsymbol{q}_1\boldsymbol{q}_2\\ \boldsymbol{q}_3\lambda}}\left(\sigma_{\boldsymbol{q}_1\lambda}\sigma_{\boldsymbol{q}_2\lambda} + \sigma^*_{\boldsymbol{q}_1\lambda}\sigma^*_{\boldsymbol{q}_2\lambda}\right)Q_{\boldsymbol{q}_3\lambda}\delta_{\boldsymbol{q}_1+\boldsymbol{q}_2+\boldsymbol{q}_3+\boldsymbol{G}} + \cdots \end{aligned} \tag{5.9}$$

where $\cdots$ indicate positive terms of the fourth order. The translational symmetry of the Hamiltonian reflects into the free energy density and requires that $\boldsymbol{q}_1 + \boldsymbol{q}_2 + \boldsymbol{q}_3$ is equal to a reciprocal lattice vector $\boldsymbol{G}$.

Far enough from T_V, the amplitude of the critical fluctuations is small. In general, terms of second order in σ are negligible. However, intrinsic instabilities of the pseudospin variables cause terms with large generalized susceptibility $\chi_{\sigma\boldsymbol{q}\lambda}$, responsible for precursor effects with continuous character. The most unstable modes are located at incommensurate wave vectors around $\langle 0.75, 0, 0\rangle$ [65–68]. In the following, let us consider the modes at $\langle 0.5, 0, 0\rangle$ and the TA branch, at the focus of our experiments. For simplicity, we drop the wave vector $\boldsymbol{q}$ and branch index λ, and we treat Q and σ as real variables. Accordingly, the explicit expression of the nonnegligible terms in the small-amplitude regime is

$$\mathscr{F}(Q,\sigma) = \omega_0^2 Q^2 + \gamma_{\sigma 0} k_B (T - T_0)\sigma^2 + 2gQ\sigma + \beta Q^4 + \gamma\sigma^4 \tag{5.10}$$

where β and γ are positive constants. The phenomenological model introduced in Subsection 5.3.1 refers to the above equation. The critical temperature of the pseudospin-phonon coupled system $T_c = T_0 + g^2/k_B\gamma_{\sigma 0}\omega_0^2$ is derived from the stability condition $\omega_0^2\gamma_{\sigma 0}k_B(T - T_0) - g^2 > 0$

for the $Q = \sigma = 0$ value of the OP in the cubic phase. Due to the finite resolution of the spectrometer, in fact the measured intensity of diffuse scattering is the integrated intensity around zero energy. Its approximate expression is given by the product between the $\omega \to 0$ limit of $\phi_{QQ}(\omega)$ (see Eqs. 5.2, 5.5 and 5.6) and Γ_{cp} (see Eq. 5.7) for $\gamma_Q = 0$. As a result, in the small-amplitude regime, the temperature-to-intensity ratio scales with temperature according to $T - T_c$. Indeed, it is possible to fit the data in Fig. 5.6(c) with a linear function, in the 135–180 K temperature range, which is thus identified with the small-amplitude regime. The fitting function extrapolates to zero temperature-to-intensity ratio at $T_c < T_V$. T_c represents the critical temperature of the potential transition that would occur if higher-order coupling between pseudospin and phonon variables was absent.

Fluctuations of significant amplitude develop near T_V. As a consequence, linear-quadratic Q-σ coupling is not negligible anymore. On the contrary, it grows into the dominant terms, which govern the discontinuous modifications at T_V. In particular, according to the explanation first advanced by Iizumi with reference to the structural degree of freedom [137], the third-order terms prevail over the energy gain from the onset of incommensurate fluctuations, and they eventually lock in the monoclinic phase.

In the critical regime between T_V and 129 K, the data in Fig. 5.6(c) lie on a straight line, which crosses zero at T_V. This resembles the characteristic divergence of the susceptibility in a continuous transition. In principle, different interpretations of the onset of spotlike scattering can be proposed. For instance, it is possible to argue that, in contrast to diffuse scattering, spotlike scattering is observable only over a narrow temperature range above T_V, which is consistent with the typical temperature dependences of overdamped excitations in phase transitions. However, we provided conclusive evidence that the Δ_5 mode does not soften (see Figs. 5.3 and 5.7). In fact, our general interpretation of the Verwey transition rules out the occurrence of phonon softening altogether (see Subsection 5.2.2). Moreover, overdamped excitations are supposed to show a noticeable change in intensity profile as a function of temperature, with progressive transfer of spectral weight from finite to zero energy. This is clearly incompatible with the characteristics of the central peak of spotlike scattering in our observations, centered at zero energy and within the instrumental resolution (see Fig. 5.7(a)).

It is also arguable whether critical scattering in general is essential to the mechanism of the Verwey transition or a consequence of the impurity content in natural single crystals of magnetite such as our sample. In this regard, let us note that spotlike scattering was not always observed, in contrast to diffuse scattering, which was reported also in systematic studies on synthetic samples with controlled stoichiometry [65–70, 138].

Let us now discuss the comparison between data from neutron and light probes. In Subsection 3.2.4, we showed that in the cubic phase the time dependence of the correlation between the fluctuations of the ordering field and the atomic displacements upon impulsive photoexcitation, $\langle \rho_{\boldsymbol{q}} Q_{-\boldsymbol{q}} \rangle$, modulates the optical response, through its dependence on the dielectric susceptibility $\boldsymbol{\chi}$ (see Eq. 3.10). We also showed that, in turn, the time dependence of $\langle \rho_{\boldsymbol{q}} Q_{-\boldsymbol{q}} \rangle$

can be computed via the Kubo formula, in the response regime linear in fluence, under the assumption of a classical ordering field (see Eq. 3.9). We now introduce the additional hypothesis of a relaxational response of the critical fluctuations, with a single relaxation time $\tau_{\rho \boldsymbol{q}}$, such that the autocorrelation of fluctuations of the ordering field can be expressed as

$$\langle \rho_{\boldsymbol{q}}(t)\rho_{-\boldsymbol{q}}(t')\rangle = \langle \rho_{\boldsymbol{q}}\rho_{-\boldsymbol{q}}\rangle\, e^{-(t-t')/\tau_{\rho q}}. \tag{5.11}$$

Let us note that the equal-time autocorrelation $\langle \rho_{\boldsymbol{q}}\rho_{-\boldsymbol{q}}\rangle$ is a constant because correlation functions are stationary. The time dependences of the correlations that govern the coherent response, respectively in the cubic and monoclinic phase, can thus be written as the below equations. In the monoclinic phase, the coherent phonons generated via TSRS [87] are at $\boldsymbol{q} = 0$.

$$\langle \rho_{\boldsymbol{q}} Q_{-\boldsymbol{q}}\rangle(t) = -\int_{-\infty}^{t} dt' \langle \rho_{\boldsymbol{q}}\rho_{-\boldsymbol{q}}\rangle \frac{e^{-(t-t')/\tau_q} \sin[\omega_{\boldsymbol{q}}(t-t')]}{\omega_{\boldsymbol{q}}} g_{\boldsymbol{q}}(t'), \text{ for } T > T_V. \tag{5.12}$$

$$\langle Q_0\rangle(t) = -\int_{-\infty}^{t} dt' \frac{e^{-(t-t')/\tau_{ph}} \sin[\omega_0(t-t')]}{\omega_0} g_0(t'), \text{ for } T < T_V. \tag{5.13}$$

Different effective forces $g_{\boldsymbol{q}}$ and g_0 act in the excitation processes of FASRS and TSRS, respectively, in the cubic and monoclinic phase, defined according to Eqs. 3.8 and 2.9. In the cubic phase, the coherence time of each oscillation, labeled as $\tau_{\boldsymbol{q}}$, is determined by the competition of two different processes, namely, the loss of phase memory of the coherent phonon and the correlation decay of the critical fluctuations. To a first approximation, let us assume that for equal fluence the effects of oscillation dephasing are the same in the temperature range from 10 to 140 K, and thus the faster damping in the cubic phase compared to the monoclinic phase is only due to the assistance of critical fluctuations in the excitation process. Indeed, the duration of each oscillation does not change noticeably throughout the monoclinic phase (see Fig. 3.4). Under the above simplifying assumption, the coherence time of each oscillation in the monoclinic phase constitutes an approximate estimate of the phenomenological phonon lifetime τ_{ph}. Therefore, the coherence times above and below the transition temperature are related by

$$\frac{1}{\tau_{\boldsymbol{q}}} = \frac{1}{\tau_{ph}} + \frac{1}{\tau_{\rho \boldsymbol{q}}}. \tag{5.14}$$

Hereafter, let us refer to the Δ_2 mode and the ordering field mode at the Δ point, which are coupled to each other by the impulsive photoexcitation (the wave vector $\boldsymbol{q}$ is dropped). Equation 5.14 provides an approximate estimate of the correlation time of the ordering field, $\tau_\rho = \left(\tau_c^{-1} - \tau_m^{-1}\right)^{-1} \approx 0.5$ ps.

The condensation of atomic displacements of Δ_5 symmetry in the monoclinic phase provides the most important contribution to the intensity of the superlattice reflections at the Δ point, with particular reference to the $(4,0,4)$ Brillouin zone, at focus in our INS experiments [24] (the dynamical factor of the Δ_5 mode at the $(8,0,0.5)$ and $(8,0,3.5)$ reflections is even larger, however, neither of them was accessible). Therefore, the symmetry of the fluctuation mode that gives rise to the central peak at the Δ point must be Δ_5. Our observation of strong coupling between the central peak at the Δ point itself and the Δ_5 mode is a further confirmation. Indeed, in order for the Hamiltonian to be totally symmetric, in each term of bilinear coupling, the symmetry of the fluctuation mode needs to be the same as that of the phonon mode (see Eq. 5.9). For the same reason, the symmetry of the fluctuation mode being considered in our pump-probe experiments must be Δ_2.

Strictly speaking, being of different symmetry, the fluctuation modes measured with neutron and light probes are different modes, even if they are degenerate at the Δ point. Therefore, it is not surprising that their correlation times are different. However, let us point out that, in the same temperature range around 135 K, the ratio between the 3.7 and 0.5 ps correlation times measured with respectively neutron and light probes is close to one order of magnitude. Clearly, symmetry differences for equal wave vectors are not enough to explain large inconsistencies between time scales.

The conclusions that it is possible to draw from our comparison are consistent with those of Chapter 4. If structural order is coupled to charge and orbital order by means of a meaningful pseudospin-phonon coupling constant, then the large inertia of the ions slows down the modifications of the charge and orbital configurations, consequent to intrinsic instabilities (see Eq. 5.1). The collective dynamics is thus better described in terms of correlations within a liquid of polarons, wherein all degrees of freedom of structural, charge and orbital order fluctuate together. The typical time scales of critical modes of polaronic nature with large effective mass are on the order of picoseconds. This is in agreement with our approximate estimates of the correlation times from neutron probes.

In sharp contrast, light probes, whether they be pump-probe or spontaneous Raman scattering experiments, provide evidence of faster correlations, over time scales on the order of hundreds of femtoseconds. Since both techniques based on light-matter interaction are directly sensitive to the electronic degree of freedom, this suggests that they are simply probing electronic modes, which either are not dressed by phonons altogether, or are coupled to structural modes only through weak interactions.

Our results point out the need to better understand the role of charge and orbital order, and how it relates to structural order, in the Verwey transition. A possible scenario is that the polarons are in fact characterized by an internal structure. Namely, in a pictorial representation, the strong interactions between electrons and dynamic atomic displacements give rise to the core of the polaron. Instead, electronic modes constitute its external shell. The coupling between the two components of the polaron is weak. Therefore, they preserve independent dynamics. In agreement with the above speculations, based on resonant x-ray diffraction experiments, it was argued that the temperature dependences of electronic and structural order around the transition temperature are different [62, 64]. In particular, in contrast to structural order, which sets in over meaningful lengths only below the transition temperature, a significant degree of charge and orbital order develops starting from the isotropic point. Further experimental studies are required. Indeed, both the interpretation of the experimental data from resonant x-ray diffraction and the microscopic causes of sample-dependent effects remain ambiguous [62–64]. Furthermore, as suggested at the end of Chapter 4, it is highly desirable to carry out RIXS experiments with high energy resolution, to directly measure the correlation time of charge and orbital order.

6 Spin-Reorientation Transitions in Magnetite

In this Chapter, we present magnetic data across the spin-reorientation transitions in magnetite, on the surface of a natural single crystal, oriented along the [110] direction, such that easy, intermediate and hard axes are all in the plane of the sample.

We intentionally write transitions, *in the plural form, because multiple phenomena, mutually related, but different, take place in the magnetic structure of magnetite. Discontinuous changes reflect the modifications of the crystal and electronic structure through the Verwey transition. Precursor effects of the Verwey transition include continuous changes in the magnetocrystalline anisotropy and magnetostriction constants. As a consequence, a spin-reorientation occurs in a temperature range of 10 K above the Verwey temperature. Whether it is a unique or multistep process is not yet clear. Our experiments provide evidence more consistent with the latter case.*

In addition, we show that the coercive field at the surface is anomalously large, compared to the data available in literature, referred to the bulk. Remarkably, it increases, instead of decreasing, on cooling from room temperature to the Verwey temperature. This is in contrast with previous measurements from bulk-sensitive probes, and the softening of the magnetocrystalline anisotropy and magnetostriction constants with decreasing temperature. We propose possible explanations of our observations, based on micromagnetics. We also discuss the results of preliminary simulations of the micromagnetic dynamics to gain better insight into the origin of the magnetic stability at the surface.

6.1 Introduction

The magnetocrystalline anisotropy of magnetite is intimately related to the Verwey transition, for different reasons. Of all possible considerations, the most obvious is that the crystal symmetry is reflected in the magnetic structure and, in particular, in the functional form of the magnetocrystalline anisotropy energy E_a. Clearly, for the cubic symmetry of the high-temperature phase, E_a is invariant upon inversion and permutation of the m_x, m_y and m_z projections of the normalized magnetization vector $\boldsymbol{m}$ along the crystal axes $x \equiv [100]$, $y \equiv [010]$ and $z \equiv [001]$. The definitions of the first and second anisotropy constants K_1 and K_2 are given in Eq. 6.1. The first term is the leading order of the series expansion of E_a over m_x, m_y and m_z.

$$E_\mathrm{a} = K_1 \left(m_x^2 m_y^2 + m_x^2 m_z^2 + m_y^2 m_z^2 \right) + K_2\, m_x^2 m_y^2 m_z^2. \tag{6.1}$$

In the low-temperature phase, the cubic axes become inequivalent. A set of orthorhombic axes rotated by -45° compared to the cubic axes is defined according to $a \equiv (x - y)$, $b \equiv (x + y)$ and $c \equiv 2z$. In addition, for the monoclinic distortion, the c axis is canted from [001] towards $[\bar{1}10]$ by about 0.2°. The expression of E_a in the monoclinic phase provided in Eq. 6.2 is more complex than its counterpart in the cubic phase. The terms in the m_a and m_b projections of $\boldsymbol{m}$ along the crystal axes a and b account for the symmetry lowering from cubic to orthorhombic. Instead, the monoclinic distortion is responsible for the additional contribution of uniaxial anisotropy about the monoclinic diagonal $[\bar{1}01]_\mathrm{m}$ (the subscript m refers to the monoclinic scheme), implied by the term $-K_\mathrm{u} m_{\bar{1}01}^2$.

$$E_\mathrm{a} = K_a m_a^2 + K_b m_b^2 + K_{aa} m_a^4 + K_{bb} m_b^4 + K_{ab} m_a^2 m_b^2 - K_\mathrm{u} m_{\bar{1}01}^2 \tag{6.2}$$

At room temperature, K_1 is negative. Accordingly, the easy, intermediate and hard axes are respectively ⟨111⟩, ⟨110⟩ and ⟨100⟩. Throughout the low-temperature phase, in the orthorhombic approximation, all anisotropy constants are positive, with large predominance of K_a [139]. Therefore, the easy, intermediate and hard axes are respectively c, b and a.

Modifications of the magnetic structure do not occur only at the Verwey transition, upon symmetry breaking. More subtle effects take place in the cubic phase. In particular, starting from about 250 K, K_1 shows an anomalous increase with decreasing temperature [60, 140]. As illustrated in Fig. 6.1(a), the sign of K_1 changes from negative to positive at a sample-dependent temperature, about 10 K above T_V, referred to as the isotropic point. Close to the isotropic point, the magnitudes of the first two terms of E_a become comparable. Depending on the sign of K_2 around the isotropic point, in the simplifying assumption of constant K_2, two different scenarios are possible. Figures 6.1(b,c) exemplify the temperature dependence of the magnetocrystalline energy in both cases. For negative K_2, the sign change of K_1 is supposed to cause a discontinuous rotation of the easy axes from ⟨111⟩ to ⟨100⟩, at a temperature lower than the isotropic point. Instead, for positive K_2, two separate, consecutive transitions are expected, namely, a continuous spin-reorientation from ⟨111⟩ to ⟨110⟩, above the isotropic

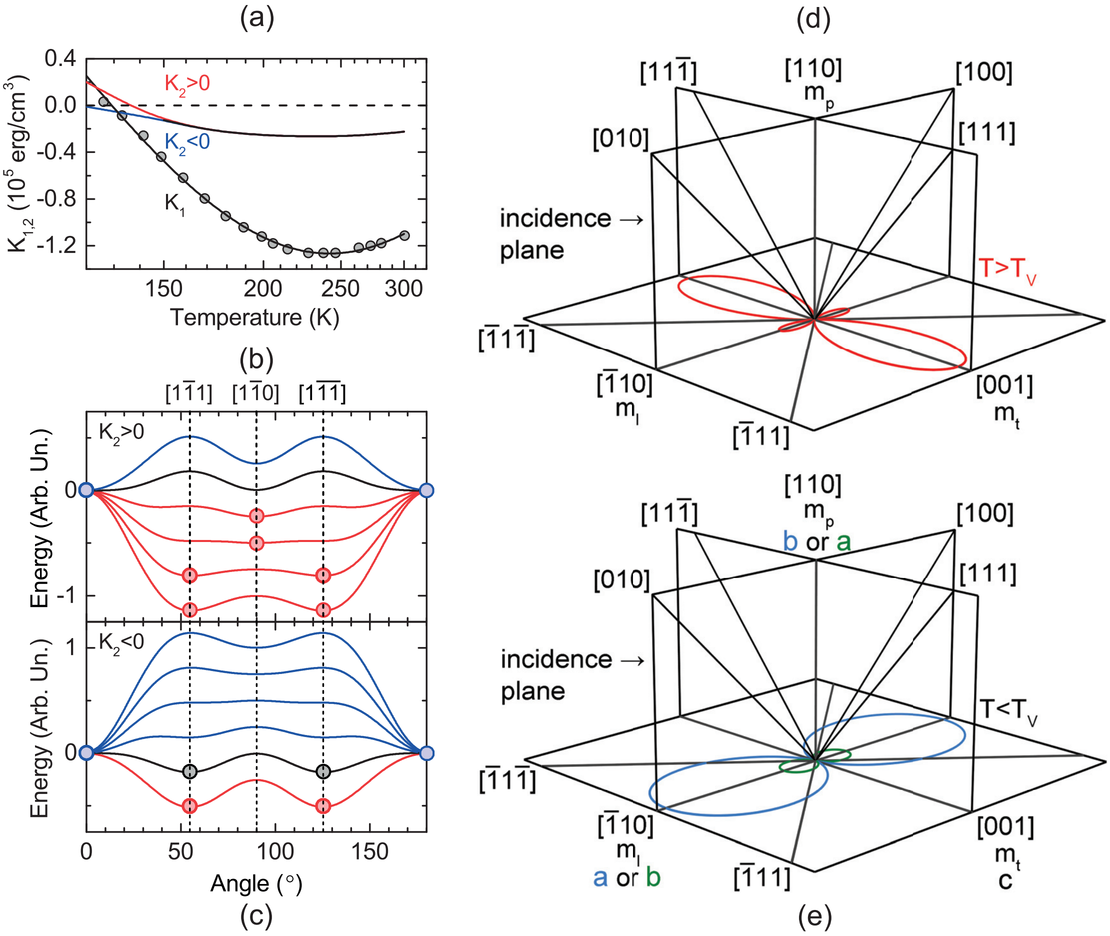

Figure 6.1 – (a) Temperature dependence of the first anisotropy constant K_1 according to the data of Ref. [59]. The line superimposed to the data points is a guide to the eye. The two possible scenarios for the second anisotropy constant K_2 are also plotted with different lines. Qualitative illustration of the temperature dependence of the magnetocrystalline anisotropy energy as a function of the angle from the [001] direction (red) above and (blue) below the isotropic point in the case of (b) positive and (c) negative K_2. Schematic representation of the experimental geometry and polar plot of the magnetocrystalline anisotropy energy in the sample surface in the (d) cubic and (e) monoclinic phase. Labels denote the orientations of the cubic and orthorhombic axes, and the projections of the magnetization. If the sample is cooled through the Verwey transition with a 310 mT field applied along the [001] direction, a unique c axis is established, but two alternative orientations of the a and b axes are possible, as shown in blue and green colors in panel (e).

point, followed by a sudden modification of the preferential directions from ⟨110⟩ to ⟨100⟩, at the isotropic point.

To date, the large uncertainty in the available measurements of the temperature dependence of K_2 [139, 141–143] leaves open the question whether a unique spin reorientation or a multistep process takes place above T_V. Reference [143] provides evidence of the latter scenario, by means of observations in real space. However, the (001) orientation of the sample does not allow any conclusion, since it gives access to the hard and intermediate axes, but not to the easy axes of the high-temperature phase.

We carried out MOKE experiments across the spin-reorientation transitions, on a sample analogous to those under study in Chapters 3–5, with $T_V = 116$ K. In contrast to Ref. [143], our technique only provides space-averaged observations. On the other hand, the surface of our sample contains all three high-symmetry directions, and in principle our technique gives access to all three components of the average magnetization in the probed region.

6.2 Experiments

The magnetite sample measured in our experiments was a natural single crystal purchased from Surface Preparation Laboratory (SPL), Zaandam, Netherlands. The sample was shaped into a 2 mm thick, 5 mm diameter disk, with axis parallel to the [110] direction, and two 1 mm deep side grooves parallel to the [$1\bar{1}0$] direction, to clamp the sample to the sample holder. The top surface of the sample was polished to optical quality. Figures 6.1(d,e) show the orientation of the sample with respect to the laser incidence plane, and the in-plane contribution of the magnetocrystalline anisotropy in each phase. The field was applied in the [001] direction. $\boldsymbol{m}$ is decomposed into projections defined according to their orientations with respect to the incidence plane. Namely, the transverse and longitudinal components, m_t and m_l, are in the sample surface, respectively, perpendicular and parallel to the incidence plane. Instead, the polar component m_p is perpendicular to the sample surface.

MOKE experiments were conducted in the temperature range from 80 K to room temperature. In different sets of experiments, we measured the hysteresis loops of m_t and of all three $\boldsymbol{m}$ components, on cycling the field between -310 and 310 mT, in 200 steps per cycle, with 400 ms acquisition time per step. The hysteresis loops of m_t were measured both with and without field cooling in a 310 mT field in the [001] direction. The application of a large enough field along one of the degenerate ⟨100⟩ directions on crossing the Verwey transition favors in energy the formation of twin domains with c axis aligned to the same direction [133]. A unique preferential axis is thereby set throughout the sample volume (see Fig. 6.1(e)). Close to, but below T_V, it is also possible to change the preferential axis to a different ⟨100⟩ direction via the application of a large enough field along the same direction [144]. To measure only m_t, the transmission axis of the analyzer was set parallel to the polarization direction of light, in p wave. Measurements of all three $\boldsymbol{m}$ components in the monoclinic phase were only carried out upon field cooling.

The experimental procedure to measure all three $\boldsymbol{m}$ components is described in the following. Let us define θ_p (θ_a) the angle between the incidence plane and the polarization direction of light (the transmission axis of the analyzer). Hysteresis loops were acquired at small, symmetric angles from extinction $\pm\varepsilon$, both in s ($\theta_p = 90°$) and p wave ($\theta_p = 0°$). Namely, for $\theta_p = 90°$ ($\theta_p = 0°$), measurements were carried out at $\theta_a = \pm\varepsilon$ ($\theta_a = 90° \pm \varepsilon$). Throughout our experiments, as a compromise between signal-to-noise ratio and ε accuracy, ε was set to 10.2°, based on the relations $I_s(\theta_a = \pm 10.2°) = I_s(\theta_a = 90°)/32$ and $I_p(\theta_a = 90° \pm 10.2°) = I_p(\theta_a = 0°)/32$, where I_s and I_p denote the reflected to incident intensity ratios, respectively, in s and p wave. To estimate the incident intensities, the intensities after the analyzer, with transmission axis parallel to the polarization direction of light, were divided by the Fresnel coefficients, $|r_{ss}|^2$ and $|r_{pp}|^2$, respectively, in s and p wave.

The ε dependence of I_s and I_p given in Eq. 6.3 is derived based on Fresnel scattering matrix formalism, under the assumption of negligible terms of the second order in m_t, m_l and m_p. The real parameters denoted with capital letters depend on the Fresnel coefficients according to the definitions given in Eqs. 2.33–2.39. The computation details are provided in Section 2.4. Approximate estimates of m_t, m_l and m_p were calculated according to Eq. 6.4, starting from sums and differences of I_s and I_p for opposite ε, $\Sigma I_p \equiv I_p(\theta_a = 90° - \varepsilon) + I_p(\theta_a = 90° + \varepsilon)$, $\Delta I_p \equiv I_p(\theta_a = 90° - \varepsilon) - I_p(\theta_a = 90° + \varepsilon)$ and $\Delta I_s \equiv I_s(\theta_a = \varepsilon) - I_s(\theta_a = -\varepsilon)$.

$$\begin{cases} I_p(\theta_a = 90° \pm \varepsilon) = (A + B m_t)\sin^2\varepsilon \mp \left(C m_l + D m_p\right)\cos\varepsilon\sin\varepsilon \\ I_s(\theta_a = \pm\varepsilon) = E\sin^2\varepsilon \pm \left(F m_l + G m_p\right)\cos\varepsilon\sin\varepsilon \end{cases} \tag{6.3}$$

$$\begin{cases} m_t = \Sigma I_p \cdot \left(2B\sin^2\varepsilon\right)^{-1} \\ m_l = \left(G\Delta I_p - D\Delta I_s\right)\cdot[2\,(CG - DF)\sin\varepsilon\cos\varepsilon]^{-1} \\ m_p = \left(C\Delta I_s - F\Delta I_p\right)\cdot[2\,(CG - DF)\sin\varepsilon\cos\varepsilon]^{-1} \end{cases} \tag{6.4}$$

6.3 Results

In our multidomain sample, both the magnitude and the direction of the magnetization change with field. For completeness, Figs. 6.2(a,b) show perspective views of the magnetization paths in our experimental geometry. For illustrative purposes, data within the temperature range of the magnetic transitions (130 K) are compared with reference data above (145 K) and below the spin reorientations (84 K). Above T_V, close to the coercive field of m_t, the total magnetization takes on the smallest magnitude, concomitant to the largest angle to the sample surface. Figure 6.2(c) shows the corresponding ratio between the magnitude of the in-plane component of the magnetization $(m_t^2 + m_l^2)^{1/2}$ and the total magnitude of the magnetization m. At 130 K, a pronounced rotation of the magnetization takes place out of the plane, responsible for a sudden, significant decrease in the minimum ratio between $(m_t^2 + m_l^2)^{1/2}$ and m. Apart from that, throughout the temperature range of our measurements, the minimum ratio between $(m_t^2 + m_l^2)^{1/2}$ and m never decreases below 2/3. Therefore, in the following, focus is

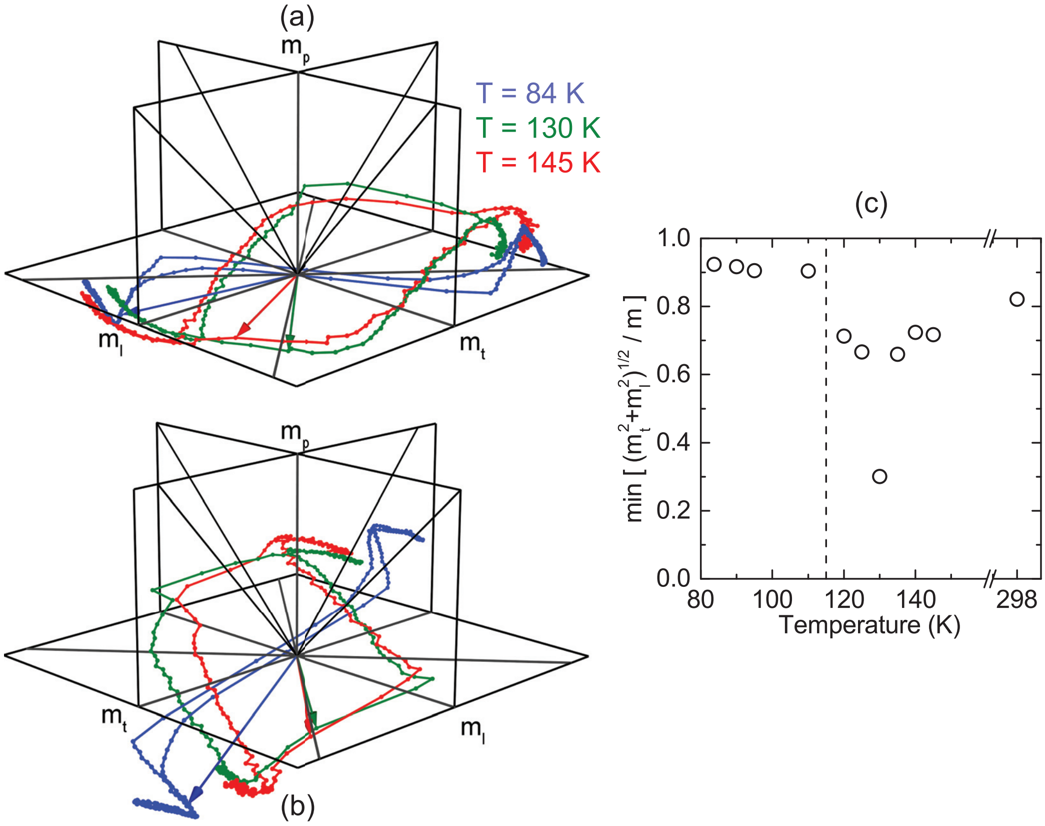

Figure 6.2 – (a,b) Experimental reconstruction of the magnetization trajectories in three dimensions, from two different perspectives, with the external field varying between -310 and 310 mT, at 84, 130 and 145 K. Vectors represent the magnetization in correspondence of the minimum ratio between the projection of the magnetization on the sample surface $(m_t^2 + m_l^2)^{1/2}$ and the total magnitude of the magnetization m. Black lines correspond to the same high-symmetry directions as in Figs. 6.1(d,e). (c) Temperature dependence of the minimum $(m_t^2 + m_l^2)^{1/2}$ to m ratio between 84 K and room temperature.

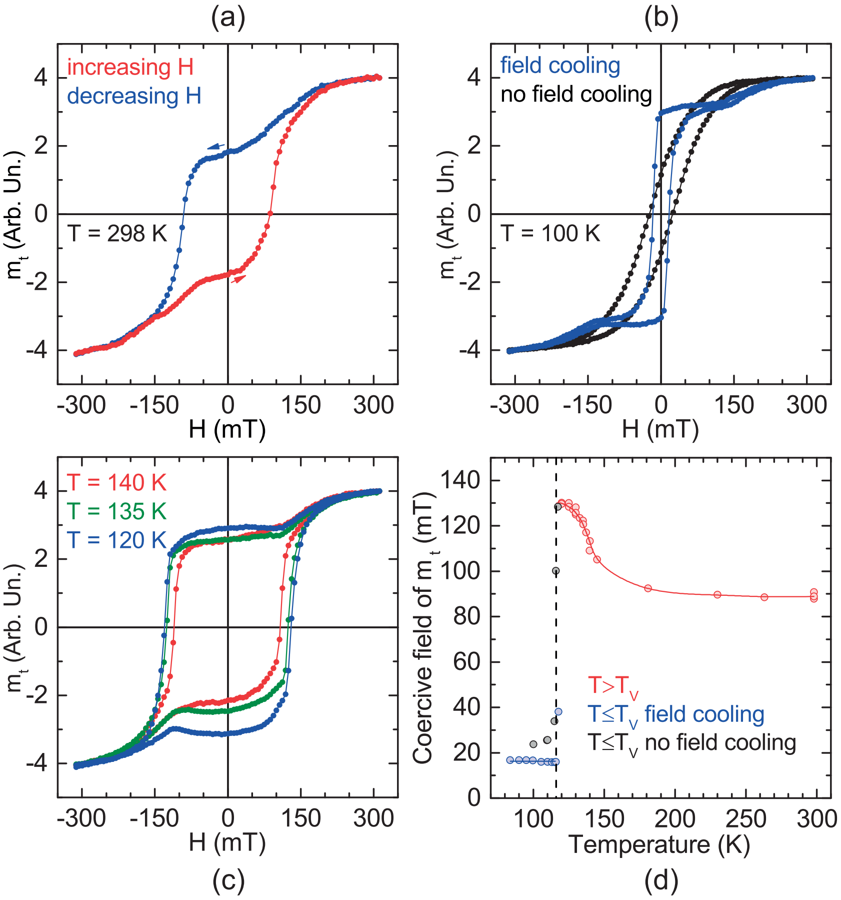

Figure 6.3 – Hysteresis loops of the transverse projection of the magnetization at (a) room temperature, (b) 100 K and (c) between 120 and 140 K. In panel (b), blue and black colors denote measurements, respectively, with and without 310 mT field applied on cooling across T_V. (d) Temperature dependence of the coercive field between 84 K and room temperature, with the same color coding as panel (b) to indicate measurements in the presence or in the absence of field cooling. Colored lines are guides to the eye. A vertical dashed line denotes T_V.

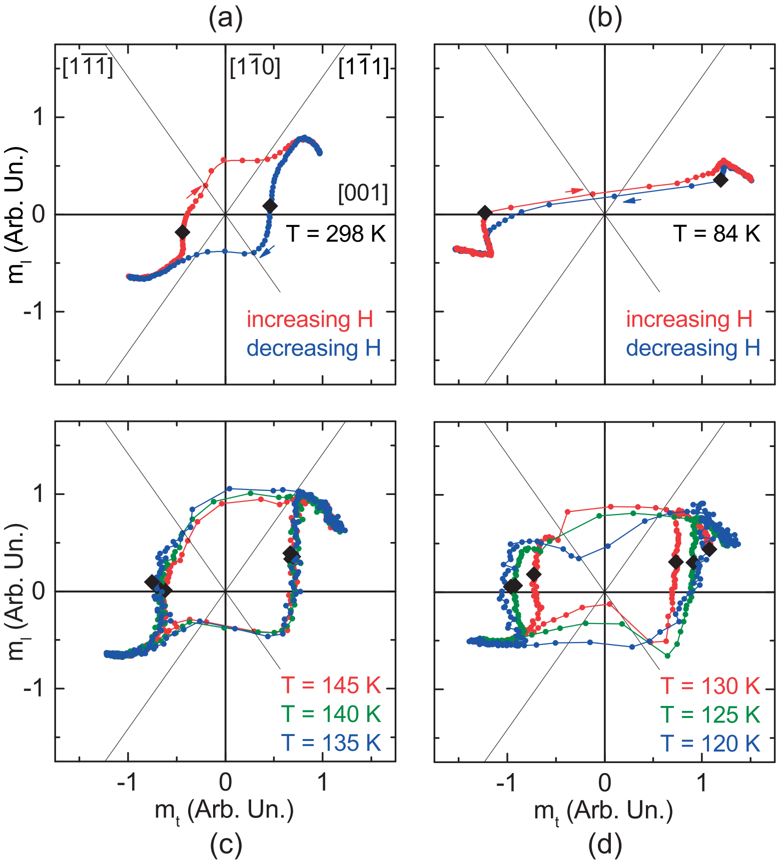

Figure 6.4 – Experimental reconstruction of the magnetization trajectories projected on the sample surface, on increasing and decreasing field between -310 and 310 mT (respectively, in red and blue colors, in panels (a) and (b)), at (a) room temperature, (b) 84 K and (c,d) between 120 and 145 K. Black diamonds mark the remanent magnetization in the sample surface. The high-symmetry directions are labeled in panel (a).

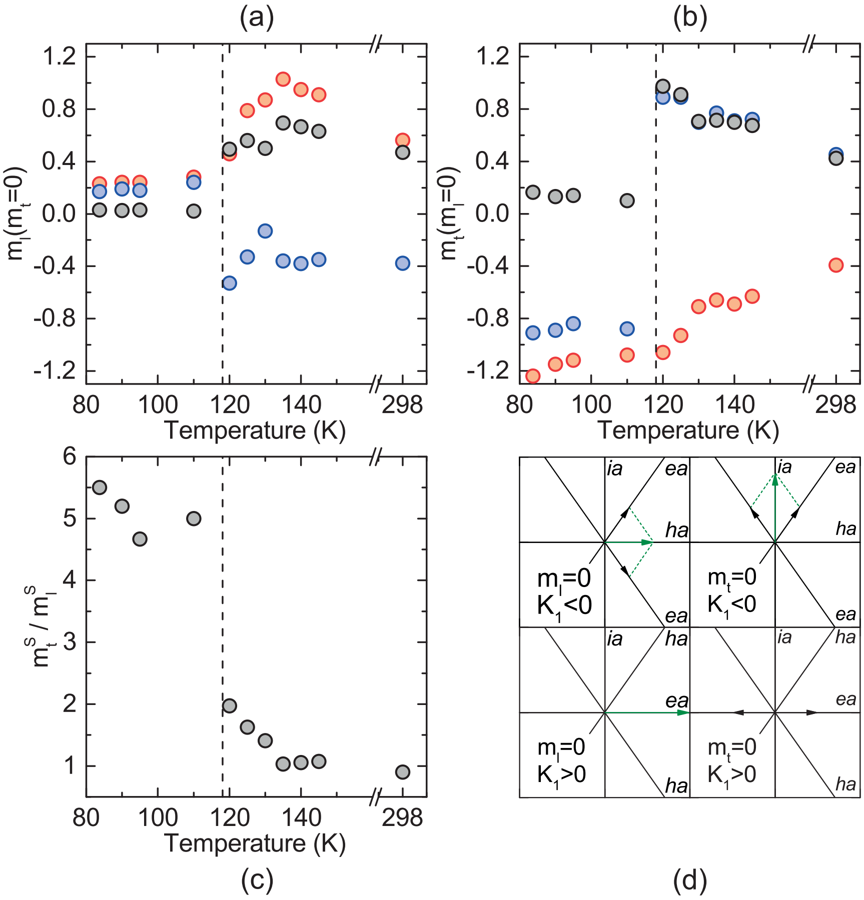

Figure 6.5 – Temperature dependence of (a) m_l and (b) m_t, respectively, for $m_t = 0$ and $m_l = 0$, on increasing (m^+, red symbols) and decreasing field (m^-, blue symbols) between -310 and 310 mT. The symmetric component, $m^S = \left|m^+ - m^-\right|/2$, is plotted with black symbols. (c) Temperature dependence of the ratio between the symmetric components of m_t and m_l. A vertical dashed line denotes T_V. (d) Schematic representation of the simplest two- or single-domain configuration, with magnetizations aligned to the easy axes, and zero m_l or m_t, for positive or negative K_1 and zero K_2. Black and green colors denote the magnetization in each domain and the sum vector, respectively. Easy, intermediate and hard axes are labeled *ea*, *ia* and *ha*, respectively.

placed on the magnetization paths in the sample surface.

Figures 6.3(a–c) show the hysteresis loops of the transverse projection of the magnetization across the spin reorientations. Starting from room temperature, the data display an anomalously large coercivity, above 90 mT, which further increases on cooling down to T_V. At the same time, the hysteresis loops progressively become more squared. As illustrated in Fig. 6.3(b), in the monoclinic phase, different behaviors are observed, depending on whether or not the temperature is lowered below T_V via field cooling. Figure 6.3(d) shows the temperature dependence of the coercive field of m_t across the spin reorientations, both with and without field cooling. To improve the statistics, measurements of all three $\boldsymbol{m}$ components and m_t alone are combined together. The consistency of the two data sets further confirms the reliability of our experimental procedure to measure of all three $\boldsymbol{m}$ components. After a plateau without any meaningful change, the coercive field increases from 92 to 105 mT in between 180 and 145 K. Remarkably, nearby the isotropic point, it further grows to 130 mT at a high rate. In contrast, the onset of the monoclinic phase coincides with a drop in the coercive field by one order of magnitude. No additional modification is observed below T_V in the presence of field cooling. Instead, in the absence of field cooling, rounding effects set in near the critical region.

Figure 6.4 shows the projection of the magnetization trajectories on the sample surface across the spin reorientations. In particular, Figs. 6.4(c,d) focus on the temperature range preceding the Verwey transition, between 120 and 145 K. Data points are less dense in correspondence of large changes of m_t between values of opposite sign, around the coercive field of m_t. Anomalies are evident both above and below T_V. For instance, in the monoclinic phase, on increasing field between 0 and 130 mT, the magnetization moves away from the [001] direction, although in the presence of field cooling it is supposed to become the easy axis (see Fig. 6.4(b)). For higher fields, the component aligned to the [001] direction gradually increases, as reflected in the S shape of the hysteresis loop (see Fig. 6.3(b)). The asymmetry of the magnetization path in the sample surface with respect to the origin also eludes simple explanations. The uncertainty on the alignment of our sample (some degrees), the presence of imperfections, such as misaligned crystallites and impurities, and the contribution of the shape anisotropy from the side grooves perpendicular to the [001] direction are among the most probable causes for the above anomalies.

Noticeable features in our data are also the increase in the area delimited by the magnetization projection in the sample surface and the occurrence of two different regimes in the pre-transition region. Namely, the data between 135 and 145 K are superposable (see Fig. 6.4(c)). Instead, distortions in the shape of the magnetization path develop between 120 and 130 K (see Fig. 6.4(d)). The possible relations between the above observations and the spin-reorientation transitions will be examined in the next Section.

6.4 Discussion

6.4.1 Spin-Reorientation Transitions

The ensemble of our results is more consistent with the scenario of a positive K_2 and a multistep process, than that of a negative K_2 and a unique spin reorientation. Both the Verwey temperature and the isotropic point change as function of impurity content and departure from ideal stoichiometry. According to typical values and a systematic study on the effects of nonstoichiometry [60], for samples that preserve a Verwey transition of the first order, the difference between the above critical temperatures is about 10 K. The onset of important anomalies in the temperature dependence of our results, 130 K, is 4 K above our approximate estimate of the isotropic point, $T_V + 10$ K = 126 K. Indeed, at 130 K, the magnetization path suddenly changes (see Figs. 6.4(c,d)) and, in particular, at the coercive field of m_t, the magnetization rotates out of the plane (see Fig. 6.2). The occurrence itself of effects starting from above the isotropic point, rather than below it, points to the scenario of two separate, consecutive transitions. Besides, in that case, a magnetization trajectory out of the plane, with preferential alignment to the [110] direction, would not be surprising, but the natural consequence of the change of the easy axes from ⟨111⟩ to ⟨110⟩, in the first step of the spin reorientation.

In order to proceed to more quantitative considerations, let us compute $m_l(m_t = 0)$ $(m_t(m_l = 0))$, defined as the longitudinal (transverse) magnetization component in correspondence of zero transverse (longitudinal) counterpart, both for increasing and decreasing field. Let us also separate the above quantities into symmetric and asymmetric contributions, m_l^S (m_t^S) and m_l^A (m_t^A), according to the general definition $m^{S,A} = \left| m^+ \mp m^- \right| / 2$, where m^+ (m^-) denotes the magnetization component under consideration for increasing (decreasing) field. $m_l(m_t = 0)$ and $m_t(m_l = 0)$, together with m_l^S and m_t^S, are plotted against temperature in Figs. 6.5(a,b). Figure 6.5(c) shows the temperature dependence of the ratio between m_t^S and m_l^S.

To rationalize our results, let us consider the simplest possible model, comprised of either one or two domains, with magnetizations oriented along the easy axes in the sample surface, such that the total longitudinal or transverse magnetization is equal to zero. Figure 6.5(d) depicts the different configurations which correspond to opposite signs of K_1. For negative K_1, there are two degenerate easy axes, $[1\bar{1}1]$ and $[1\bar{1}\bar{1}]$. The conditions $m_l = 0$ and $m_t = 0$ are satisfied in the presence of two domains with magnetizations at respectively 109.5° and 70.5° angles. Instead, for positive K_1, there is a unique easy axis, [001]. Zero longitudinal (transverse) total magnetization requires the occurrence of a single domain (two domains with opposite magnetizations) aligned to [001]. At 130 K, m_l^S suddenly decreases, in the absence of concomitant changes of m_t^S, as a result of the magnetization path upon m_t reversal, here interpreted as the first stage of the transformation, comprised of a change of the easy axes from ⟨111⟩ to ⟨110⟩. Below 130 K, the spin reorientation progresses towards more and more favorable ⟨100⟩ directions. Both m_t^S and m_l^S change, with a gradual increase in the m_t^S to m_l^S ratio, which mirrors the increase in the aspect ratio of the magnetization trajectory in

Sample	H_c / mT	Technique	Ref.
Thin films on $SrTiO_3$, $BaTiO_3$ and MgO	39, 31 and 19	MOKE	[145]
70 μm grain, synthetic	14	MOKE	[146]
2.7, 16.6 and 65 μm grains, natural	13, 7 and 3	Magnetometry	[147]
12.5, 35 and 125 μm grains, natural	7.3, 2.6 and 1.7	Magnetometry	[148]
230 μm grain, natural	3.2	Magnetometry	[149]
1.7 and 1.5 mm single crystals, natural	0.18 and 0.11	Magnetometry	[150]

Table 6.1 – Typical values of surface and bulk coercive field from respectively MOKE and magnetometric experiments on samples of different origin and size. All values refer to room temperature.

the sample surface. Larger m_t^S to m_l^S ratios are a direct consequence of the crossover from negative to positive K_1 exemplified in our trivial model. Finally, below T_V, the removal of the degeneracy and the sizable increase of the anisotropy constants cause the predominant orientation of the magnetization in the [001] direction throughout the hysteresis loops.

6.4.2 Anomalous Coercive Field

The penetration depth of light at our 1.6 eV photon energy and 60° incidence angle is about 60–80 nm, equivalent to 70–100 unit cells in the cubic phase. Only the surface magnetization contributes to our measured H_c, which is thus referred to as *surface* H_c. Table 6.1 summarizes the dependence of H_c on sample size and origin, and technique sensitivity. It is clear that our measured H_c is from one to three orders of magnitude larger than the typical values of the *bulk* H_c from magnetometric measurements. Indeed, in 1–100 μm sized grains from crushed and sieved crystals both of natural and synthetic origin, H_c is on the order of 1–10 mT [147–149, 151], and in 1 mm sized rocks of natural origin, H_c does not exceed 0.2 mT [150]. In the same measurements, in contrast to our observations, H_c sizably decreases, rather than increasing, on cooling from room temperature to T_V.

H_c values closer to ours, yet a factor 2–4 lower, were measured by MOKE on magnetite films, for instance, in Ref. [145], on $SrTiO_3$, $BaTiO_3$ and MgO substrates. In the same study, H_c ranges between 19 and 39 mT, and the different values for different substrates were related to the surface roughness, in turn, regarded to as a consequence of misfit strain. An anomalous, intrinsic property of magnetite films, independent of substrate and deposition process, is that the magnetization does not saturate in fields as high as 7 T, in contrast to the values of the anisotropy constants measured for the same films [152]. Proposed explanations account for the formation of antiphase boundaries during the deposition processes [153].

In general, the relation between magnetic stability and nonidealities, along with the temperature dependence of the micromagnetic configuration in real materials, are puzzling problems, whose solution requires numerical computations. In the following, to understand the origin of H_c, let us start from simple considerations on the different contributions to the magnetic energy. Shape, magnetocrystalline and magnetoelastic anisotropy all compete to determine preferential directions of magnetic order. In the presence of high surface to volume ratio, demagnetization effects dominate the micromagnetic configuration. Instead, in large enough samples with multiple domains, either or both terms of magnetocrystalline and magnetoelastic anisotropy prevail. In the absence of external forces, magnetoelastic anisotropy arises from the coupling between the magnetization and the internal stress, namely, slowly- and rapidly-varying components, respectively referred to as macrostress and microstress. Macrostress modifies the average value of the effective anisotropy constant on a macroscopic scale. Instead, microstress produces local fluctuations in the effective anisotropy which govern the dynamics on a microscopic scale. The crystal defects able to pin the domain walls are the most common origin of microstress. The causes for the energy barriers to the propagation of the domain walls also include the presence of nonmagnetic inclusions and any departure of the surface morphology from an ideal plane.

Let us take into account the size dependence of the typical values of bulk H_c in table 6.1. An immediate observation is that bulk H_c decreases with increasing size, a characteristic behavior of magnetic samples, which goes under the name of Brown's paradox [154]. In large enough samples, magnetization reversal progresses via nucleation and motion of domain walls. The presence of imperfections in real crystal is known to change the local activation energy for the reversal of the magnetic moments. Depending on their nature, they can either decrease or increase the field required for nucleation and motion of domain walls. In the former case, they serve as nucleation centers for domain walls, at applied fields lower than the nominal anisotropy field. Instead, in the latter case, they pin the motion of domain walls, and thus cause the persistence of reversed domains, even at high applied fields. Surfaces are the most natural sources of imperfections which act as potential nucleation centers of domain walls. Therefore, a general, qualitative explanation of Brown's paradox is the following. The larger the surface area of a magnetic sample, the higher the probability that it contains imperfections which give rise to domain walls at low applied fields. Note, however, that the shape of the hysteresis loop depends on the total distribution of imperfections. Characteristics independent of size, for instance, the degree of surface roughness, might be crucial. More rigorous considerations on the size dependence of bulk H_c are only possible in systematic studies on ensembles of magnetic particles with the same characteristics [155].

Hodych first proposed that among the different contributions to the magnetic energy discussed in the previous paragraphs, the magnetoelastic anisotropy due to the internal stress plays the most important role in the magnetic stability of magnetite [156]. The condition for the nucleation of domain walls is that the magnetic energy for an external field equal to bulk H_c is stored in the magnetoelastic energy, according to the approximate relation $H_c M_s = \lambda\sigma$. Here, λ is a suitable magnetostriction constant, given by a linear combination of λ_{111} and λ_{100}, and σ is the internal stress. In reasonable agreement with the above equation, the temperature dependence of bulk H_c reflects that of λ / M_s, with particular reference to the softening of λ_{111} between room temperature and T_V.

The outcome of our and previous MOKE measurements, respectively, on a natural single crystal and films [145], appears to contradict Hodych's considerations. Surfaces and interfaces are important sources of crystal defects, and themselves constitute a type of macroscopic imperfection. However, in contrast to the consequences of internal stress in Hodych's picture, surface H_c is larger, instead of smaller, than the nominal anisotropy field in magnetite, equal to 31 mT [154], and it hardens, rather than softening, on cooling from room temperature to T_V.

Different explanations are possible, based on basic notions of micromagnetics. The main consequence of a continuity solution at the surface is an additional cost of magnetostatic energy, whenever the local magnetization $\boldsymbol{M}$ is not lined up with the surface itself. The source of the demagnetizing field at the surface or surface density of magnetic charge is equal to $\boldsymbol{M} \cdot \boldsymbol{n}$, with $\boldsymbol{n}$ the surface normal. Clearly, the type of defect needful to rationalize our observations is supposed to increase the energy barrier for magnetization reversal, and thereby oppose to nucleation and motion of domain walls. Pits are textbook examples of surface features which counteract the reversing field [154]. The distribution of magnetic charges on the inner walls of pits generates demagnetizing fields parallel (antiparallel) to the magnetization (the reversing field). The action of the demagnetizing fields is localized at the bases of pits, negligible in bulk measurements, but not for probes sensitive only to the surface, such as MOKE. In analogy to our considerations, in Ref. [145] it has been proposed a correlation between surface H_c of magnetite films and roughness, which in turn is proportional to the difference between the lattice constants of magnetite and substrate. The reported values of root mean square (rms) roughness and surface H_c are respectively in the ranges 0.25–2.5 nm and 20–40 mT. According to SPL's specifications, the rms roughness of the top surface of our sample is about 30 nm, from one to two orders of magnitude greater than in Ref. [145]. Therefore, our H_c values, from 2 to 4 times larger compared to Ref. [145], are compatible with a direct proportionality between surface H_c and roughness. In any case, for more reliable considerations, further experiments are needful, to measure the dependence of surface H_c on surface morphology and, in particular, rms roughness after different polishing steps, characterized by means of microscopy techniques.

6.5 Preliminary Simulations

For a complementary analysis of the possible origin of the anomalous surface H_c, we carried out preliminary simulations of the micromagnetic dynamics, in the Object Oriented Micromagnetic Framework (OOMMF) [157]. We set up models of the cubic phase, with suitable values of the material parameters, namely, exchange stiffness $A = 12 \times 10^{-12}$ J/m and saturation magnetization $M_S = 5 \times 10^5$ A/m. The simulation volume was divided into a grid of cubic cells. Magnetic force microscopy (MFM) is able to provide experimental estimates of the domain sizes and the magnetization profiles across the walls. In particular, according to MFM measurements on the (110) surface of a single crystal shaped into a slab of 1 mm thickness, the surface area per domain is on the order of 10^3 μm^2, and the coarse and fine features of

Model	Bulk		Top surface		Bottom surface	
	m_x	m_y	m_x	m_y	m_x	m_y
6.6(a)	0	0	-0.297	-0.081	-0.330	0.063
6.6(b)	0	0	0.045	-0.007	-0.335	-0.028
6.6(c)	0	0	0.081	-0.009	-0.166	-0.176
6.7(a)	0.001	0	-0.216	-0.006	-0.217	0.007
6.7(b)	0.011	0.002	-0.096	-0.098	-0.097	-0.106
6.7(c)	0	0	-0.185	0.016	-0.247	0
6.7(d)	0.005	0.005	-0.295	-0.065	-0.232	-0.198
6.8(a)	0.009	0	0.027	-0.024	-0.134	0.030
6.8(b)	0.004	0.007	0.073	0.253	-0.233	0.193

Table 6.2 – Remanences integrated over the entire bulk, and the top and bottom layers of the magnetic body. The values are the ratios to the saturation magnetization. The strong shape anisotropy forces the magnetization in the plane of the magnetic body, with the consequence that all z components are negligible.

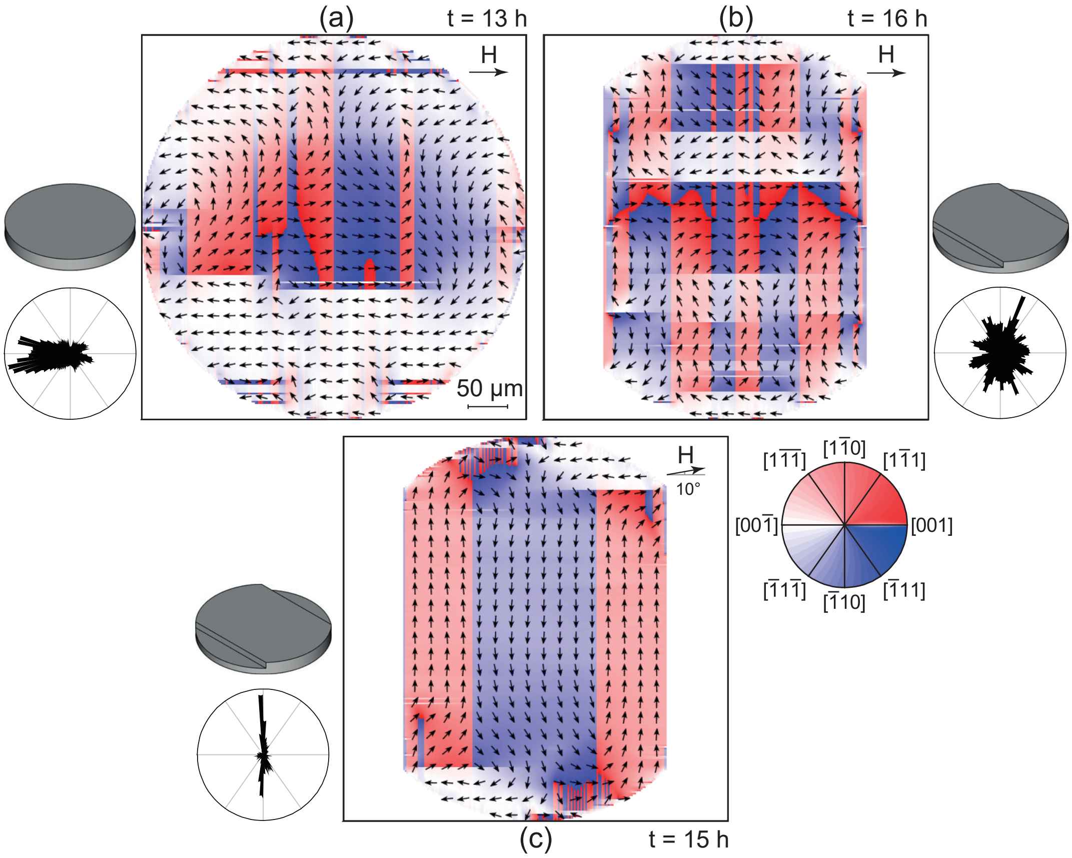

Figure 6.6 – Color-coded maps of the simulated magnetization at the top surface, in the absence of magnetocrystalline anisotropy, both (a) without and (b,c) with side grooves. Arrows at the top right corners indicate the field direction. Sketches of the simulation geometry and polar histograms of the magnetization at the top surface are displayed along the margins. The computation time is specified for each simulation.

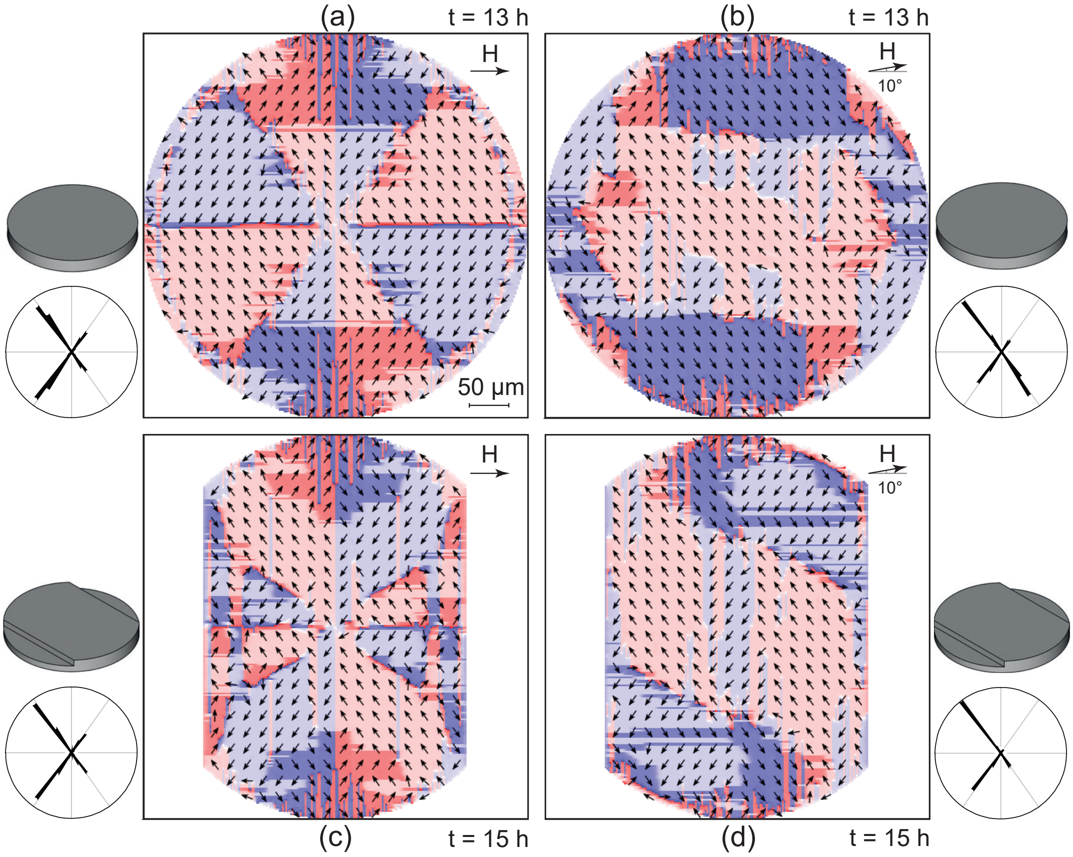

Figure 6.7 – Color-coded maps of the simulated magnetization at the top surface, in the presence of magnetocrystalline anisotropy, both (a,b) without and (c,d) with side grooves.

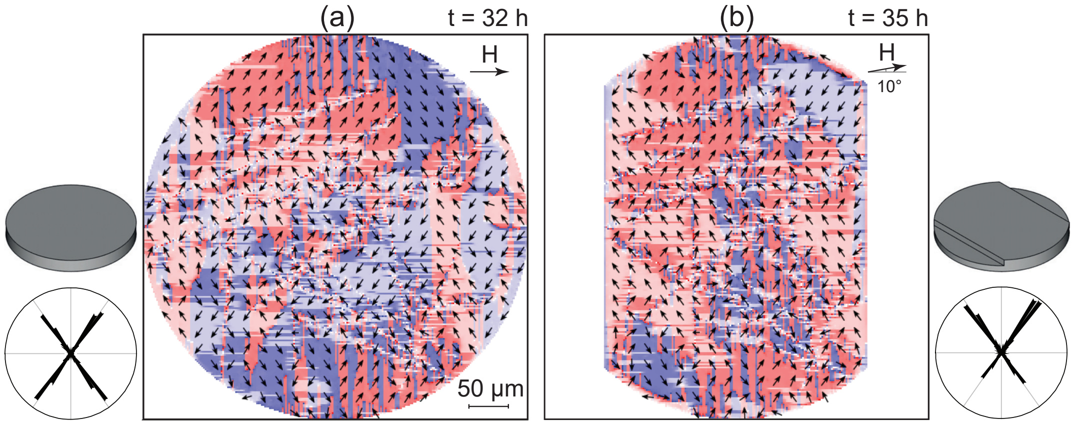

Figure 6.8 – Color-coded maps of the simulated magnetization at the top surface, in the presence of magnetocrystalline anisotropy and randomly oriented line defects, both (a) without and (b) with side grooves. Here and in Fig. 6.7, arrows at the top right corners indicate the direction of the external field. Sketches of the simulation geometry and polar histograms of the magnetization at the top surface are displayed along the margins. The computation time is specified for each simulation. The color coding is the same as Fig. 6.6.

the walls extend over approximate lengths of respectively 3 and 0.2 μm [158]. Based on that, we chose compromise values for cell and grid size, to reproduce a large enough ensemble of domains and the essential structure of the walls, in reasonable computation times on the order of tens of hours. Namely, our simulation geometry consists of a disk of 478 μm diameter and 50 μm thickness, with cells of 1 μm side and, therefore, a total number of cells of about 9×10^6.

The first purpose of our simulations is to understand under what conditions the remanence at the top surface is nonzero, and tune them to reproduce the square hysteresis loops in our observations, *i.e.* large remanence at the top surface. To compute the remanence in the shortest possible time, our simulations involved two stages. In the first stage, starting from a random micromagnetic configuration, the external field was set to a large value of 320 mT, in the [001] direction. In the second stage, the external field was switched off. The micromagnetic configuration at equilibrium was calculated by the minimization of the total energy, with the conjugate gradient method available in OOMMF. We set a stop condition of 10 A/m on the maximum $|\boldsymbol{m} \times \boldsymbol{H_e} \times \boldsymbol{m}|$, where $\boldsymbol{H_e}$ is the effective field, which is given by the sum of the external, demagnetizing, exchange and anisotropy fields.

First, we addressed the effect of the shape anisotropy alone (see Fig. 6.6). Then, we studied the consequences of the magnetocrystalline anisotropy (see Fig. 6.7). In particular, we assumed cubic symmetry, with axis orientation identical to our experimental geometry, the value of the first anisotropy constant at room temperature, $K_1 = -1.1 \times 10^4$ J/m^3 [59], and zero second anisotropy constant. Finally, we introduced a random distribution of 20 line defects at the top surface, with 20 μm length, 1 μm thickness and 20 μm depth, associated with an anomalous effective anisotropy constant, equal to 500 times K_1 (see Fig. 6.8). The number of line defects was chosen so that, at most, the surface is divided into regions of area comparable to the domains observed via MFM. In each of the above cases, simulations were repeated in the presence of side grooves, with the same relative width and depth as in our sample, to better reproduce the effect of the shape anisotropy, and with external field at 10° from the [001] direction. This angle was chosen based on the maximum misalignment possible for a sample mounted on our sample holder.

The remanences integrated over the entire bulk, and the bottom and top layers of the magnetic body are summarized in table 6.2. In the absence of magneticrystalline anisotropy (see Fig. 6.6), the bulk remanence is zero. In the presence of magnetocrystalline anisotropy (see Figs. 6.7(a,c)), the bulk remanence is considered negligible, since it does not exceed 1‰ of the saturation magnetization. If in addition line defects or a field component in the $[1\bar{1}0]$ direction are introduced (see Figs. 6.7(b,d) and 6.8), then the bulk remanence is not negligible anymore, and ranges between 0.7 and 1.1% of the saturation remanence.

In the presence of magnetocrystalline anisotropy, in the simulations without line defects, the remanences at the top and bottom surfaces are similar, and opposite to the bulk remanence, regardless of whether or not side grooves are present. The external field in the x direction favors configurations with opposite y components and same signs of the x components, and therefore the formation of 109.5° domain walls (see Fig. 6.7). Instead, 70.5° domain walls are present only in two flux closure configurations within the surface, at opposite positions with respect to the axis of the disk, and with opposite chirality. At both surfaces, the net magnetization prefers to orient antiparallel to the external field; conversely in the inner layers. This holds true both for external field in the [001] direction and at 10° from the [001] direction. In the latter case, the surface is divided into three main regions of large area. In the simulations with line defects, the remanences at the top and bottom surface are different. The configuration at the bottom surface, free from defects, is analogous to the simulations without line defects. Instead, the sign of the remanence at the top surface, where line defects are located, is the same as the external field.

Overall, our preliminary simulations show that demagnetization effects are responsible for large remanence at the surface, compared to the bulk, with magnetization oriented such that the field lines close within the magnetic body. If the external field is in the [001] direction, then all easy axes are equivalent, and for the effective formation of flux closure configurations, the bulk remanence is negligible. However, the perfect alignment of the external field to the crystal axes is never possible in reality. In addition, surface domains oriented in the direction of the external field are preserved only if line defects able to pin the domain walls are introduced. In the presence of side grooves, whenever the remanence in the bulk or at the top surface is meaningful and with the same sign as the external field, m_y is comparable of larger than m_x, owing to the shape anisotropy. None of the effects accounted for in our preliminary simulations is able to reproduce our data, with particular reference to the characteristics of the remanence at the surface. This suggests that the surface roughness, here disregarded, may in fact play the most important role in the magnetic stability at the surface.

Further simulations on a larger scale are needful for a twofold reason. On one hand, in the presence of edges, the dipolar anisotropy does not depend only on the shape of the magnetic body, but also on its absolute size, with particular reference to edge effects themselves. The surface to volume ratio of our models is too large compared to reality, with the result that the ranges of edge and surface effects in the bulk are overestimated. On the other hand, our experiments are sensitive to the magnetization within a thickness of 100–200 nm, one order of magnitude smaller than the cell size of our simulations. It is needful to decrease the cell sizes in multiple layers below the top surface, not only to account for our probing range, but also to simulate the effects of surface roughness.

7 Clean Transfer of Graphene

Among its widespread applications in industry, magnetite played an important role at the dawn of the information age, in the 1940s. Indeed, in early commercial tapes for magnetic recording, often, magnetite particles were dispersed in organic binders on suitable supports. However, magnetite is not stable enough to preserve information for a long time, since in ambient conditions it is progressively oxidized to hematite. Soon, ferric iron oxides replaced magnetite in most devices based on particulate media. Further developments in information technology were responsible for the introduction of magnetic disks based on cobalt alloys in the late 1950s. Thereafter, they became the most popular and cost-effective devices for the permanent storage of large data sets.

Nowadays, data science is constantly gaining importance in diverse disciplines, for the relentless increase in the rate of data generation, processing and storage, and the growing significance of data exchange in human interactions. This motivates continuous efforts to improve information density in hard disk drives. The transition from longitudinal to out-of-plane recording represented an important step forward to combine high thermal stability, writeability and signal-to-noise ratio in magnetic media. To enable a further increase in information density, from Tbits to hundreds of Tbits per square inch, novel solutions are being developed, such as heat-assisted and bit-patterned magnetic recording.

The parallel project discussed in this Chapter is intended to facilitate the route toward the clean transfer of graphene in ultrahigh vacuum. This allows the fabrication of nanostructures for data storage comprised of self-assembled arrays of atom clusters alternated with single-layer graphene. By that, atom clusters are piled up into vertical nanopillars, which meet the specifications for ultrahigh density bit-patterned magnetic recording.

7.1 Introduction

The storage and processing of information represents the cornerstone of today's technology. The demand for increasing information density in data storage fuels basic research on alternative solutions to the current recording media. In commercial hard disk drives, to overcome the uneven distribution of the magnetization directions, one bit is associated with the average magnetization of multiple grains [159]. Instead, in prototypes fabricated via lithography, there is a one-to-one correspondence between bits and grains [160]. State-of-art devices consist of bit arrays with 1 Tbit in^{-2} areal density. However, they still suffer from cross-talk effects and expensive manufacturing.

The assembly of vertical nanopillars into superlattices holds promise for a further improvement of the density limit by two orders of magnitude. The atom clusters that compose the nanopillars are supposed to behave as Ising superspins, aligned out-of-plane, to reduce the mutual dipolar interactions, and stable against thermal fluctuations at room temperature for at least 10 years. Quantitatively speaking, this implies a 1.2 eV energy barrier for magnetization reversal, equivalent to a cluster size of more than 10^3 atoms, even if magnetically hard alloys are used, or interline and interface effects are combined [161–166]. To preserve nanometer spacing, and thus avoid any possible coalescence and cross-talk effect, atoms are supposed to self-assemble into clusters with high aspect ratio in the plane perpendicular to the surface.

Remanence at room temperature was experimentally demonstrated for an array of Co nanopillars buried in Au(111) [167]. Co nanostructures were fabricated starting from the self-assembly of 2 ML thick Co nanodots on Au(111). Seed Co nanodots nucleate at the elbow sites of the Au(111) herringbone reconstruction [168]. The deposition of 4 ML Au and submonolayer Co results in the propagation of the built-in pattern in the vertical direction by means of double layer exchange between incoming Co atoms and surface Au atoms. The study being discussed is an important proof of principle. However, the lateral order of the Co clusters, restricted to a range of about 100 nm, is unsuitable for applications. Moreover, the measured remanence is far below saturation, for the occurrence of antiferromagnetic dipolar coupling in pillar chains.

A possible solution to assemble ordered clusters with the characteristics discussed in the foregoing is to scale down to the nanometer range current techniques for the fabrication of nanowires via evaporation onto nanoporous templates. Potential matrices are comprised of anodic aluminum oxide [169] and bock copolymers [170], characterized by a high density of nanopores, ordered on the long range. However, typically, the diameter and center-to-center distance of the nanopores are comparable, and both above 10 nm. Thus, again, antiferromagnetic dipolar coupling would probably occur among the atom clusters thereby produced.

A more promising solution is the self-assembly of nanostructure superlattices on the moiré pattern of single-layer graphene (SLG) on close-packed metal surfaces with suitable lattice mismatch. In particular, the moiré pattern of SLG on Ir(111), with 2.54 nm periodicity, provides an excellent template for self-assembly, with particular reference to the structural coherence, on the micrometer scale, and the narrow distribution of the cluster sizes [171–173]. Ir has a

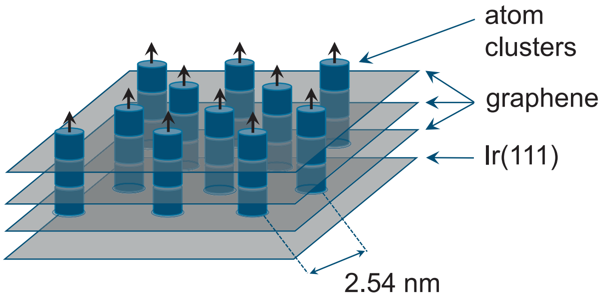

Figure 7.1 – Pictorial representation of a *mille-feuille* structure comprised of three cluster arrays separated by SLG. Arrows denote the magnetic moments of the pillars at saturation.

high occupation probability of the moiré cells. Therefore, it represents an effective nucleation seed for the growth of ordered clusters [174, 175]. Experimental efforts are also underway to engineer the most suitable cluster composition and morphology for both large magnetic anisotropy energy and negligible dipolar coupling [176].

To increase the cluster volume, it is possible to repeat the building block SLG – cluster array, in the three dimensional stacking illustrated in Fig. 7.1, colloquially referred to as a *mille-feuille* structure.

Different strategies are viable to cover the cluster array with SLG (which serves as growth substrate for a new cluster array). A solution which has already been taken into consideration is the chemical vapour deposition (CVD) of SLG onto the cluster array. Provisional results provide evidence of ethylene dissociation on Ni clusters at 750 K without any meaningful coalescence effect [175]. However, data from angle-resolved photoelectron spectroscopy do not contain any signature of graphene formation.

The solution discussed in this Chapter is the iterated, clean transfer of graphene from the growth substrate onto the nanostructure superlattice. Conceptually speaking, it is the most straightforward solution. On the other hand, from an experimental viewpoint, it constitutes an unprecedented challenge.

In the scope of our project, the requirements on quality degradation of graphene are demanding. Particular attention must be devoted to the presence of impurities on graphene. The morphological and magnetic properties of the atom clusters are highly sensitive to the contamination level and thus only preserved either in UHV or in an inert atmosphere. For instance, for the high reactivity of edge atoms with low coordination, the exposure of Co clusters to more than 0.3 langmuir of O_2 completely suppresses magnetism [177, 178]. In UHV, changes in the magnetic properties are detectable 1 hour after deposition. For the same reason, *in situ* characterization is routinely carried out immediately upon growth.

Therefore, our final objective is to perform graphene transfer in UHV. This also allows the removal of contaminants at the surfaces, and thus improves both graphene quality and the adhesion of graphene to the target substrate. Recently, transfer in medium vacuum has been experimentally demonstrated, using both a polymethilmethacrylate (PMMA) support and a polyethylene naphthalate (PEN) frame [179]. According to the proposed procedure, the PEN/PMMA/graphene block is placed at a small distance from the target substrate and at a small angle from the parallel direction. The PEN/PMMA/graphene block bounds spontaneously to the target substrate, upon heating up above a threshold temperature. The contact region rapidly propagates throughout the surface starting from a corner of the sample. According to characterization by means of Raman spectroscopy and performance measurements of graphene based devices, transfer yield, carrier mobility and stability over time are better upon transfer in medium vacuum, compared to transfer in air.

Lyding and collaborators have been developing a technique for transfer in UHV via direct contact [180, 181]. They used a fiberglass sheath impregnated with graphene flakes and brought into contact with the target substrate by means of a linear translator manipulator inside a vacuum chamber. The purpose of the fiberglass is to ensure a uniform pressure, and to limit it, to avoid any damage. However, no transfer of a continuous layer of graphene has ever been experimentally demonstrated.

In this Chapter, we report the results of graphene growth by means of CVD on a Cu foil, and graphene transfer in air via state-of-art methods, with a twofold purpose. On one hand, a comprehensive understanding of procedures in air is essential to design new, effective procedures in UHV. On the other hand, the growth substrate is not a suitable support for the final transfer in UHV, for the preferential adhesion of graphene to the metal catalyst, instead of graphene itself. Our efforts are devoted to preserve graphene quality throughout the transfer process, for continuous films on the centimeter scale, formed by the largest possible grains.

7.2 Methods

Growth

To date, the best known procedure for the growth of large area graphene is the decomposition of a precursor gas at high temperature and low pressure on a metal catalyst, which provides single-crystal domains with lateral sizes up to 1 mm and carrier mobility above 4×10^3 $\mathrm{cm}^2\ \mathrm{V}^{-1}\ \mathrm{s}^{-1}$ [182, 183]. Alternative methods, such as exfoliation of graphite and thermal decomposition of SiC, result in worse structural coherence, limited to the micrometer range, and multilayer instead of single-layer graphene [184]. In basic research, to demonstrate the fabrication of atomically flat graphene [185] and record carrier mobility above 10^5 $\mathrm{cm}^2\ \mathrm{V}^{-1}\ \mathrm{s}^{-1}$ [186], single-layer flakes are singled out upon a careful scan of the surface by means of microscopy. Instead, in methods based on CVD, the choice of the process parameters, such as temperature, pressure, flow rate and type of precursor gas, allows a better control on the output, which is more oriented towards reproducibly and scalability standards for industrial applications [187, 188].

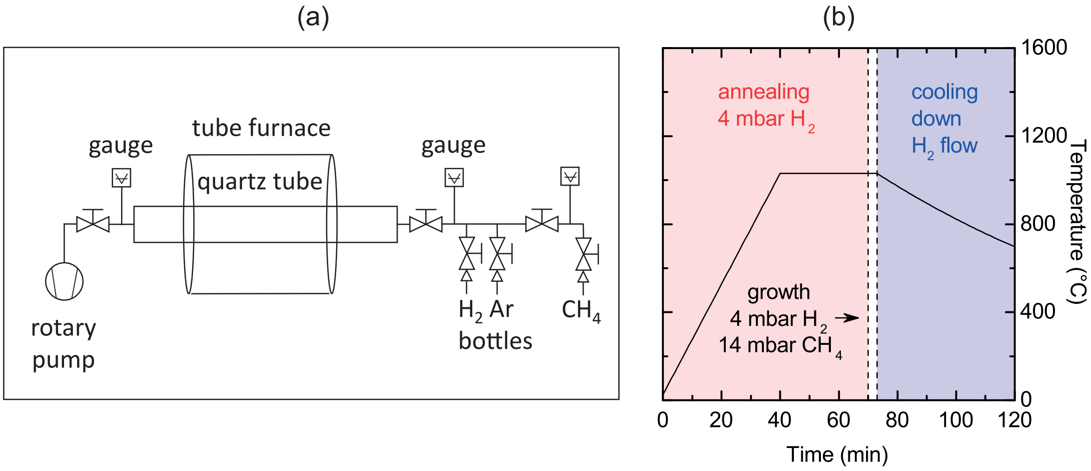

Figure 7.2 – (a) Schematic layout of the set-up for CVD of graphene at the Crystal Growth Facility, EPFL. (b) Temperature profile and reactor content during our growth procedure of graphene on Cu foils.

In our experiments, we repeatedly performed CVD of graphene on Cu foils (99.8% purity, 25 μm thickness, Sigma-Aldrich), at the Crystal Growth Facility, EPFL. The set-up used for the purpose is comprised of a quartz tube inside a tube furnace, connected by valves to H_2, CH_4 and Ar bottles, at one end, and to a rotary pump, at the opposite end (see Fig. 7.2(a)). Our growth procedure consists of the following steps (see Fig. 7.2(b)). (i) The characteristics of the growth substrate are of particular importance for the final quality of graphene. A Cu foil is cleaned by immersion in acetone and isopropanol, and dried under a nitrogen flow. (ii) The Cu foil is inserted inside the reactor. Starting from a base pressure of 5×10^{-3} mbar and room temperature, H_2 is introduced in the quartz tube to a pressure of 4 mbar, and the reactor is heated to 1031°C in about 40 min. In the same atmosphere, the Cu foil is further annealed at 1031°C for 30 min, to reduce the oxide layer at the surface. (iii) In the growth step, CH_4 is introduced in the reactor. A total pressure of 18 mbar is maintained for 3 min. (iv) The reactor is cooled down to room temperature under a H_2 flow.

Transfer in air

The most common procedure to transfer as-grown graphene onto arbitrary substrates is comprised of the following steps [189]. (i) Free-standing graphene is sensitive to any external perturbation. To avoid any possible damage during transfer, a polymer support is spin coated or adhered onto graphene. (ii) The growth substrate is chemically etched to free the polymer/graphene block. (iii) The polymer/graphene block is scooped out of the etching solution and laid down on the target substrate. To remove possible adsorbates, and to improve the contact between graphene and the target substrate, additional cleaning and heat treatment procedures are carried out. (iv) The polymer is dissolved in a suitable solvent.

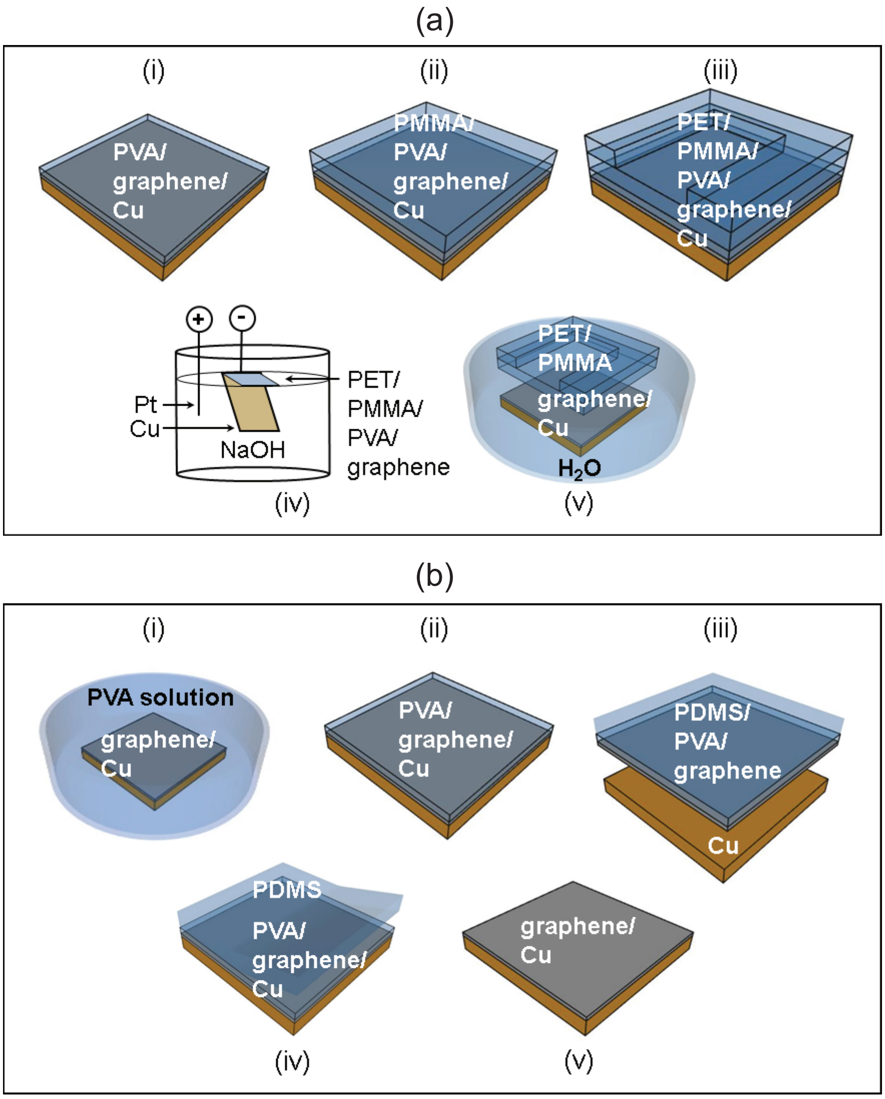
(a)
(i)
PVA/
graphene/
Cu
(ii)
PMMA/
PVA/
graphene/
Cu
(iii)
PET/
PMMA/
PVA/
graphene/
Cu
+
-
Pt
Cu
NaOH
PET/
PMMA/
PVA/
graphene
(iv)
PET/
PMMA
graphene/
Cu
H_2O
(v)
(b)
(i)
PVA solution
graphene/
Cu
(ii)
PVA/
graphene/
Cu
(iii)
PDMS/
PVA/
graphene
Cu
PDMS
PVA/
graphene/
Cu
(iv)
graphene/
Cu
(v)

Figure 7.3 – Schematic illustration of our procedures to transfer graphene from growth to target substrates made of Cu foils, namely, (a) electrolytic delamination and (b) direct exfoliation.

The most critical issues during transfer are the conformal contact between layers, damage and doping effects from chemical etching [190], and the presence of contaminants, namely, impurities from the etching solution, and metal and polymer residues, respectively, from incomplete etching and polymer dissolution. Alternative transfer procedures have been recently developed to avoid chemical etching. For instance, chemical etching can be replaced by direct exfoliation [191] or electrolytic delamination [192–194]. Analogously, the customary use of PMMA, soluble in acetone, can be replaced by the use of polyvinyl alcohol (PVA), soluble in water [195]. An additional layer made of a more rigid polymer, such as PMMA itself, is needed in any case, for mechanical support.

In our experiments, we repeatedly transferred in air both home-made and commercial graphene (grown by CVD on a Cu foil of 20 μm thickness, Graphene Supermarket), from the growth substrate to a different Cu foil. Batches of Cu foils covered with commercial and home-made graphene, with dimensions of respectively 5×5 cm^2 and 4×2 cm^2, were cut into multiple 1×0.5 cm^2 sized samples. The same Cu foils used for CVD served as target substrates. Before each transfer step, to remove the oxide layer at the surface, the target substrate was treated in acetic acid for 5 min.

In our first set of attempts, we combined the two most promising alternatives to customary processes, namely electrolytic delamination and the use of an interfacial PVA layer. Our first transfer procedure is comprised of the following steps, illustrated in Fig. 7.3(a). (i) A 2% aqueous solution of PVA is spin coated on top of graphene on the growth substrate at 1000 rpm for 60 s, and baked at 100°C for 60 s on a hotplate. To prepare the solution, 800 mg of PVA powder (9000–10000 molecular weight, 80% hydrolyzed, Sigma-Aldrich) are dissolved in 40 ml of deionized water at 95°C by stirring for 2 hours. (ii) A 4% anisole solution of PMMA (950000 molecular weight, MicroChem) is spin coated on top of the PVA layer at 500 rpm for 45 s, and cured at 180°C for 10 min on a hotplate. Spinning time and speed are chosen based on product specifications (PMMA datasheet, MicroChem) and the inverse relation between the thickness and the square root of the spinning speed, so that the thickness is about 600 nm. This represents a compromise value, which accounts for the trade-off between flexibility and impermeability to water of the polymer support, both important for the transfer procedure, with particular reference to electrolytic delamination. (iii) A semirigid frame of polyethylene terephtalate (PET) is cut into a U shape, attached on the PMMA layer using a drop of the same above PMMA solution as a glue, and cured at 180°C for 10 min on a hotplate. (iv) To release the PET/PMMA/PVA/graphene block from the Cu substrate, electrolytic delamination is carried out in a 0.2 M aqueous solution of NaOH at 0°C. A Pt wire and the Cu substrate itself serve respectively as anode and cathode. The reaction responsible for the formation of H_2 bubbles at the cathode can be written as $2H_2O_{(l)} + 2e \rightarrow H_{2(g)} + 2OH^-_{(aq)}$. In the event of accidental pole inversion, O_2 instead of H_2 bubbles are formed, with consequent corrosion of the Cu substrate and contamination of the electrolytic solution. The current through the electrodes is progressively ramped up to 0.5 A and switched off after 1 min. Excess PMMA wrapped around the Cu substrate prevents the spontaneous detachment of the PET/PMMA/PVA/graphene block from the Cu substrate. Nevertheless, the two surfaces are separated at a microscopic level. It is possible to easily handle the PET/PMMA/PVA/graphene block with metal tweezers by means of the PET frame. If the polymer support is not thick enough, water penetrates through it during electrolytic delamination. Protons are reduced at the interface between graphene and the Cu foil, and H_2 bubbles are thereby created in the middle of graphene. The pressure that builds up inside them can cause the formation of pores in graphene. Instead, the choice of an optimal thickness of the PMMA layer ensures that delimination progresses gradually, from the edges towards the center of graphene, and thus reduces possible damage during the process.

(v) In principle, the transfer is completed upon the dissolution of the interfacial PVA layer in hot water, with consequent release of the PET and PMMA layers. To avoid that the PET/PMMA/PVA/graphene block floats away from the target substrate after hot water is poured, we applied pressure by means of metal tools and elastomeric stamps. The PMMA layer appeared to protect the interfacial PVA layer from dissolution in hot water. Thus, in a preliminary step, we also dissolved PMMA in acetone. Nevertheless, we did not manage to ensure effective binding between graphene and the target substrate, simultaneous to the removal of the polymer layers. Throughout our first set of attempts, for the insufficient adhesion of graphene to the target substrate, the integrity of graphene was compromised by the dissolution of the polymer support, with the result that only isolated flakes were transferred.

In our second set of attempts, we replaced electrolytic delamination with direct exfoliation. Our second transfer procedure consists of the following steps, illustrated in Fig. 7.3(b). (i) As-grown graphene is immersed in a 1% aqueous solution of PVA maintained at 50°C for 18 hours on a hotplate. The purpose of the pretreatment step is to allow enough time for the spontaneous absorption of the PVA molecules on graphene. This is driven by the hydrophobic nature of the graphene surface and the consequent decrease in interface energy upon coverage with PVA molecules [196]. The molecular layer of PVA thereby produced increases the binding between graphene and the thin PVA film deposited during the second step. After the pretreatment step, graphene on the growth substrate is rinsed with deionized water and dried under a nitrogen flow. (ii) The same above PVA solution is drop coated on top of graphene on the growth substrate, and baked at 80°C for 10 min on a hotplate. (iii) To delaminate graphene from the growth substrate, an elastomeric stamp made of a polydimethylsiloxane (PDMS) hemisphere is brought into contact with the PVA layer and retracted at high speed. (vi) Graphene covered with a PVA layer is delivered onto the target substrate by manually pressing the PDMS/PVA/graphene block onto the target substrate at 130°C for 1 min and retracting the stamp slowly. (v) The PVA layer is dissolved in deionized water at 35°C. Overall, our second set of attempts was successful. To compare graphene before and after transfer, we performed Raman characterization, as discussed in next Section.

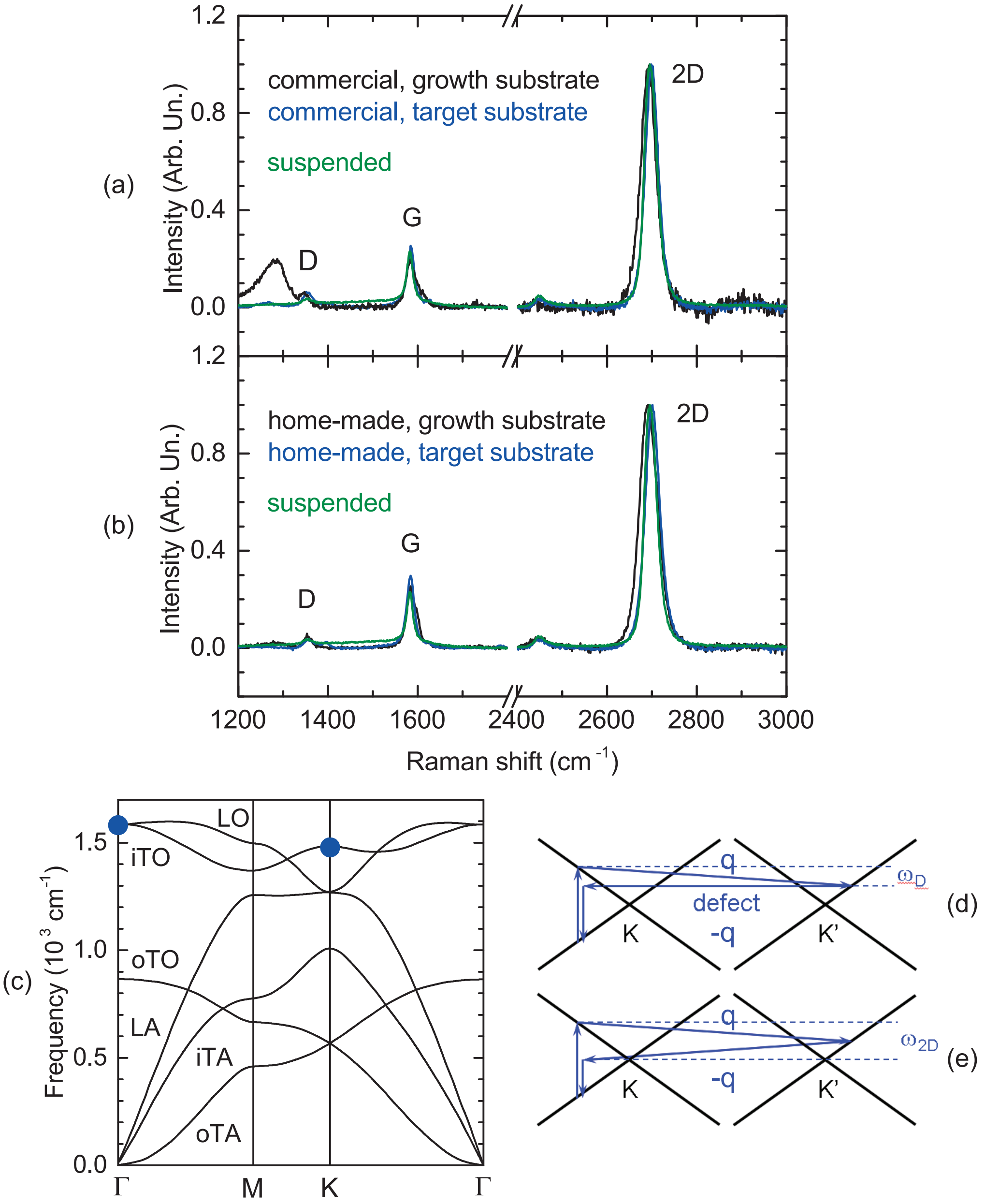

Figure 7.4 – Representative Raman spectra of (a) commercial and (b) home-made graphene on Cu (black) before and (blue) after transfer, and of (green) suspended SLG on a transmission electron microscopy (TEM) grid. (c) *Ab initio* computation of the phonon dispersion curves of SLG along high-symmetry directions [197]. The phonons responsible for the main Raman bands are highlighted with blue circles. Pictorial schematics of the Raman processes responsible for the (d) D and (e) 2D bands. Crosses represent the electronic dispersion near the K and K' points. Vertical arrows represent the photoexcitation or the recombination of an electron-hole pair. Horizontal and oblique arrows represent the scattering with respectively a defect and an iTO phonon around the K point.

7.3 Results and Discussion

Raman Spectrum of Graphene

In the following, we describe the most important features of Raman scattering of light from graphene [198]. Figures 7.4(a,b) compare typical Raman spectra from our Raman characterization of graphene before and after transfer. The most intense peaks are located at 2700, 1580 and 1350 cm^{-1} and respectively referred to as the 2D, G and D bands, where G stands for *graphite* and D stands for *disorder* or *defect*.

The starting point for the assignment of the Raman modes is the phonon dispersion of graphene, plotted in Fig. 7.4(c), according to theoretical calculations [197]. The primitive cell of graphene is comprised of two atoms which oscillate in three acoustic (A) and three optical (O) modes. One acoustic and one optical mode are out of plane (o). The remaining four modes are in plane (i), with eigenvectors perpendicular (transverse, T) or parallel (longitudinal, L) to the propagation direction.

The only Raman-active mode at the center of the Brillouin zone is the double degenerate iO mode of E_{2g} symmetry at 1580 cm^{-1} comprised of bond stretching of C atom pairs. Based on energy and the absence of dispersion, typical of first-order Raman scattering, the G band is identified with the above mode.

To a first approximation, all four modes at the K point are Raman active. However, as a result of anisotropy and electron-phonon coupling, only the iTO phonon is associated with a meaningful cross section in Raman scattering. In particular, the mechanism at the origin of the D band is a double-resonance process, which involves the following steps (see Fig. 7.4(d)). (i) Photoexcitation of an electron-hole pair in valence and conduction states of energy E_0 and E_1 close to the K point (with $\hbar\omega_1 = E_1 - E_0$, where ω_1 is the photoexcitation frequency). (ii) The electron is scattered by an iTO phonon of energy $\hbar\omega_D$ and wave vector $\boldsymbol{q}$ slightly longer than the wave vector of the K point, $\boldsymbol{q}_K$, to a state nearby the K' point of energy $E_2 = E_1 - \hbar\omega_D$. (iii) The same electron is then scattered back by a defect of zero energy which provides the wave vector $-\boldsymbol{q}$ required to conserve momentum. (iv) Recombination of the electron-hole pair with emission of radiation at frequency $\omega_2 = \omega_1 - \omega_D$. An analogous description is possible for the hole in the valence band. The reason why iTO phonons of wave vector $\boldsymbol{q}$ equal or shorter than $\boldsymbol{q}_K$ are not associated with meaningful Raman cross section is the asymmetry of the electronic structure. In particular, for the trigonal warping of the dispersion curves around the K and K' points, the number of states available is meaningful only for processes with $\boldsymbol{q}$ slightly longer than $\boldsymbol{q}_K$.

The 2D band is an overtone of the D band. The mechanism at the origin of the 2D band is similar to the above, with the difference that electron-defect scattering is replaced by a second scattering event with an iTO phonon of energy $\hbar\omega_D$ and wave vector $-\boldsymbol{q}$, so that the energy loss of the photon is $2\hbar\omega_D$ (see Fig. 7.4(e)).

Different features in the Raman response of graphene are regarded to as spectral indicators for the characteristics of graphene itself. Both the shape of the 2D band and the intensity ratio between the 2D band and the G band provide information on the number of graphene layers. If it is known *a priori* that the stacking is of the Bernal type, for instance, in graphene exfoliated from highly oriented pyrolytic graphite, then the shape of the 2D band is enough to draw conclusions on the number of graphene layers [199, 200]. In particular, in SLG the 2D band is a single Lorentzian peak, 2–4 times more intense than the G band. Bilayer graphene shows a splitting of the 2D band into four subbands, with intrinsic relative intensities, which only depend on the excitation energy [201]. The fine structure of the 2D band is univocal also for trilayer and tetralayer graphene. Instead, it is not possible to identify the number of layers in thicker multilayer graphene. In all cases of multilayer graphene with AB stacking, the intensities of the 2D band and the G band are comparable.

Often, graphene grown by CVD does not show Bernal stacking [198]. In that case, the Raman response depends on possible interlayer interactions, which in turn depend on the relative orientations of the layers. The general effect of the symmetry lowering is a broadening of the 2D band, which remains a single Lorentzian peak. However, for weak interactions between two misoriented layers of graphene, a narrowing of the 2D band has also been reported [202]. In general, it is not possible to single out single-layer from multilayer graphene based on Raman characterization alone, in the absence of complementary measurements with different techniques. A typical approach consists of comparing observations from optical and electron microscopy and Raman spectroscopy to retrieve an approximate relation between the intensity ratio between the 2D and G band and the number of layers or simply determine whether graphene is single layer or multilayer. Indeed, a comparable intensity of the 2D band and the G band implies that graphene is multilayer, although, vice versa, an intensity ratio between the 2D and G band larger than one is not necessarily a signature of SLG [203]. It is interesting to note that doping and structural disorder also produce meaningful effects on the G and 2D bands. In different cases it is not easy to separate them from spectral indicators for the number of layers.

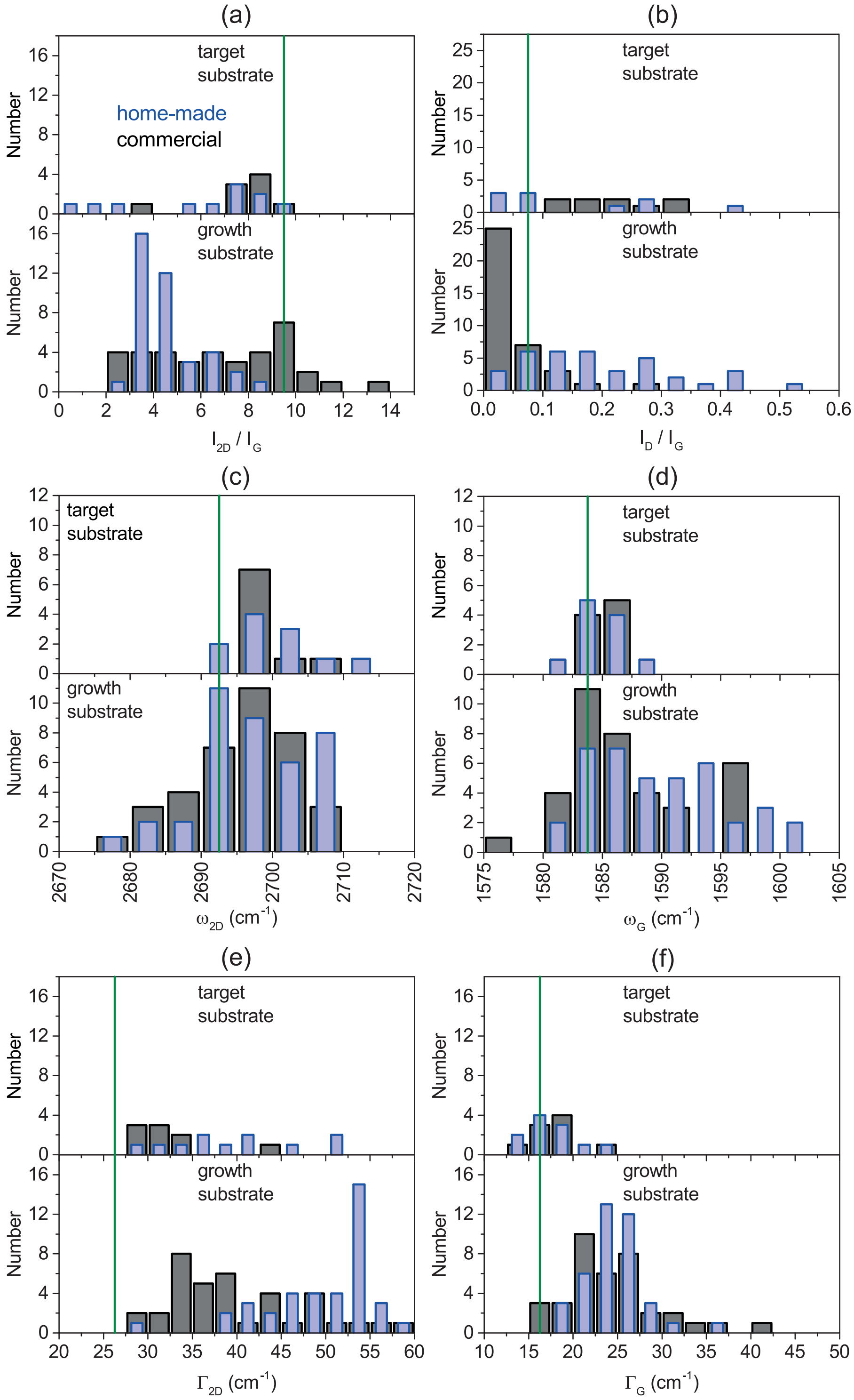

Figure 7.5 – Distribution of the most important parameters of the Raman bands for (black bars) commercial and (blue bars) home-made graphene (lower panels) before and (upper panels) after transfer, namely, (a) intensity ratio between the 2D and G band, and (b) between the D and G band, and (c,d) 2D and G band frequency and (e,f) linewidth. Reference values for suspended graphene on a TEM grid are plotted with green lines.

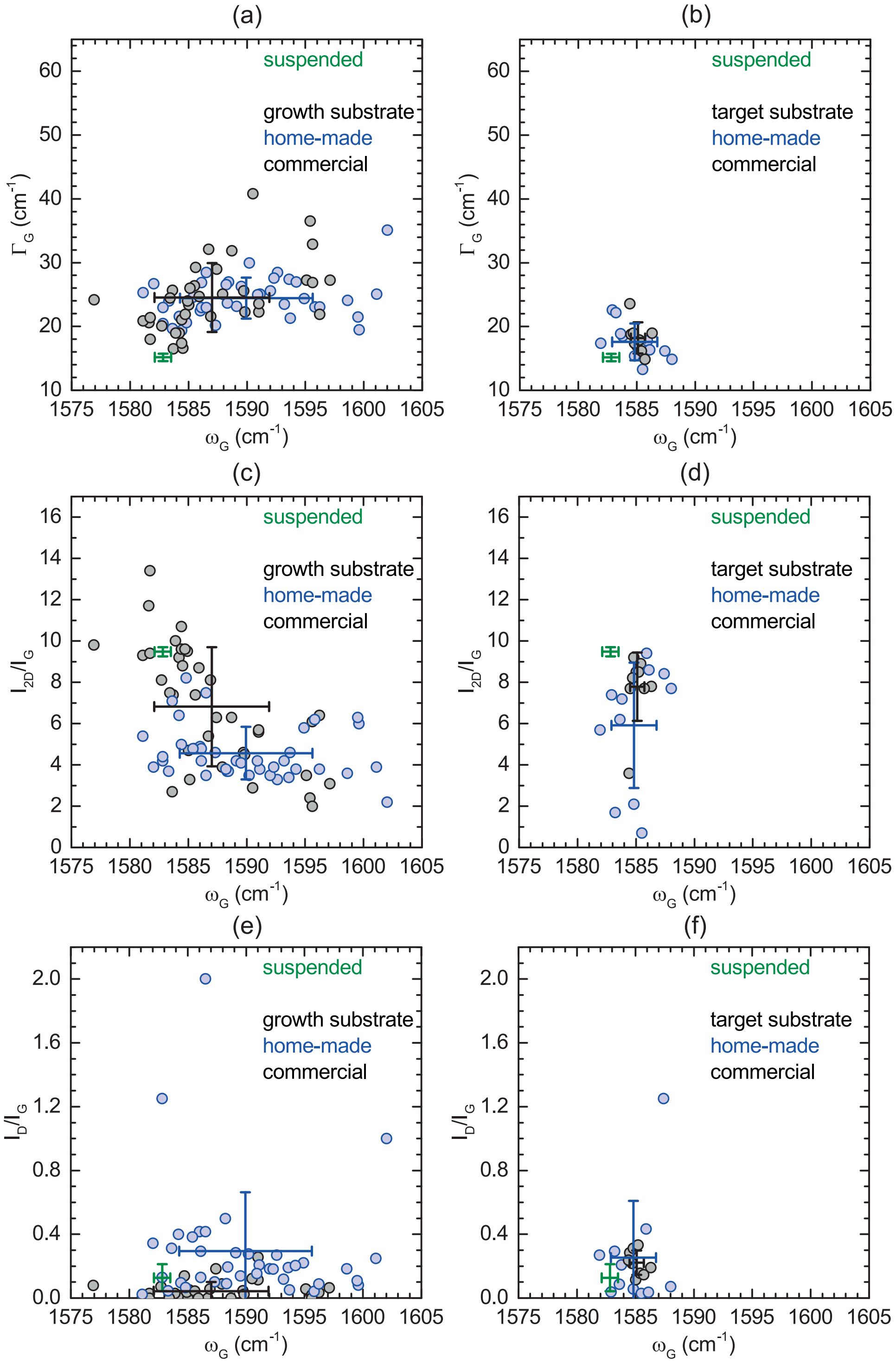

Figure 7.6 – Scatter plots of (a,b) G band linewidth, (c,d) intensity ratio between the 2D and G band, and (e,f) between the D and G band versus G band frequency, for (black symbols) commercial and (blue symbols) home-made graphene (left panels) on the growth substrate and (right panels) upon transfer onto the target substrate. Bars indicate intervals within one standard deviation for the different data sets. Reference values for suspended graphene on a TEM grid are plotted with green bars.

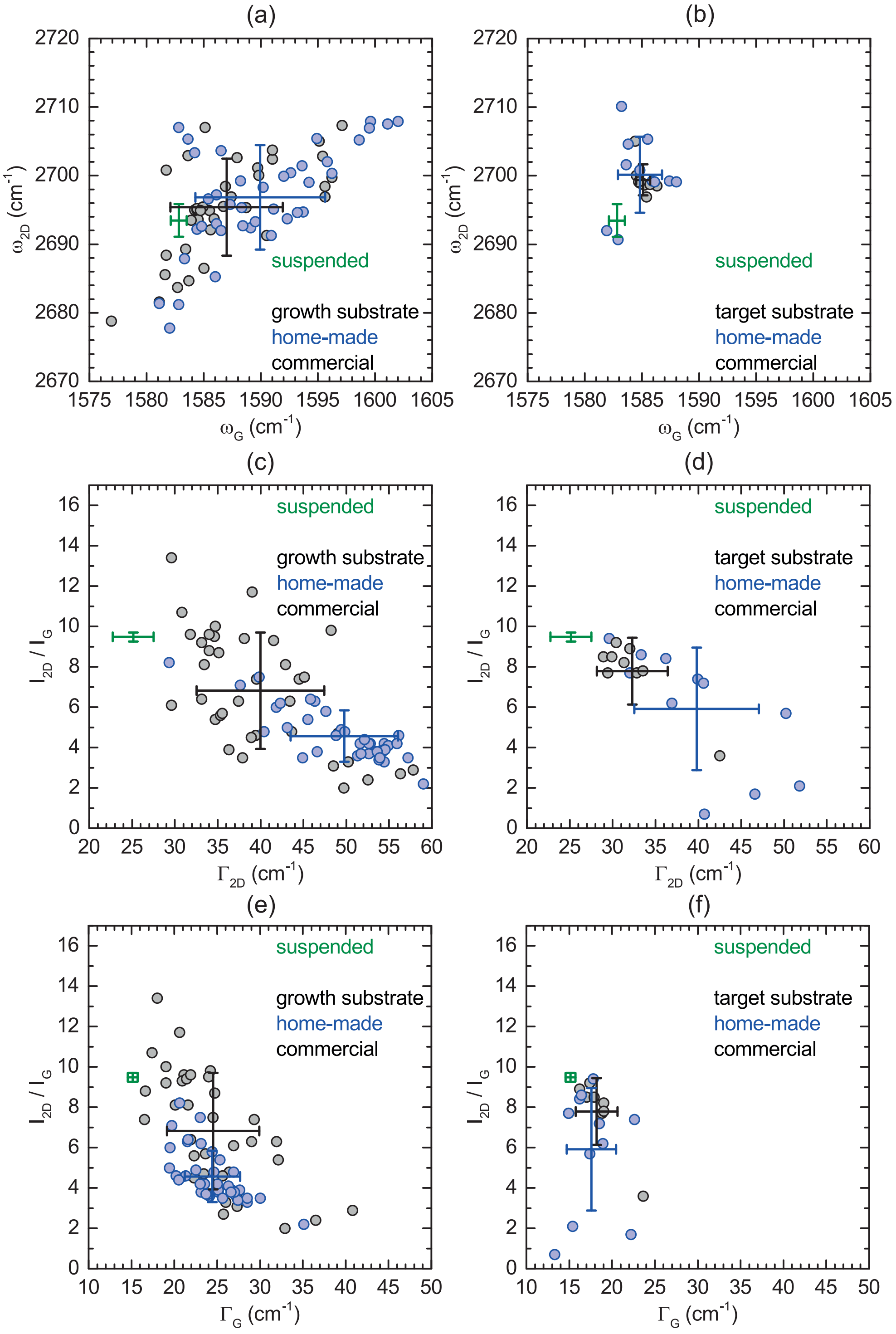

Figure 7.7 – Scatter plots of (a,b) 2D vs G band frequency and intensity ratio between the 2D and G band versus (c,d) 2D and (e,f) G band linewidth, for (black symbols) commercial and (blue symbols) home-made graphene (left panels) on the growth substrate and (right panels) upon transfer onto the target substrate. Bars indicate intervals within one standard deviation for the different data sets. Reference values for suspended graphene on a TEM grid are plotted with green bars.

	ω_{2D}	Γ_{2D}	ω_G	Γ_G	I_{2D}/I_G	I_D/I_G
ω_{2D}	–	0.01	0.65	0.15	-0.32	0.27
Γ_{2D}	–	–	0.27	0.42	-0.74	0.32
ω_G	–	–	–	0.37	-0.53	0.06
Γ_G	–	–	–	–	-0.59	0.16
I_{2D}/I_G	–	–	–	–	–	-0.28
I_D/I_G	–	–	–	–	–	–

Table 7.1 – Correlation coefficients between pairs of parameters from our Raman characterization of home-made and commercial graphene grown on Cu. For clarity, only the upper half of the table is shown.

Raman Characterization

Our samples were characterized by Raman spectroscopy at the Material Characterization Platform, EPFL. The set-up for Raman spectroscopy is comprised of a Renishaw InVia Raman microscope equipped with lasers of 405, 488, 532 and 785 nm excitations. In our experiments, the laser beam is focused onto the sample surface through a 100× objective lens. Backscattered light is collected and collimated by the same optical system. The typical diameter of the laser spot at the focus is about 1 μm. The approximate power incident onto the sample surface is 2.5 mW. The choice of the excitation to characterize graphene by Raman spectroscopy is a compromise between the suppression of the background from the substrate and the benefits on the signal-to-noise ratio from resonance conditions for the graphene bands. In the case of Cu, a large photoluminescence background centered around 600 nm originates from the radiative recombination of electrons excited from the *d* bands to the conduction band [204]. The G and 2D bands resonate for excitation within or close to the spectral range between 514 and 568 nm [205]. However, in our preliminary measurements, we did not notice any meaningful improvement of the signal-to-noise ratio if 532 nm excitation instead of 488 nm excitation was used. On the contrary, spectra taken with 488 nm excitation show less intense, flatter backgrounds, which grow monotonically with increasing Raman shift, compared to spectra taken with 532 nm excitation. Therefore, throughout our Raman characterization, we used 488 nm excitation.

To demonstrate the effectiveness of our transfer procedure, our samples of commercial and home-made graphene were characterized on the growth substrate and, after each transfer attempt, on the target substrate. Additional Raman spectra, not discussed here, were collected at intermediate steps, to study possible degradation at critical stages of the transfer procedure. Reference measurements were performed on suspended SLG on a TEM grid (prepared by Graphenea, on C-Flat, Electron Microscopy Sciences). On average, before each transfer attempt, our samples were characterized at five different spots, to ensure uniformity. The considerations in the following refer to both data sets from home-made and commercial graphene combined together. Commercial graphene has also been grown by customary methods of CVD of graphene on Cu foils in a H_2 and CH_4 atmosphere in a reactor heated up to about

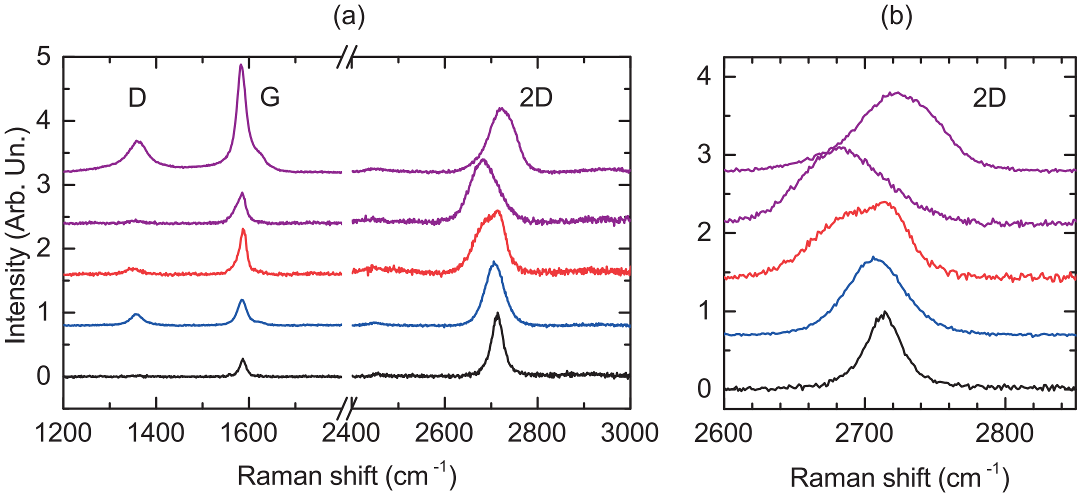

Figure 7.8 – (a) Representative Raman spectra of home-made graphene on Cu, after CVD with 30 min, instead of 3 min, growth step. The characteristic Raman responses in different regions of the sample surface are plotted with different colors. (b) Zoom on the 2D band, to emphasize differences in lineshape and linewidth. Raman spectra are plotted with the same color coding as panel (a). For clarity, data are normalized to the intensity of the 2D band and offset by constant vertical increments.

1000°C (datasheet, Graphene Supermarket). The results from our Raman characterization are summarized in Figs. 7.5–7.8 and table 7.1.

The first issue to address is whether or not graphene is indeed single layer. In general, for the immiscibility of C and Cu [206], CVD of graphene on Cu foils is supposed to produce only SLG. However, segregation of C to the substrate has also been reported [207]. Moreover, by comparing results from Raman spectroscopy, optical and scanning electron microscopy, and electron diffraction, it has been shown that, although overall the decomposition rate of CH_4 on Cu is low, the energy barrier for decomposition of CH_4 is significantly decreased at step edges and grain boundaries of the Cu surface [203]. As a result, they act as nucleation sites for additional flakes, which can form before the completion of the first layer. The lateral sizes of possible multilayer regions depend on the quality of the Cu surface and on the growth parameters. Noteworthy, in the same above work, it was pointed out that in the absence of AB stacking, the spectral features of single-layer and bilayer graphene are similar, and thus it is not easy to single out differences due to the number of layers alone.

In our data on home-made graphene, all three parameters regarded to as the most important references for considerations on the number of layers, *i.e.* the lineshape and linewidth of the 2D band, and the intensity ratio between the 2D and G band, show a unimodal distribution. Specifically, in all Raman spectra, the 2D band consists of a single peak, with predominance of Gaussian over Lorentzian content in lineshape (see Fig. 7.4(a)), large linewidth between 45 and 55 cm^{-1} (see Fig. 7.5(e)) and intensity ratio to the G band between 3 and 5 (see Fig. 7.5(a)). Thus, there is no evidence of regions with different number of layers, homogeneous on length scales longer than the dimension of the laser spot.

Instead, if the duration of the growth step is increased from 3 to 30 min, different Raman responses are measured in different regions. As illustrated in different colors in Fig. 7.8, for 30 min growth step, five types of spectra are identified by means of Raman characterization. The spectrum in blue is analogous to the typical spectrum for 3 min growth step. Remarkably, the spectrum in black is closer to that of suspended SLG on a TEM grid, shown in Fig. 7.4(a). This kind of spectrum is never observed for samples with 3 min growth step. The lineshape of the 2D band of the spectrum in red resembles that of bilayer graphene with Bernal stacking [201]. Both spectra in purple show an anomalous linewidth of the 2D band around 70 cm^{-1}. In particular, the upper spectrum also shows large intensity ratio between the G and 2D band, typical of graphite, and great intensity of the D band, indicative of a high level of defects.

If in samples with 3 min growth step graphene was already multilayer, then we could not explain the occurrence of regions with graphene quality close to suspended SLG on a TEM grid for 30 min growth step. Instead, it appears that the features of the Raman spectra are intrinsic to the interaction between graphene and the Cu surface, and disorder with homogeneous distribution and characteristic length scales smaller that the dimension of the laser spot. Possible causes of disorder are structural defects and the formation of multilayer flakes at the nucleation sites. On one hand, longer growth steps seem to improve graphene quality, for instance, as a result of better continuity of the single-layer grains or more effective decoupling from the Cu surface. On the other hand, the spectra in red and purple in Fig. 7.8 demonstrate that large multilayer flakes are formed in different regions, respectively, with and without AB stacking.

The typical spectra of commercial graphene are intermediate betweeen those of home-made graphene after 3 min growth step and the spectrum in black in Fig. 7.8 referred to 30 min growth step, *i.e.* they reflect variable degrees of disorder, with dishomogeneous distribution, and weaker interactions with the growth substrate. In fact, the 2D band linewidth, and the intensity ratio between the 2D and G band are spread over broad ranges, respectively, between 30 and 50 cm^{-1}, and between 3 and 10 (see Figs. 7.5(a,e)). Furthermore, in most cases, the D band is either small or absent (see Fig. 7.5(b)). Additional peaks observable below 1300 cm^{-1} originate from contaminants. Instead, the features of the G band examined below are the same for both commercial and home-made graphene.

As illustrated in Figs. 7.6 and 7.5(d), the G band frequency shows a broad distribution between 1582 and 1596 cm^{-1}, above the reference value for suspended SLG on a TEM grid. Data on SLG fabricated by microcleavage of graphite are in the same range [208]. Based on correlations between the G band frequency and linewidth, and the intensity ratio between the 2D and G band, it has been proposed that the variable upshift of the G band originates from effects of inhomogeneous doping by extra charges, with different possible causes. The dependence of the G band frequency and linewidth on the doping level has been investigated by means of both theoretical calculations and an experimental study in which the Fermi level was modulated by the application of a gate voltage [209]. Indeed, it has been shown that, in the presence of moderate doping, the Kohn anomaly in the longitudinal optical branch moves from the center of the Brillouin zone to finite wave vector, and thus the G band is upshifted (see Fig. 7.4(c)). Based on a comparison with Ref. [209], both our observations and the data in Ref. [208] are equivalent to variations of hole and electron concentrations on a scale of 10^{13} cm^{-2}. As evident from table 7.1 and Fig. 7.6(c), similarly to the data in Ref. [208], in our observations the intensity ratio between the 2D and G band decreases with increasing G band frequency and thus, according the above interpretation, with increasing doping level.

In principle, the modulation of the Fermi level from doping decreases the number of states available for the decay of E_{2g} phonons into electron-hole pairs, responsible for the G band linewidth [210]. As predicted by theoretical calculations and confirmed by experimental studies, the G band linewidth is supposed to decrease from about 16 cm^{-1} to values close to the experimental resolution on increasing hole or electron concentration [209]. In contrast to the data in Ref. [208], we do not observe any correlation between the G band linewidth and frequency (see table 7.1 and Fig. 7.6(a)). In our observations the G band linewidth is distributed between 20 and 30 cm^{-1}. Instead, both in intentionally and nonintentionally doped samples, the typical range of the G band linewidth is 6–16 cm^{-1} [208, 210]. An anomalously broad G band is a fingerprint of additional effects from disorder in the structural orientation of the grains, superimposed to the above doping effects [211, 212]. After transfer, the distribution of the G band linewidth downshifts to the typical range in the absence of structural disorder (see Fig. 7.5(f)). This raises the possibility that structural disorder mainly resides in the multilayer flakes at the nucleation sites, which are not transferred to the target substrate in our successful transfer procedure based on direct exfoliation. With reference to table 7.1 and Fig. 7.6(e), let us note that we do not observe any correlation between the G band frequency and the relative intensity of the D peak. Thus, it is not possible to experimentally demonstrate any relationship between defect content and G band frequency.

We now address the effectiveness of our transfer procedure and the possible sources of the extra charges. An inspection by eye of the Raman spectra in Figs. 7.4(a,b), referred to typical examples, already provides useful information. In particular, all features of the Raman spectra suggest that, on average, graphene quality is not compromised after transfer, and is characteristic of a single layer. In fact, the linewidths of the 2D and G bands of transferred graphene (blue line) are closer to those of suspended SLG on a TEM grid (green line) than to those of as-grown graphene (black line), both for home-made and commercial graphene (see Figs. 7.5(e,f) for a statistical analysis). The overall distribution of the data also shows a meaningful increase in the intensity ratio between the 2D and G band (see Fig. 7.5(a)). With reference to the doping effects, let us note that, upon transfer, the G band frequency decreases to values more consistent with undoped graphene (see Fig. 7.5(d)). Conversely, Fig. 7.5(b) shows a decrease in the relative number of spots with negligible D peak after transfer, and thus an increase in defect content, which is a consequence of moderate graphene damage, unavoidable during transfer. As already noted, the G band frequency and the relative intensity of the D peak are uncorrelated (see table 7.1 and Fig. 7.6(e)).

Both last observations suggest that defects intrinsic to graphene are not the main sources of extra charges. Instead, interactions with the substrate play the most important role. The increase in the intensity ratio between the 2D and G band after transfer is probably the result of both the absence of multilayer flakes and better isolation from the substrate. Based on theoretical predictions, the physisorption of graphene on Cu was shown to cause a shift of the Fermi level, equivalent to n- or p-type doping, depending not only on the difference between the work functions of graphene and Cu, but also on the interface potential that originates from their direct interactions [213, 214]. Therefore, the charge distribution at the interface, including whether electrons or holes are in excess, depends on the local distance between graphene and Cu, with possible inhomogeneity from the occurrence of ripples and multilayer flakes under the uppermost layer.

The presence of an oxide layer at the surface explains the suppression of the interactions between graphene and Cu on the target substrate. Indeed, the treatment in acetic acid of the target substrate before transfer is not effective to completely remove it, in contrast to the annealing of the growth substrate at high temperature in a H_2 atmosphere before growth. In addition, in the second-last step of transfer, the target substrate is in air at 130°C, *i.e.* in conditions suitable for the growth of a thin oxide layer. A recent study which combines electron diffraction, Raman spectroscopy and atomic force microscopy showed that the formation of an oxide layer between as-grown graphene and the Cu substrate from oxidation in humid air causes a meaningful decoupling between graphene and Cu [215]. In particular, in analogy to our data, the 2D band narrows and the intensity ratio between the 2D and G band increases. In the same study, the observation of a decrease in the adhesion force between graphene and Cu substrate provides additional experimental evidence of weaker interactions after oxidation.

7.4 Conclusions and Perspectives

In summary, in the framework of a project on the fabrication of the first heterostructure comprised of SLG alternated with arrays of atom clusters, we succeeded in the CVD of graphene on a Cu foil, and graphene transfer onto a different Cu foil via a method that combines direct exfoliation and the use of a polymer support soluble in water. We carried out systematic Raman characterization of graphene on the growth and target substrate.

Data on graphene on the growth substrate for two different exposure times to the precursor gas suggest that, in prevalence, our growth procedure produces SLG, with a homogeneous distribution of disorder from structural defects or multilayer flakes confined in small areas around step edges and grain boundaries of the Cu surface. For increasing duration of the growth step, the quality of the uppermost graphene layer is improved, but the multilayer flakes become large. Interactions with the substrate cause inhomogeneous doping by extra charges, equivalent to modifications in the hole and electron concentrations over a range up to 10^{13} cm^{-2}, reflected in the variable upshift of the G band. The anomalous linewidth of the G band is a signature of structural disorder, probably related to the random orientation of the multilayer flakes within the probed area. The transfer onto the target substrate inevitably introduces defects. However, at the same time, different features of the Raman spectra point to a decrease in both the degree of structural disorder and the doping level. Indeed, direct exfoliation is supposed to transfer only the uppermost graphene layer. Moreover, the presence of an oxide layer at the surface of the target substrate provides effective decoupling between graphene and Cu.

The next steps of our project are intended to (i) improve the quality of graphene grown by CVD, (ii) transfer graphene in air, from the growth substrate onto a suitable support, designed for the last step, (iii) transfer graphene in UHV, from the suitable support onto a cluster superlattice on graphene grown *in situ* by CVD onto Ir(111).

In the first step, graphene will be grown on a different metal, able to provide larger single-crystal domains. According to a recent publication, Pt foils allow the formation of grains with lateral sizes of 1 mm, two orders of magnitude greater compared to Cu [193]. However, CVD of graphene on Pt foils is regarded to as problematic, for the high solubility of C in Pt [216]. The growth step consists of a balance between deposition at the surface and absorption in the bulk of the Pt foil [217]. During the cooling step from the growth temperature to room temperature, in the absence of the precursor gas, C segregation causes the formation of multilayer graphene. For this reason, our future attempts will also focus on alternatives to Pt, such as Ir, although to date recipes for graphene growth on Ir are only available in UHV [218–220]. Indeed, the solubility of C in Ir is even lower than in Cu [216, 221].

Weak van der Waals forces mediate the interactions between graphene layers. In contrast, the interactions between graphene and metal substrates consist of bonding at the interface with mixed covalent and ionic character. The strength of the coupling changes from metal to metal, but in any case it exceeds that of dispersive forces. Therefore, metals are not suitable supports for the final step. Instead, possible candidates commercially available are layers of amorphous C, patterned with arrays of holes, to reduce the contact area between the carrier substrate and graphene, and by that provide preferential adhesion to the target substrate (C-Flat, Electron Microscopy Sciences). A metal grid under the carrier substrate also ensures mechanical rigidity. In preliminary attempts, we tested the transfer of graphene from the above support (prepared by Graphenea) to graphene grown by CVD on a Cu foil, by means of direct contact, under preheating temperatures between 50 and 100°C, both in air and in a vacuum oven. The adhesion between the carrier substrate and graphene resulted in the transfer of both the layer of amorphous C and graphene, probably, for the presence of a buffer layer of adsorbates. An alternative solution is represented by hexagonal boron nitride (h-BN) films. Indeed, experimental studies showed considerable similarity between the properties of graphene on h-BN films and suspended graphene, since typical h-BN films are inert, atomically flat and free of dangling bonds and extra charges [222]. Single and multilayer h-BN films on Cu foils are commercially available and being tested at the time of writing.

Additional procedures are needful to suppress the adhesion of graphene to the carrier substrate. For instance, heating procedures decrease the magnitude of the dispersion forces, generate spontaneous ripples of graphene from thermal fluctuations, and expansion mismatch between graphene and the carrier substrate. Annealing of both graphene on the carrier substrate and the target substrate in UHV before transfer allows the desorption of adsorbates at the surfaces, which otherwise impede adhesion.

Conclusions and Perspectives

This Thesis demonstrated that the combination of time-resolved and steady-state spectroscopy offers effective means to solve fundamental problems in phase transitions of solids. We proposed a mechanism for the coherent generation of phonons at finite wave vectors by means of transient stimulated Raman scattering, in second-order or nearly first-order transitions, in the presence of critical fluctuations, able to assist the photoexcitation process. We thereby developed a methodology which provides direct information on the dynamics of the critical fluctuations in the time domain, in particular, whether they are propagating or diffusive, and estimates of their frequencies and correlation times as a function of external fields. In general, our approach is suitable to test hypotheses on critical scaling, in transformation processes accessible by optical probes.

In the case of the Verwey transition, further ultrafast broadband or single-wavelength reflectivity experiments with better temperature control and signal-to-noise ratio are needful, to study the temperature and fluence dependence of the critical fluctuations close to the transition temperature, and determine whether suitable pump pulses induce buildup of long-range order. Additional spontaneous Raman scattering experiments on a set of samples with controlled impurity content and stoichiometry deviations are also required, for a systematic investigation of the effects of imperfections on the degree of local order, notably, the onset temperature and the occurrence itself of precursor effects mediated by the critical fluctuations.

Overall, this Thesis presented experimental evidence of ordering field modes with relaxational response, which can be described by pseudospin variables, in better accordance with an order-disorder, rather than a Peierls process intrinsic to the Verwey transition. Indeed, in our ultrafast broadband reflectivity experiments, Raman-active phonons at finite wave vectors were coherently generated in the cubic phase, with the assistance of ordering field modes at the same points in reciprocal space, with consequences on the correlation times, but not on the frequencies of the oscillations. In our spontaneous Raman scattering experiments, for the steady-state analogue of the above processes, Raman-active phonons of the monoclinic phase are observable close to, but above the transition temperature. Furthermore, the background intensity of the Raman response contains a diffusive contribution, from pairs of ordering field modes at opposite wave vectors around the critical points in reciprocal space. The central peaks visible in our inelastic neutron scattering experiments were also regarded to as manifestations of precursor order coupled with phonons.

Our study of phonons of the same symmetries suggested as the primary order parameters of the atomic displacements ruled out phonon softening. Therefore, we argued that scenarios based on structural driving forces or phonon dynamics coupled with the dynamics of the critical modes do not hold true in the transformation process of the Verwey transition. Instead, we proposed that the elementary excitations which first become unstable are the polaron modes with large inertia which give rise to the central peaks. They are strongly coupled to the phonons, but characterized by slow dynamics, such that the phonons follow them adiabatically, and not vice versa.

The ratio between our estimates of the correlation times of the ordering field modes from neutron and light probes is close to one order of magnitude. Therefore, we suggested that the critical fluctuations observed by means of time-resolved and steady-state optical spectroscopy are electron density modulations with small inertia, either weakly coupled to or independent of the above polaron modes. More solid considerations demand resonant inelastic x-ray scattering experiments at suitable absorption edges and reflections. If critical modes of mainly electronic nature are indeed at play in the Verwey transition, they are supposed to give rise to central peaks of large linewidth, on the order of 10 meV, at the critical wave vectors of their intrinsic instabilities.

Bibliography

[1] W. Bragg, "The structure of magnetite and the spinels," *Nature*, vol. 95, no. 2386, p. 561, 1915.

[2] E. Verwey, "Electronic conduction of magnetite (Fe_3O_4) and its transition point at low temperatures," *Nature*, vol. 144, no. 3642, pp. 327–328, 1939.

[3] T. Kołodziej, A. Kozłowski, P. Piekarz, W. Tabiś, Z. Kąkol, M. Zając, Z. Tarnawski, J. M. Honig, A. M. Oleś, and K. Parlinski, "Nuclear inelastic scattering studies of lattice dynamics in magnetite with a first-and second-order Verwey transition," *Phys. Rev. B*, vol. 85, no. 10, p. 104301, 2012.

[4] J. Honig, "Electrical transitions in metal oxides," *J. Solid State Chem.*, vol. 45, no. 1, pp. 1–13, 1982.

[5] K. Momma and F. Izumi, "VESTA: a three-dimensional visualization system for electronic and structural analysis," *J. Appl. Crystallogr.*, vol. 41, no. 3, pp. 653–658, 2008.

[6] J. Wright, J. Attfield, and P. Radaelli, "Long range charge ordering in magnetite below the Verwey transition," *Phys. Rev. Lett.*, vol. 87, no. 26, p. 266401, 2001.

[7] J. P. Wright, J. P. Attfield, and P. G. Radaelli, "Charge ordered structure of magnetite Fe_3O_4 below the Verwey transition," *Phys. Rev. B*, vol. 66, no. 21, p. 214422, 2002.

[8] R. W. Millar, "The heat capacities at low temperatures of "ferrous oxide," magnetite and cuprous and cupric oxides," *J. Am. Chem. Soc.*, vol. 51, no. 1, pp. 215–222, 1929.

[9] P. Weiss and R. Forrer, "La saturation absolue des ferromagnétiques et les lois d'approche en fonction du champ et de la température," *Ann. Phys.*, vol. 10, pp. 279–372, 1929.

[10] E. Verwey, P. Haayman, and F. Romeijn, "Physical properties and cation arrangement of oxides with spinel structures II. Electronic conductivity," *J. Chem. Phys.*, vol. 15, no. 4, pp. 181–187, 1947.

[11] P. W. Anderson, "Ordering and antiferromagnetism in ferrites," *Phys. Rev.*, vol. 102, no. 4, p. 1008, 1956.

[12] F. Walz, “The Verwey transition – a topical review,” *J. Phys.: Condens. Matter*, vol. 14, no. 12, p. R285, 2002.

[13] J. R. Cullen and E. Callen, “Collective Electron Theory of the Metal-Semiconductor Transition in Magnetite,” *J. Appl. Phys.*, vol. 41, no. 3, pp. 879–880, 1970.

[14] J. García, G. Subías, M. Proietti, J. Blasco, H. Renevier, J. Hodeau, and Y. Joly, “Absence of charge ordering below the Verwey transition temperature in magnetite,” *Phys. Rev. B*, vol. 63, no. 5, p. 054110, 2001.

[15] J. García, G. Subías, J. Blasco, and M. G. Proietti, “Comment on "Long range ordering in magnetite below the Verwey transition",” *arXiv:cond-mat/0211407*, 2002.

[16] S. Abrahams and B. Calhoun, “The low-temperature transition in magnetite,” *Acta Crystallogr.*, vol. 6, no. 1, pp. 105–106, 1953.

[17] W. C. Hamilton, “Neutron diffraction investigation of the 119 K transition in magnetite,” *Phys. Rev.*, vol. 110, no. 5, p. 1050, 1958.

[18] N. Tombs and H. Rooksby, “Structure transition and antiferromagnetism in magnetite,” *Acta Crystallogr.*, vol. 4, no. 5, pp. 474–475, 1951.

[19] H. Rooksby and B. Willis, “The low-temperature crystal structure of magnetite,” *Acta Crystallogr.*, vol. 6, no. 6, pp. 565–566, 1953.

[20] T. Yamada, K. Suzuki, and S. Chikazumi, “Electron microscopy of orthorhombic phase in magnetite,” *Appl. Phys. Lett.*, vol. 13, no. 5, pp. 172–174, 1968.

[21] E. J. Samuelsen, E. Bleeker, L. Dobrzynski, and T. Riste, “Neutron scattering from magnetite below 119 K,” *J. Appl. Phys.*, vol. 39, no. 2, pp. 1114–1115, 1968.

[22] J. Yoshida and S. Iida, “X-ray diffraction study on the low temperature phase of magnetite,” *J. Phys. Soc. Jpn.*, vol. 42, no. 1, pp. 230–237, 1977.

[23] M. Iizumi, T. Koetzle, G. Shirane, S. Chikazumi, M. Matsui, and S. Todo, “Structure of magnetite (Fe_3O_4) below the Verwey transition temperature,” *Acta Crystallogr. Sect. B: Struct. Crystallogr. Cryst. Chem.*, vol. 38, no. 8, pp. 2121–2133, 1982.

[24] Y. Yamada, C. Graham, Jr, G. Lander, and J. Rhyne, “Charge ordering and lattice instability in magnetite,” *AIP Conf. Proc.*, vol. 24, no. 1, pp. 79–85, 1975.

[25] P. Piekarz, K. Parlinski, and A. M. Oleś, “Mechanism of the Verwey transition in magnetite,” *Phys. Rev. Lett.*, vol. 97, no. 15, p. 156402, 2006.

[26] P. Piekarz, K. Parlinski, and A. M. Oleś, “Origin of the Verwey transition in magnetite: Group theory, electronic structure, and lattice dynamics study,” *Phys. Rev. B*, vol. 76, no. 16, p. 165124, 2007.

[27] M. S. Senn, J. P. Wright, and J. P. Attfield, “Charge order and three-site distortions in the Verwey structure of magnetite,” *Nature*, vol. 481, no. 7380, pp. 173–176, 2012.

[28] M. S. Senn, J. P. Wright, J. Cumby, and J. P. Attfield, “Charge localization in the Verwey structure of magnetite,” *Phys. Rev. B*, vol. 92, no. 2, p. 024104, 2015.

[29] F. Randi, I. Vergara, F. Novelli, M. Esposito, M. Dell’Angela, V. Brabers, P. Metcalf, R. Kukreja, H. A. Dürr, D. Fausti, *et al.*, “Phase separation in the nonequilibrium Verwey transition in magnetite,” *Phys. Rev. B*, vol. 93, no. 5, p. 054305, 2016.

[30] S. Park, T. Ishikawa, and Y. Tokura, “Charge-gap formation upon the Verwey transition in Fe_3O_4,” *Phys. Rev. B*, vol. 58, no. 7, p. 3717, 1998.

[31] I. Leonov, A. Yaresko, V. Antonov, and V. Anisimov, “Electronic structure of charge-ordered Fe_3O_4 from calculated optical, magneto-optical Kerr effect, and O K-edge x-ray absorption spectra,” *Phys. Rev. B*, vol. 74, no. 16, p. 165117, 2006.

[32] I. Leonov, A. Yaresko, V. Antonov, M. Korotin, and V. Anisimov, “Charge and orbital order in Fe_3O_4,” *Phys. Rev. Lett.*, vol. 93, no. 14, p. 146404, 2004.

[33] H.-T. Jeng, G. Guo, and D. Huang, “Charge-orbital ordering and Verwey transition in magnetite,” *Phys. Rev. Lett.*, vol. 93, no. 15, p. 156403, 2004.

[34] H.-T. Jeng, G. Guo, and D. Huang, “Charge-orbital ordering in low-temperature structures of magnetite: GGA+U investigations,” *Phys. Rev. B*, vol. 74, no. 19, p. 195115, 2006.

[35] K. Yamauchi, T. Fukushima, and S. Picozzi, “Ferroelectricity in multiferroic magnetite Fe_3O_4 driven by noncentrosymmetric Fe^{2+}/Fe^{3+} charge-ordering: First-principles study,” *Phys. Rev. B*, vol. 79, no. 21, p. 212404, 2009.

[36] M. S. Senn, I. Loa, J. P. Wright, and J. P. Attfield, “Electronic orders in the Verwey structure of magnetite,” *Phys. Rev. B*, vol. 85, no. 12, p. 125119, 2012.

[37] A. Chainani, T. Yokoya, T. Morimoto, T. Takahashi, and S. Todo, “High-resolution photoemission spectroscopy of the Verwey transition in Fe_3O_4,” *Phys. Rev. B*, vol. 51, no. 24, p. 17976, 1995.

[38] J.-H. Park, L. Tjeng, J. Allen, P. Metcalf, and C. Chen, “Single-particle gap above the Verwey transition in Fe_3O_4,” *Phys. Rev. B*, vol. 55, no. 19, p. 12813, 1997.

[39] D. Schrupp, M. Sing, M. Tsunekawa, H. Fujiwara, S. Kasai, A. Sekiyama, S. Suga, T. Muro, V. Brabers, and R. Claessen, “High-energy photoemission on Fe_3O_4: Small polaron physics and the Verwey transition,” *Europhys. Lett.*, vol. 70, no. 6, p. 789, 2005.

[40] F.-Y. Ran, Y. Tsunemaru, T. Hasegawa, Y. Takeichi, A. Harasawa, K. Yaji, S. Kim, and A. Kakizaki, “Angle-resolved photoemission study of Fe_3O_4 (001) films across Verwey transition,” *J. Phys. D: Appl. Phys.*, vol. 45, no. 27, p. 275002, 2012.

[41] S. Alvarado, M. Erbudak, and P. Munz, “Final-state effects in the $3d$ photoelectron spectrum of Fe_3O_4 and comparison with Fe_xO,” *Phys. Rev. B*, vol. 14, no. 7, p. 2740, 1976.

[42] K. Shiratori, S. Suga, M. Taniguchi, K. Soda, S. Kimura, and A. Yanase, “Photoemission study of Fe_3O_4,” *J. Phys. Soc. Jpn.*, vol. 55, no. 2, pp. 690–698, 1986.

[43] R. J. Lad and V. E. Henrich, “Photoemission study of the valence-band electronic structure in Fe_xO, Fe_3O_4, and α-Fe_2O_3 single crystals,” *Phys. Rev. B*, vol. 39, no. 18, p. 13478, 1989.

[44] W. Wang, J.-M. Mariot, M. Richter, O. Heckmann, W. Ndiaye, P. De Padova, A. Taleb-Ibrahimi, P. Le Fevre, F. Bertran, F. Bondino, *et al.*, “Fe t_{2g} band dispersion and spin polarization in thin films of $Fe_3O_4(001)/MgO(001)$: Half-metallicity of magnetite revisited,” *Phys. Rev. B*, vol. 87, no. 8, p. 085118, 2013.

[45] P. F. Maldague, “Optical spectrum of a Hubbard chain,” *Phys. Rev. B*, vol. 16, no. 6, p. 2437, 1977.

[46] L. Gasparov, D. Tanner, D. Romero, H. Berger, G. Margaritondo, and L. Forro, “Infrared and Raman studies of the Verwey transition in magnetite,” *Phys. Rev. B*, vol. 62, no. 12, p. 7939, 2000.

[47] Z. Zhang and S. Satpathy, “Electron states, magnetism, and the Verwey transition in magnetite,” *Phys. Rev. B*, vol. 44, no. 24, p. 13319, 1991.

[48] D. Ihle and B. Lorenz, “Small-polaron conduction and short-range order in Fe_3O_4,” *J. Phys. C: Solid State Phys.*, vol. 19, no. 26, p. 5239, 1986.

[49] G. D. Mahan, *Many-particle physics.* New York: Plenum Press, 1990.

[50] A. Schlegel, S. Alvarado, and P. Wachter, “Optical properties of magnetite (Fe_3O_4),” *J. Phys. C: Solid State Phys.*, vol. 12, no. 6, p. 1157, 1979.

[51] A. Schlegel and P. Wachter, “Optical properties of magnetite (Fe_3O_4) in the infrared,” *J. Phys. Colloq.*, vol. 41, no. C5, pp. C5–19, 1980.

[52] I. Balberg and J. Pankove, “Optical measurements on magnetite single crystals,” *Phys. Rev. Lett.*, vol. 27, no. 9, p. 596, 1971.

[53] N. Mott, “Materials with mixed valency that show a Verwey transition,” *Philos. Mag. B*, vol. 42, no. 3, pp. 327–335, 1980.

[54] I. Austin and N. F. Mott, “Polarons in crystalline and non-crystalline materials,” *Adv. Phys.*, vol. 18, no. 71, pp. 41–102, 1969.

[55] Y. Yamada, H. Takatera, and D. L. Huber, “Critical dynamical phenomena in pseudospin-phonon coupled systems,” *J. Phys. Soc. Jpn.*, vol. 36, no. 3, pp. 641–648, 1974.

[56] T. Moran and B. Lüthi, "Elastic and magnetoelastic effects in magnetite," *Phys. Rev.*, vol. 187, no. 2, p. 710, 1969.

[57] H. Schwenk, S. Bareiter, C. Hinkel, B. Lüthi, Z. Kakol, A. Koslowski, and J. Honig, "Charge ordering and elastic constants in $Fe_{3-x}Zn_xO_4$," *Eur. Phys. J. B*, vol. 13, no. 3, pp. 491–494, 2000.

[58] L. Bickford, J. Brownlow, and R. Penoyer, "Magnetocrystalline anisotropy in cobalt-substituted magnetite single crystals," *Proc. IEE B Radio Electron. Eng.*, vol. 104, no. 5S, pp. 238–244, 1957.

[59] K. Abe, Y. Miyamoto, and S. Chikazumi, "Magnetocrystalline anisotropy of low temperature phase of magnetite," *J. Phys. Soc. Jpn.*, vol. 41, no. 6, pp. 1894–1902, 1976.

[60] R. Řezníček, V. Chlan, H. Štěpánková, P. Novák, and M. Maryško, "Magnetocrystalline anisotropy of magnetite," *J. Phys.: Condens. Matter*, vol. 24, no. 5, p. 055501, 2012.

[61] V. Brabers and J. Hendrinks, "Magnetostriction of aluminium substituted magnetite," *J. Magn. Magn. Mater.*, vol. 26, no. 1-3, pp. 300–302, 1982.

[62] J.-E. Lorenzo, C. Mazzoli, N. Jaouen, C. Detlefs, D. Mannix, S. Grenier, Y. Joly, and C. Marin, "Charge and orbital correlations at and above the Verwey phase transition in magnetite," *Phys. Rev. Lett.*, vol. 101, no. 22, p. 226401, 2008.

[63] J. García, G. Subías, J. Herrero-Martín, J. Blasco, V. Cuartero, M. C. Sanchez, C. Mazzoli, and F. Yakhou, "Reexamination of the temperature dependences of resonant reflections in highly stoichiometric magnetite," *Phys. Rev. Lett.*, vol. 102, no. 17, p. 176405, 2009.

[64] W. Tabis, J. Lorenzo, A. Kozłowski, T. Kołodziej, Z. Tarnawski, Z. Kąkol, C. Mazzoli, H. Walker, N. Jaouen, D. Mannix, *et al.*, "Effect of surface polishing and oxidization induced strain on electronic order at the Verwey transition in Fe_3O_4," *J. Phys.: Condens. Matter*, vol. 25, no. 5, p. 055603, 2013.

[65] K. Chiba, K. Suzuki, and S. Chikazumi, "Diffuse electron scattering from magnetite above the Verwey transition temperature," *J. Phys. Soc. Jpn.*, vol. 39, no. 3, pp. 839–840, 1975.

[66] S. Shapiro, M. Iizumi, and G. Shirane, "Neutron scattering study of the diffuse critical scattering associated with the Verwey transition in magnetite (Fe_3O_4)," *Phys. Rev. B*, vol. 14, no. 1, p. 200, 1976.

[67] Y. Yamada, N. Wakabayashi, and R. Nicklow, "Neutron diffuse scattering in magnetite due to molecular polarons," *Phys. Rev. B*, vol. 21, no. 10, p. 4642, 1980.

[68] K. Siratori, Y. Ishii, Y. Morii, S. Funahashi, S. Todo, and A. Yanase, "Neutron diffuse scattering study of the high temperature phase of $Fe_3O_4 - \mathrm{I}$, Determination of atomic displacements at the X point in the Brillouin zone," *J. Phys. Soc. Jpn.*, vol. 67, no. 8, pp. 2818–2827, 1998.

[69] A. Bosak, D. Chernyshov, M. Hoesch, P. Piekarz, M. Le Tacon, M. Krisch, A. Kozłowski, A. M. Oleś, and K. Parlinski, “Short-range correlations in magnetite above the Verwey temperature,” *Phys. Rev. X*, vol. 4, no. 1, p. 011040, 2014.

[70] Y. Fujii, G. Shirane, and Y. Yamada, “Study of the 123-K phase transition of magnetite by critical neutron scattering,” *Phys. Rev. B*, vol. 11, no. 5, p. 2036, 1975.

[71] M. Hoesch, P. Piekarz, A. Bosak, M. Le Tacon, M. Krisch, A. Kozłowski, A. M. Oleś, and K. Parlinski, “Anharmonicity due to electron-phonon coupling in magnetite,” *Phys. Rev. Lett.*, vol. 110, no. 20, p. 207204, 2013.

[72] G. Subías, J. García, and J. Blasco, “EXAFS spectroscopic analysis of the Verwey transition in Fe_3O_4,” *Phys. Rev. B*, vol. 71, no. 15, p. 155103, 2005.

[73] S. Mukamel, *Principles of Nonlinear Optics and Spectroscopy.* Oxford University Press, 1995.

[74] M. Born and K. Huang, *Dynamical Theory of Crystal Lattices.* Oxford Clarendon Press, 1954.

[75] R. Cowley, “The theory of Raman scattering from crystals,” *Proc. Phys. Soc.*, vol. 84, no. 2, p. 281, 1964.

[76] D. E. Spence, P. N. Kean, and W. Sibbett, “60-fsec pulse generation from a self-mode-locked Ti:sapphire laser,” *Opt. Lett.*, vol. 16, no. 1, pp. 42–44, 1991.

[77] D. Strickland and G. Mourou, “Compression of amplified chirped optical pulses,” *Opt. Commun.*, vol. 55, no. 6, pp. 447–449, 1985.

[78] D. Auston and C. Shank, “Picosecond ellipsometry of transient electron-hole plasmas in germanium,” *Phys. Rev. Lett.*, vol. 32, no. 20, p. 1120, 1974.

[79] S. L. Shapiro, *Ultrashort Light Pulses: Picosecond Techniques and Applications.* Springer, New York, 1977.

[80] V. A. Lobastov, R. Srinivasan, and A. H. Zewail, “Four-dimensional ultrafast electron microscopy,” *Proc. Natl. Acad. Sci. U.S.A.*, vol. 102, no. 20, pp. 7069–7073, 2005.

[81] E. Baldini, A. Mann, S. Borroni, C. Arrell, F. Van Mourik, and F. Carbone, “A versatile setup for ultrafast broadband optical spectroscopy of coherent collective modes in strongly correlated quantum systems,” *Structural Dynamics*, vol. 3, no. 6, p. 064301, 2016.

[82] A. Othonos, “Probing ultrafast carrier and phonon dynamics in semiconductors,” *J. Appl. Phys.*, vol. 83, no. 4, pp. 1789–1830, 1998.

[83] N. Del Fatti, C. Voisin, M. Achermann, S. Tzortzakis, D. Christofilos, and F. Vallée, “Nonequilibrium electron dynamics in noble metals,” *Phys. Rev. B*, vol. 61, no. 24, p. 16956, 2000.

[84] J. Lorenzana, B. Mansart, A. Mann, A. Odeh, M. Chergui, and F. Carbone, “Investigating pairing interactions with coherent charge fluctuation spectroscopy,” *Eur. Phys. J. Spec. Top.*, vol. 222, no. 5, pp. 1223–1239, 2013.

[85] R. Merlin, “Generating coherent THz phonons with light pulses,” *Solid State Commun.*, vol. 102, no. 2-3, pp. 207–220, 1997.

[86] H. Zeiger, J. Vidal, T. Cheng, E. Ippen, G. Dresselhaus, and M. Dresselhaus, “Theory for displacive excitation of coherent phonons,” *Phys. Rev. B*, vol. 45, no. 2, p. 768, 1992.

[87] T. Stevens, J. Kuhl, and R. Merlin, “Coherent phonon generation and the two stimulated Raman tensors,” *Phys. Rev. B*, vol. 65, no. 14, p. 144304, 2002.

[88] J. Li, J. Chen, D. A. Reis, S. Fahy, and R. Merlin, “Optical probing of ultrafast electronic decay in Bi and Sb with slow phonons,” *Phys. Rev. Lett.*, vol. 110, no. 4, p. 047401, 2013.

[89] U. Stuhr, B. Roessli, S. Gvasaliya, H. M. Rønnow, U. Filges, D. Graf, A. Bollhalder, D. Hohl, R. Bürge, M. Schild, *et al.*, “The thermal triple-axis-spectrometer EIGER at the continuous spallation source SINQ,” *Nucl. Instrum. Methods Phys. Res., Sect. A*, vol. 853, pp. 16–19, 2017.

[90] W. Cochran, “Dynamical, scattering and dielectric properties of ferroelectric crystals,” *Adv. Phys.*, vol. 18, no. 72, pp. 157–192, 1969.

[91] J. Harada, J. Axe, and G. Shirane, “Neutron-scattering study of soft modes in cubic $BaTiO_3$,” *Phys. Rev. B*, vol. 4, no. 1, p. 155, 1971.

[92] A. Lehnert, *Magnetism of Individual Adatoms and of Epitaxial Monolayers.* PhD thesis, EPFL, 2009.

[93] W. Voigt, *Magneto-und elektrooptik*, vol. 3. B.G. Teubner, 1908.

[94] Z. Yang and M. Scheinfein, “Combined three-axis surface magneto-optical Kerr effects in the study of surface and ultrathin-film magnetism,” *J. Appl. Phys.*, vol. 74, no. 11, pp. 6810–6823, 1993.

[95] E. Carpene, E. Mancini, C. Dallera, E. Puppin, and S. De Silvestri, “Three-dimensional magnetization evolution and the role of anisotropies in thin Fe/MgO films: Static and dynamic measurements,” *J. Appl. Phys.*, vol. 108, no. 6, p. 063919, 2010.

[96] J. Florczak and E. D. Dahlberg, “Magnetization reversal in (100) Fe thin films,” *Phys. Rev. B*, vol. 44, no. 17, p. 9338, 1991.

[97] V. Skumryev, H. Blythe, J. Cullen, and J. Coey, “AC susceptibility of a magnetite crystal,” *J. Magn. Magn. Mater.*, vol. 196, pp. 515–517, 1999.

[98] M. Bałanda, A. Wiecheć, D. Kim, Z. Kąkol, A. Kozłowski, P. Niedziela, J. Sabol, Z. Tarnawski, and J. Honig, “Magnetic AC susceptibility of stoichiometric and low zinc doped magnetite single crystals,” *Eur. Phys. J. B*, vol. 43, no. 2, pp. 201–212, 2005.

[99] K. Parlinski, Z. Li, and Y. Kawazoe, "First-principles determination of the soft mode in cubic ZrO_2," *Phys. Rev. Lett.*, vol. 78, no. 21, p. 4063, 1997.

[100] K. Parlinski, "PHONON software," 2013.

[101] P. E. Blöchl, "Projector augmented-wave method," *Phys. Rev. B*, vol. 50, no. 24, p. 17953, 1994.

[102] J. P. Perdew, K. Burke, and M. Ernzerhof, "Generalized gradient approximation made simple," *Phys. Rev. Lett.*, vol. 77, no. 18, p. 3865, 1996.

[103] G. Kresse and J. Furthmüller, "Efficient iterative schemes for ab initio total-energy calculations using a plane-wave basis set," *Phys. Rev. B*, vol. 54, no. 16, p. 11169, 1996.

[104] A. I. Liechtenstein, V. I. Anisimov, and J. Zaanen, "Density-functional theory and strong interactions: Orbital ordering in Mott-Hubbard insulators," *Phys. Rev. B*, vol. 52, pp. R5467–R5470, 1995.

[105] A. Mann, E. Baldini, A. Tramontana, E. Pomjakushina, K. Conder, C. Arrell, F. Van Mourik, J. Lorenzana, and F. Carbone, "Probing the electron-phonon interaction in correlated systems with coherent lattice fluctuation spectroscopy," *Phys. Rev. B*, vol. 92, no. 3, p. 035147, 2015.

[106] P. Giannozzi, S. Baroni, N. Bonini, M. Calandra, R. Car, C. Cavazzoni, D. Ceresoli, G. L. Chiarotti, M. Cococcioni, I. Dabo, *et al.*, "QUANTUM ESPRESSO: a modular and open-source software project for quantum simulations of materials," *J. Phys.: Condens. Matter*, vol. 21, no. 39, p. 395502, 2009.

[107] A. Marini, C. Hogan, M. Grüning, and D. Varsano, "Yambo: An ab initio tool for excited state calculations," *Comput. Phys. Commun.*, vol. 180, no. 8, pp. 1392–1403, 2009.

[108] E. Samuelsen and O. Steinsvoll, "Low-Energy Phonons in Magnetite," *Phys. Status Solidi B*, vol. 61, no. 2, pp. 615–620, 1974.

[109] P. M. Chaikin and T. C. Lubensky, *Principles of condensed matter physics.* Cambridge university press, 2000.

[110] A. Bruce, W. Taylor, and A. Murray, "Precursor order and Raman scattering near displacive phase transitions," *J. Phys. C: Solid State Phys.*, vol. 13, no. 4, p. 483, 1980.

[111] P. Lee, T. Rice, and P. Anderson, "Conductivity from charge or spin density waves," *Solid State Commun.*, vol. 14, no. 8, pp. 703–709, 1974.

[112] S. De Jong, R. Kukreja, C. Trabant, N. Pontius, C. Chang, T. Kachel, M. Beye, F. Sorgenfrei, C. Back, B. Bräuer, *et al.*, "Speed limit of the insulator–metal transition in magnetite," *Nat. Mater.*, vol. 12, no. 10, pp. 882–886, 2013.

[113] J. L. Verble, “Temperature-dependent light-scattering studies of the Verwey transition and electronic disorder in magnetite,” *Phys. Rev. B*, vol. 9, no. 12, p. 5236, 1974.

[114] R. Waldron, “Infrared spectra of ferrites,” *Phys. Rev.*, vol. 99, no. 6, p. 1727, 1955.

[115] O. N. Shebanova and P. Lazor, “Raman spectroscopic study of magnetite ($FeFe_2O_4$): a new assignment for the vibrational spectrum,” *J. Solid State Chem.*, vol. 174, no. 2, pp. 424–430, 2003.

[116] B. Handke, A. Kozłowski, K. Parliński, J. Przewoźnik, T. Ślęzak, A. Chumakov, L. Niesen, Z. Kąkol, and J. Korecki, “Experimental and theoretical studies of vibrational density of states in Fe_3O_4 single-crystalline thin films,” *Phys. Rev. B*, vol. 71, no. 14, p. 144301, 2005.

[117] A. D. Rowan, C. H. Patterson, and L. Gasparov, “Hybrid density functional theory applied to magnetite: Crystal structure, charge order, and phonons,” *Phys. Rev. B*, vol. 79, no. 20, p. 205103, 2009.

[118] O. N. Shebanova and P. Lazor, “Raman study of magnetite (Fe_3O_4): laser-induced thermal effects and oxidation,” *J. Raman Spectrosc.*, vol. 34, no. 11, pp. 845–852, 2003.

[119] J. Blasco, J. García, and G. Subías, “Structural transformation in magnetite below the Verwey transition,” *Phys. Rev. B*, vol. 83, no. 10, p. 104105, 2011.

[120] M. B. Yazdi, K. Choi, D. Wulferding, P. Lemmens, and L. Alff, “Raman study of the Verwey transition in magnetite thin films,” *New J. Phys.*, vol. 15, no. 10, p. 103032, 2013.

[121] T. Hart, H. Temkin, and S. Adams, “Light scattering in magnetite, Fe_3O_4,” in *Proc. 4th Int. Conf. Light Scattering in Solids 3rd*, pp. 254–8, 1976.

[122] L. Degiorgi, I. Blatter-Mörke, and P. Wachter, “Magnetite: Phonon modes and the Verwey transition,” *Phys. Rev. B*, vol. 35, no. 11, p. 5421, 1987.

[123] P. Graves, C. Johnston, and J. Campaniello, “Raman scattering in spinel structure ferrites,” *Mater. Res. Bull.*, vol. 23, no. 11, pp. 1651–1660, 1988.

[124] M. L. Glasser and F. J. Milford, “Spin wave spectra of magnetite,” *Phys. Rev.*, vol. 130, no. 5, p. 1783, 1963.

[125] R. Gupta, A. Sood, P. Metcalf, and J. Honig, “Raman study of stoichiometric and Zn-doped Fe_3O_4,” *Phys. Rev. B*, vol. 65, no. 10, p. 104430, 2002.

[126] L. Gasparov, A. Rush, G. Güntherodt, and H. Berger, “Electronic Raman scattering in magnetite: Spin versus charge gap,” *Phys. Rev. B*, vol. 79, no. 14, p. 144303, 2009.

[127] A. Kumar, S. Chaudhary, D. K. Pandya, and S. K. Sharma, “Evidence of electron-phonon and spin-phonon couplings at the Verwey transition in Fe_3O_4,” *Phys. Rev. B*, vol. 90, no. 2, p. 024302, 2014.

[128] R. McQueeney, M. Yethiraj, W. Montfrooij, J. Gardner, P. Metcalf, and J. M. Honig, "Investigation of the presence of charge order in magnetite by measurement of the spin wave spectrum," *Phys. Rev. B*, vol. 73, no. 17, p. 174409, 2006.

[129] M. G. Cottam and D. J. Lockwood, *Light scattering in magnetic solids.* Wiley, New York, 1986.

[130] P. Fleury and R. Loudon, "Scattering of light by one- and two-magnon excitations," *Phys. Rev.*, vol. 166, no. 2, p. 514, 1968.

[131] T. P. Devereaux and R. Hackl, "Inelastic light scattering from correlated electrons," *Rev. Mod. Phys.*, vol. 79, no. 1, p. 175, 2007.

[132] S. Caprara, C. Di Castro, M. Grilli, and D. Suppa, "Charge-fluctuation contribution to the Raman response in superconducting cuprates," *Phys. Rev. Lett.*, vol. 95, no. 11, p. 117004, 2005.

[133] R. S. Coe, R. Egli, S. A. Gilder, and J. P. Wright, "The thermodynamic effect of nonhydrostatic stress on the Verwey transition," *Earth Planet. Sci. Lett.*, vol. 319, pp. 207–217, 2012.

[134] W. McMillan, "Theory of discommensurations and the commensurate-incommensurate charge-density-wave phase transition," *Phys. Rev. B*, vol. 14, no. 4, p. 1496, 1976.

[135] E. Specht, M. Sutton, R. Birgeneau, D. Moncton, and P. Horn, "Phase diagram and phase transitions of krypton on graphite in the one-to-two-layer regime," *Phys. Rev. B*, vol. 30, no. 3, p. 1589, 1984.

[136] K. N. Pak and W. Kinase, "Dynamic critical behaviors of pseudospin-phonon coupled system," *J. Phys. Soc. Jpn.*, vol. 38, no. 1, pp. 1–9, 1975.

[137] M. Iizumi, "Verwey transition in magnetite as a potentially incommensurate but evantually commensurate phase transition," *AIP Conf. Proc.*, vol. 53, no. 1, pp. 184–186, 1979.

[138] R. Aragón, P. Gehring, and S. Shapiro, "Stoichiometry, percolation, and Verwey ordering in magnetite," *Phys. Rev. Lett.*, vol. 70, no. 11, p. 1635, 1993.

[139] R. Aragón, "Cubic magnetic anisotropy of nonstoichiometric magnetite," *Phys. Rev. B*, vol. 46, no. 9, p. 5334, 1992.

[140] L. Bickford Jr, "Ferromagnetic resonance absorption in magnetite single crystals," *Phys. Rev.*, vol. 78, no. 4, p. 449, 1950.

[141] Y. Syono and Y. Ishikawa, "Magnetocrystalline anisotropy of x $Fe_2TiO_4 \cdot$ (1-x) Fe_3O_4," *J. Phys. Soc. Jpn.*, vol. 18, no. 8, pp. 1230–1231, 1963.

[142] K. P. Belov, “Electronic processes in magnetite (or Enigmas of magnetite),” *Phys. Usp.*, vol. 36, no. 5, pp. 380–391, 1993.

[143] L. Martín-García, A. Mascaraque, B. M. Pabón, R. Bliem, G. S. Parkinson, G. Chen, A. K. Schmid, J. de la Figuera, *et al.*, “Spin reorientation transition of magnetite (001),” *Phys. Rev. B*, vol. 93, no. 13, p. 134419, 2016.

[144] B. Calhoun, “Magnetic and electric properties of magnetite at low temperatures,” *Phys. Rev.*, vol. 94, no. 6, p. 1577, 1954.

[145] J. Cheng, G. Sterbinsky, and B. Wessels, “Magnetic and magneto-optical properties of heteroepitaxial magnetite thin films,” *J. Cryst. Growth*, vol. 310, no. 16, pp. 3730–3734, 2008.

[146] F. Heider and V. Hoffmann, “Magneto-optical Kerr effect on magnetite crystals with externally applied magnetic fields,” *Earth Planet. Sci. Lett.*, vol. 108, no. 1-3, pp. 131–138, 1992.

[147] A. Morrish and L. Watt, “Coercive force of iron oxide micropowders at low temperatures,” *J. Appl. Phys.*, vol. 29, no. 7, pp. 1029–1033, 1958.

[148] P. Dankers and N. Sugiura, “The effects of annealing and concentration on the hysteresis properties of magnetite around the PSD-MD transition,” *Earth Planet. Sci. Lett.*, vol. 56, pp. 422–428, 1981.

[149] J. Hodych, “Evidence for magnetostrictive control of intrinsic susceptibility and coercive force of multidomain magnetite in rocks,” *Phys. Earth Planet. Inter.*, vol. 42, no. 3, pp. 184–194, 1986.

[150] Ö. Özdemir, “Coercive force of single crystals of magnetite at low temperatures,” *Geophys. J. Int.*, vol. 141, no. 2, pp. 351–356, 2000.

[151] S. Xu and R. T. Merrill, “Stress, grain size, and magnetic stability of magnetite,” *J. Geophys. Res.*, vol. 97, no. B4, pp. 4321–4329, 1992.

[152] D. Margulies, F. Parker, F. Spada, R. Goldman, J. Li, R. Sinclair, and A. Berkowitz, “Anomalous moment and anisotropy behavior in Fe_3O_4 films,” *Phys. Rev. B*, vol. 53, no. 14, p. 9175, 1996.

[153] D. Margulies, F. Parker, M. Rudee, F. Spada, J. Chapman, P. Aitchison, and A. Berkowitz, “Origin of the anomalous magnetic behavior in single crystal Fe_3O_4 films,” *Phys. Rev. Lett.*, vol. 79, no. 25, p. 5162, 1997.

[154] B. D. Cullity and C. D. Graham, *Introduction to magnetic materials.* John Wiley & Sons, 2011.

[155] F. E. Luborsky, “Development of elongated particle magnets,” *J. Appl. Phys.*, vol. 32, no. 3, pp. S171–S183, 1961.

[156] J. Hodych, "Magnetostrictive control of coercive force in multidomain magnetite," *Nature*, vol. 298, no. 5874, pp. 542–544, 1982.

[157] M. Donahue and D. Porter, "OOMMF user's guide, version 1.0, interagency report NISTIR 6376, National Institute of Standard and Technology, gaithersburg, MD, 1999," *URL: http://math. nist. gov/oommf*, 2010.

[158] S. Foss, B. M. Moskowitz, R. Proksch, and E. D. Dahlberg, "Domain wall structures in single-crystal magnetite investigated by magnetic force microscopy," *J. Geophys. Res.*, vol. 103, no. B12, pp. 30551–30560, 1998.

[159] H. Richter, "The transition from longitudinal to perpendicular recording," *J. Phys. D: Appl. Phys.*, vol. 40, no. 9, p. R149, 2007.

[160] T. R. Albrecht, H. Arora, V. Ayanoor-Vitikkate, J.-M. Beaujour, D. Bedau, D. Berman, A. L. Bogdanov, Y.-A. Chapuis, J. Cushen, E. E. Dobisz, *et al.*, "Bit-patterned magnetic recording: Theory, media fabrication, and recording performance," *IEEE Trans. Magn.*, vol. 51, no. 5, pp. 1–42, 2015.

[161] P. Beauvillain, A. Bounouh, C. Chappert, R. Mégy, S. Ould-Mahfoud, J. Renard, P. Veillet, D. Weller, and J. Corno, "Effect of submonolayer coverage on magnetic anisotropy of ultrathin cobalt films M/Co/Au (111) with M= Au, Cu, Pd," *J. Appl. Phys.*, vol. 76, no. 10, pp. 6078–6080, 1994.

[162] D. Weller, J. Stöhr, R. Nakajima, A. Carl, M. Samant, C. Chappert, R. Mégy, P. Beauvillain, P. Veillet, and G. Held, "Microscopic origin of magnetic anisotropy in Au/Co/Au probed with x-ray magnetic circular dichroism," *Phys. Rev. Lett.*, vol. 75, no. 20, p. 3752, 1995.

[163] N. Nakajima, T. Koide, T. Shidara, H. Miyauchi, H. Fukutani, A. Fujimori, K. Iio, T. Katayama, M. Nỳvlt, and Y. Suzuki, "Perpendicular magnetic anisotropy caused by interfacial hybridization via enhanced orbital moment in Co/Pt multilayers: magnetic circular x-ray dichroism study," *Phys. Rev. Lett.*, vol. 81, no. 23, p. 5229, 1998.

[164] D. Weller, A. Moser, L. Folks, M. E. Best, W. Lee, M. F. Toney, M. Schwickert, J.-U. Thiele, and M. F. Doerner, "High K_u materials approach to 100 Gbits/in^2," *IEEE Trans. Magn.*, vol. 36, no. 1, pp. 10–15, 2000.

[165] J. Dorantes-Dávila, H. Dreyssé, and G. M. Pastor, "Magnetic anisotropy of transition-metal interfaces from a local perspective: reorientation transitions and spin-canted phases in Pd capped Co films on Pd (111)," *Phys. Rev. Lett.*, vol. 91, no. 19, p. 197206, 2003.

[166] S. Ouazi, S. Vlaic, S. Rusponi, G. Moulas, P. Buluschek, K. Halleux, S. Bornemann, S. Mankovsky, J. Minár, J. B. Staunton, *et al.*, "Atomic-scale engineering of magnetic anisotropy of nanostructures through interfaces and interlines," *Nat. Commun.*, vol. 3, p. 1313, 2012.

[167] O. Fruchart, M. Klaua, J. Barthel, and J. Kirschner, “Self-organized growth of nanosized vertical magnetic Co pillars on Au (111),” *Phys. Rev. Lett.*, vol. 83, no. 14, p. 2769, 1999.

[168] J. Barth, H. Brune, G. Ertl, and R. Behm, “Scanning tunneling microscopy observations on the reconstructed Au (111) surface: Atomic structure, long-range superstructure, rotational domains, and surface defects,” *Phys. Rev. B*, vol. 42, no. 15, p. 9307, 1990.

[169] W. Lee and S.-J. Park, “Porous anodic aluminum oxide: anodization and templated synthesis of functional nanostructures,” *Chem. Rev.*, vol. 114, no. 15, pp. 7487–7556, 2014.

[170] H.-Y. Hsueh, C.-T. Yao, and R.-M. Ho, “Well-ordered nanohybrids and nanoporous materials from gyroid block copolymer templates,” *Chem. Soc. Rev.*, vol. 44, no. 7, pp. 1974–2018, 2015.

[171] H. Hattab, A. T. N’Diaye, D. Wall, C. Klein, G. Jnawali, J. Coraux, C. Busse, R. van Gastel, B. Poelsema, T. Michely, *et al.*, “Interplay of wrinkles, strain, and lattice parameter in graphene on Iridium,” *Nano Lett.*, vol. 12, no. 2, pp. 678–682, 2012.

[172] T. Gerber, C. Busse, J. Mysliveček, J. Coraux, T. Michely, *et al.*, “A versatile fabrication method for cluster superlattices,” *New J. Phys.*, vol. 11, no. 10, p. 103045, 2009.

[173] F. Natterer, S. Rusponi, and H. Brune, “Graphene on close-packed metal surfaces–long range order and band gap engineering,” *SPG Mitteilungen*, vol. 34, p. 31, 2011.

[174] S. Bleikamp, P. J. Feibelman, T. Michely, *et al.*, “Two-dimensional Ir cluster lattice on a graphene moiré on Ir (111),” *Phys. Rev. Lett.*, vol. 97, no. 21, p. 215501, 2006.

[175] A. Cavallin, *Growth and Magnetism of Nanostructures Investigated by STM, MOKE, and XMCD.* PhD thesis, EPFL, 2013.

[176] C. Vo-Van, S. Schumacher, J. Coraux, V. Sessi, O. Fruchart, N. B. Brookes, P. Ohresser, and T. Michely, “Magnetism of cobalt nanoclusters on graphene on iridium,” *Appl. Phys. Lett.*, vol. 99, no. 14, p. 142504, 2011.

[177] T. Cren, S. Rusponi, N. Weiss, M. Epple, and H. Brune, “Oxidation induced enhanced magnetic susceptibility of Co islands on Pt (111),” *J. Phys. Chem. B*, vol. 108, no. 38, pp. 14685–14691, 2004.

[178] H. Elmers, J. Hauschild, and U. Gradmann, “Reorientation of magnetization states in Fe-nanostripe arrays on stepped W (110) caused by adsorption of CO, H_2 and O_2,” *J. Magn. Magn. Mater.*, vol. 198, pp. 222–224, 1999.

[179] S. Lee, S. K. Lee, C. G. Kang, C. Cho, Y. G. Lee, U. Jung, and B. H. Lee, “Graphene transfer in vacuum yielding a high quality graphene,” *Carbon*, vol. 93, pp. 286–294, 2015.

[180] P. Albrecht and J. Lyding, “Ultrahigh-vacuum scanning tunneling microscopy and spectroscopy of single-walled carbon nanotubes on hydrogen-passivated Si (100) surfaces,” *Appl. Phys. Lett.*, vol. 83, no. 24, pp. 5029–5031, 2003.

[181] J. C. Koepke, J. D. Wood, C. M. Horvath, J. W. Lyding, and S. Barraza-Lopez, “Preserving the 7×7 surface reconstruction of clean Si (111) by graphene adsorption,” *Appl. Phys. Lett.*, vol. 107, no. 7, p. 071603, 2015.

[182] X. Li, W. Cai, J. An, S. Kim, J. Nah, D. Yang, R. Piner, A. Velamakanni, I. Jung, E. Tutuc, *et al.*, “Large-area synthesis of high-quality and uniform graphene films on copper foils,” *Science*, vol. 324, no. 5932, pp. 1312–1314, 2009.

[183] X. Li, C. W. Magnuson, A. Venugopal, R. M. Tromp, J. B. Hannon, E. M. Vogel, L. Colombo, and R. S. Ruoff, “Large-area graphene single crystals grown by low-pressure chemical vapor deposition of methane on copper,” *J. Am. Chem. Soc.*, vol. 133, no. 9, pp. 2816–2819, 2011.

[184] X. Chen, B. Wu, and Y. Liu, “Direct preparation of high quality graphene on dielectric substrates,” *Chem. Soc. Rev.*, vol. 45, no. 8, pp. 2057–2074, 2016.

[185] C. H. Lui, L. Liu, K. F. Mak, G. W. Flynn, and T. F. Heinz, “Ultraflat graphene,” *Nature*, vol. 462, no. 7271, pp. 339–341, 2009.

[186] S. Morozov, K. Novoselov, M. Katsnelson, F. Schedin, D. Elias, J. A. Jaszczak, and A. Geim, “Giant intrinsic carrier mobilities in graphene and its bilayer,” *Phys. Rev. Lett.*, vol. 100, no. 1, p. 016602, 2008.

[187] S. Bae, H. Kim, Y. Lee, X. Xu, J.-S. Park, Y. Zheng, J. Balakrishnan, T. Lei, H. R. Kim, Y. I. Song, *et al.*, “Roll-to-roll production of 30-inch graphene films for transparent electrodes,” *Nat. Nanotechnol.*, vol. 5, no. 8, pp. 574–578, 2010.

[188] C. Mattevi, H. Kim, and M. Chhowalla, “A review of chemical vapour deposition of graphene on copper,” *J. Mater. Chem.*, vol. 21, no. 10, pp. 3324–3334, 2011.

[189] J. W. Suk, A. Kitt, C. W. Magnuson, Y. Hao, S. Ahmed, J. An, A. K. Swan, B. B. Goldberg, and R. S. Ruoff, “Transfer of CVD-grown monolayer graphene onto arbitrary substrates,” *ACS Nano*, vol. 5, no. 9, pp. 6916–6924, 2011.

[190] S. K. Hong, S. M. Song, O. Sul, and B. J. Cho, “Carboxylic group as the origin of electrical performance degradation during the transfer process of CVD growth graphene,” *J. Electrochem. Soc.*, vol. 159, no. 4, pp. K107–K109, 2012.

[191] S. Y. Yang, J. G. Oh, D. Y. Jung, H. Choi, C. H. Yu, J. Shin, C.-G. Choi, B. J. Cho, and S.-Y. Choi, “Metal-etching-free direct delamination and transfer of single-layer graphene with a high degree of freedom,” *Small*, vol. 11, no. 2, pp. 175–181, 2015.

[192] Y. Wang, Y. Zheng, X. Xu, E. Dubuisson, Q. Bao, J. Lu, and K. P. Loh, "Electrochemical delamination of CVD-grown graphene film: toward the recyclable use of copper catalyst," *ACS Nano*, vol. 5, no. 12, pp. 9927–9933, 2011.

[193] L. Gao, W. Ren, H. Xu, L. Jin, Z. Wang, T. Ma, L.-P. Ma, Z. Zhang, Q. Fu, L.-M. Peng, *et al.*, "Repeated growth and bubbling transfer of graphene with millimetre-size single-crystal grains using platinum," *Nat. Commun.*, vol. 3, p. 699, 2012.

[194] Z. Zhan, J. Sun, L. Liu, E. Wang, Y. Cao, N. Lindvall, G. Skoblin, and A. Yurgens, "Pore-free bubbling delamination of chemical vapor deposited graphene from copper foils," *J. Mater. Chem. C*, vol. 3, no. 33, pp. 8634–8641, 2015.

[195] H. Van Ngoc, Y. Qian, S. K. Han, and D. J. Kang, "PMMA-etching-free transfer of wafer-scale chemical vapor deposition two-dimensional atomic crystal by a water soluble polyvinyl alcohol polymer method," *Sci. Rep.*, vol. 6, p. 33096, 2016.

[196] M. Kozlov and T. J. McCarthy, "Adsorption of poly (vinyl alcohol) from water to a hydrophobic surface: effects of molecular weight, degree of hydrolysis, salt, and temperature," *Langmuir*, vol. 20, no. 21, pp. 9170–9176, 2004.

[197] R. Jishi, L. Venkataraman, M. Dresselhaus, and G. Dresselhaus, "Phonon modes in carbon nanotubules," *Chem. Phys. Lett.*, vol. 209, no. 1-2, pp. 77–82, 1993.

[198] A. Jorio, M. Dresselhaus, R. Saito, and G. Dresselhaus, *Raman spectroscopy in graphene related systems.* John Wiley & Sons, 2011.

[199] L. Malard, M. Pimenta, G. Dresselhaus, and M. Dresselhaus, "Raman spectroscopy in graphene," *Phys. Rep.*, vol. 473, no. 5, pp. 51–87, 2009.

[200] A. C. Ferrari, J. Meyer, V. Scardaci, C. Casiraghi, M. Lazzeri, F. Mauri, S. Piscanec, D. Jiang, K. Novoselov, S. Roth, *et al.*, "Raman spectrum of graphene and graphene layers," *Phys. Rev. Lett.*, vol. 97, no. 18, p. 187401, 2006.

[201] J.-U. Lee, N. M. Seck, D. Yoon, S.-M. Choi, Y.-W. Son, and H. Cheong, "Polarization dependence of double resonant Raman scattering band in bilayer graphene," *Carbon*, vol. 72, pp. 257–263, 2014.

[202] P. Poncharal, A. Ayari, T. Michel, and J.-L. Sauvajol, "Raman spectra of misoriented bilayer graphene," *Phys. Rev. B*, vol. 78, no. 11, p. 113407, 2008.

[203] W. Liu, H. Li, C. Xu, Y. Khatami, and K. Banerjee, "Synthesis of high-quality monolayer and bilayer graphene on copper using chemical vapor deposition," *Carbon*, vol. 49, no. 13, pp. 4122–4130, 2011.

[204] A. Mooradian, "Photoluminescence of metals," *Phys. Rev. Lett.*, vol. 22, no. 5, p. 185, 1969.

[205] S. D. Costa, A. Righi, C. Fantini, Y. Hao, C. Magnuson, L. Colombo, R. S. Ruoff, and M. A. Pimenta, "Resonant Raman spectroscopy of graphene grown on copper substrates," *Solid State Commun.*, vol. 152, no. 15, pp. 1317–1320, 2012.

[206] R. B. McLellan, "The solubility of carbon in solid gold, copper, and silver," *Scr. Metall.*, vol. 3, no. 6, pp. 389–391, 1969.

[207] H. Bi, F. Huang, W. Zhao, X. Lü, J. Chen, T. Lin, D. Wan, X. Xie, and M. Jiang, "The production of large bilayer hexagonal graphene domains by a two-step growth process of segregation and surface-catalytic chemical vapor deposition," *Carbon*, vol. 50, no. 8, pp. 2703–2709, 2012.

[208] C. Casiraghi, S. Pisana, K. Novoselov, A. Geim, and A. Ferrari, "Raman fingerprint of charged impurities in graphene," *Appl. Phys. Lett.*, vol. 91, no. 23, p. 233108, 2007.

[209] S. Pisana, M. Lazzeri, C. Casiraghi, K. S. Novoselov, A. K. Geim, A. C. Ferrari, and F. Mauri, "Breakdown of the adiabatic Born–Oppenheimer approximation in graphene," *Nat. Mater.*, vol. 6, no. 3, pp. 198–201, 2007.

[210] M. Lazzeri, S. Piscanec, F. Mauri, A. Ferrari, and J. Robertson, "Phonon linewidths and electron-phonon coupling in graphite and nanotubes," *Phys. Rev. B*, vol. 73, no. 15, p. 155426, 2006.

[211] P. Lespade, A. Marchand, M. Couzi, and F. Cruege, "Caracterisation de materiaux carbones par microspectrometrie Raman," *Carbon*, vol. 22, no. 4-5, pp. 375–385, 1984.

[212] A. C. Ferrari and J. Robertson, "Interpretation of Raman spectra of disordered and amorphous carbon," *Phys. Rev. B*, vol. 61, no. 20, p. 14095, 2000.

[213] G. Giovannetti, P. Khomyakov, G. Brocks, V. Karpan, J. Van den Brink, and P. J. Kelly, "Doping graphene with metal contacts," *Phys. Rev. Lett.*, vol. 101, no. 2, p. 026803, 2008.

[214] P. Khomyakov, G. Giovannetti, P. Rusu, G. v. Brocks, J. Van den Brink, and P. J. Kelly, "First-principles study of the interaction and charge transfer between graphene and metals," *Phys. Rev. B*, vol. 79, no. 19, p. 195425, 2009.

[215] A.-Y. Lu, S.-Y. Wei, C.-Y. Wu, Y. Hernandez, T.-Y. Chen, T.-H. Liu, C.-W. Pao, F.-R. Chen, L.-J. Li, and Z.-Y. Juang, "Decoupling of CVD graphene by controlled oxidation of recrystallized Cu," *RSC Adv.*, vol. 2, no. 7, pp. 3008–3013, 2012.

[216] R. Siller, W. Oates, and R. B. McLellan, "The solubility of carbon in palladium and platinum," *J. Less-Common Met.*, vol. 16, no. 1, pp. 71–73, 1968.

[217] J. Sun, Y. Nam, N. Lindvall, M. T. Cole, K. B. Teo, Y. Woo Park, and A. Yurgens, "Growth mechanism of graphene on platinum: Surface catalysis and carbon segregation," *Appl. Phys. Lett.*, vol. 104, no. 15, p. 152107, 2014.

[218] J. Coraux, A. T. N 'Diaye, C. Busse, and T. Michely, "Structural coherency of graphene on Ir (111)," *Nano Lett.*, vol. 8, no. 2, pp. 565–570, 2008.

[219] J. Coraux, M. Engler, C. Busse, D. Wall, N. Buckanie, F.-J. M. Zu Heringdorf, R. Van Gastel, B. Poelsema, T. Michely, *et al.*, "Growth of graphene on Ir (111)," *New J. Phys.*, vol. 11, no. 2, p. 023006, 2009.

[220] C. Vo-Van, A. Kimouche, A. Reserbat-Plantey, O. Fruchart, P. Bayle-Guillemaud, N. Bendiab, and J. Coraux, "Epitaxial graphene prepared by chemical vapor deposition on single crystal thin iridium films on sapphire," *Appl. Phys. Lett.*, vol. 98, no. 18, p. 181903, 2011.

[221] W. J. Arnoult and R. B. McLellan, "The solubility of carbon in rhodium, ruthenium, iridium and rhenium," *Scr. Metall.*, vol. 6, no. 10, pp. 1013–1018, 1972.

[222] C. R. Dean, A. F. Young, I. Meric, C. Lee, L. Wang, S. Sorgenfrei, K. Watanabe, T. Taniguchi, P. Kim, K. L. Shepard, *et al.*, "Boron nitride substrates for high-quality graphene electronics," *Nat. Nanotechnol.*, vol. 5, no. 10, pp. 722–726, 2010.

Acknowledgements

First of all, I would like to thank my Thesis advisor, Prof. Fabrizio Carbone. His enthusiasm and scientific vision guided me throughout my research. Since the first day, he trusted me and encouraged me to pursue my scientific ideas. I am grateful to my Thesis co-advisor, Prof. Harald Brune. He gave me the opportunity to carry out experiments in his labs. I learned a lot during my projects in his group.

I would like to thank Prof. José Lorenzana for his essential role in the interpretation of our data. I owe my entire understanding of phase transitions in solids to our scientific discussions. I am grateful to all of our collaborators. In particular, our experiments would not be successful without the expertise and the genuine interest of Prof. Henrik Rønnow, Dr. Gregory Tucker, Dr. Jérémie Teyssier and Dr. Stefano Rusponi. The interpretation of our data benefited from our fruitful exchange of scientific ideas with Prof. Andrzej Oleś, Prof. Przemysław Piekarz, Prof. Oleg Yazyev and Dr. Vamshi Katukuri.

Thanks to my group mates Andreas and Edoardo for introducing me to ultrafast optics. I learned a great deal from them. The success of our experiments also depended on the help of Dr. Frank van Mourik and Dr. Christopher Arrell. Thanks to my group mates Francesco and Raji for their support during our first beamtime at PSI. Thanks to all my group mates in LUMES and LNS, and our neighbors in LSU. They managed to create a respectful and stimulating environment, and were close to me during the most intense challenges of the last four years.

Je voudrais remercier les ateliers de mécanique et d'électronique des départements de physique et de chimie, et le service informatique, pour leur disponibilité à résoudre toutes sortes de problèmes techniques, avec rapidité et efficacité.

Desidero ringraziare tutti i maestri e i professori che hanno contribuito alla mia educazione, alle scuole e all'università, e che mi hanno insegnato che il valore dell'onestà intellettuale non è negoziabile. Da ultimo, ma più importante, grazie di cuore alla mia famiglia e ai miei amici più cari. Non esistono parole adeguate per esprimere la mia gratitudine nei loro confronti.

Curriculum Vitæ

Simone Borroni

Birth:	Busto Arsizio (Italy), November 8, 1989
Nationality:	Italian
Languages:	Italian, English, French
E-mail:	simone.borroni@epfl.ch

Education

2014 – 2018	EPFL – PhD in Physics
2011 – 2013	Politecnico di Milano – Master in Physics Engineering (110/110 cum laude)
2008 – 2011	Politecnico di Milano – Bachelor in Physics Engineering (110/110)

Publications

"Coherent generation of symmetry-forbidden phonons by light-induced electron-phonon interactions in magnetite", **S. Borroni**, E. Baldini, V. M. Katukuri, A. Mann, K. Parlinski, D. Legut, C. Arrell, F. van Mourik, J. Teyssier, A. Kozłowski, P. Piekarz, O. V. Yazyev, A. M. Oleś, J. Lorenzana, and F. Carbone, *Phys. Rev. B*, vol. 96, p. 104308, 2017.

"Mapping the lattice dynamical anomaly of the order parameters across the Verwey transition in magnetite", **S. Borroni**, G. S. Tucker, F. Pennacchio, J. Rajeswari, U. Stuhr, A. Pisoni, J. Lorenzana, H. M. Rønnow and F. Carbone, *New J. Phys.*, vol. 19, p. 103013, 2017.

"A versatile setup for ultrafast broadband optical spectroscopy of coherent collective modes in strongly correlated quantum systems", E. Baldini, A. Mann, **S. Borroni**, C. Arrell, F. van Mourik, and F. Carbone, *Structural Dynamics*, vol. 3, p. 064301, 2016.

"Real-Time Observation of Phonon-Mediated σ-π Interband Scattering in MgB_2", E. Baldini, A. Mann, L. Benfatto, E. Cappelluti, A. Acocella, V. M. Silkin, S. V. Eremeev, A. B. Kuzmenko, **S. Borroni**, T. Tan, X. Xi, F. Zerbetto, R. Merlin, and F. Carbone, *Phys. Rev. Lett.*, vol. 119, p. 097002, 2017.